



HAL
open science

A multi-physics modelling framework to describe the behaviour of nano-scale multilayer systems undergoing irradiation damage

Aurélien Villani

► **To cite this version:**

Aurélien Villani. A multi-physics modelling framework to describe the behaviour of nano-scale multilayer systems undergoing irradiation damage. Materials and structures in mechanics [physics.class-ph]. Ecole Nationale Supérieure des Mines de Paris, 2015. English. NNT : 2015ENMP0002 . tel-01139357

HAL Id: tel-01139357

<https://pastel.hal.science/tel-01139357>

Submitted on 4 Apr 2015

HAL is a multi-disciplinary open access archive for the deposit and dissemination of scientific research documents, whether they are published or not. The documents may come from teaching and research institutions in France or abroad, or from public or private research centers.

L'archive ouverte pluridisciplinaire **HAL**, est destinée au dépôt et à la diffusion de documents scientifiques de niveau recherche, publiés ou non, émanant des établissements d'enseignement et de recherche français ou étrangers, des laboratoires publics ou privés.

École doctorale 432: Sciences des métiers de l'ingénieur

THÈSE

pour obtenir le grade de docteur délivré par

L'École Nationale Supérieure des Mines de Paris

Spécialité: "Sciences et Génie des matériaux"

Présentée et soutenue publiquement par:

VILLANI Aurélien

le 12 février 2015

A Multi-Physics Modelling Framework to Describe the Behaviour of Nano-Scale Multilayer Systems Undergoing Irradiation Damage

Modélisation Multiphysique de l'Endommagement par Irradiation de Laminés Nanocristallins

Directeurs de thèse: **Esteban P. BUSSO**

Samuel FOREST

Jury:

Pr. Fionn Dunne, Imperial College London
Pr. Marc G.D. Geers, Technische Universiteit Eindhoven
Dr. Laurent Capolungo, Georgia Tech Lorraine
Pr. Mohammed Cherkaoui, Georgia Tech Lorraine
Dr. Lionel Gélébart, CEA
Pr. Esteban P. Busso, ONERA
Pr. Samuel Forest, Ecole des Mines de Paris

Rapporteur
Rapporteur
Examinateur
Président
Examinateur
Directeur de thèse
Directeur de thèse

T
H
È
S
E



Abstract

Radiation damage is known to lead to material failure and thus is of critical importance to lifetime and safety within nuclear reactors. While mechanical behaviour of materials under irradiation has been the subject of numerous studies, the current predictive capabilities of such phenomena appear limited. The clustering of point defects such as vacancies and self interstitial atoms gives rise to creep, void swelling and material embrittlement. Nanoscale metallic multilayer systems have been shown to have the ability to evacuate such point defects, hence delaying the occurrence of critical damage. In addition, they exhibit outstanding mechanical properties.

The objective of this work is to develop a thermodynamically consistent continuum framework at the meso and nano-scales, which accounts for the major physical processes encountered in such metallic multilayer systems and is able to predict their microstructural evolution and behaviour under irradiation. Mainly three physical phenomena are addressed in the present work: stress-diffusion coupling and diffusion induced creep, the void nucleation and growth in multilayer systems under irradiation, and the interaction of dislocations with the multilayer interfaces.

In this framework, the microstructure is explicitly modeled, in order to account accurately for their effects on the system behaviour. The diffusion creep strain rate is related to the gradient of the vacancy flux. A Cahn-Hilliard approach is used to model void nucleation and growth, and the diffusion equations for vacancies and self interstitial atoms are complemented to take into account the production of point defects due to irradiation cascades, the mutual recombination of defects and their evacuation through grain boundaries. In metallic multilayers, an interface affected zone is defined, with an additional slip plane to model the interface shearable character, and where dislocation cores are able to spread.

The model is then implemented numerically using the finite elements method. Simulations of biaxial creep of polycrystalline aggregates coupled with vacancy diffusion are performed for the first time, and predict strongly heterogeneous viscoplastic strain fields. The classical macroscopic strain rate dependence on the stress and grain size is also retrieved. Void denuded zones close to the multilayer interfaces are obtained in irradiation simulations of a multilayer, in agreement with experimental observations. Finally, tensile tests of Cu-Nb multilayers are simulated in 3D, where it is shown that the effect of elastic anisotropy is negligible, and evidencing a complex deformation mode.

Keywords: stress-diffusion coupling, creep, voids, Cahn-Hilliard, multilayers, irradiation.



Preface

Le jour est court, le travail est grand et les travailleurs sont paresseux, mais la récompense est immense et notre maître nous exhorte à nous hâter.

Frank Herbert

La citation, qui aurait pu être de Samuel, est l'œuvre de mon auteur de science fiction préféré, et convient tout à fait à l'ouvrage de SF qu'est ce manuscrit. Il est bien évident qu'elle est à prendre au second degré; du moins, concernant la récompense. Samuel répète toujours, à juste titre, que ce qu'on fait est "tout à fait passionnant". Je suis bien d'accord, même si certains de ses thésards, moi en tête, semblons nous acharner à le démotiver par nos pitreries et nos élucubrations sans queue ni tête.

Merci mille fois donc, Samuel, pour m'avoir supporté pendant 3 ans, pour avoir partagé vos connaissances, pour m'avoir appris à me faire mieux comprendre lors des présentations, et pour m'avoir donné un aperçu du monde de la recherche. J'espère sincèrement garder le contact pour de futurs travaux. Je remercie grandement Esteban pour ses conseils avisés, ses relectures attentives, et pour m'avoir permis d'améliorer mon côté relationnel. Je n'aurai pas pu participer à un projet Européen sans vous.

J'ai eu la chance, pendant ces dernières années, d'avoir pu côtoyer les chercheurs du centre, mais aussi d'ailleurs. En particulier, Benoît Appolaire, dont j'apprécie l'humour et le franc parler autant que le savoir-faire, et Marc Geers, qui a toujours su me consacrer un peu de son temps et m'a permis de travailler sur des sujets complémentaires très intéressants.

Il y a également dans cette thèse beaucoup de Victor de Rancourt, le binôme idéal, toujours prêt à débattre de n'importe quel problème, à me faire perdre mon temps sur des questions farfelues, et à m'en faire gagner en répondant aux miennes.

Et puis, père mèle, merci à tout les autres: Djamel, Kais et Nikolai, sans qui Zebulon aurait eu ma peau; mes compagnons de baigne en B127, toujours prêts à creuser avec nous quand on touchait le fond; Arina, et sa langue bien pendue; Vlad, toujours humble et prêt à aider; Marie-Hélène Berger, pour avoir choisi une formidable stagiaire; et tous ceux qui ont contribué à cette thèse de près ou de loin.



Contents

Abstract	i
Preface	iii
Contents	v
1 Introduction	1
1.1 Context	2
1.2 The Radinterfaces project	4
1.3 Objectives	6
1.4 Methodology	7
1.5 Outline	8
1.6 General notation	9
2 Stress diffusion coupling	11
2.1 Introduction	13
2.2 Continuum thermodynamic coupled diffusion-stress theory	14
2.2.1 Balance equations	14
2.2.2 Constitutive equations	14
2.2.3 Equilibrium composition field	17
2.3 Finite element implementation of the coupled formulation	19
2.4 Analytical and numerical solutions to some boundary values problems	21
2.4.1 Rotating disc	21
2.4.2 Vacancy diffusion around the core of an edge dislocation	23
2.4.3 Perforated plate subject to a far-field tensile stress	26
2.5 Conclusions	28
3 Field theory and simulation of creep in polycrystalline aggregates	31
3.1 Introduction	33
3.2 Kinetics of vacancy diffusion induced creep in crystals	34
3.2.1 Definition of a material point in the presence of diffusion	34

3.2.2	Coupling creep deformation and the gradient of the vacancy flux	35
3.2.3	Balance of species	37
3.2.4	Linearized theory	38
3.3	Balance laws and constitutive equations in elasto-viscoplasticity	38
3.3.1	Balance laws	38
3.3.2	Constitutive equations	38
3.4	Simulation of diffusional creep in a polycrystalline aggregates	40
3.4.1	Grain boundary description	40
3.4.2	Problem description	43
3.4.3	Results	44
3.5	Conclusions	52
4	Modeling radiation damage: a stress-diffusion - Cahn-Hilliard framework	53
4.1	Introduction	55
4.2	The Cahn-Hilliard equation	56
4.3	Choice of homogeneous free energy	58
4.3.1	Polynomial energy	59
4.3.2	Logarithmic form	60
4.4	Choice of mobility	60
4.4.1	Summary	62
4.5	Elementary solutions to the Cahn Hilliard equations	62
4.5.1	Identification of interface width and energy	62
4.5.2	Critical wavelength	66
4.6	Application of the micromorphic approach to the Cahn-Hilliard equation	67
4.7	Stress-diffusion coupled Cahn-Hilliard framework for nuclear reactors applications	68
4.7.1	Balance laws	69
4.7.2	Constitutive equations	69
4.8	Choice of parameters	73
4.9	Single void growth	76
4.10	Damage evolution in an irradiated Fe polycrystal	78
4.11	Concluding remarks and future work	78
5	Mechanical and irradiation behaviour of nano-crystalline multilayers	83
5.1	Introduction	85
5.2	Modeling approach	87
5.3	Application: mechanical behaviour of Cu-Nb systems	89
5.3.1	Interface orientation relationship influence on the macroscopic mechanical behaviour	89
5.3.2	Effect of elastic anisotropy	94
5.3.3	Hard and shearable interfaces	96
5.4	Void nucleation and evolution under irradiation	98
5.5	Conclusions and recommendations for future work	99
6	Conclusions and prospects for future work	103
6.1	Coupling stress, strain, and diffusion of point defects	104
6.2	Void nucleation and growth in irradiated crystalline materials	105
6.3	Mechanical behaviour of Cu-Nb multilayers	106
6.4	Long-term perspectives	106

A	Derivation of open system elastic constants	109
B	Finite element derivatives	111
B.1	Terms K_{uX}	111
B.2	Terms K_{c^iX}	111
B.3	Terms K_{c^vX}	112
B.4	Terms $K_{c_\chi X}$	112
C	Cahn Hilliard framework	115
C.1	Normalisation	115
C.2	Derivatives needed for numerical implementation	116
C.2.1	Diffusion potential	116
C.2.2	Free energy	119
C.2.3	Misc	121
D	Code samples	123
	Bibliography	125
	Index	137

Introduction

Résumé

Entre 2005 et 2020, la demande énergétique aura crû de 50%, satisfaite en grande partie grâce aux énergies fossiles. L'énergie nucléaire, fission ou fusion, représente une part importante du mix énergétique du futur. Dans ces centrales, les matériaux subissent des conditions de service extrêmes: très haute pression et température, corrosion, irradiation. De la génération III à la génération IV, ces conditions ne feront qu'empirer: la température maximum passera de 325°C à 600°C, la dose d'irradiation doublera, etc. Le coeur du réacteur ne peut être remplacé et conditionne donc la durée de vie de toute la centrale.

L'endommagement par irradiation commence toujours avec la création de défauts ponctuels, tels que les lacunes et les auto-interstitiels, générés par les collisions entre les atomes du réseau cristallin et les particules énergétiques incidentes (hélium, neutrons, ...). Ces défauts diffusent dans le matériau, et s'agrègent en structures 2D et 3D, modifiant considérablement ses propriétés, provoquant fluage, gonflement, et fragilisation. La dose d'irradiation s'exprime souvent en déplacements par atome: 40 dpa pendant 40 ans signifie qu'au cours de cette période chaque atome aura été déplacé 40 fois.

La vocation première des matériaux pour le nucléaire est donc d'offrir des capacités de tolérance à l'irradiation importante. L'émergence de nouveaux concepts, s'appuyant sur les nanotechnologies, promet d'augmenter ces capacités de manière significative. Du fait d'une haute densité d'interface, ces nano-matériaux sont capables de s'auto-réparer et de piéger les défauts d'irradiation, ralentissant considérablement l'endommagement. L'approche présentée dans cette thèse s'inscrit dans le projet Européen Radinterfaces, dont l'objectif est d'étudier et caractériser le comportement sous irradiation de multi-couches nanométriques, via une approche multi-échelle. Les objectifs de cette thèse sont, dans le cadre de la mécanique des milieux continus, les suivants:

- *Les défauts ponctuels sont les premiers types de défauts d'irradiation. Il est donc critique de modéliser précisément leur diffusion dans un champ de contraintes hétérogène, dans un matériau complexe.*

- *La diffusion de lacunes produisant du fluage, le second objectif est de relier de manière explicite la vitesse locale de fluage au flux de lacunes, permettant ainsi une description détaillée du champ de déformation dans un polycristal.*
- *Du fait de leur densité d'interface élevée, les mécanismes de déformation des nano-matériaux sont souvent pilotés par les interactions entre les interfaces et les défauts 1D, 2D, et 3D. Il est donc nécessaire d'étudier comment le type d'interface et l'orientation relative des cristaux influencent la résistance mécanique.*
- *Enfin, si le matériau est incapable d'évacuer les défauts ponctuels suffisamment vite, ceux-ci se rassemblent en clusters et cavités. Un cadre thermodynamique est donc mis en place afin d'identifier les propriétés du nano-matériau permettant de retarder au mieux ces phénomènes délétères.*

Dans l'approche considérée dans cette thèse, la microstructure est explicitement modélisée, afin de traiter au mieux l'interaction défauts/interfaces. De plus, il est connu que la force motrice pour la diffusion est fortement affectée par les joints de grains, via un couplage chimie-mécanique. Leur modélisation explicite permet donc d'obtenir un flux de lacunes, et donc une déformation de fluage, réaliste dans le polycristal. Le modèle vient combler un fossé présent dans la littérature, dont les travaux soit négligeaient le caractère couplé de la force motrice, soit limitaient la déformation de fluage aux joints de grains. Le cadre de modélisation est ensuite étendu afin de prendre en compte l'interaction entre les défauts d'irradiation, ainsi que la formation de cavités via un modèle de type Cahn-Hilliard, couplé à la plasticité cristalline.

Contents

1.1	Context	2
1.2	The Radinterfaces project	4
1.3	Objectives	6
1.4	Methodology	7
1.5	Outline	8
1.6	General notation	9

1.1 Context

The need for energy in the world is ever-growing, +50% from 2005 to 2020, and will be mainly satisfied by fossil fuel in the near future [73]. However, nuclear power is considered as an important part of the energetic mix, taking into account efficiency and environmental impact. In these power plants, materials experience harsh service conditions: extreme pressure, thermal and chemical loading, and irradiation damage. Components have to preserve their integrity during the lifetime of the plant, typically planned initially 40 years. Those situated inside the concrete containment building, fig. 1.1, will sustain large irradiation dose [13].

In the generation III Pressurised Water Reactor (PWR), the reactor fuel is either uranium or plutonium. It is usually made up of low alloy steels, 20 cm thick, coated by a 5mm thin stainless steel to prevent corrosion. The core of the pressure vessel is cooled by the primary water circuit, with internal pressure of up to 150 bars. The water temperature is approximately

towards the development of fast neutron reactor are concentrated on solutions using sodium as the primary cooling media, known as Sodium Fast Reactor (SFR). The main differences, compared to PWR, are as follows:

- the distance from the fuel assembly to the pressure vessel walls is larger, hence leading to an almost negligible level of irradiation.
- the service temperature ranges from 350°C in the primary circuit, to 650°C in the fuel assembly.

The design in the fuel pin has to be modified so as to minimise swelling since combustion rates will be relatively high (i.e. 100 dpa over 10 years). For the generation IV reactors, the main materials being considered are 316L steel, Ni alloys, oxide dispersed strengthening alloys, and 9% Cr steel. However, due to the high irradiation loads in the fuel assembly and relatively high temperatures, it is of crucial importance to explore alternative original material solutions.

1.2 The Radinterfaces project

A common goal for materials in nuclear reactors, like containment vessels or fuel cladding materials, is to exhibit the highest radiation tolerance. The emergence of new concepts using nanoscience in the design of bulk structural materials shows potential for providing the breakthroughs needed for future nuclear energy systems. Regardless of the type of reactor (fusion or fission), and its generation, the irradiation damage first appears as point defects within the material: vacancies, self interstitial atoms (denoted SIA), or extrinsic defects such as hydrogen or helium. New advances in nano sciences allow for the design of self-healing materials, in particular, carefully constructed interfaces have the potential to absorb defects, see for example He in Cu-Nb multilayers in fig. 1.2 [17, 59, 70]. If points defects are prevented from clustering,

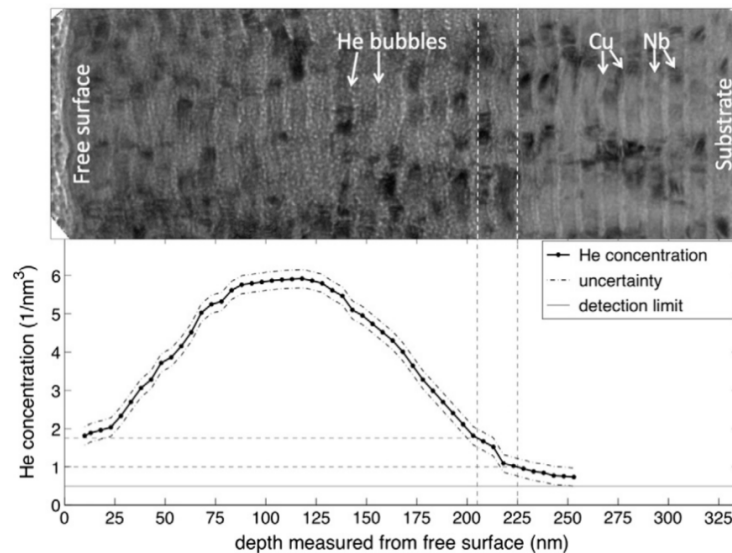


Figure 1.2: A comparison between the TEM micrograph of a He^3 -implanted Cu–Nb multilayer (top) and the corresponding He concentration profile measured by Nuclear Reaction Analysis (bottom) reveals a critical depth at which no He bubbles are observed (indicated by dashed lines), even though the He concentration is not zero. [38]

the original microstructure of the material will be preserved for a longer period of time, hence

extending the lifetime of the component. In order to unlock the full potential of nanoscience in designing materials for nuclear systems, it is necessary to develop an extensive physical and chemical understanding of defect production, diffusion, and trapping under extreme conditions of temperature, radiation, and stresses. Theory, modelling and simulation tools can provide detailed understanding and predictive capabilities for nanostructured functional materials applied to nuclear energy systems.

The study of such materials is by nature multiscale, both in time and space: the initial irradiation cascade lasts only a few picoseconds and is extremely localised, whereas the processes leading to creep and void swelling can take months and lead to large volume change in a reactor component. It is then necessary to understand the physics behind all these processes, starting from point defect production and diffusion, to void growth and mechanical failure. At each scale, physically sound parameters need to be determined and passed on to the upper scales, from atomistic to continuum mechanics, assisted by experimental observations.

The approach to be developed in this thesis will be applied to nanoscale metallic multilayer composites, whose interfaces have been studied extensively in the past few years, both experimentally and theoretically, with promising results [21, 124, 78]. The interfaces between two neighboring alloys has been observed to be preferential recombination zones for point defects. Since the density of interfaces in these nanomaterials is very high, this effectively allows for self-healing. Moreover, interfaces also modify the behaviour of dislocations in the layer, which may lead to outstanding mechanical properties.

The present PhD work is part of the European Radinterfaces project, involving nine universities, fig. 1.3, which aims to control radiation damage in nanocrystalline materials through interface design using multiscale modelling concepts and techniques. The project was part of the seventh framework programme, and addressed the call “Modelling of degradation and reliability of crystalline materials”.



Figure 1.3: Academic partners of the Radinterfaces consortium

The multiphysics approach developed in the European project combined density functional theory (DFT) to characterise the interface structure at the electronic level, molecular dynamics, kinetic Monte Carlo and dislocation dynamics to study defect interactions at the atomistic and defect level, and continuum approaches to study void evolution and mechanical behaviour at the

scale of the global multilayer system. The DFT simulations of interface structure and diffusion barriers were carried out by the Universities of Oviedo, Tartu, and Uppsala. Study of interfacial radiation damage, using OKMC simulations, were realised by the IMDEA, the Polytechnic University of Madrid, and the University of Oviedo. The development of the multiphysics meso-scale framework predicting the evolution and effects of the irradiation damage was carried out by GeorgiaTech Lorraine and the Ecole des Mines de Paris. Finally, the multilayer processing and characterisation was assigned to the IMDEA and the Universities of Cagliari and Prague. An example of voids observed by the IMDEA team in a Cu-Nb sample is shown in fig. 1.4.

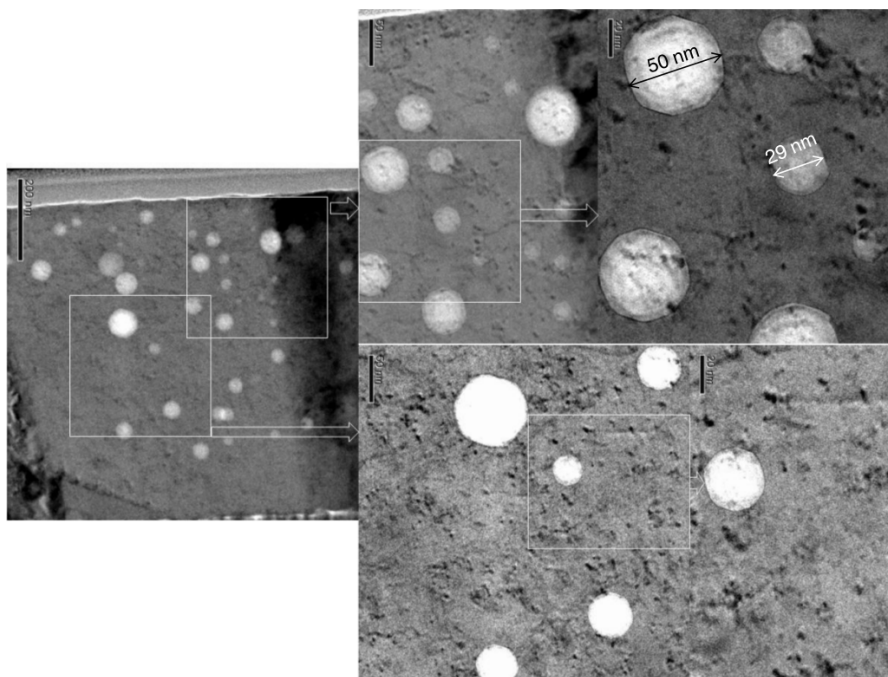


Figure 1.4: Voids in the copper layer of a Cu-Nb sample obtained by physical vapor deposition, observed by the IMDEA team by TEM after 1 dpa.

1.3 Objectives

The present work is focused on the meso and nano-scales. A continuum modelling framework is developed to predict the evolution of the irradiation damage and the material behaviour. The objectives are as follows.

- Point defects are the primary type of defects produced by irradiation damage. It is thus critical to model accurately their motion in complex material systems operating under severe loading and environmental conditions. The first objective is then to derive a continuum stress-diffusion coupled framework at the macro and meso scale.
- As stated previously, irradiation produces many point defects, in particular, vacancies, whose diffusion leads to creep. In crystalline metallic materials, the driving force for vacancy diffusion is the difference between chemical potentials in the grain boundaries. The second objective of this work is thus to describe strain fields inside the grains arising from diffusion processes and dislocation slip in a polycrystal subjected to a constant applied mechanical load.

- In nanoscale materials, the density of interfaces is very high, and the macroscopic mechanical behaviour is driven by interface processes. For instance, dislocation glide and climb is strongly impacted by the nanoscale features of the microstructure. It is necessary investigate how the type of interface and the orientation of the crystals affect the mechanical resistance, in order to obtain the desired system properties.
- If the multilayer is unable to evacuate or recombine point defects at a sufficient rate, the defects form clusters and voids. It is then necessary to identify the multilayer properties leading to the best lifetime, such as interface orientation relationship, layer thickness, etc. The last objective is to develop a continuum framework to describe evolution of self interstitials and vacancies, and their interactions with interfaces, as well as void nucleation and growth in a multilayer.

1.4 Methodology

Most deleterious effects of irradiation on material properties - e.g. void swelling, irradiation creep, radiation-induced hardening and embrittlement - can be traced back to the formation and migration of the aforementioned point defects. It is well known that stresses influence the diffusion of point defects, and vice versa. The larger the inhomogeneities in stresses, the larger their influence on diffusion. The Cottrell atmospheres, which consist of the redistribution of point defects around a dislocation, is a well known example [64]. Recently, Cahn [25] published a paper on these atmospheres, to “correct the misconception in the literature that the solute distribution does not affect the stress field of the dislocation”.

It is then critical to lay out a fundamental thermodynamic framework, coupling stress and diffusion, on which to base the work of this thesis. Podstrigach and coworkers [101] were the first to develop a thermodynamic theory of stress diffusion coupling, relying on the choice of a free energy. Analytical solutions were proposed for a loaded plate with a void [102] and a bended plate [98]. Cahn and Larché [27] later developed a coupled stress-diffusion theory, where the coupling came from the mechanical constitutive laws. Indeed, the use of a concentration-dependent eigenstrain gives rise to a stress-dependent diffusion potential. Furthermore, Cahn and Larché presented a systematic procedure to solve stress diffusion coupled problems, provided an elastic behaviour was considered. It relies on open system elastic constants, or elastic constants derived at constant diffusion potential, in order to obtain a linearised version of the non-linear coupled problem. It is the latter approach that is developed in the work, and extended to elasto-viscoplastic behaviour, using internal variable concepts [16].

The previous framework describes the migration of point defects in a heterogeneous stress field, but their contribution to the deformation is reversible, while the diffusion of vacancies at high temperatures is known to induce creep deformation [63]. The associated driving force in polycrystals is the difference of the diffusion potential from one grain boundary to another, which is modified by the normal traction on the corresponding grain boundary surfaces. This is of interest for the present nanolayered material since the grain boundary volume fraction is large and since they are expected to operate at high temperatures. Furthermore, a detailed description of the grain boundary is necessary to accurately describe their interaction with radiation induced defects. It has been shown by molecular dynamics simulations that grain boundaries play a critical role in defects recombination [99, 106, 8, 60]. Hence, the previous framework will be extended to account for diffusion creep in an original and detailed manner. The work is conducted at the mesoscale, with an explicit geometrical description of grain and grain boundaries in order to model the change of diffusion potential at grain boundaries, and hence the vacancy diffusion driving force. Then, the viscoplastic deformation rate will be shown

to be proportional to the gradient of the vacancy flux [15, 111]. In the literature, similar works modelling diffusion creep have been proposed, however they lack either a natural driving force [56, 117], or were confining the strain to the grain boundary region [14, 49]. The present model addresses these gaps, and enables the description of deformation fields inside the grains arising from diffusion processes and dislocation slip in a polycrystal subjected to constant applied loads.

Up to this point, the proposed framework describes the point defects migration, with a strong coupling with stress. The natural next step is then to describe the formation of voids when the vacancy concentration becomes larger than a critical value. Phase field methods have proven useful for that purpose [105, 87], along with modified point defects balance equations to account for irradiation effects. Such phase field models have also been used to simulate the void denuded zones close to grain boundaries [86, 7]. However, previous work lack an explicit mechanical coupling with the stress. For instance in [11], it was proposed that, during creep, voids grow by receiving stress-driven vacancy fluxes from nearby grain boundary sources. The presently proposed framework, with its detailed description of grain boundaries, can then be complemented by a phase field model to study the influence of stress on the growth kinetics of voids.

Finally, nanoscale multilayers composed of alternate layers of two immiscible metals are considered. In such materials, the macroscopic behaviour is mainly driven by the interfaces between each layer [78, 59]. In the literature, most of the effort has been focused on experimental techniques and atomistic scale modelling, see for instance [18, 79]. Here, a continuum approach is followed at the nanoscale, whereby a diffuse interface-affected zone with specific properties is defined. Regarding mechanical properties, as molecular dynamics simulations reveal significant dislocation core spreading at interfaces [108], the latter are defined in the continuum model as a dislocation sink. Furthermore, the interface is treated as a crystallographic slip plane to model its shearable character [123]. Concerning interface interaction with point defects, the interface affected zone is modeled as a preferential defect recombination zone [70, 76].

1.5 Outline

The thesis is divided in four chapters, each corresponding to one of the above mentioned objectives.

First, a stress-diffusion coupled framework is presented in Chapter 2 based on the Cahn and Larché approach, complemented by the introduction of internal variables necessary to address plasticity. The model is implemented numerically into a finite element code and used to solve three boundary value problems. The numerical solutions are validated against analytical ones, and the influence of plasticity on the defect distribution is discussed.

Next, in Chapter 3, the creep kinetics is formulated. The diffusion creep strain-rate tensor is derived as the deviatoric symmetric part of the gradient of the vacancy flux. A crystal plasticity model is used to describe the inelastic strain arising from dislocation glide and climb. Then, a coupled framework, retrieving Herring Nabarro's diffusion relation, is presented and used to predict creep behaviour of a polycrystal. The numerical results are in good agreement with the experimental ones, and detailed deformation fields inside the grains are obtained.

In order to model void nucleation and growth, a Cahn-Hilliard based framework is proposed in Chapter 4 and implemented numerically using a micromorphic approach [46]. The diffusion equations are modified to account for point defects recombination and evacuation in sinks such as interfaces. The stress diffusion couplings developed in the previous chapter are included in the framework, leading to a modified Cahn-Hilliard equation, where the kinetics is influenced by elastic energy in the solid. Two applications are presented: the point defect evolution in a

polycrystal is studied first, using constant or dose dependent material parameters obtained by cluster dynamics simulation. Then, the influence of mechanical coupling on the growth kinetics of a void is investigated.

Finally, in Chapter 5, the mechanical behaviour and resistance to irradiation of nano multilayers is investigated. Simulations using the finite element method are performed to compare the hard and shearable interface models in terms of macroscopic stress strain curves on Cu-Nb systems. Using the Cahn-Hilliard model developed in Chapter 4, the irradiation of a generic bilayer is simulated. Void nucleation and growth is observed in the bulk, while the interface affected zone remains void free. This model is combined with the previously developed stress diffusion coupled phase field framework to study the behaviour of an irradiated Cu-Nb bilayer.

1.6 General notation

A Cartesian coordinate system, with unit vectors $\underline{e}_1, \underline{e}_2, \underline{e}_3$, is used throughout the manuscript, unless specified otherwise. Following the Einstein summation convention, repeated indices are summed. The following notations are generally used in the present work.

Scalar	a
Vector	\underline{v}
Second order tensor	$\underline{\sigma}$
Fourth order tensor	$\underline{\underline{C}}$
Tensor product	$c = \underline{a} \cdot \underline{b} = a_i b_i$
Open product	$\underline{c} = \underline{a} \otimes \underline{b} = a_i b_j \underline{e}_i \otimes \underline{e}_j = c_{ij} \underline{e}_i \otimes \underline{e}_j$
Concentration fields	c^i, c^v, \dots
Fluxes	$\underline{J}^i, \underline{J}^v, \dots$
Generalized stresses	$\pi, \underline{\xi}$
Displacement	\underline{u}
Strain tensors	$\underline{\varepsilon}$
Phase fields	$\phi, \phi^{GB}, \phi^{int}, \dots$

Stress diffusion coupling

Most deleterious effects of irradiation on material properties - e.g. void swelling, irradiation creep, radiation-induced hardening and embrittlement - can be traced back to the formation and migration of the point defects. It is well known that stresses influence the diffusion of point defects, but the effect of point defects on the stress field is often neglected. It is critical to lay out a fundamental thermodynamic framework, coupling stress and diffusion, on which to base the work of this thesis. This chapter is reproduced from [120].

Résumé

Un cadre thermodynamique couplant la mécanique non linéaire et la diffusion est proposé et implémenté numériquement via la méthode des éléments finis. Celle-ci est validée sur des solutions analytiques, reposant sur la méthode de Cahn et Larché étendue à la plasticité. Une attention particulière est donnée aux constantes élastiques à système ouvert, i.e. celles dérivées à potentiel de diffusion constant, puisqu'elles permettent d'obtenir la solution du problème couplé complet uniquement à partir d'une solution élastique équivalente. Enfin, les effets de la plasticité sur l'équilibre global du système sont discutés.

Summary

A macroscopic coupled stress-diffusion theory which account for the effects of non-linear material behaviour, based on the framework proposed by Cahn and Larché, is presented and implemented numerically into the finite element method. The numerical implementation is validated against analytical solutions for different boundary valued problems. Particular attention is paid to the open system elastic constants, i.e. those derived at constant diffusion potential, since they enable the equilibrium composition field for any generic chemical-mechanical coupled problem to be obtained through the solution of an equivalent elastic problem. Finally, the effects of plasticity on the overall equilibrium state of the coupled problem solution are discussed.

Contents

2.1	Introduction	13
2.2	Continuum thermodynamic coupled diffusion-stress theory	14
2.2.1	Balance equations	14
2.2.2	Constitutive equations	14
2.2.2.1	General theory	14
2.2.2.2	Choice of potential and energy functions	16
2.2.3	Equilibrium composition field	17
2.2.3.1	Theory	17
2.2.3.2	Methodology for deriving analytical solutions of a stress-diffusion coupled problem	19
2.3	Finite element implementation of the coupled formulation	19
2.4	Analytical and numerical solutions to some boundary values problems	21
2.4.1	Rotating disc	21
2.4.2	Vacancy diffusion around the core of an edge dislocation	23
2.4.3	Perforated plate subject to a far-field tensile stress	26
2.5	Conclusions	28

2.1 Introduction

Problems involving diffusion in a stressed material system can be found in numerous applications generally concerned with high homologous temperatures, such as thin films in semiconductor devices and power plant and aero-engine components. The transport of matter by diffusion under stress can generally result in the gradual degradation of the material microstructure, leading to the nucleation of local damage (e.g., stable vacancy clusters or micro-voids, micro-cracks). The presence of such local damage events could impede the correct performance of the component or device and limit its targeted service life. It is thus critical to model accurately the motion of diffusing species and point defects in complex material systems operating under severe loading and environmental conditions.

Podstrigach and coworkers [101] were the first to develop a thermodynamic theory of stress diffusion coupling. It relies on the choice of a free energy, and analytical solutions are proposed for a loaded plate with a void [102] and a bended plate [98]. Cahn and Larché [27] later developed a coupled stress-diffusion theory, where the coupling came from the mechanical constitutive laws. In their thermodynamic theory (see [28] for full details, and [9] for a broad discussion), the convenient concept of network is introduced, whereby all atoms are assumed to be capable of diffusing. In a crystal, for instance, the lattice itself can be assumed to act as the network and to remain coherent. Equilibrium can then be attained by considering a constant and homogeneous diffusion potential. Cahn and Larché also introduced the concept of open system elastic constants, or elastic constants derived at constant diffusion potential, in order to obtain a linearised version of the non-linear coupled problem. Maugin [80] also addressed extensively the thermodynamic problem of a diffusive variable, without stress-coupling, albeit considering the first gradient of the concentration as well.

Other approaches have been used to model specific problems involving the coupling between stress and diffusion. For instance, the diffusion of vacancies within the heterogeneous stress field around an edge dislocation core has been treated in [104] using Bessel functions. In contrast, boundary value problems involving coupled diffusion-stress phenomena have been solved analytically using Cosserat spectrum theory in [97]. In [130] and [131], finite element solutions involving stress-induced diffusion in a plate subject to different types of boundary conditions were reported. In [116], the authors relied on Lambert functions to derive an analytical solution of the chemical concentration in a loaded rod, and compared it to a coupled finite element formulation. Finally, Anand [6] developed a thermodynamical theory which accounts for diffusion of hydrogen and heat coupled with the mechanical problem.

The theory is implemented numerically using the finite element method and used to solve three elastic and elasto-plastic stress-diffusion boundary value problems, out of which two were never addressed in the literature before. The first one involves a coupled diffusion-stress formulation for a disc rotating at high speeds and temperature, i.e. at conditions similar to those encountered in gas turbine engine components. The second concerns the classical redistribution of vacancies around an edge dislocation, as described in [64], which can be related to a recent paper by Cahn [25]. Finally, a problem relevant to vacancy diffusion-driven cavitation in nuclear reactor components is studied, i.e. the redistribution of vacancies in a loaded perforated plate, influenced by plasticity.

The objective of the present paper is to provide a validation of the fully coupled implementation against the systematic analytical solution given by Cahn and Larché, complemented by the introduction of internal variables necessary to address plasticity. The introduction of plasticity in the constitutive equations allows for a direct extension of the solution of Cahn and Larché, given for an elastic behaviour. If the stress diffusion coupling had been dependant on the choice of free energy, it would have been less straightforward to obtain coupled analytical solution for

plasticity.

The formulation is limited to the small strain isothermal case for which analytical solutions can be derived.

2.2 Continuum thermodynamic coupled diffusion-stress theory

2.2.1 Balance equations

The diffusing species are assumed to be solute atoms and vacancies. Their concentration obeys the mass balance equation, which relates the concentration, c , to the flux vector, $\underline{\mathbf{J}}$,

$$\begin{aligned} \dot{c} &= -\operatorname{div} \underline{\mathbf{J}} \text{ on } V \\ j &= \underline{\mathbf{J}} \cdot \underline{\mathbf{n}} \text{ on } \partial V \end{aligned} \quad (2.1)$$

where no source term is considered. The concentration is defined as the ratio between the lattice sites occupied by solute atoms or vacancies and the total number of lattice sites in the crystalline solid. The mechanical static equilibrium is defined by:

$$\begin{aligned} \operatorname{div} \underline{\boldsymbol{\sigma}} + \underline{\mathbf{f}} &= 0 \text{ on } V \\ \underline{\mathbf{t}} &= \underline{\boldsymbol{\sigma}} \cdot \underline{\mathbf{n}} \text{ on } \partial V \end{aligned} \quad (2.2)$$

where $\underline{\boldsymbol{\sigma}}$ is the stress tensor, $\underline{\mathbf{f}}$ is the body force vector in V and $\underline{\mathbf{t}}$ the traction vector acting on ∂V .

2.2.2 Constitutive equations

2.2.2.1 General theory

The total strain is partitioned as:

$$\underline{\boldsymbol{\varepsilon}} = \underline{\boldsymbol{\varepsilon}}^e + \underline{\boldsymbol{\varepsilon}}^p + \underline{\boldsymbol{\varepsilon}}^*(c) \quad (2.3)$$

where $\underline{\boldsymbol{\varepsilon}}^e$ is the elastic strain tensor, $\underline{\boldsymbol{\varepsilon}}^p$ the plastic strain tensor, and $\underline{\boldsymbol{\varepsilon}}^*$ the eigenstrain tensor, representing the volume change associated with the substitution of species in lattice sites. The latter typically depends on the concentration, c , as

$$\underline{\boldsymbol{\varepsilon}}^*(c) = (c - c_{ref}) \underline{\boldsymbol{\eta}} + \underline{\boldsymbol{\varepsilon}}_{ref}^* . \quad (2.4)$$

Here, $\underline{\boldsymbol{\varepsilon}}^{*,ref}$ is the eigenstrain tensor corresponding to the reference concentration, c_{ref} , and the tensor $\underline{\boldsymbol{\eta}} = \frac{\partial \underline{\boldsymbol{\varepsilon}}}{\partial c}$ scales the concentration change. Recall the first law of thermodynamics:

$$\int_V \dot{e} dV = \int_V \underline{\boldsymbol{\sigma}} : \dot{\underline{\boldsymbol{\varepsilon}}} dV \quad (2.5)$$

where, e , is the internal energy density per unit volume and $\underline{\boldsymbol{\sigma}}$ the stress tensor. The second law states that:

$$\int_V \dot{s} dV - \int_{\partial V} \frac{\mu \underline{\mathbf{J}}}{T} \cdot \underline{\mathbf{n}} dS \geq 0 \quad (2.6)$$

where, s , is the entropy density, T , the absolute temperature, and μ the diffusion potential¹. The local form of the second law (2.6), for constant temperature, reads:

$$T \dot{s} - \operatorname{div} (\mu \underline{\mathbf{J}}) \geq 0 \quad (2.7)$$

¹In the sense of Cahn and Larché: $\mu = \mu^s - \mu^h$, where μ^s is the chemical potential of the species under consideration, and μ^h is the chemical potential of the host atoms

Recalling $\psi = e - Ts$, the free energy density per unit volume at constant temperature, then equation (2.7) yields the local form of the dissipation inequality:

$$\mathcal{D} = \underline{\boldsymbol{\sigma}} : \dot{\underline{\boldsymbol{\xi}}} - \operatorname{div}(\mu \underline{\mathbf{J}}) - \dot{\psi} \geq 0 \quad (2.8)$$

Here, the free energy volumetric density function is assumed to consist of a mechanical and a chemical part, which depend on several independent state variables, i.e. the elastic strain tensor $\underline{\boldsymbol{\xi}}^e$, an isotropic scalar hardening variable r , a traceless kinematic tensorial hardening variable, $\underline{\boldsymbol{\alpha}}$ [72], and the vacancy concentration, c . Then,

$$\psi(\underline{\boldsymbol{\xi}}^e, r, \underline{\boldsymbol{\alpha}}, c) = \psi^{mech}(\underline{\boldsymbol{\xi}}^e, r, \underline{\boldsymbol{\alpha}}, c) + \psi^{chem}(c). \quad (2.9)$$

The mechanical part of the free energy is defined as,

$$\psi^{mech}(\underline{\boldsymbol{\xi}}^e, r, \underline{\boldsymbol{\alpha}}, c) = \frac{1}{2} \underline{\boldsymbol{\xi}}^e : \underline{\underline{\Lambda}}(c) : \underline{\boldsymbol{\xi}}^e + \psi^{mech,p}(r, \underline{\boldsymbol{\alpha}}, c), \quad (2.10)$$

where $\underline{\underline{\Lambda}}$ is elastic moduli fourth order tensor, and $\psi^{mech,p}(r, \underline{\boldsymbol{\alpha}}, c)$ corresponds to the energy stored by work-hardening. The dissipation can then be expressed in terms of equations (2.8), (2.1) and (2.9) as:

$$\mathcal{D} = \left(\underline{\boldsymbol{\sigma}} - \frac{\partial \psi}{\partial \underline{\boldsymbol{\xi}}^e} \right) : \dot{\underline{\boldsymbol{\xi}}^e} + \left(\mu + \underline{\boldsymbol{\sigma}} : \underline{\boldsymbol{\eta}} - \frac{\partial \psi}{\partial c} \right) \dot{c} - \underline{\mathbf{j}} \cdot \underline{\nabla} \mu + \underline{\boldsymbol{\sigma}} : \underline{\boldsymbol{\xi}}^p - \frac{\partial \psi}{\partial r} \dot{r} - \frac{\partial \psi}{\partial \underline{\boldsymbol{\alpha}}} : \dot{\underline{\boldsymbol{\alpha}}} \geq 0 \quad (2.11)$$

The condition (2.11) depends linearly on the independent variables $\underline{\boldsymbol{\xi}}^e$, \dot{c} , and the terms in brackets are independent of $\underline{\boldsymbol{\xi}}^e$ and \dot{c} . The state laws then follow for the stress and diffusion potential (Coleman-Noll argument):

$$\underline{\boldsymbol{\sigma}} = \frac{\partial \psi}{\partial \underline{\boldsymbol{\xi}}^e}, \quad (2.12)$$

and the diffusion potential,

$$\mu = \frac{\partial \psi}{\partial c} - \underline{\boldsymbol{\sigma}} : \underline{\boldsymbol{\eta}}, \quad (2.13)$$

The following thermodynamic forces can be inferred from equation (2.11). Thus,

$$R_p = \frac{\partial \psi}{\partial r}, \quad \mathbf{X} = \frac{\partial \psi}{\partial \underline{\boldsymbol{\alpha}}} \quad (2.14)$$

The dissipation inequality then simplifies to:

$$-\underline{\mathbf{j}} \cdot \underline{\nabla} \mu + \underline{\boldsymbol{\sigma}} : \underline{\boldsymbol{\xi}}^p - R_p \dot{r} - \mathbf{X} : \dot{\underline{\boldsymbol{\alpha}}} \geq 0 \quad (2.15)$$

To ensure positiveness of the dissipation, the existence of a convex dissipation potential $\Omega(\underline{\boldsymbol{\sigma}}, R_p, \mathbf{X}, \underline{\nabla} \mu)$, is assumed so that :

$$\dot{r} = -\frac{\partial \Omega}{\partial R_p}, \quad \dot{\underline{\boldsymbol{\alpha}}} = -\frac{\partial \Omega}{\partial \mathbf{X}}, \quad \underline{\boldsymbol{\xi}}^p = \frac{\partial \Omega}{\partial \underline{\boldsymbol{\sigma}}}, \quad \underline{\mathbf{j}} = -\frac{\partial \Omega}{\partial \underline{\nabla} \mu} \quad (2.16)$$

In the case of rate-independent plasticity, which is of practical interest here for enabling analytical solutions, two distinct potentials, Ω^{mech} and Ω^{chem} , are introduced such that

$$\dot{r} = -\dot{\lambda} \frac{\partial \Omega^{mech}}{\partial R_p}, \quad \dot{\underline{\boldsymbol{\alpha}}} = -\dot{\lambda} \frac{\partial \Omega^{mech}}{\partial \mathbf{X}}, \quad \underline{\boldsymbol{\xi}}^p = \dot{\lambda} \frac{\partial \Omega^{mech}}{\partial \underline{\boldsymbol{\sigma}}}, \quad \underline{\mathbf{j}} = -\frac{\partial \Omega^{chem}}{\partial \underline{\nabla} \mu} \quad (2.17)$$

where $\dot{\lambda}$ is the plastic multiplier. A yield function, $g(\underline{\sigma}, \underline{\mathbf{X}}, R_p)$, can be defined so that $\dot{\lambda}g = 0, \dot{\lambda} \geq 0, g \leq 0$. The consistency condition under plastic loading reads:

$$\dot{g} = 0 = \frac{\partial g}{\partial \underline{\sigma}} : \dot{\underline{\sigma}} + \frac{\partial g}{\partial \underline{\mathbf{X}}} : \dot{\underline{\mathbf{X}}} + \frac{\partial g}{\partial R_p} \dot{R}_p, \quad (2.18)$$

from which the plastic multiplier is obtained,

$$\dot{\lambda} = \frac{\frac{\partial g}{\partial \underline{\sigma}} : \frac{\partial^2 \psi}{\partial \underline{\varepsilon}^2} : \dot{\underline{\varepsilon}} + \left(\frac{\partial g}{\partial \underline{\sigma}} : \frac{\partial^2 \psi}{\partial \underline{\varepsilon}^e \partial c} \right) \dot{c}}{\frac{\partial g}{\partial \underline{\sigma}} : \frac{\partial^2 \psi}{\partial \underline{\varepsilon}^2} : \frac{\partial \Omega^{mech}}{\partial \underline{\sigma}} + \frac{\partial g}{\partial R_p} \frac{\partial^2 \psi}{\partial r^2} \frac{\partial \Omega^{mech}}{\partial R_p} + \frac{\partial g}{\partial \underline{\mathbf{X}}} : \frac{\partial^2 \psi}{\partial \underline{\alpha}^2} : \frac{\partial \Omega^{mech}}{\partial \underline{\mathbf{X}}}}. \quad (2.19)$$

In the equation (2.19), $\psi^{mech,p}$ is assumed to be independent of c .

2.2.2.2 Choice of potential and energy functions

The chemical free energy component in equation (2.9) is expressed in a standard form [35]:

$$\psi^{chem}(c) = \frac{E_f c}{\Omega_0} + \frac{RT}{\Omega_0} (c \ln(c) + (1 - c) \ln(1 - c)), \quad (2.20)$$

where, E_f , is the formation enthalpy of a mole of the considered species, T , is the absolute temperature and, R , is the universal gas constant. The tensor $\underline{\eta}$ takes the form $\underline{\eta} = \eta \underline{\mathbf{1}}$ for the particular case of isotropy, where $\underline{\mathbf{1}}$ is the second order identity tensor and

$$\eta = \frac{1}{3} \frac{\Delta v}{\Omega_0}. \quad (2.21)$$

In the above equation, Δv , is the relaxed lattice volume after one mole of atoms is removed from the lattice, and Ω_0 , the volume occupied by a mole of atoms. Equation (2.4) then becomes,

$$\underline{\varepsilon}^*(c) = \eta(c - c_{ref}) \underline{\mathbf{1}} + \underline{\varepsilon}_{ref}^*. \quad (2.22)$$

Finally, the diffusion potential is expressed as:

$$\mu = \frac{\partial \psi}{\partial c} - \underline{\sigma} : \underline{\eta} = \frac{RT}{\Omega_0} \left(\ln \left(\frac{c}{1 - c} \right) + \frac{E_f}{RT} \right) - \eta \text{tr}(\underline{\sigma}). \quad (2.23)$$

Following [72], the plastic term in the free energy (2.10) is taken as:

$$\psi^{mech,p} = R_\infty \left(r + \frac{1}{b} [\exp(-br) - 1] \right) + \frac{1}{3} C \underline{\alpha} : \underline{\alpha} \quad (2.24)$$

where R_∞ , b and C are material parameters. The thermodynamic forces are expressed from equation (2.14) as:

$$\begin{aligned} R_p &= \frac{\partial \psi}{\partial r} = R_\infty (1 - \exp(-br)), \\ \underline{\mathbf{X}} &= \frac{\partial \psi}{\partial \underline{\alpha}} = \frac{2}{3} C \underline{\alpha}. \end{aligned} \quad (2.25)$$

The yield function, $g(\underline{\sigma}, \underline{\mathbf{X}}, R_p)$, is defined by:

$$g(\underline{\sigma}, \underline{\mathbf{X}}, R_p) = \sigma_{eq} - R_p - \sigma_y, \quad (2.26)$$

where σ_y is the initial yield strength, σ_{eq} is the effective equivalent stress, defined as:

$$J_2(\underline{\sigma} - \underline{\mathbf{X}}) = \sqrt{\frac{3}{2} (\underline{\sigma}^{dev} - \underline{\mathbf{X}}^{dev}) : (\underline{\sigma}^{dev} - \underline{\mathbf{X}}^{dev})} \quad (2.27)$$

$\underline{\sigma}^{dev}$ and $\underline{\mathbf{X}}^{dev}$ are defined as the deviators of $\underline{\sigma}$ and $\underline{\mathbf{X}}$, respectively.

For time-dependent plasticity, the dissipation potential is taken to be:

$$\Omega(R_p, \underline{\boldsymbol{\sigma}}, \underline{\nabla} \mu) = \frac{K_a}{n+1} \left\langle \frac{g(\underline{\boldsymbol{\sigma}}, \underline{\mathbf{X}}, R_p)}{K_a} \right\rangle^{n+1} + \frac{1}{2} \underline{\mathbf{L}}(c) : \underline{\nabla} \mu \otimes \underline{\nabla} \mu \quad (2.28)$$

where K_a and n are material parameters. The term $\langle a \rangle = a$ if $a > 0$, else $\langle a \rangle = 0$.

Using the functions introduced in this section, equation (2.16) becomes :

$$\begin{aligned} \dot{r} &= -\frac{\partial \Omega}{\partial R_p} = \left\langle \frac{\sigma_{eq} - R_p - \sigma_y}{K_a} \right\rangle^n \\ \dot{\underline{\boldsymbol{\varepsilon}}}^p &= \frac{\partial \Omega}{\partial \underline{\boldsymbol{\sigma}}} = \frac{\partial \Omega}{\partial \sigma_{eq}} \frac{\partial \sigma_{eq}}{\partial \underline{\boldsymbol{\sigma}}} = \frac{3}{2} \left\langle \frac{\sigma_{eq} - R_p - \sigma_y}{K_a} \right\rangle^n \frac{\underline{\boldsymbol{\sigma}}^{dev} - \underline{\mathbf{X}}}{\sigma_{eq}} \\ \dot{\underline{\boldsymbol{\varepsilon}}}^p &= -\frac{\partial \Omega}{\partial \underline{\mathbf{X}}} = -\frac{\partial \Omega}{\partial \sigma_{eq}} \frac{\partial \sigma_{eq}}{\partial \underline{\mathbf{X}}} = \frac{3}{2} \left\langle \frac{\sigma_{eq} - R_p - \sigma_y}{K_a} \right\rangle^n \frac{\underline{\boldsymbol{\sigma}}^{dev} - \underline{\mathbf{X}}}{\sigma_{eq}} = \dot{\underline{\boldsymbol{\varepsilon}}}^p \end{aligned} \quad (2.29)$$

For time-independent plasticity, the dissipation potentials considered reads [72]:

$$\Omega^{mech} = g(\underline{\boldsymbol{\sigma}}, \underline{\mathbf{X}}, R_p) \quad , \quad \Omega^{chem} = \frac{1}{2} \underline{\mathbf{L}}(c) : \underline{\nabla} \mu \otimes \underline{\nabla} \mu, \quad (2.30)$$

The evolution of the plastic internal variable given by equation (2.17) becomes:

$$\begin{aligned} \dot{r} &= -\dot{\lambda} \frac{\partial \Omega^{mech}}{\partial R_p} = \dot{\lambda} \\ \dot{\underline{\boldsymbol{\varepsilon}}}^p &= \dot{\lambda} \frac{\partial \Omega^{mech}}{\partial \underline{\boldsymbol{\sigma}}} = \dot{\lambda} \frac{3}{2} \frac{\underline{\boldsymbol{\sigma}}^{dev} - \underline{\mathbf{X}}^{dev}}{\sigma_{eq}} \\ \dot{\underline{\boldsymbol{\varepsilon}}}^p &= -\dot{\lambda} \frac{\partial \Omega^{mech}}{\partial \underline{\mathbf{X}}} = \dot{\lambda} \frac{3}{2} \frac{\underline{\boldsymbol{\sigma}}^{dev} - \underline{\mathbf{X}}^{dev}}{\sigma_{eq}} = \dot{\underline{\boldsymbol{\varepsilon}}}^p \end{aligned} \quad (2.31)$$

It is assumed that, for the isotropic case,

$$\underline{\mathbf{L}}(c) = L(c) \underline{\mathbf{1}} = \frac{D\Omega_0}{RT} c(1-c) \underline{\mathbf{1}}, \quad (2.32)$$

with D being the diffusivity. Then, substitution of equation (2.32) and the gradient of equation (2.23) into equation (2.17) leaves,

$$\underline{\mathbf{j}} = -D \underline{\nabla} c + \frac{1}{3} \frac{D\Delta v}{RT} c(1-c) \underline{\nabla} (\text{tr}(\underline{\boldsymbol{\sigma}})) \quad (2.33)$$

Equation (2.33) clearly reveals the two main driving forces controlling the vacancy flux: the concentration gradient term arising from inhomogeneities in the composition, and the mechanical contribution via the stress gradient.

2.2.3 Equilibrium composition field

2.2.3.1 Theory

In this part, it will be shown that, provided that an elastic solution of the purely mechanical problem is known, an equilibrium composition field can be obtained taking the two-way coupling into account. The plastic deformation field, $\underline{\boldsymbol{\varepsilon}}^p$, will be assumed to be known in the whole body and to be constant.

At equilibrium, the diffusion potential is constant and satisfies the mass balance equation (2.1). Following the work of Cahn and Larché [28], the composition c is a function of stress alone. An expression for the equilibrium chemical concentration is obtained in terms of the corresponding diffusion potential, μ_{eq} , from equation (2.23) assuming that $c \ll 1$. For the fully anisotropic case (where $\boldsymbol{\eta} \neq \eta \mathbf{1}$):

$$c_{eq} = \exp\left(\frac{\Omega_0}{RT}\mu_{eq} - \frac{E_f}{RT}\right) \exp\left(\frac{\Omega_0}{RT}\boldsymbol{\eta} : \boldsymbol{\sigma}\right). \quad (2.34)$$

Let us define

$$\left.\frac{\partial \mu}{\partial c}\right|_{\sigma_{ij}=0} = \frac{1}{\chi}, \quad (2.35)$$

Using (2.23) and (2.35) for small values of c implies that

$$\chi = \frac{\Omega_0}{RT}c \quad (2.36)$$

Denoting $c_0 = \exp\left(\frac{\Omega_0}{RT}\mu_{eq} - \frac{E_f}{RT}\right)$, the composition field is linearized in the form given by [28]:

$$c_{eq} = c_0 + \chi \boldsymbol{\eta} : \boldsymbol{\sigma} \quad (2.37)$$

where χ has been evaluated for $c = c_0$. Using (2.37) in (2.4), at equilibrium:

$$\begin{aligned} \boldsymbol{\varepsilon}^* &= (c_{eq} - c_{ref})\boldsymbol{\eta} + \boldsymbol{\varepsilon}_{ref}^* \\ &= (c_0 - c_{ref})\boldsymbol{\eta} + \chi \boldsymbol{\eta} \otimes \boldsymbol{\eta} : \boldsymbol{\sigma} + \boldsymbol{\varepsilon}_{ref}^* \end{aligned} \quad (2.38)$$

According to Hooke's law, $\boldsymbol{\sigma} = \boldsymbol{\Lambda} : (\boldsymbol{\varepsilon} - \boldsymbol{\varepsilon}^*(c) - \boldsymbol{\varepsilon}^p)$, and using (2.38), the total strain tensor can be expressed as,

$$\boldsymbol{\varepsilon} = \left(\boldsymbol{\mathcal{S}} + \chi \boldsymbol{\eta} \otimes \boldsymbol{\eta}\right) : \boldsymbol{\sigma} + \boldsymbol{\varepsilon}^p + \boldsymbol{\varepsilon}_{ref}^* + (c_0 - c_{ref})\boldsymbol{\eta} \quad (2.39)$$

where $\boldsymbol{\mathcal{S}} = \boldsymbol{\Lambda}^{-1}$. In the above equation, the term in parenthesis is called the open system compliance² by Cahn and Larché [28]:

$$\boldsymbol{\mathcal{S}}_{ijkl}^0 = \boldsymbol{\mathcal{S}}_{ijkl} + \chi \eta_{ij} \eta_{kl}. \quad (2.40)$$

The remaining equation to be solved is the mechanical balance equation, which now takes the form:

$$\operatorname{div} \boldsymbol{\sigma} + \boldsymbol{f} = \operatorname{div} \left(\boldsymbol{\mathcal{S}}_0^{-1}(\boldsymbol{\varepsilon} - \boldsymbol{\varepsilon}^p - \boldsymbol{\varepsilon}_{ref}^* - (c_0 - c_{ref})\boldsymbol{\eta})\right) + \boldsymbol{f} = \mathbf{0} \quad (2.41)$$

The equilibrium mechanical-diffusion problem is now equivalent to solving the purely elastic problem (2.41) for a given fictitious compliance field, $\boldsymbol{\mathcal{S}}_0$.

For an elastic isotropic material, the compliance components are

$$\boldsymbol{\mathcal{S}}_{ijkl} = -\frac{\nu}{E} \delta_{ij} \delta_{kl} + \frac{1}{2G} (\delta_{ik} \delta_{jl} + \delta_{il} \delta_{jk}), \quad (2.42)$$

so that equation (2.40) gives,

$$\boldsymbol{\mathcal{S}}_{ijkl}^0 = \left(-\frac{\nu}{E} + \chi \eta^2\right) \delta_{kl} + \frac{1}{2G} (\delta_{ik} \delta_{jl} + \delta_{il} \delta_{jk}). \quad (2.43)$$

²They are derived at constant diffusion potential, as shown in appendix A.

The above expression for \mathbf{S}_{ijkl}^0 can be further simplified if it is expressed in terms of the corresponding open system elastic constants defined as

$$\nu_0 = \frac{\nu - \chi\eta^2 E}{1 + \chi\eta^2 E}, \quad E_0 = \frac{E}{1 + \chi\eta^2 E}, \quad G_0 = G, \quad (2.44)$$

so that equation (2.43) becomes,

$$\mathbf{S}_{ijkl}^0 = -\frac{\nu_0}{E_0} \delta_{ij} \delta_{kl} + \frac{1}{2G_0} (\delta_{ik} \delta_{jl} + \delta_{il} \delta_{jk}). \quad (2.45)$$

If the concentration, c , and the coupling parameter, η , are small, then the open system constants reduce to the standard elastic constants.

2.2.3.2 Methodology for deriving analytical solutions of a stress-diffusion coupled problem

Consider a body \mathcal{B} , with boundary $\partial\mathcal{B}$. Furthermore, let $\partial\mathcal{B}$ be sub-divided into

$$\begin{aligned} \partial\mathcal{B} &= (\partial\mathcal{B})_{m1} \cup (\partial\mathcal{B})_{m2} \\ \partial\mathcal{B} &= (\partial\mathcal{B})_{c1} \cup (\partial\mathcal{B})_{c2} \end{aligned} \quad (2.46)$$

For the mechanical sub-problem, either a displacement or a force should be applied on the boundaries $(\partial\mathcal{B})_{m1}$ and $(\partial\mathcal{B})_{m2}$, respectively. Similarly for the chemical sub-problem, either a concentration or a flux should be applied on $(\partial\mathcal{B})_{c1}$ and $(\partial\mathcal{B})_{c2}$.

Suppose that the analytical stress solution to the associated uncoupled mechanical problem, represented by (2.2) and (2.46)₁, is known. Given the modified mechanical balance (2.41), then the same stress solution for the coupled problem as that for the uncoupled one can be used provided that the modified elastic constants are employed.

Then the equilibrium value, μ_{eq} (2.23), can be inferred from the boundary conditions of the coupled problem. For an extensive discussion on the possible cases, the reader is referred to [28]. Finally, the concentration field c_{eq} can be obtained from equation (2.37).

2.3 Finite element implementation of the coupled formulation

The coupled formulation described in the previous section has been implemented into the finite element code Z-set in a fully coupled way, using the methodology described in [16]. The nodal variables are the concentration c and the displacement \mathbf{u} . The tensors $\boldsymbol{\sigma}$ and $\boldsymbol{\varepsilon}$, are written in columnar format as:

$$\{\tilde{\boldsymbol{\sigma}}\} = \begin{Bmatrix} \sigma_{11} \\ \sigma_{22} \\ \sigma_{33} \\ \sqrt{2}\sigma_{12} \\ \sqrt{2}\sigma_{23} \\ \sqrt{2}\sigma_{31} \end{Bmatrix}, \quad \{\tilde{\boldsymbol{\varepsilon}}\} = \begin{Bmatrix} \epsilon_{11} \\ \epsilon_{22} \\ \epsilon_{33} \\ \sqrt{2}\epsilon_{12} \\ \sqrt{2}\epsilon_{23} \\ \sqrt{2}\epsilon_{31} \end{Bmatrix} \quad (2.47)$$

The vector and matrix shape functions are defined, respectively, as:

$$\begin{aligned} \{N\} &= \{N_1, N_2, \dots, N_n\} \\ [\tilde{N}] &= \begin{bmatrix} N_1 & 0 & N_2 & 0 & \dots & N_n & 0 \\ 0 & N_1 & 0 & N_2 & \dots & 0 & N_n \end{bmatrix} \end{aligned} \quad (2.48)$$

The corresponding 2D gradient operators are:

$$\begin{aligned} [B] &= \begin{bmatrix} \frac{\partial N_1}{\partial x_1} & \dots & \frac{\partial N_n}{\partial x_1} \\ \frac{\partial N_1}{\partial x_2} & \dots & \frac{\partial N_n}{\partial x_2} \end{bmatrix} \\ [\tilde{B}] &= \begin{bmatrix} \frac{\partial N_1}{\partial x_1} & 0 & \frac{\partial N_2}{\partial x_1} & 0 & \dots & \frac{\partial N_n}{\partial x_1} & 0 \\ 0 & \frac{\partial N_1}{\partial x_2} & 0 & \frac{\partial N_2}{\partial x_2} & 0 & \dots & \frac{\partial N_n}{\partial x_2} \\ \frac{1}{\sqrt{(2)}} \frac{\partial N_1}{\partial x_2} & \frac{1}{\sqrt{(2)}} \frac{\partial N_1}{\partial x_1} & \frac{1}{\sqrt{(2)}} \frac{\partial N_2}{\partial x_2} & \frac{1}{\sqrt{(2)}} \frac{\partial N_2}{\partial x_1} & \dots & \frac{1}{\sqrt{(2)}} \frac{\partial N_n}{\partial x_2} & \frac{1}{\sqrt{(2)}} \frac{\partial N_n}{\partial x_1} \end{bmatrix} \end{aligned} \quad (2.49)$$

The equation (2.2) is multiplied by a test function \underline{v} and integrated to obtain the weak form:

$$\int_V (-\underline{\sigma} : \underline{\varepsilon}(\underline{v}) + \mathbf{f} \cdot \underline{v}) dV + \int_{\partial V} \mathbf{t} \cdot \underline{v} dS = 0 \quad (2.50)$$

where it is recalled that \mathbf{t} is the traction on the surface ∂V , and $\underline{\varepsilon}(\underline{v}) = \frac{1}{2} (\underline{\nabla} \underline{v} + \underline{\nabla} \underline{v}^T)$. The virtual test function $\{v\}$ and the physical field $\{u\}$ are discretised using the shape functions N as

$$\{v\} = [\tilde{N}] \{\hat{v}\}, \quad \{u\} = [\tilde{N}] \{\hat{u}\} \quad (2.51)$$

The virtual and real strain fields are:

$$\{\tilde{\varepsilon}\}(\{v\}) = [\tilde{B}] \{\hat{v}\}, \quad \{\tilde{\varepsilon}\}(\{u\}) = [\tilde{B}] \{\hat{u}\} \quad (2.52)$$

Equation (2.50) has to hold $\forall \{\hat{v}\}$ and thereby reduces to the discretized mechanical equilibrium residual:

$$\{r_u\} = \int_V (-\{\tilde{\sigma}\}^T [\tilde{B}] + [\tilde{N}] \{f\}) dV + \int_{\partial V} [\tilde{N}] \{t\} dS \quad (2.53)$$

The mass balance (2.1) is multiplied by a test function c^* and integrated to obtain the weak form:

$$\int_V (\dot{c} c^* - \{j\} \{\nabla w\}) dV + \int_{\partial V} \{j\} \{n\} c^* dS = 0 \quad (2.54)$$

The virtual and real concentration fields, c^* and c , are discretized as:

$$c^* = \{N\} \{\hat{c}^*\}, \quad c = \{N\} \{\hat{c}\} \quad (2.55)$$

The equation (2.54) is expressed as the discretised concentration residual as:

$$\{r_c\} = \int_V (\{N\} \{N\}^T \{\dot{\hat{c}}\} - [B]^T \{j\}) dV + \int_{\partial V} \{N\} j dS, \quad (2.56)$$

In order to solve the non linear sets of equations represented by (2.53) and (2.56) with a Newton-Raphson algorithm, a global tangent stiffness matrix, \mathbf{K} , is needed. Four terms are identified in the stiffness matrix:

$$[K] = \begin{bmatrix} [K_{uu}] & [K_{uc}] \\ [K_{cu}] & [K_{cc}] \end{bmatrix} \quad (2.57)$$

with components

$$\begin{aligned}
 [K_{cc}]_{ij} &= \frac{\partial \{r_c\}_i}{\partial \hat{c}_j} = \int_V N_i N_j \frac{1}{\Delta t} - B_{ik} \frac{\partial j_k}{\partial \hat{c}_j} dV \\
 [K_{cu}]_{ij} &= \frac{\partial \{r_c\}_i}{\partial \hat{u}_j} = \int_V -B_{ik} \frac{\partial j_k}{\partial \hat{u}_j} dV \\
 [K_{uu}]_{ij} &= \frac{\partial \{r_u\}_i}{\partial \hat{u}_j} = \int_V -\tilde{B}_{ik} \frac{\partial \tilde{\sigma}_k}{\partial \hat{u}_j} dV \\
 [K_{uc}]_{ij} &= \frac{\partial \{r_u\}_i}{\partial \hat{c}_j} = \int_V -\tilde{B}_{ik} \frac{\partial \tilde{\sigma}_k}{\partial \hat{c}_j} dV
 \end{aligned} \tag{2.58}$$

It can be shown that the stiffness matrix derivatives need to be consistent with the choice of free energy made in Section 2.2.2.2 :

$$\begin{aligned}
 \frac{\partial j_k}{\partial \hat{c}_j} &= -N_j \frac{\partial L}{\partial c} \frac{\partial \mu}{\partial x_k} - LN_j \frac{\partial^3 \psi}{\partial c^3} \frac{\partial c}{\partial x_k} - L \frac{\partial^2 \psi}{\partial c^2} \frac{\partial N_j}{\partial x_k} \\
 \frac{\partial j_k}{\partial \hat{u}_j} &= 0 \\
 \frac{\partial \tilde{\sigma}_k}{\partial \hat{u}_j} &= \left[\frac{\partial^2 \psi}{\partial \xi \partial \xi} \right]_{ki} \tilde{B}_{ij} \\
 \frac{\partial \tilde{\sigma}_k}{\partial \hat{c}_j} &= \left[\frac{\partial^2 \psi}{\partial c \partial \xi} \right]_k N_j
 \end{aligned} \tag{2.59}$$

where:

$$\frac{\partial \mu}{\partial x_k} = \frac{\partial^2 \psi}{\partial c^2} \frac{\partial c}{\partial x_k} - H^{mn} \frac{\partial^2 \psi}{\partial \epsilon_{mn} \partial \epsilon_{pq}} \frac{\partial \epsilon_{pq}}{\partial x_k} \tag{2.60}$$

Concerning local integration of the resulting equations, classical procedures are used in the Z-set code [16]. In the above equation, and in the calculation of the flux (2.33), the gradient of the total strain tensor is needed. To avoid the use of particular elements, the strain is extrapolated from the Gauss points to the nodes and its gradient is computed with the use of the derivatives of the shape functions. This method is the same as the one used by Thomas and Chopin [116] and Abrivard et al [2].

2.4 Analytical and numerical solutions to some boundary values problems

In this section, the steady state concentration field in three examples is determined solving the coupled problem both numerically and analytically. The analytic equilibrium solution is obtained by solving directly the coupled equation driving the system for the first example, and the procedure described in the Section 2.2.3 for the other two.

2.4.1 Rotating disc

The first problem is a disc with an initial homogeneous vacancy concentration, c_0 , which is rotating at a constant velocity, ω . Only elasticity is taken into account. An illustration of the rotating disc is given in Figure 2.1. The boundary conditions are chosen so that an exact solution can be found in an axisymmetric setting. The vanishing flux on top and bottom surfaces ($z = 0$ and $z = h$) enforces a quasi-1D character (radial only) to the solution. The numerical parameters chosen for the calculations are given in Table 2.1. The dimension of the disc are

Table 2.1: Simulation parameters used for the rotating disc problem, nickel.

c_0	T	Ω_0	E	ν	η	ω
[.]	[K]	[$mm^3.mol^{-1}$]	[GPa]	[.]	[.]	[$rad.s^{-1}$]
1.10^{-4}	900	$6,6.10^3$	200	0.34	-0.05	$2,09.10^3$

$d = 400$ mm and $h = 10$ mm. The parameter χ from equation (2.36) is evaluated for $c = c_0$ in the analytical treatment: the boundary condition on the external surface (at $r = d$) represents a *chemical reservoir*, where a constant concentration is maintained. From equations (2.1) and (2.17), it can be seen that the rate of change of the concentration is given by:

$$\dot{c} = -\text{div } \underline{j} = \text{div} (L \underline{\nabla} \mu) = 0. \quad (2.61)$$

Furthermore, the stress state at a generic radial position, r , of the disc can be expressed in polar coordinates in terms of its outer radius, d , its mass density, ρ , the angular velocity ω , and open system Poisson's ratio, ν_0 ,

$$\sigma_{rr} = \frac{(3 + \nu_0)}{8} \rho \omega^2 (d^2 - r^2), \quad (2.62)$$

and

$$\sigma_{\theta\theta} = \frac{\rho \omega^2}{8} [(3 + \nu_0)d^2 - (1 + 3\nu_0)r^2]. \quad (2.63)$$

The corresponding trace of the stress tensor is then,

$$\text{tr}(\boldsymbol{\sigma}) = \frac{\rho \omega^2}{4} [(3 + \nu_0)d^2 - 2r^2(1 + \nu_0)]. \quad (2.64)$$

The equilibrium solution to the boundary value problem can be found by combining equations (2.61) with (2.33) and (2.64), i.e.

$$0 = \text{div} (L \underline{\nabla} \mu) = D \frac{\partial^2 c}{\partial r^2} + D \left(\frac{\Delta v \rho \omega^2 (1 + \nu_0)}{3RT} r + \frac{1}{r} \right) \frac{\partial c}{\partial r} + 2D \frac{\Delta v \rho \omega^2 (1 + \nu_0)}{3RT} c. \quad (2.65)$$

Leading to the following differential equation:

$$\frac{\partial^2 c}{\partial r^2} + \left(Ar + \frac{1}{r} \right) \frac{\partial c}{\partial r} + 2Ac = 0. \quad (2.66)$$

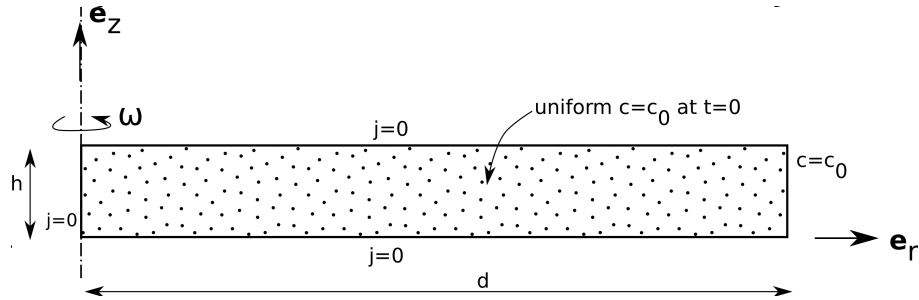


Figure 2.1: Definition of the rotating disc set-up: geometry, boundary conditions and mechanical loading.

with

$$A = \frac{\Delta v \rho \omega^2 (1 + \nu_0)}{3RT}, \quad (2.67)$$

A general solution for equation (2.66) is,

$$c(r) = C_1 \exp\left(-\frac{1}{2}Ar^2\right) + C_2 \exp\left(-\frac{1}{2}Ar^2\right) \int_1^\infty \frac{\exp(\frac{1}{2}Ar^2x)}{x} dx, \quad (2.68)$$

where C_1 and C_2 are two integration constants to be determined from the boundary conditions shown on Figure 2.1, that is, $j_r = 0$ at $r=0$, and a prescribed concentration, $c = c_0$, on the external surface at $r = d$. Thus

$$j_r(0) = \frac{\partial \mu}{\partial r}(0) = \frac{\partial c}{\partial r}(0) = 0, \quad \text{and} \quad c(d) = c_0. \quad (2.69)$$

and the solution given by equation (2.68) becomes:

$$c(r) = c_0 \exp\left(\frac{1}{2}A(d^2 - r^2)\right). \quad (2.70)$$

The equilibrium diffusion potential, μ_{eq} , can be obtained from equations (2.34) and equation (2.64),

$$\mu_{eq} = \frac{RT}{\Omega_0} \ln c_0 + \frac{E_f}{\Omega_0} + \frac{\Delta v}{\Omega_0} \rho \omega^2 \frac{\nu_0 - 1}{12} d^2. \quad (2.71)$$

However, for the particular example of interest here, the value of μ_{eq} is actually known *a priori* at $r = d$ since both the concentration and stresses are known at that free boundary. In this case, it would also have been possible to calculate μ_{eq} from equation (2.23) using the boundary condition and analytical stress at $r = d$, and directly use it in equation (2.34) to retrieve equation (2.70).

The numerical simulation recovers exactly the analytical coupled solution of this problem, as shown by the profile of concentration given on Figure 2.2. For this example, a reduction of 17 % of the initial concentration at $r = 0$ ($\eta = -0.05$), and 1.7% for $\eta = -5.10^{-3}$ is found. Note that the stress σ_{rr} is approximately 1000MPa, which would in reality induce plasticity. The value of η is critical, and also subject of discussion since estimates various parameters can be found in the literature, even with positive signs in aluminium (e.g. see [125] and [33]).

2.4.2 Vacancy diffusion around the core of an edge dislocation

Consider an edge dislocation of Burgers vector b , located at a point with coordinates $(x, y) = (0, 0)$ in an infinite plate with an initial homogeneous vacancy concentration, $c_{ref} = c_0$. The edge dislocation was introduced in the finite element model by imposing a shear eigenstrain in a thin semi-infinite strip of thickness h , with magnitude $-b/h$, and only elasticity is taken into account. In order to determine the equilibrium vacancy concentration state in the system, the following boundary conditions are imposed: a vanishing flux is assumed on the dislocation core boundary (with a radius equal to $2b$), and a constant concentration $c = c_0$, on the far-field boundaries, i.e. the dislocation is considered to be in a *chemical reservoir*. The setup is illustrated on Figure 2.3.

In the analytical solution, the parameter χ from equation (2.36) was determined for $c = c_0$ using the chemical reservoir boundary conditions. The stress field in Cartesian coordinates

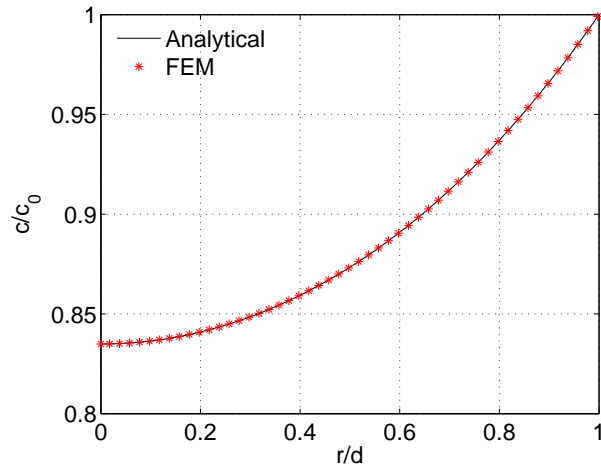


Figure 2.2: Concentration profile in the rotating disc, normalised by c_0 , as a function of the normalised distance from the axisymmetric axis.

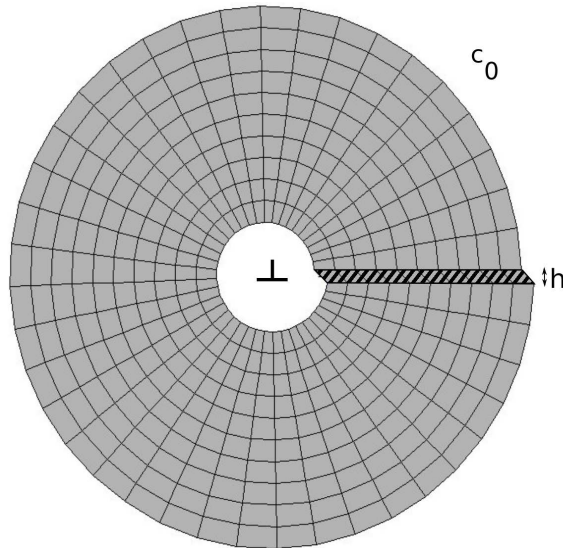


Figure 2.3: Model of the edge dislocation problem (deformed configuration, zoomed on the core): an eigenstrain $\varepsilon_{12}^* = -\frac{b}{h}$ is imposed in the stripped zone, and a cutout of radius $2b$ is made to exclude the core, with a vanishing flux boundary condition. A concentration c_0 is imposed on the far-field boundaries.

around the edge dislocation takes the form of the Hirth and Lothe [64] solution, albeit with the open system elastic constants instead of the standard ones. Here,

$$\sigma_{xx} = -\frac{G_0 b}{2\pi(1-\nu_0)} \frac{y(3x^2 + y^2)}{(x^2 + y^2)^2}, \quad (2.72)$$

$$\sigma_{yy} = \frac{G_0 b}{2\pi(1-\nu_0)} \frac{y(x^2 - y^2)}{(x^2 + y^2)^2}, \quad (2.73)$$

$$\sigma_{zz} = \nu_0(\sigma_{xx} + \sigma_{yy}), \quad (2.74)$$

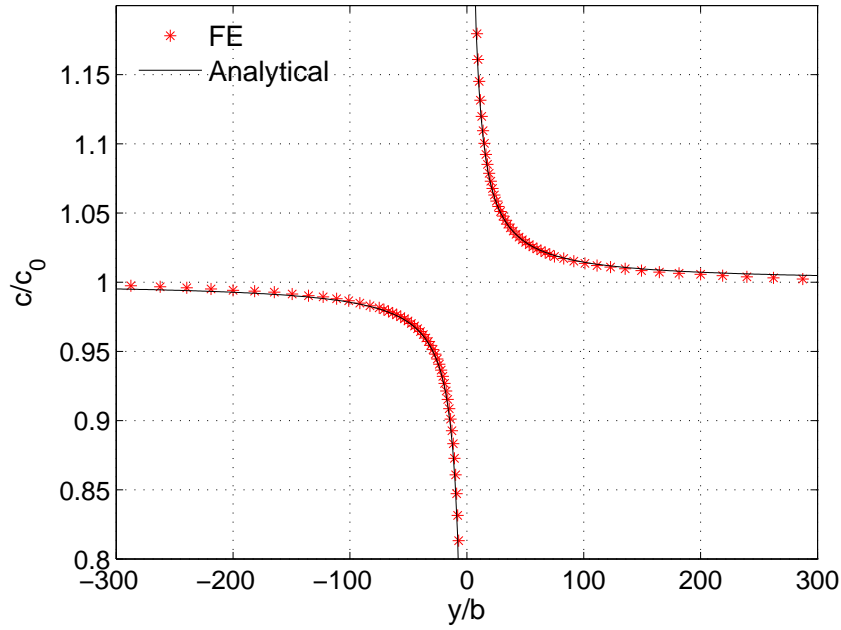


Figure 2.4: Variations of the normalised steady state vacancy concentration profile along y/b at $x = 0$, obtained both analytically and numerically.

$$\sigma_{xy} = \frac{G_0 b}{2\pi(1 - \nu_0)} \frac{x(x^2 - y^2)}{(x^2 + y^2)^2} \quad (2.75)$$

The analytical vacancy concentration solution can be approximated with the linearised equation (2.37):

$$c_{eq} = c_0 - \chi\eta(1 + \nu_0) \frac{G_0 b}{\pi(1 - \nu_0)} \frac{x^2 y + y^3}{(x^2 + y^2)^2} \quad (2.76)$$

The parameters used to obtain the numerical and analytical results are given in Table 2.2. The vacancy formation energy is close to the value given in [107], from which c_0 is obtained. Other values are taken from [48] for aluminium. The analytical and numerical results are given in

Table 2.2: Parameters used to simulate vacancy diffusion around an edge dislocation

h	c_0	T	Ω_0	η	E	ν
[nm]	[.]	[K]	[$m^3 \cdot mol^{-1}$]	[.]	GPa	[.]
0.5	10^{-4}	700	10^{-5}	-0.05	70	0.34

Figures 2.4 and 2.5.

The evolution of the normalised steady state vacancy concentration profiles around the dislocation core (along y/b at $x = 0$) obtained both analytically and numerically are depicted in figure 2.4, where an excellent correlation is found even at a location as close as $5b$ from the centre of the dislocation core. The corresponding contour plots of the steady state normalised vacancy concentration around the edge dislocation core is given in Figure 2.5. As expected, vacancies tend to relieve the hydrostatic pressure around the dislocation core by migrating from the tensile

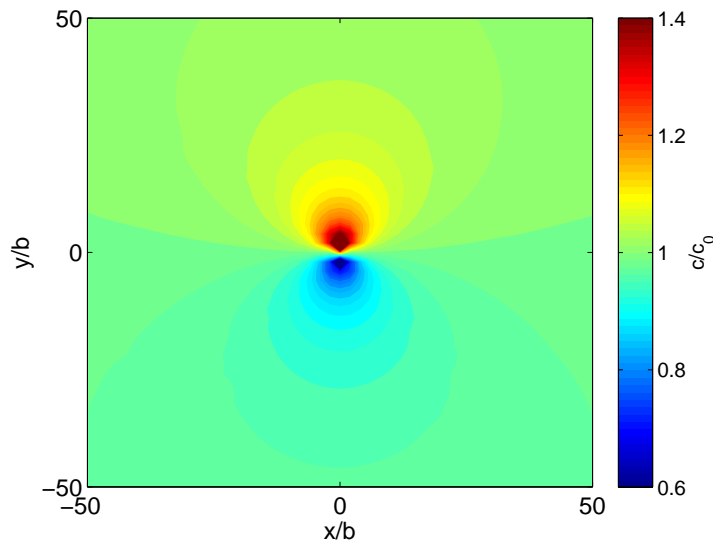


Figure 2.5: Contour plot of the numerically obtained equilibrium vacancy concentration distribution normalised by c_0 . The vacancies tend to relieve the hydrostatic pressure around the dislocation core by migrating from the tensile regions to the compression ones.

regions to the compressive ones, a classical result given by Hirth and Lothe [64]. Finally, it is possible to analytically obtain the effect of the vacancy concentration on the stress. If P_{ref} and P are the pressure around the dislocation core, without and with vacancies respectively, then:

$$\frac{P}{P_{ref}} = \frac{(1 + \nu_0)(1 - \nu)}{(1 + \nu)(1 - \nu_0)} \quad (2.77)$$

which is independent of position. For instance, $\frac{P}{P_{ref}} = 0.9991$ and 0.9242 for $c_0 = 10^{-3}$ and $c_0 = 10^{-1}$, respectively. Even considering the typical concentrations values encountered at homologous temperature, the influence of vacancies on the stress state is negligible in most cases.

2.4.3 Perforated plate subject to a far-field tensile stress

The last example concerns the analysis of an infinite plate with a centred hole of radius $R_h = 1\mu m$ subject to a far-field tensile stress σ_∞ . First, a pure elastic case will be discussed, then an elastic perfectly plastic model with yield stress σ_y will be considered. The far-field stress σ_∞ is applied along the x -axis (see Figure 2.6). The steady state solution to the coupled diffusion elasticity problem in polar coordinates (r, θ) - θ being the angle with respect to the x axis - is given by

Table 2.3: Simulation parameters used in the infinite plate with a centred hole case

c_0	T	Ω_0	E	σ_y	ν	η	R_h
[.]	[K]	[$m^3.mol^{-1}$]	[GPa]	[MPa]	[.]	[.]	[μm]
10^{-4}	700	10^{-5}	70	200	0.34	-0.05	1.

the classical one in terms of the open system Poisson's ratio, ν_0 , namely

$$\begin{aligned}
 \sigma_{rr} &= \frac{\sigma_\infty}{2} \left(1 - \left(\frac{R_h}{r} \right)^2 \right) + \frac{\sigma_\infty}{2} \left(1 + 3 \left(\frac{R_h}{r} \right)^4 - 4 \left(\frac{R_h}{r} \right)^2 \right) \cos(2\theta), \\
 \sigma_{\theta\theta} &= \frac{\sigma_\infty}{2} \left(1 + \left(\frac{R_h}{r} \right)^2 \right) - \frac{\sigma_\infty}{2} \left(1 + 3 \left(\frac{R_h}{r} \right)^4 \right) \cos(2\theta), \\
 \sigma_{zz} &= \sigma_\infty \nu_0 \left(1 - 2 \left(\frac{R_h}{r} \right)^2 \cos(2\theta) \right), \\
 \sigma_{r\theta} &= -\frac{\sigma_\infty}{2} \left(1 - 3 \left(\frac{R_h}{r} \right)^4 + 2 \left(\frac{a}{r} \right)^2 \right) \sin(2\theta).
 \end{aligned} \tag{2.78}$$

Then, the corresponding trace of the stress tensor is

$$tr(\boldsymbol{\sigma}) = (1 + \nu_0) \sigma_\infty \left(1 - 2 \left(\frac{R_h}{r} \right)^2 \cos(2\theta) \right). \tag{2.79}$$

The far-field stress was chosen so that the plate deforms uniaxially along the x-axis at the far field by 0.2%. The parameters used in the analytical and numerical calculations are given in Table 2.3 for aluminium. The analytical vacancy concentration field is obtained from equation (2.37) using the expression for the trace of the stress tensor, equation (2.79). The value of the parameter χ is taken for $c = c_0$, again, due to the chemical reservoir type of the boundary condition.

A contour plot of the numerically obtained distribution of the vacancy concentration at equilibrium within the plate, normalised by c_0 , is shown for the elastic case in Figure 2.6. The stress concentration factors, defined as the ratio $\sigma_{yy}/\sigma_\infty$ at the inner hole boundary are known to be -1 and 3 for $\theta = 0^\circ$ and 90° , respectively. As a result of these stress concentration effects, vacancies redistribute around the hole, see Figure 2.6. Red regions ($\theta = 0$) exhibit a concentration above the initial value and the blue ones ($\theta = 90$) a decrease relative to c_0 . The hole radius being small, the stress gradients act in this case as a strong driving force for the vacancy fluxes.

To illustrate the extended theory, a perfectly plastic behaviour is now incorporated in the model. Here, plasticity is expected to relax the stresses locally, leading to smaller stress gradients and hence affecting the fluxes and the equilibrium state. The trace of the stress distribution around the hole ($r = R_h$) at different angles θ , is given in Figure 2.7 for various initial concentrations. The coupled open system elastic constants influence the stresses only for high vacancy concentrations, the term χ being negligible in equation (2.44) when $c = 10^{-4}$. When the hypothesis $c \ll 1$ made in the analytical developments is verified, the FE solution is indistinguishable from the analytical solution. However, this is no longer true when $c = 0.1$, explaining the small discrepancy observed between the analytical and FE solutions. When c is large, the analytical

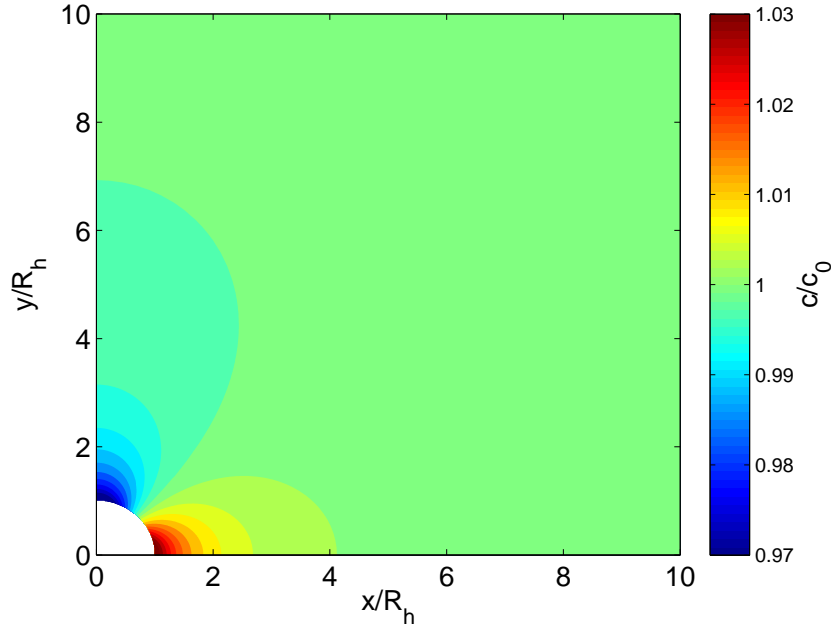


Figure 2.6: Contour plot of the numerically obtained equilibrium vacancy concentration distribution normalised by c_0 , obtained numerically in the elastic case

solution tends to underestimate the stress compared to the FE solution. The reduction of the stress gradient in the plastic case is clearly visible for $\theta > 40^\circ$.

The results in Figure 2.8 are shown in terms of the normalised vacancy concentration along the surface of the hole. Also shown are the concentration profiles predicted analytically using both the standard elastic constants and the open-system elastic ones (denoted 'Coupled Analytical' in the figure), and the numerically obtained results (FE) in the elastic and plastic cases. In the plastic case, the methodology presented in Section 2.2.3 is applied. The stress field calculated numerically is used to compute the concentration field analytically, using equation (2.37), and an adequate agreement is found with the coupled FE solution and the semi-analytical one.

Finally, in the plastic case, the plate is loaded as before until equilibrium is reached, and then unloaded. Due to the plastic deformation that has occurred on the top side of the hole, the unloaded configuration is not homogeneously deformed. This leads to residual stresses upon unloading giving a non-uniform distribution of vacancies in the unloaded configuration. This is visible in Figure's 2.9 numerical results.

2.5 Conclusions

A thermodynamically consistent diffusion-stress coupling framework has been developed for elasto-viscoplastic solids. To obtain the equilibrium stress and composition fields, a coupled solution of the equations governing mechanical and chemical equilibrium is normally required. However, it is possible to obtain both fields by only solving a modified mechanical equilibrium equation, in which modified elastic constants account implicitly for the chemical equilibrium. First introduced by Cahn and Larché for an elastic solid, they are called open system elastic constants, derived at constant diffusion potential, the procedure being similar to the one giving adiabatic compliance instead of isothermal one. It has been shown that, in presence of plasticity, these derivations are still valid, and enable an analytical solution of the concentration field to

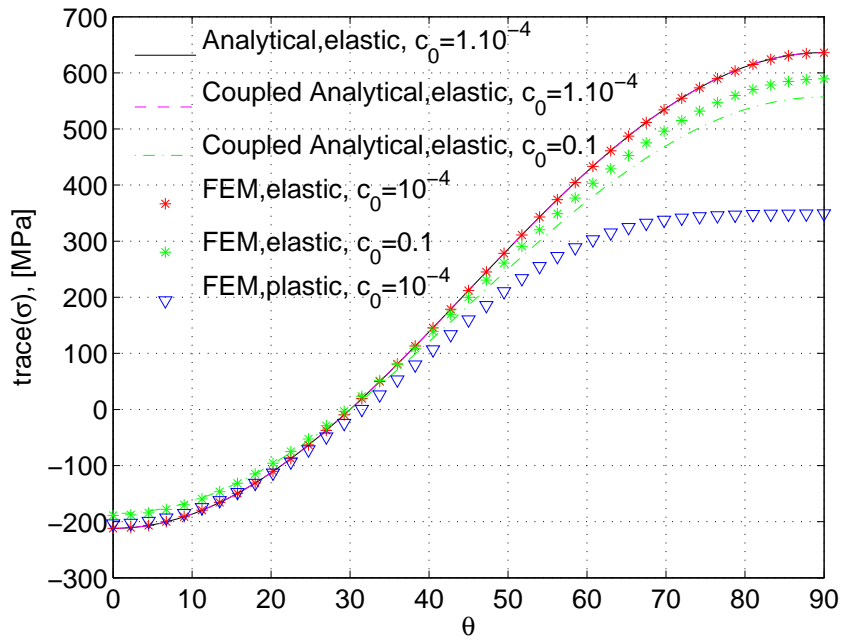


Figure 2.7: Variation of the trace of the stress tensor around the hole for two different values of initial vacancy concentration, without and with the effect of the open system (ie, coupled) elastic constants. The effect of the concentration on the stress is noticeable for high concentrations.

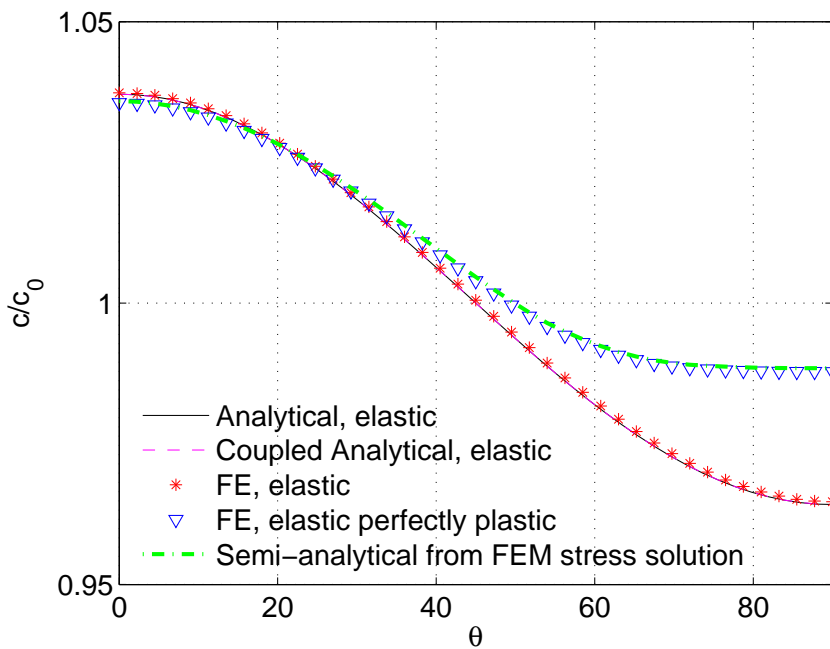


Figure 2.8: Concentration profile around the hole of a plate loaded uni-axially, obtained analytically and numerically for the elastic case, and numerically for the elasto-plastic one.

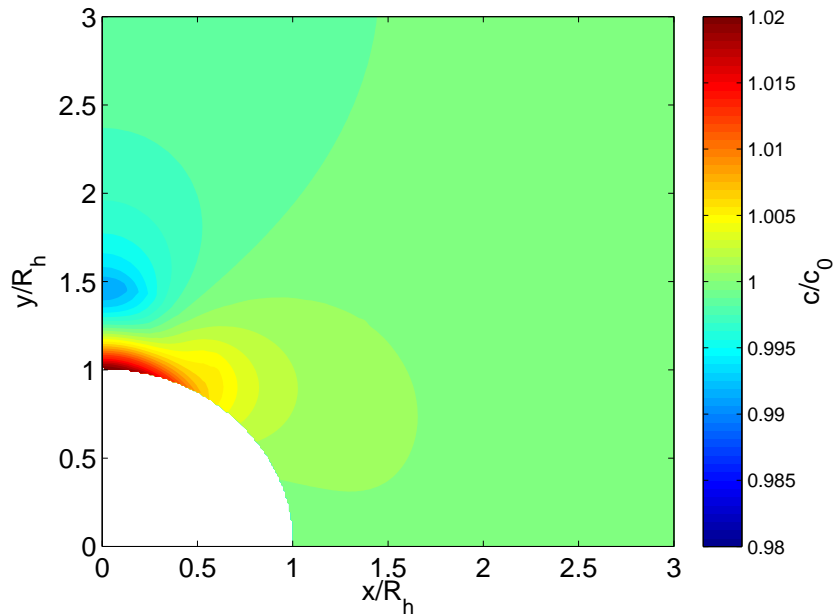


Figure 2.9: Residual distribution of vacancies obtained after unloading in the plastic case. Due to the stress concentration factor on the top of the hole, plastic deformation heterogeneities upon unloading give rise to residual stresses that lead, in turn, to vacancy redistributions.

be obtained knowing the numerical stress field. Three coupled problems have been treated analytically and numerically to illustrate the efficiency of this method.

The coupled diffusion-stress formulation has been implemented in a finite element framework in a fully-coupled way. The resulting numerical predictions of different problems capture the main features of the coupled phenomena predicted analytically. When the concentration is very small, the values of the open system constants are close to the conventional values, and the concentration field can be calculated from the stress field obtained using either set of constants. However, when the concentration is relatively high, it becomes necessary to use the open system compliances for the simulations to remain in agreement with the analytical solutions. Finally, if the concentration is not negligible compared to 1, a discrepancy between the FEM and analytical solutions arises.

The role of plasticity on the local relaxation of the stress state and its effects on the corresponding equilibrium concentration field has been illustrated in a simple example. The plasticity model was limited to a perfect one in the simulations, although the proposed theory accounts for hardening. The study of the redistribution of vacancies around an edge dislocation is of interest, amongst other applications, for the modelling of dislocation climb assisted by diffusion, by providing an explicit framework to determine the local vacancy concentration distribution around the dislocation core. Accounting for the effects of stress on point defect diffusion is also relevant for modelling the formation of stable vacancy clusters in irradiated materials. In this case, the concentration of vacancies is high, which has been shown to have a non-negligible effect on the open system constants. Recent work in this area by [86], based on phase-field techniques, neglected the effects of stress so that no effect of applied load could be accounted for on void growth. If omitted, stress gradients are unable to affect the vacancy fluxes responsible for altering the shape of the void and their kinetics. The framework presented here provides the necessary analytical tools to pursue such goal.

Field theory and simulation of creep in polycrystalline aggregates

In the previous chapter, a thermodynamically consistent diffusion-stress coupling framework has been developed for elasto-viscoplastic solids. It describes the migration of point defects in a heterogeneous stress field, and the associated reversible stress relaxation. In polycrystals, the diffusion potential in the grain boundaries (GB) is affected by the normal traction vector on the grain boundary surface. Hence, vacancies migrate from GB in traction to GB in compression. The well known Herring-Nabarro creep corresponds to the strain associated with this vacancy flux.

The large amount of grain boundaries in Cu-Nb nanolayers, associated with the excess of vacancies produced by irradiation, will lead to important diffusion current. In order to obtain detailed insight of creep strain fields inside the grains, it is then necessary to develop constitutive laws where the strain rate is directly related to the vacancy flux, which has not been done yet at this polycrystalline meso-scale.

Résumé

La diffusion de lacunes à haute température dans les polycristaux engendre une déformation inélastique. Un cadre thermodynamique, dans lequel les grains et les joints de grain sont explicitement modélisés, est proposé afin d'obtenir des champs de déformation détaillés au niveau intragranulaire. Un choix judicieux de déformation libre dans les joints de grain permet d'obtenir la force motrice du fluage diffusion, et on montre que le tenseur vitesse de déformation inélastique est proportionnel au gradient du flux de lacunes. La contribution des dislocations est prise en compte via l'introduction d'un modèle standard de plasticité cristalline reposant sur la densité de dislocations. Le modèle est implémenté numériquement via la méthode des éléments finis et appliqué à des agrégats polycristallins. Des simulations de fluage couplé à la diffusion de lacunes sont réalisées pour la première fois et prédisent un champ de déformation intragranulaire fortement hétérogène. De plus, la vitesse de fluage macroscopique obtenue met en évidence les dépendances classiques à la taille de grain ainsi qu'à la contrainte appliquée. Enfin, une

transition douce entre les régimes de fluage diffusion/dislocation est obtenue et comparée à des résultats expérimentaux.

Summary

In polycrystals, vacancy diffusion at high homologous temperatures leads to inelastic deformation. In order to obtain the corresponding strain field inside a polycrystalline aggregate, a continuum framework is developed, in which grains and grain boundaries are explicitly modeled. The choice of an anisotropic eigenstrain in the grain boundary region provides the driving force for the diffusive creep processes. The corresponding inelastic strain rate is shown to be related to the gradient of the vacancy flux. Dislocation driven deformation is then introduced as an additional mechanism, through standard crystal plasticity constitutive equations. The coupled diffusion-mechanical model is implemented in the finite element method. Simulations of biaxial creep of polycrystalline aggregates coupled with vacancy diffusion are performed for the first time. They predict strongly heterogeneous viscoplastic strain fields, especially close to triple points grain boundaries. The classical macroscopic strain rate dependence on the stress and grain size is retrieved. Finally, a smooth transition from Herring and Coble to dislocation creep behaviour is predicted and compared to experimental results.

Contents

3.1	Introduction	33
3.2	Kinetics of vacancy diffusion induced creep in crystals	34
3.2.1	Definition of a material point in the presence of diffusion	34
3.2.2	Coupling creep deformation and the gradient of the vacancy flux	35
3.2.3	Balance of species	37
3.2.4	Linearized theory	38
3.3	Balance laws and constitutive equations in elasto-viscoplasticity	38
3.3.1	Balance laws	38
3.3.2	Constitutive equations	38
3.4	Simulation of diffusional creep in a polycrystalline aggregates	40
3.4.1	Grain boundary description	40
3.4.2	Problem description	43
3.4.3	Results	44
3.4.3.1	Case study one: Dirichlet conditions at the grain boundaries	44
3.4.3.2	Case study two: Source term in the grain boundaries	46
3.4.3.3	Case study three: Dirichlet conditions at the grain boundary and crystal plasticity	47
3.4.3.4	Discussion	49
3.5	Conclusions	52

3.1 Introduction

In crystalline metallic materials, the two main elementary creep mechanisms are crystallographic slip produced by dislocation glide and the deformation associated with vacancy diffusion. As far as vacancies are concerned, two mechanisms are known: Coble creep, where vacancies diffuse along grain boundaries, and Herring-Nabarro creep [63], where vacancies diffuse through the bulk material. They operate, respectively, at low and high homologous temperatures. Vacancy diffusion can induce permanent deformations in the material, which raises the question as to how the corresponding strain rate can be related to the vacancy flux at the scale of individual grains.

Continuum mechanics is embodied by the deformation of material lines drawn on a deforming specimen. When such lines are too blurred due to severe diffusion processes, continuum mechanics fails as it is unable to describe such material behaviour. In this work, it will be shown that continuum mechanics can still be used as a compromise between detailed atomistic analysis and field theory when the blurring of material lines is not too severe, as mentioned by Berdichevsky and coworkers [15] very clearly in 1997. In addition to these material point considerations, polycrystals modelling poses several challenges. In particular, grain boundaries introduce a geometrical discontinuity, and provide the main driving force for diffusive creep processes.

In the literature, two classes of models can generally be found for diffusion creep: marker based models [111] and lattice based models [28, 49]. In the first class, the existence of indestructible entities is assumed, which are tied to the material and convect with it, such that the definition of strain remains possible. In lattice based models, the creep deformation is assumed to be linked to lattice based mechanisms, such as site creation/annihilation and diffusion of species in the lattice. In [49], the authors develop a model that accounts for the plastic deformation in grain boundary zones of finite width, but not in the bulk. In their work, the plastic deformation rate is assumed to be proportional to a sink term in the vacancy diffusion equation, and to be only active in the grain boundary region. Their model was later extended to account for grain boundary migration, using a level-set method [92]. To our knowledge, Berdichevsky et al. [15] were the first to relate the viscoplastic deformation rate to the gradient of the vacancy flux, see eq. (60) and eq. (62) in [15]. In [56] and [117], the plastic strain rate is postulated as the symmetric part of the vacancy flux gradient, and the driving force arises from stress dependent boundary conditions imposed for the vacancy concentration. This formulation has also been used in [52], and is generally not applicable to a generic polycrystalline simulation. It is only recently that Mishin and coworkers [88] combined the two models and adopted a non-classical approach to account for grain boundaries migration. The authors identified three minimum ingredients required for creep modelling: a thermodynamic framework accounting for lattice site evolution, a model of microstructure evolution and an appropriate set of kinetics equations. Their model was applied to an elementary bicrystal with a symmetrical grain boundary. Other important contributions made on diffusion creep are those from [113, 45, 44, 112], in which creep equations for a solid are derived with a continuous distribution of vacancy sinks and sources, for instance associated with dislocation climb mechanisms.

Classically, mechanical models are built using representative volume elements (RVE), whereby stress or strain heterogeneities are ignored or averaged. However, these heterogeneities contribute strongly to the behaviour of the material, and polycrystalline aggregates simulations are now relied upon in order to obtain intragranular stress and deformation fields. It is known that heterogeneities originate from elastic anisotropy, crystallographic slip [12], and play a major role in crack nucleation [114, 82]. In [51], the transport equations for dislocations are complemented to account for climb mediated by diffusion processes, at the scale of precipitates. In turn, the

plastic strain rate tensor is extended to incorporate this climb kinematics. However in these works, the heterogeneities arising from diffusion processes are not accounted for.

The objective of this work is to describe deformation fields inside the grains arising from diffusion processes and dislocation slip in a polycrystal subject to constant applied load. In the present paper, the set of processes and associated equations necessary for a field theory of diffusional creep, where the viscoplastic deformation rate is related to the gradient of the vacancy flux, will be presented. This work is conducted at the meso-scale, with a detailed description of concentration and displacement fields inside a polycrystalline element, and with an explicit geometrical description of grains and grain boundaries. Fully coupled diffusion creep-crystal plasticity simulations of polycrystalline aggregates, including the effects of the vacancy flux gradient, are also presented for the first time. The proposed framework encompasses Herring, Coble and dislocation creep mechanisms at the local intergranular and intragranular levels.

The first section is dedicated to the formulation of the creep kinetics in the spirit of Berdichevsky's work, and the diffusion induced creep strain-rate tensor is identified as the deviatoric and symmetric part of the gradient of the vacancy flux. Then, a chemical-mechanical coupled framework is developed from which Herring's diffusion relation [63] is naturally recovered, thus yielding the correct overall creep driving forces. In the proposed formulation, creep processes start naturally by applying mechanical boundary conditions on a polycrystal. It is assumed for simplicity that any grain boundary motion can be neglected.

In the second part, finite element (FE) creep simulations of polycrystalline copper are conducted using diffusion data available in the literature to predict the average creep strain rates. Then, the FE results are compared to classic analytical solutions [47], and the numerical treatment of a grain boundary is emphasized and compared to the literature [49, 117]. In the present work, grain boundaries are first treated with Dirichlet conditions; then, grains and grain boundaries are described by phase-field like variables [2]. Finally, crystal plasticity [31] is introduced as an additional deformation mechanism: incompatibilities arising close to grain boundaries modify the stress state which, in turn, influences the vacancy flux.

3.2 Kinetics of vacancy diffusion induced creep in crystals

3.2.1 Definition of a material point in the presence of diffusion

The pioneering work carried out by Cahn and Larché in the 70's and 80's [27, 28] introduced the notion of network to deal with some of the problems mentioned in the introduction. One would then think of a material point as a collection of lattice sites. A second possible definition would be to consider the material point as a collection of atoms. Indeed, the material lines of continuum mechanics, used for instance for strain field measurements, will not be drawn on the lattice in such case but rather on the atoms themselves. Both choices are illustrated in fig. 3.1. In this work, the latter definition of the material point as a collection of atoms will be adopted. The motivation for choosing the marker-based definition of the material point is the growing use of strain field measurement methods in experimental mechanics based on deposited grids or patterns. The measured strain does not refer to lattice based volume elements but rather to collection of atoms coinciding, at least partially, with the deposited lines or points of the grid. Simulations of the type presented in the present work will be necessary for quantitative interpretation of strain field measurements at high temperature and high resolution in metal polycrystals. This implies that the analysis presented in this work will be based on the following hypotheses:

- The positions of the atoms and vacancies are constrained by the lattice of the crystalline

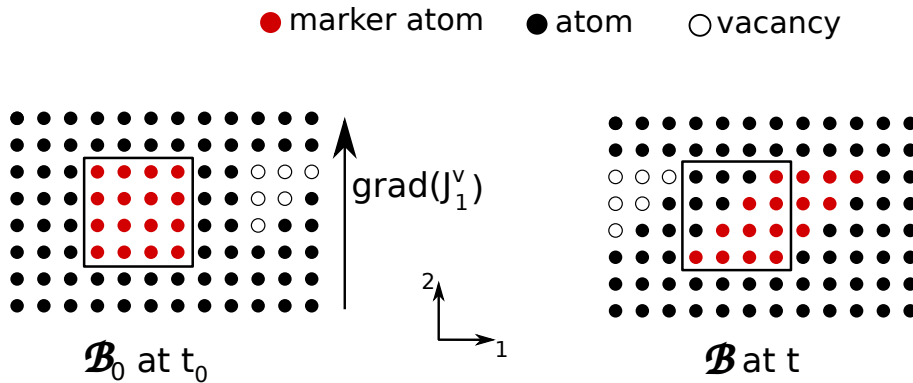


Figure 3.1: In this idealised figure, the atoms of a material point at $t = 0$ are represented by red dots. Due to an imposed gradient of the vacancy flux, $\frac{\partial J_1^v}{\partial x_2} \neq 0$, the vacancies move from right to left, accompanied by an opposite motion of atoms. Here, the material element is sheared whereas the lattice volume element denoted by the box remains unchanged. In reality, the picture is correct at a much larger scale than a few atoms, so that larger volume elements must be considered than represented here.

solid, i.e. they can only occupy substitutional sites in the crystalline lattice. Also, creation or annihilation of lattice sites associated with defects like climbing dislocations are not considered for simplicity. The coupling between vacancy diffusion and continuum modelling of dislocation climb was tackled in the references [112, 51].

- The volume element associated with the material point, V , is a bounding box encompassing this collection of atoms and any vacancies which may be trapped inside. This is the so-called marker-based definition of the material volume element.
- The diffusion processes should not be too severe for the material lines to keep their identity. Copper is well-suited for the present treatment. For instance in [127], experiments show a transition in creep curves from diffusion creep to dislocation creep at half the melting temperature (that is, as low as $\simeq 700\text{K}$), for grain size of a few tens of microns.
- Direct exchange between atoms does not occur. Any atom motion is accompanied by an opposite motion of a vacancy. This is a frequent assumption, and its justification lies on the fact that a direct exchange between substitutional atoms is energetically more expensive than when involving vacancies [100].

The latter mainly applies to material volume elements in the grain's interior. The hypothesis of absence of site sources and sinks will be relaxed in the case of grain boundary behaviour.

3.2.2 Coupling creep deformation and the gradient of the vacancy flux

In the following section, the considered species are atoms and vacancies, denoted with a superscript, k , equal to either a (atoms), or, v (vacancies). The reference configuration of the body is denoted by \mathcal{B}_0 , made of material points \mathcal{M} , occupying the initial spatial position, $\underline{\mathbf{X}}$. In the current configuration at time, t , the body is denoted by \mathcal{B} , and its material points are located at, $\underline{\mathbf{x}}$. The function $\underline{\mathbf{x}} = \chi_u(\underline{\mathbf{X}}, t)$ maps the material points to the current configuration at time t . The following quantities are defined at each material point, \mathcal{M} :

- $n^\#(\underline{\mathbf{x}}, t)$ is the mole number of substitutional sites per unit volume [$mol.m^{-3}$] in the current state.
- $N^\#(\underline{\mathbf{X}})$ is the mole number of substitutional sites per unit volume [$mol.m^{-3}$] in the reference state.
- $n^k(\underline{\mathbf{x}}, t)$ is the mole number of substitutional species k per unit volume [$mol.m^{-3}$] in the current state.
- $N^k(\underline{\mathbf{X}})$ is the mole number of substitutional species k per unit volume [$mol.m^{-3}$] in the reference state.
- $c^k(\underline{\mathbf{x}}, t) = \frac{n^k}{n^\#}$ is the fraction of sites occupied by species k in the current state.

Furthermore, the network constraint imposes that

$$\sum_k n^k = n^\# . \quad (3.1)$$

In this subsection, the crystalline lattice is supposed fixed in space with respect to the observer [9], and undeformable. Elastic straining of the lattice will be added later on. In the proposed analysis, interaction between vacancy and defects like dislocations is not considered for the sake of simplicity. Coupling between diffusion and climb was explicitly investigated in the reference [51]. By definition, the material point velocity is the average velocity of the atoms in the material volume element, V , here expressed in the referential of the lattice as:

$$\underline{\mathbf{v}}(\underline{\mathbf{x}}, t) = \frac{1}{n^a V} \sum_{n=1}^{n^a V} \underline{\mathbf{v}}^{a,n}(\underline{\mathbf{x}}, t) , \quad (3.2)$$

where $\underline{\mathbf{v}}^{a,n}(\underline{\mathbf{x}}, t)$ is the velocity of the n^{th} atom in V , and $n^a V$ the number of moles of atoms in V . Similarly for the vacancies:

$$\underline{\mathbf{v}}^v(\underline{\mathbf{x}}, t) = \frac{1}{n^v V} \sum_{n=1}^{n^v V} \underline{\mathbf{v}}^{v,n}(\underline{\mathbf{x}}, t) . \quad (3.3)$$

Since the n^{th} atom is either immobile ($\underline{\mathbf{v}}^{a,n} = 0$) or exchanging position with the m^{th} vacancy ($\underline{\mathbf{v}}^{a,n} = -\underline{\mathbf{v}}^{v,m}$),

$$\sum_{n=1}^{n^a V} \underline{\mathbf{v}}^{a,n} + \sum_{m=1}^{n^v V} \underline{\mathbf{v}}^{v,m} = 0 . \quad (3.4)$$

Using the network constraint, eq. (3.1), and the definitions of the mean velocities given by eq. (3.2) and eq. (3.3), in 3.4, the following relation is obtained:

$$n^a \underline{\mathbf{v}} + n^v \underline{\mathbf{v}}^v = 0 . \quad (3.5)$$

The definition of the vacancy flux in $m^{-2}s^{-1}$ is defined as:

$${}^n \underline{\mathbf{J}}^v = n^v \underline{\mathbf{v}}^v , \quad (3.6)$$

where the left superscript, n , reminds us that this definition is valid for molar concentrations. Substituting eq. (3.6) into eq. (3.5), a relation between the velocity of the atoms and the vacancy flux is obtained,

$$\underline{\mathbf{v}} = -\frac{1}{n^a} {}^n \underline{\mathbf{J}}^v . \quad (3.7)$$

The motion of the atoms described by eq. (3.7) gives rise to a deformation rate, defined as the symmetric part of the velocity gradient. Then,

$$D_{ij} = \frac{1}{2} \left(\frac{\partial v_i}{\partial x_j} + \frac{\partial v_j}{\partial x_i} \right). \quad (3.8)$$

Using eq. (3.7), the deformation rate can be finally related to the gradient of the vacancy flux, as,

$$D_{ij} = -\frac{1}{2} \left(\frac{\partial}{\partial x_j} \left(\frac{1}{n^a} {}^n J_i^v \right) + \frac{\partial}{\partial x_i} \left(\frac{1}{n^a} {}^n J_j^v \right) \right). \quad (3.9)$$

3.2.3 Balance of species

Consider the material domains, \mathcal{D} and \mathcal{D}_0 , as subdomains of \mathcal{B} and \mathcal{B}_0 , respectively. In this section, it is assumed that the number of substitutional sites remains practically constant. Hence,

$$\int_{\mathcal{D}_0} N^\#(\underline{\mathbf{X}}) dV = \int_{\mathcal{D}} n^\#(\underline{\mathbf{x}}, t) dv. \quad (3.10)$$

Differentiating eq. (3.10) with respect to time and using Reynold's transport equation yields,

$$0 = \frac{\partial}{\partial t} \int_{\mathcal{D}} n^\#(\underline{\mathbf{x}}, t) dv = \int_{\mathcal{D}} \left(\frac{\partial n^\#}{\partial t} + n^\# \frac{\partial v_i}{\partial x_i} \right) dv, \quad (3.11)$$

which leads to the local form of the sites balance equation:

$$\frac{\partial n^\#}{\partial t} + n^\# \text{Div } \underline{\mathbf{v}} = 0. \quad (3.12)$$

The balance law for vacancies, is then expressed in terms of c^v , the lattice site fraction of vacancies, as,

$$\frac{d}{dt} \int_{\mathcal{D}} n^\# c^v dv = - \int_{\partial \mathcal{D}} {}^n \underline{\mathbf{j}}^v \cdot \underline{\mathbf{n}}, \quad (3.13a)$$

$$\int_{\mathcal{D}} n^\# \dot{c}^v + c^v \left(\dot{n}^\# + n^\# \text{Div}(\underline{\mathbf{v}}) \right) dv = - \int_{\partial \mathcal{D}} {}^n \underline{\mathbf{j}}^v \cdot \underline{\mathbf{n}}, \quad (3.13b)$$

$$\int_{\mathcal{D}} n^\# \dot{c}^v dv = - \int_{\partial \mathcal{D}} {}^n \underline{\mathbf{j}}^v \cdot \underline{\mathbf{n}}, \quad (3.13c)$$

where the Reynolds transport theorem and the conservation of sites, eq. (3.12), has been used. Since $n^\#$ is practically constant, the local form of (3.13) can be divided by $n^\#$ to obtain new definitions in terms of c^v instead of n^v . Hence, a new definition of the vacancy flux having units of [ms^{-1}] will be henceforth used [9],

$$\underline{\mathbf{j}}^v = c^v \underline{\mathbf{v}}^v, \quad (3.14)$$

which satisfies the field equation,

$$\dot{c}^v = -\text{Div}(\underline{\mathbf{j}}^v). \quad (3.15)$$

It is recalled that the latter balance equation is valid for the bulk grain behaviour in the absence of sources and sinks, thus excluding the interaction of vacancies with crystal defects for simplicity.

3.2.4 Linearized theory

It is here assumed that $c^v \ll 1$. The components of the strain rate equation, (3.9), is now expressed as:

$$D_{ij} = -\frac{1}{2} \left(\frac{\partial}{\partial x_j} \left(\frac{1}{(1-c^v)} j_i^v \right) + \frac{\partial}{\partial x_i} \left(\frac{1}{(1-c^v)} j_j^v \right) \right). \quad (3.16)$$

The linearized strain rate components are finally given by,

$$D_{ij} = -\frac{1}{2} \left(\frac{\partial j_i^v}{\partial x_j} + \frac{\partial j_j^v}{\partial x_i} \right). \quad (3.17)$$

The strain rate can be split into two parts, as follows,

$$\underline{\underline{D}} = \frac{\text{trace}(\underline{\underline{D}})}{3} \underline{\underline{1}} + \underline{\underline{D}}^{dev}. \quad (3.18)$$

The volumetric part corresponds to an accumulation or loss of vacancies and is associated with an eigenstrain proportional to the vacancy concentration, since $\text{trace}(\underline{\underline{D}}) = -\text{Div} \underline{\underline{j}}^v = \dot{c}^v = -\dot{c}^a$. The deviatoric part, $\underline{\underline{D}}^{dev}$, can be defined as the inelastic creep strain rate. Its integrated form leads to the sheared deformation illustrated in fig. 3.1. Finally, an elastic deformation can be superimposed on the previous contributions. Note that Berdichevsky [15] introduces elastic and plastic velocities. However, there is generally not such a thing like an elastic or plastic velocity, since elastic and plastic strain tensors are generally incompatible.

3.3 Balance laws and constitutive equations in elasto-viscoplasticity

3.3.1 Balance laws

The balance law for vacancies, eq. (3.15), has already been derived on the volume \mathcal{B} with boundary $\partial\mathcal{B}$ of normal $\underline{\underline{n}}$:

$$\begin{aligned} \dot{c}^v &= -\text{Div} \underline{\underline{J}}^v + s^v \text{ on } \mathcal{B} \\ j^v &= \underline{\underline{J}}^v \cdot \underline{\underline{n}} \text{ on } \partial\mathcal{B} \end{aligned} \quad (3.19)$$

Note that a source/sink term s^v has been added to eq. (3.15). This term is taken to be zero in the grain's interior, as already stated, but can be active in the grain boundary region, as explained in section Section 3.4.1. The mechanical static equilibrium in the absence of volume forces is governed by:

$$\begin{aligned} \text{div} \underline{\underline{\sigma}} &= 0 \text{ on } \mathcal{B} \\ \underline{\underline{t}} &= \underline{\underline{\sigma}} \cdot \underline{\underline{n}} \text{ on } \partial\mathcal{B} \end{aligned} \quad (3.20)$$

where $\underline{\underline{\sigma}}$ is the stress tensor and $\underline{\underline{t}}$ the traction vector on $\partial\mathcal{B}$.

3.3.2 Constitutive equations

The small strain tensor, $\underline{\underline{\xi}}$, is partitioned into four contributions

$$\underline{\underline{\xi}} = \underline{\underline{\xi}}^e + \underline{\underline{\xi}}^*(c^v) + \underline{\underline{\xi}}^{\text{in-diff}} + \underline{\underline{\xi}}^{\text{in-disl}}, \quad (3.21)$$

where

- $\underline{\underline{\xi}}^e$ is the elastic strain tensor,

- $\underline{\xi}^*(c^v)$ is the eigenstrain tensor due to the relaxation of the lattice around vacancies,
- $\underline{\xi}^{\text{in-diff}}$ is the inelastic strain tensor due to inhomogeneous vacancy motion,
- $\underline{\xi}^{\text{in-disl}}$ is the inelastic strain tensor due to dislocation motion.

The eigenstrain typically depends on the concentration, c^v , as [28]

$$\underline{\xi}^*(c^v) = \underline{\eta}^v(c^v - c_{ref}^v) + \underline{\xi}_{ref}^* \quad (3.22)$$

Here, $\underline{\xi}_{ref}^*$ is the eigenstrain tensor corresponding to the equilibrium concentration, c_{ref}^v , and $\underline{\eta}^v$ defines the direction and magnitude of the surrounding atomic relaxation. The diffusion creep term, $\underline{\xi}^{\text{in-diff}}$, is the deviatoric part of eq. (3.17)

$$\underline{\xi}^{\text{in-diff}} = - \left((\underline{\nabla} \underline{\mathbf{J}}^v)^{sym} - \frac{1}{3} \text{div}(\underline{\mathbf{J}}^v) \underline{\mathbf{I}} \right) \quad (3.23)$$

Note that in previous work (such as [31, 53]), the diffusion-induced inelastic creep strain was accounted for using a power or exponential viscous flow rule, directly, the diffusion-induced inelastic creep strain is captured using Newton's viscous law, relating $\underline{\xi}^{\text{in-diff}}$ and the deviatoric stress. In contrast, it is computed here from the gradient of the diffusion flux. The inelastic strain rate tensor due to dislocation motion, $\underline{\dot{\xi}}^{\text{in-disl}}$, can be expressed using the crystal plasticity framework as,

$$\underline{\dot{\xi}}^{\text{in-disl}} = \sum_{\alpha} \frac{1}{2} \dot{\gamma}^{\alpha} (\underline{\mathbf{m}}^{\alpha} \otimes \underline{\mathbf{n}}^{\alpha} + \underline{\mathbf{n}}^{\alpha} \otimes \underline{\mathbf{m}}^{\alpha}), \quad (3.24)$$

where the superscript, α , denotes the slip system, $\dot{\gamma}^{\alpha}$ the crystallographic slip rate, $\underline{\mathbf{n}}^{\alpha}$ the slip system plane normal, and $\underline{\mathbf{m}}^{\alpha}$ the slip direction. The kinetic equation for the crystallographic slip rate, $\dot{\gamma}^{\alpha}$, is expressed using a power law relation,

$$\dot{\gamma}^{\alpha} = \left\langle \frac{|\tau^{\alpha}| - S_T^{\alpha}}{\tau_0} \right\rangle^n \text{sign}(\tau^{\alpha}), \quad (3.25)$$

where, τ^{α} , is the resolved shear stress, τ_0 and n are material parameters, and S_T^{α} is the overall slip resistance. The latter is given by [31] :

$$S_T^{\alpha} = \lambda G b^{\alpha} \sqrt{\sum_{\beta} h_{\alpha\beta} \rho^{\beta}}, \quad (3.26)$$

in which, λ , is a coefficient, G the shear modulus, b^{α} the magnitude of the Burgers vector, ρ^{α} the overall dislocation density, and $h_{\alpha\beta}$ a dislocation interaction matrix expressed in terms of two coefficients, ω_1 and ω_2 , as

$$h_{\alpha\beta} = \omega_1 + (1 - \omega_2) \delta_{\alpha\beta}. \quad (3.27)$$

Note that, for simplicity, no direct coupling of diffusion with dislocation multiplication and annihilation is introduced in this work. The power law expression, eq. (3.25), indirectly accounts for vacancy diffusion mediated climb processes. A more direct coupling was recently proposed in [51] at a lower scale. A dependence of the diffusion coefficient on dislocation density could be introduced following, for instance, [32]. Finally, the evolutionary equation for the dislocation density reads [31]

$$\dot{\rho}^{\alpha} = \frac{C}{b^{\alpha}} \left[K \sum_{\beta} \rho^{\beta} - 2d_p \rho^{\alpha} \right] |\dot{\gamma}^{\alpha}|, \quad (3.28)$$

where C, K and d_p are material parameters. The Helmholtz free energy density is assumed to be composed of a mechanical and a chemical part:

$$\psi(c^v, \underline{\underline{\xi}}^e) = \psi^{mech}(\underline{\underline{\xi}}^e) + \psi^{chem}(c^v). \quad (3.29)$$

The mechanical part of the free energy is defined as,

$$\psi^{mech}(\underline{\underline{\xi}}^e) = \frac{1}{2} \underline{\underline{\xi}}^e : \underline{\underline{\Lambda}} : \underline{\underline{\xi}}^e, \quad (3.30)$$

where, $\underline{\underline{\Lambda}}$, is the fourth order elasticity tensor, taken independent of c^v for simplicity. The chemical free energy density is expressed in a standard form as [35],

$$\psi^{chem}(c^v) = \frac{E_f}{\Omega_0} c^v + \frac{RT}{\Omega_0} (c^v \log(c^v) + (1 - c^v) \log(1 - c^v)) \quad (3.31)$$

where, T , is the absolute temperature, R the ideal gas constant, E_f the vacancy formation energy, and Ω_0 the volume per mole of atoms. The state laws are given according to [120] :

$$\underline{\underline{\sigma}} = \frac{\partial \psi}{\partial \underline{\underline{\xi}}^e} = \underline{\underline{\Lambda}} : \underline{\underline{\xi}}^e, \quad (3.32)$$

$$\mu = \frac{\partial \psi}{\partial c^v} - \underline{\underline{\eta}}^v : \underline{\underline{\sigma}}, \quad (3.33)$$

where μ is the diffusion potential. The vacancy flux is defined as

$$\underline{\underline{J}}^v = -\underline{\underline{L}}^v(c^v) \cdot \underline{\underline{\nabla}} \mu, \quad (3.34)$$

with the mobility, $\underline{\underline{L}}^v$, expressed as

$$\underline{\underline{L}}^v = \frac{\Omega_0}{RT} c^v (1 - c^v) \underline{\underline{D}}^v. \quad (3.35)$$

Here, $\underline{\underline{D}}^v$, is the generally anisotropic diffusivity tensor [9].

3.4 Simulation of diffusional creep in a polycrystalline aggregates

3.4.1 Grain boundary description

The driving force for diffusion is the gradient of diffusion potential, defined by eq. (3.33). According to Herring's theory, the inhomogeneity in the diffusion potential is introduced by the grain boundaries, and thus here they will be modeled explicitly. In 2D, the simplification is made that each grain can be described by a single orientation, θ , defined with respect to an arbitrary reference configuration [69]. A stationary phase-field, ϕ^{GB} , is introduced to interpolate physical properties between their bulk and grain boundary values. It is arbitrarily expressed as the following explicit function,

$$\phi^{\text{GB}}(d) = \left(\cosh \left(\frac{r^{\text{GB}} \times 2d}{\delta^{\text{GB}}} \right) \right)^{-1}, \quad (3.36)$$

where, δ^{GB} , is the grain boundary thickness and, d , the distance from any point to the closest grain boundary. Also, the coefficient $r^{\text{GB}} = 5.3$ is chosen so that $\phi^{\text{GB}}\left(\frac{-\delta^{\text{GB}}}{2}\right) = \phi^{\text{GB}}\left(\frac{\delta^{\text{GB}}}{2}\right) = 0.01$.

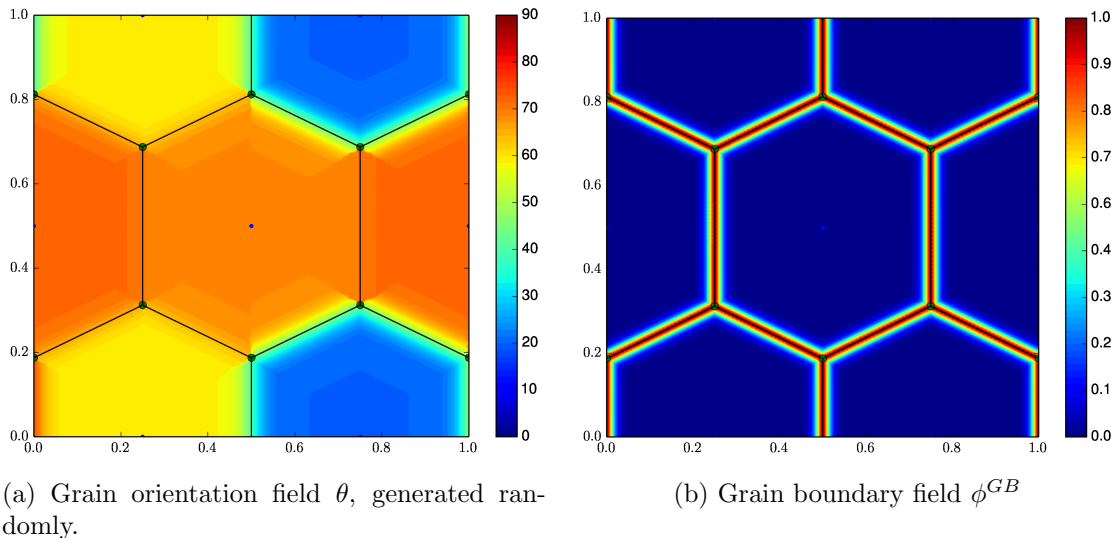


Figure 3.2: Periodic 2D polycrystal aggregate used in the simulations. The window size is varied from 20 to 200 μm . The edges of the Voronoi cells are superimposed to the fields.

Furthermore, a second stationary phase-field function, θ , is relied upon in order to represent the grain orientation to be used in the crystal plasticity model. This field function varies smoothly between two grains of orientation θ_1 and θ_2 , and is described by the following function ,

$$\theta(\bar{d}) = \frac{1}{2} (\theta_1 - \theta_2) \left[1 - \tanh \left(-\frac{2.94\bar{d}}{\delta_{GB}} \right) \right] + \theta_2 , \quad (3.37)$$

where, \bar{d} , is the algebraic distance to the grain boundary, negative in the grain oriented along θ_1 and positive in the grain with orientation θ_2 , such that $\theta(0) = \frac{\theta_1 + \theta_2}{2}$, $\theta(-\infty) = \theta_1$ and $\theta(+\infty) = \theta_2$. Both ϕ^{GB} and θ fields are shown in fig. 3.2. Note that the interpolation eq. (3.37) induces discontinuities in the θ field within the grains if more than two grains are considered. An equilibrium orientation field generated by a phase field computation as done in [2, 3] would be preferable. We have checked that this choice does not significantly affect the crystal plasticity results presented in Section 3.4.3 by comparison with computations based on uniform lattice orientation in grains as usually done in standard crystal plasticity simulations. The value of θ within each grain has been generated randomly. Furthermore, the parameter η^v is chosen such that the Herring diffusion potential formula is recovered,

$$\eta^v = (1 - \phi^{GB}) \eta^{v,\text{bulk}} \mathbf{I} + \phi^{GB} \eta^{v,\text{GB}} \mathbf{n} \otimes \mathbf{n} . \quad (3.38)$$

The diffusivity tensors are, in turn, expressed as:

$$\begin{aligned} \mathcal{D}^v &= (1 - \phi^{GB}) \mathcal{D}_{\text{bulk}}^v + \phi^{GB} \mathcal{D}_{GB}^v \\ \mathcal{D}_{\text{bulk}}^v &= D_{\text{bulk}}^v \mathbf{I} \\ \mathcal{D}_{GB}^v &= D_{GB}^v (\mathbf{I} - \mathbf{n} \otimes \mathbf{n}) \end{aligned} \quad (3.39)$$

In the above relations, the grain boundary normal is computed numerically using $\mathbf{n} = \frac{\nabla \theta}{\|\nabla \theta\|}$.

The coefficients $\eta^{v,\text{bulk}}$ and $\eta^{v,\text{GB}}$ are expressed as:

$$\eta^{v,\text{bulk}} = \frac{\Delta v^{v,\text{bulk}}}{3\Omega_0} , \eta^{v,\text{GB}} = \frac{\Delta v^{v,\text{GB}}}{3\Omega_0} , \quad (3.40)$$

where, $\Delta v^{v,\text{bulk}}$ and $\Delta v^{v,\text{GB}}$ are, respectively, the bulk and grain boundary relaxed volume around a vacancy, and Ω_0 is the atomic volume. With this definition, the diffusion potential, eq. (3.33), becomes:

$$\begin{aligned} \mu^v &= \frac{E_f}{\Omega_0} + \frac{RT}{\Omega_0} \log \left(\frac{c^v}{1 - c^v} \right) \\ &\quad - \eta^{v,\text{bulk}} \text{trace}(\boldsymbol{\sigma}) (1 - \phi^{\text{GB}}) - \eta^{v,\text{GB}} \sigma_n \phi^{\text{GB}}, \end{aligned} \quad (3.41)$$

where, $\sigma_n = \boldsymbol{\sigma} : \mathbf{n} \otimes \mathbf{n}$ is the normal GB traction. The above expression for the diffusion potential, μ^v , can be compared to the formula derived by Herring in [63]:

$$\mu - \mu_h = \mu_0 - p_{zz} \Omega_0, \quad (3.42)$$

where $(\mu - \mu_h)$ is the diffusion potential, μ_0 is defined by Herring as “*the chemical potential of [...] the same substance in equilibrium at the same temperature and at zero stress*”, p_{zz} the normal surface traction, and $\Omega_0 = \frac{\delta v}{\delta N}$ the atomic volume corresponding to the addition/removal of δN atoms causing a change in volume, δv . Albeit the physical unit difference (Herring used a flux in atoms per unit area per unit time), one can observe that the diffusion potential derived in 3.41 contains the same terms. Using eq. (3.33), the gradient of the diffusion potential becomes:

$$\begin{aligned} \nabla \mu^v &= \frac{\partial^2 \psi}{\partial c^2} \nabla c + \left(-\frac{\partial \eta^v}{\partial \phi^{\text{GB}}} : \boldsymbol{\sigma} + \frac{\partial^2 \psi}{\partial c \partial \phi^{\text{GB}}} \right) \nabla \phi^{\text{GB}} \\ &\quad + \left(-\frac{\partial^2 \psi}{\partial \xi^e \partial \xi^e} : \boldsymbol{\eta}^v \right) : \nabla \boldsymbol{\xi}, \end{aligned} \quad (3.43)$$

and it is readily seen that any mechanical loading of the grain boundaries will give a non-zero diffusion potential gradient, leading in turn to a creep deformation via eq. (3.17).

It is commonly accepted that grain boundaries, and interfaces in general, act as sources and sinks for point defects [47, 10, 37]. Grain boundaries are also known to interact with dislocations [29, 54], but this coupling is not taken into account in the present work. In what follows, two modelling options will be explored. First, a Dirichlet boundary condition imposing the equilibrium concentration of vacancies in the grain boundary region will be used, as done in [117]. Second, an additional source term in the diffusion equation 3.19 will be defined such that the grain boundary vacancy concentration is always close to its equilibrium value, as per [49, 86]. Then,

$$\begin{aligned} \dot{c}^v &= -\text{div} \mathbf{J}^v - K_{sv}^{\text{GB}} (c^v - c_{eq}^{v,\text{GB}}) \phi^{\text{GB}} && \text{on } V, \\ \dot{j}^v &= \mathbf{J}^v \cdot \mathbf{n} && \text{on } \partial V. \end{aligned} \quad (3.44)$$

Even though conservation of lattice sites has been assumed in the bulk material, this does not hold in the grain boundary regions, which act as preferential location for vacancy creation and annihilation [10]. As an example, first consider the case of a grain boundary acting as a sink for vacancies. Vacancies that migrate toward this grain boundary will eventually reach the last lattice sites located on the grain boundary surface itself. In a random grain boundary region, this row of lattice sites simply vanishes, thus producing a deformation at this grain boundary. Second, the exact inverse process happens at grain boundaries acting as sources: atoms at the surface will create a hump and leave a vacancy in the site that they previously occupied. This process is repeated until a whole new row of lattice sites is created. Hence, matter is transported from the GB that acts as a vacancy source, and which thickens in the process, toward the one acting as a sink, which shrinks. In [88] Section VII.A., Mishin and co-workers comments their

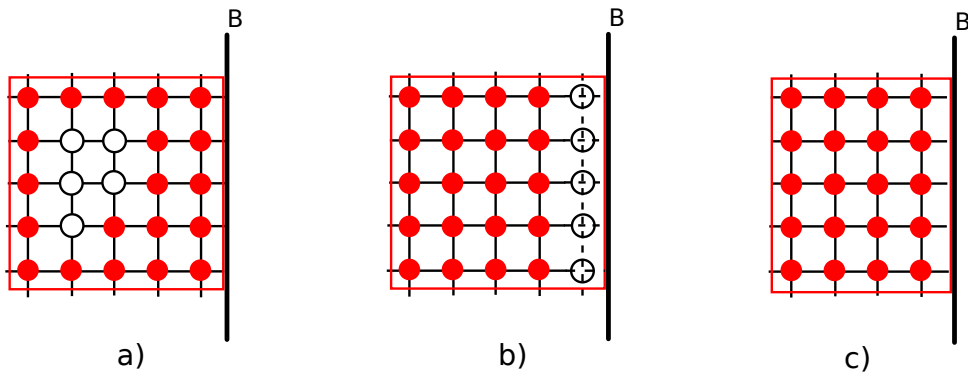


Figure 3.3: Mechanism for vacancy creep in the grain boundary region: (a) vacancies diffuse in the grain boundary vicinity, (b) when they reach the grain boundary surface, they destroy lattice sites, and (c) the grain boundary region shrinks as a result.

model, stating “*Vacancies can be generated only within the GB region and only by the growth or dissolution of lattice planes parallel to the GB.*”. Due to the fact that the molar quantity being absorbed or emitted by the grain boundary is known from 3.44, it is possible to take into account this additional phenomenon by completing the creep rate eq. (3.23) in the grain boundary region, to distinguish between bulk processes and grain boundary processes, as:

$$\begin{aligned} \dot{\varepsilon}_{ij}^{in-diff} = & - \left(\frac{1}{2} \left(\frac{\partial j_i^v}{\partial x_j} + \frac{\partial j_j^v}{\partial x_i} \right) - \frac{1}{3} \frac{\partial j_k^v}{\partial x_k} \delta_{ij} \right) (1 - \phi^{GB}) \\ & + \eta^{v,GB} K_{sv} (c^v - c_{eq}^v) \phi^{GB} n_i n_j . \end{aligned} \quad (3.45)$$

In [49], the same boundary process has been proposed and derived. However, as emphasised by the authors, this leads to creep strain accumulation only in the grain boundary regions. In the present work, viscoplastic strain is also introduced in the bulk part of the grain. Grain boundary sliding and opening are additional deformation modes of importance in the modelling of creep deformation and damage. They are not incorporated in the presented simulations for the sake of simplicity. They can be added in the finite element simulations using the theoretical and computational methodology described in the references [93, 126, 94]. These processes however involve strongly non-linear local material responses and lead to a high computational cost.

3.4.2 Problem description

To illustrate the proposed theory, a simplified copper polycrystal made up of periodic 2D hexagonal grains is constructed, see fig. 3.2. Creep simulations are conducted at 830K, and compared with experimental data from [128, 127], and to the well known analytical solution for Herring-Nabarro creep [47], namely

$$\dot{\varepsilon} = \frac{BD^v c^v \sigma^L \Omega_0}{d_g^2 kT} , \quad (3.46)$$

where, d_g , is the grain size, B , a geometrical factor (here taken equal to 2), σ^L , the applied stress, and k the Boltzmann constant.

The material parameters for copper are given in 3.1 and 3.2. The self-diffusion coefficient is expressed classically as $D = D^v c^v = D_0^v \exp\left(-\frac{Q_a^v}{RT}\right)$. An equi-axial stress $\boldsymbol{\sigma} = \sigma^L (\underline{\mathbf{e}}_y \otimes \underline{\mathbf{e}}_y - \underline{\mathbf{e}}_x \otimes \underline{\mathbf{e}}_x)$ is applied, of magnitudes ranging from 1 to 160 MPa, and for 10

to 100 μm grain sizes. The model is implemented into the finite element method, using the methodology described in [16] and [120]. The numerical implementation was carried out in the Z-set code [16], using as a fourth order Runge-Kutta method with automatic time-stepping. In the calculation of the diffusion potential gradient, 3.43, the gradient of the total strain tensor is needed. Therefore, the total strain is interpolated from the Gauss points to the nodes using the shape functions, and its gradient computed via the derivatives of the shape functions. The same technique is used to compute the gradient of the vacancy flux vector. It should be noted that this method is identical to the one used by Thomas and Chopin [116], Abrivard et al. [2], and Villani et al. [120].

C_{11} [GPa]	C_{12} [GPa]	C_{44} [GPa]	T_m [K]	D_0^v [$\text{m}^2.\text{s}^{-1}$]
179.5	126.4	82.5	1360.	3.4×10^{-5}
Q_a^v [J.mol^{-1}]	E_f^v [J.mol^{-1}]	$\eta^{v,GB}$	$\eta^{v,bulk}$	
2.0×10^5	1.225×10^5	-0.05	0	

Table 3.1: Material parameters for copper. The properties are supposed to be the same in the grain boundaries as in the bulk for simplicity, except for the coefficient η^v , eq. (3.38).

3.4.3 Results

Three cases are presented, where the proposed deformation mechanisms are progressively incorporated in the simulations. Two different boundary conditions in the GB region, either Dirichlet or K_{sv} sink term, are used. The GB is hence modelled as a perfect or potentially imperfect sink, respectively. While the Dirichlet condition is straightforward to use, the sink term offers more flexibility in the modelling, provided the sink parameter K_{sv} is carefully chosen.

In the first case, Dirichlet boundary conditions are used, and the only viscoplastic contribution is the inelastic diffusional one, 3.23. In the second case, grain boundary deformation is accounted for, by mean of the constitutive equation, 3.45, and the extended vacancy balance law, 3.44. Finally, the two inelastic deformation mechanisms, 3.23 and 3.24, are taken into account in order to compare the numerical predictions with experimental data available in [127]. Dirichlet boundary conditions are used in this last case.

All simulations have been carried out on the same polycrystalline aggregate, see fig. 3.2. Periodic boundary conditions are imposed on the vacancy concentration field c^v , and the four external surfaces are constrained to remain flat. In all plots, the x and y coordinates are given in μm .

3.4.3.1 Case study one: Dirichlet conditions at the grain boundaries

In this case, $c^v = c_{eq}^v$ is imposed on the FE node lines corresponding to the grain boundaries, where $\phi^{GB} = 1$. In 3.45, K_{sv} is taken to be equal to 0 and, except for η , the bulk and grain boundary properties are chosen to be the same in this section. For this first case, a first simulation is performed using isotropic elasticity: the symmetry in the geometry is visible in the resulting fields shown in fig. 3.4. When the stress is applied, the diffusion potential value is modified depending on the grain boundary orientation. It reaches an extremum when the GB surface normal is parallel to one of the principal stress directions, according to eq. (3.33), see fig. 3.4a. The equivalent inelastic strain, defined as $\varepsilon_{eq}^{\text{in-diff}} = \sqrt{\frac{2}{3}\tilde{\varepsilon}^{\text{in-diff}} : \tilde{\varepsilon}^{\text{in-diff}}}$, is shown on

fig. 3.4c. Stress concentration is observed close to the grain boundary triple junctions in the case of elastic isotropy. Elastic anisotropy, shown in figure 6 leads to stronger heterogeneity in the fields, higher maximum stress, and breaks the hexagonal symmetry observed in the isotropic case. The strong stress and strain concentrations occurring at the triple junctions, are due to increasing strain incompatibilities. They finally lead to lack of convergence of the computational scheme and they should be relaxed by grain boundary sliding and opening, not considered in this work. Triple junctions are known to be responsible for cavity nucleation and subsequent damage, see [47].

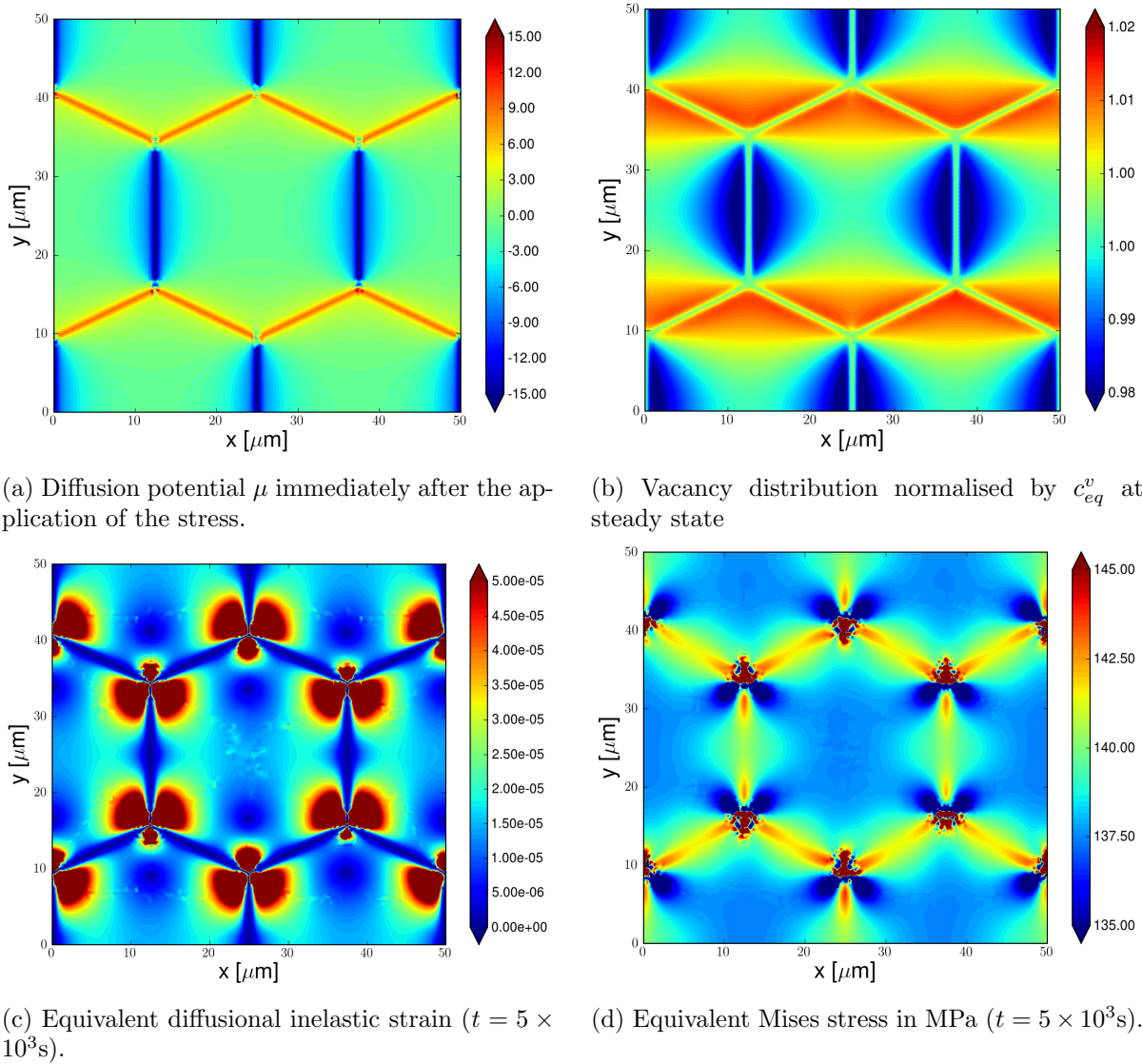
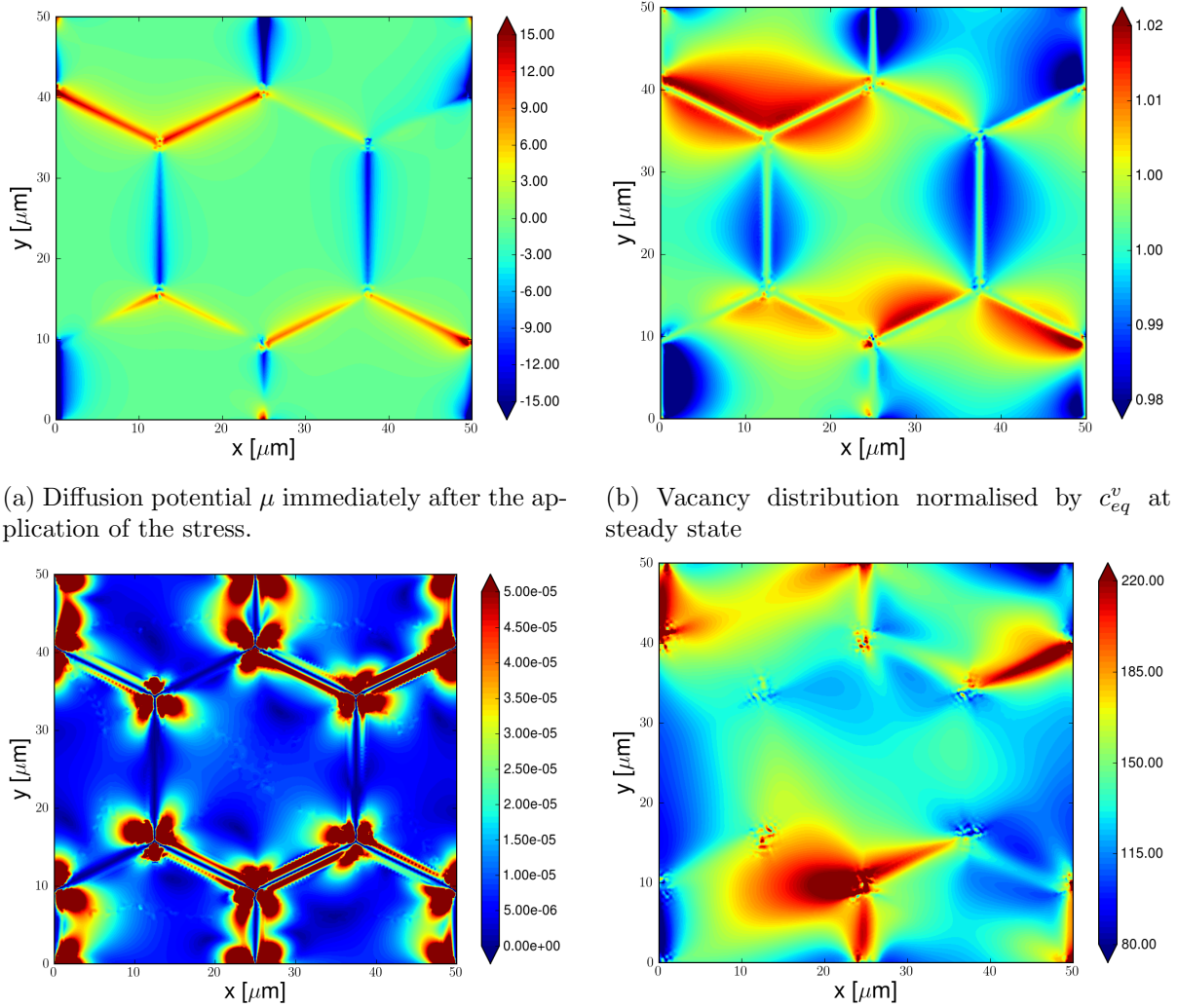


Figure 3.4: (a) Diffusion potential, (b) vacancy distribution, (c) inelastic strain and (d) equivalent Mises stress in the case of Dirichlet boundary conditions, with an applied stress of 80 MPa and a $25\mu\text{m}$ grain size, and for isotropic elasticity. The mechanical effect on the diffusion potential is clearly visible in (a): the location of each grain boundary is revealed by a different diffusion potential value, depending on the GB orientation.

The average macroscopic strain rate versus stress, and versus grain size on the other hand, are reported on figs. 3.6a and 3.6b, respectively. The model correctly predicts the strain rate



(a) Diffusion potential μ immediately after the application of the stress.

(b) Vacancy distribution normalised by c_{eq}^v at steady state

(c) Equivalent diffusional inelastic strain ($t = 5 \times 10^3$ s).

(d) Equivalent Mises stress in MPa ($t = 5 \times 10^3$ s).

Figure 3.5: (a) Diffusion potential, (b) vacancy distribution, (c) inelastic strain and (d) equivalent Mises stress in the case of Dirichlet boundary conditions, with an applied stress of 80 MPa and a $25\mu\text{m}$ grain size, and for anisotropic elasticity.

scaling with respect to load and grain size, i.e. $\dot{\epsilon} = f(\sigma, d_g^{-2})$, and the overall strain rate is of the same order of magnitude as the one given by the analytical expression, eq. (3.46). In order for the simulations to coincide with the analytical solution, the vacancy diffusivity coefficient has to be scaled up by a factor 7, which seems reasonable, since it is well within the experimental uncertainty. Finally, it should be pointed out that the simulations were carried out using two different meshes, one with 10 000 quadrangular quadratic elements, and the other with 98 000 triangular linear elements. No mesh sensitivity was found in the results.

3.4.3.2 Case study two: Source term in the grain boundaries

In this case, the Dirichlet boundary condition is dropped, and instead, the source strength parameter K_{SV} in 3.44 is set to a non-zero value and isotropic elasticity is used. In order to determine K_{SV} , a 1D case of two grains separated by a grain boundary is studied. First, a

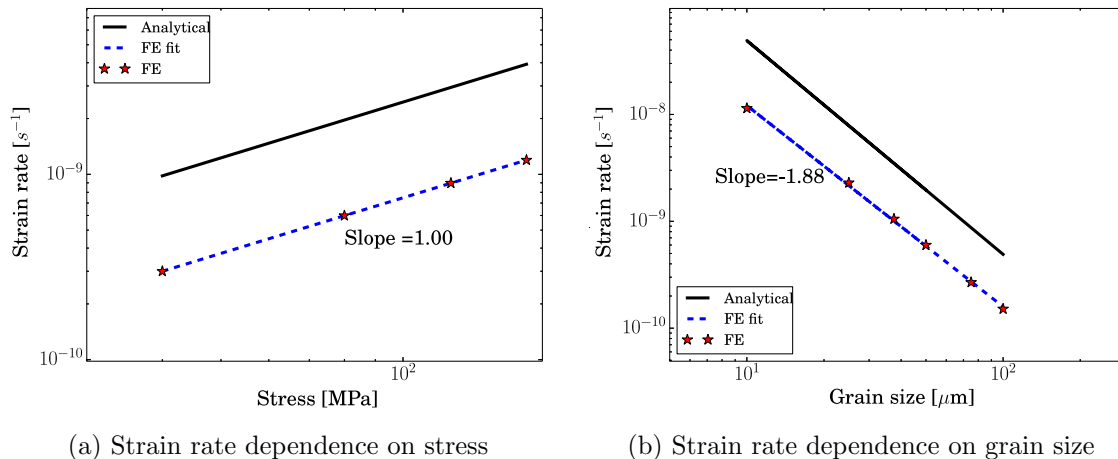


Figure 3.6: Comparison between the macroscopic Herring-Nabarro creep law and finite element simulations results using Dirichlet boundary conditions. According to the analytical solution, eq. (3.46), the slopes in figures (a) and (b) should be 1 and -2 , respectively.

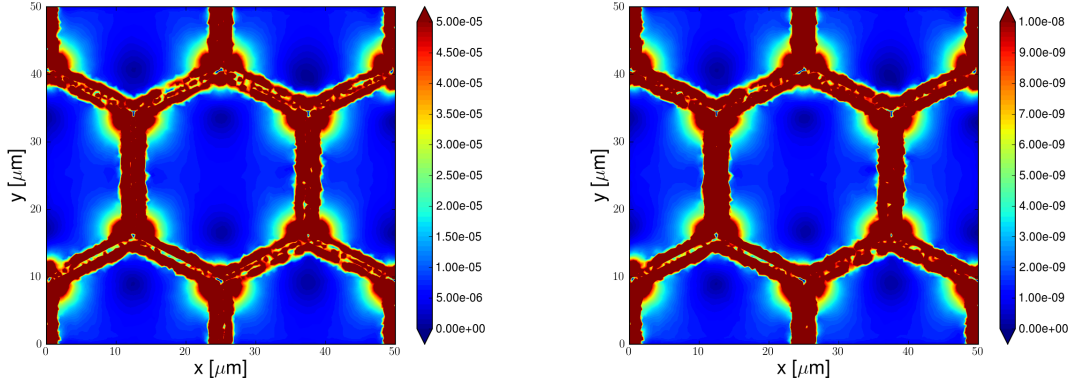
Dirichlet boundary condition on the grain boundary FE nodes is applied, as in the previous case. Then, the same problem is solved again, removing the Dirichlet condition and setting K_{sv} to be non zero at the grain boundary. The parameter K_{sv} is then chosen such that the concentration profiles given by both approaches are matched. For the range of grain sizes considered in this work, K_{sv} was found to be of the order of twice the vacancy diffusivity, $D^{v,bulk}$.

The grain boundary thickness, δ^{GB} , was kept constant and equal to $4\mu\text{m}$ across the range of simulated grain sizes, and the mesh was constructed in such a way that there were always at least 5 elements in the grain boundary region. The grain boundary thickness was chosen as a compromise between reality (a dozen Burgers vectors) and tractable computations. The grain boundary volume fraction was hence taken to vary between 0.2 and 2.2×10^{-2} for the considered range of grain sizes.

The simulated fields are shown in fig. 3.7 for the case of a $25\mu\text{m}$ grain size and a 80 MPa applied stress. One can notice that in 3.7a deformation also accumulates in the grain boundary regions, minimizing the triple junction effect. Furthermore, despite the fact that the parameter K_{sv} was fitted with a 1D case, the steady state vacancy concentration in the grain boundary region in fig. 3.7c is not exactly equal to c_{eq}^v . Instead, grain boundaries with $\sigma_n > 0$ have a lower vacancy concentration, and those with $\sigma_n < 0$, a higher one. However, the strain rate dependence on grain size is more strongly impacted when a source term is considered in the grain boundary, as it can be seen in fig. 3.8b.

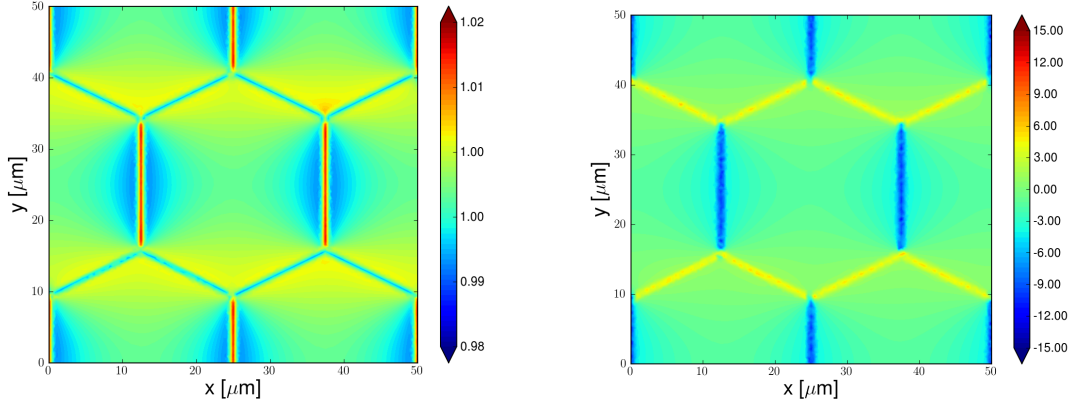
3.4.3.3 Case study three: Dirichlet conditions at the grain boundary and crystal plasticity

In this last case, both inelastic deformations arising from vacancies diffusion, 3.23, and dislocation slip, 3.24, are taken into account. Dirichlet boundary conditions are used on the grain boundary nodes, and a value of $K_{sv} = 0$ is assumed. Anisotropic elasticity is used, and the parameters of the crystal plasticity model are given in Table 3.2 for copper. Some are taken from the literature, as indicated in the table, and the other ones have been chosen so that the transition between the dislocation and diffusion regimes matches the experimental results presented in [127]. Hence, here the imposed stress is made to vary between 1 and 20 MPa.



(a) Equivalent diffusional inelastic strain ($t = 5 \times 10^3$ s).

(b) Equivalent diffusional inelastic strain rate at steady state



(c) Vacancy distribution normalised by c_{eq}^v at steady state

(d) Diffusion potential μ ($t = 5 \times 10^3$ s).

Figure 3.7: (a) Inelastic equivalent strain, (b) inelastic equivalent strain rate, (c) vacancy distribution and (d) diffusion potential μ in the case of a source term at the grain boundary, with an applied stress of 80 MPa and a $25\mu\text{m}$ grain size, and for isotropic elasticity.

τ_0 [MPa]	n	λ [31]	G [MPa] [31]	b^α [nm] [31]	$\rho_{t=0}^\alpha$ [μm^{-2}]
200	4	0.3	45000	0.257	3.2×10^4
ω_1 [31]	ω_2 [31]	C [31]	K [31]	d_p [μm] [31]	
1.5	1.2	0.5	1.4135×10^{-2}	10^{-3}	

Table 3.2: Parameters of the crystal plasticity model for pure copper.

The resulting strain and strain rate fields are shown on fig. 3.9 for the 20 MPa case. Here, the dislocation regime is predominant, and the diffusional inelastic strain is strongly impacted by the slip activity. There are several differences to be observed between the purely diffusional case (fig. 3.5) and the coupled case (fig. 3.9), while bearing in mind that the stress level is different. Even though the vacancy distribution is similar, the maximum values are greater when crystal plasticity is considered. The same trend is observed for the diffusional field: the overall field is similar, but the strain rate is accelerated by dislocation induced plasticity despite the fact that the applied stress is four times smaller. Indeed, the inhomogeneities in the stress field arising

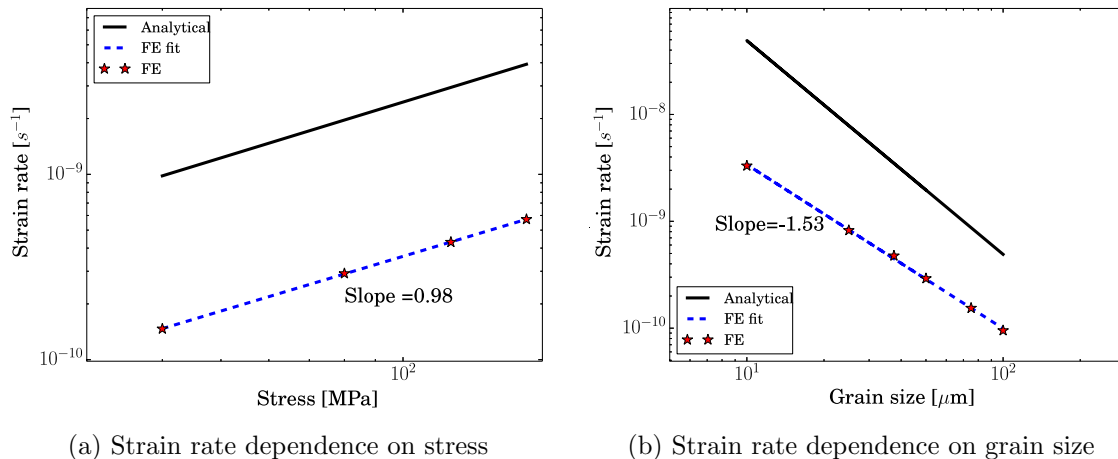


Figure 3.8: Comparison between the macroscopic Herring-Nabarro creep law and the finite element simulation results using a source term in the grain boundary of width $4\mu\text{m}$. According to the analytical solution eq. (3.46), the slopes in figures (a) and (b) should have value of 1 and -2 , respectively.

from dislocation plasticity promote diffusion, and hence, diffusional creep. Stress concentration is observed at some grain boundaries in fig. 3.9f, which is known from results of crystal plasticity finite element simulations [12].

Finally, the strain rate dependence on the applied stress is reported in fig. 3.10. There are two visible regimes in this figure. At lower stress, diffusional deformation mechanisms dominate over slip activity, whereas the latter dominates for high applied stresses. This is in relatively good agreement with [127], albeit the value of the slope in the dislocation regime, which is greater in the simulations.

3.4.3.4 Discussion

The model predicts one order of magnitude lower strain rate in the diffusion regime, which can be explained by the fact that at low homologous temperature ($\simeq 0.6T_m$), grain boundary diffusion plays an important role. The grain boundary and bulk diffusion coefficients were assumed equal in the simulations, which is not necessarily the case in fcc materials. This may explain the lower average strain rate average obtained numerically, compared to experimental data.

The value of the sink parameter, K_{sv} , was found to strongly influence the strain rate as well as the strain rate sensitivity to grain size. The value of this parameter, although critical, is not given in [49] (where it is actually called $\frac{1}{\tau}$). In this work, the sink parameter, K_{sv} , has been fitted from the results of a 1D simulation using Dirichlet boundary conditions. This approach, although very sensitive to the value of this parameter K_{sv} , is also capable of describing Herring-Nabarro creep. Furthermore, if one were to extend the proposed formalism to include migrating grain boundaries or void nucleation and growth, using for instance a phase-field approach [88, 86], the Dirichlet formulation would not be applicable. Indeed, some nodes that were once in a grain boundary region could, after grain boundary migration, be located in the bulk. In addition, voids, where $c^v = 1$, would be impossible to model, since a Dirichlet boundary condition would

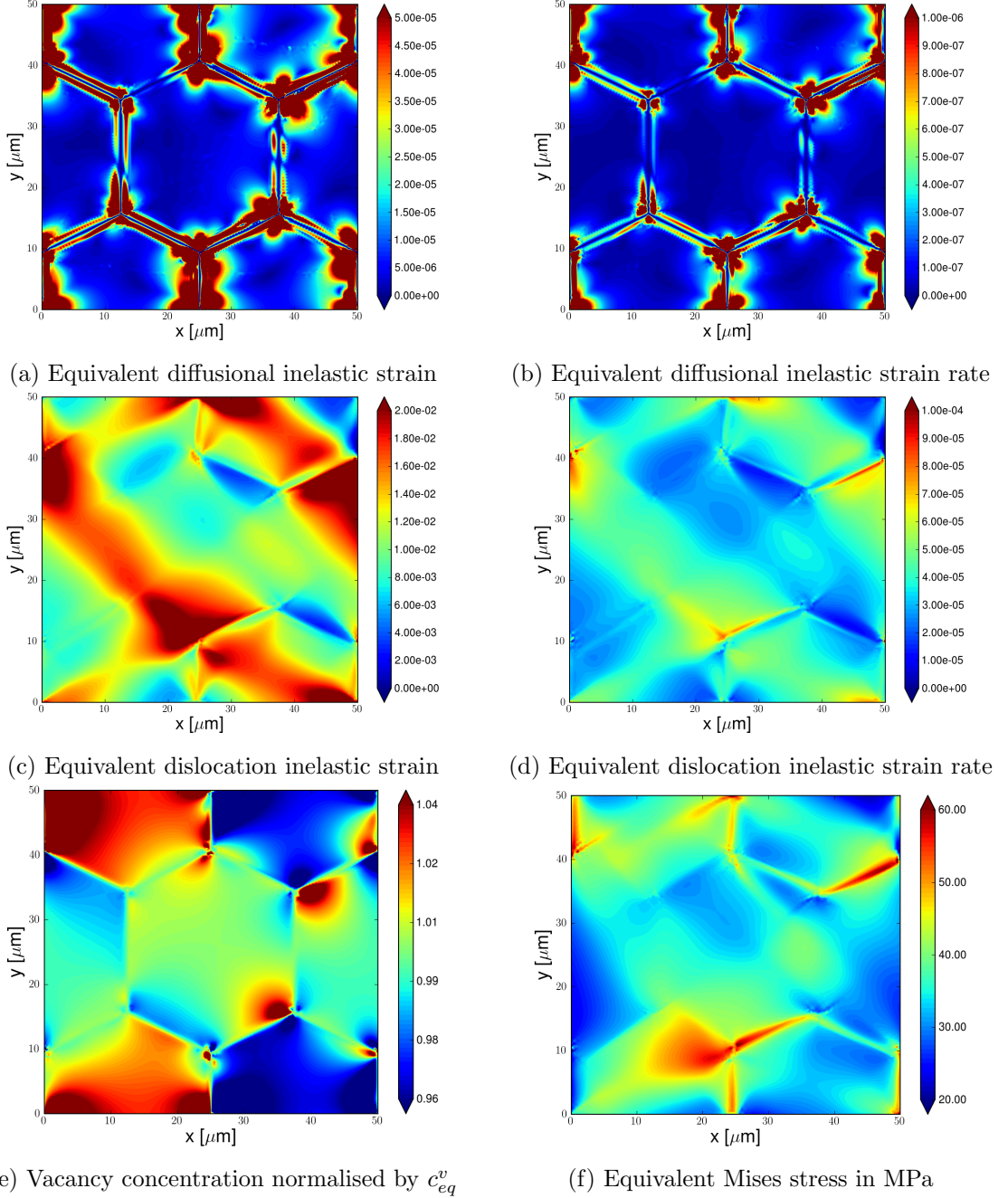


Figure 3.9: Inelastic (a) diffusional strain, (b) diffusional strain-rate, (c) dislocation strain, and (d) dislocation strain-rate, and (e) vacancy concentration and (f) equivalent Mises stress (applied stress of 20 MPa, $25\mu\text{m}$ grain size and at $t = 3.10^3\text{s}$)

impose $c^v = c_{eq}^v \ll 1$. As pointed out above, the parameter K_{sv} has a significant influence on the strain rate and on the strain rate dependence on grain size, as shown in fig. 3.8b. Keeping the grain boundary width fixed, for an increasing value of K_{sv} , the overall strain rate increases since the contribution of the grain boundary increases as per 3.45, but the $\log(\text{grain size})\text{-}\log(\text{strain rate})$ slope decreases. In contrast, for a decreasing K_{sv} , so does the macroscopic overall strain rate, but the slope increases.

Finally, the grain boundary width was reduced to $2\mu\text{m}$, as the GB region it is know to be

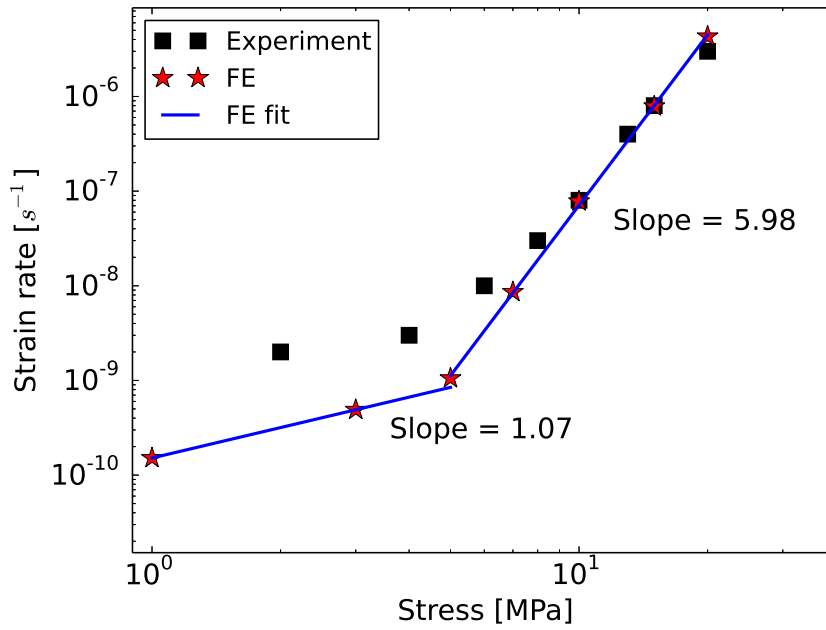
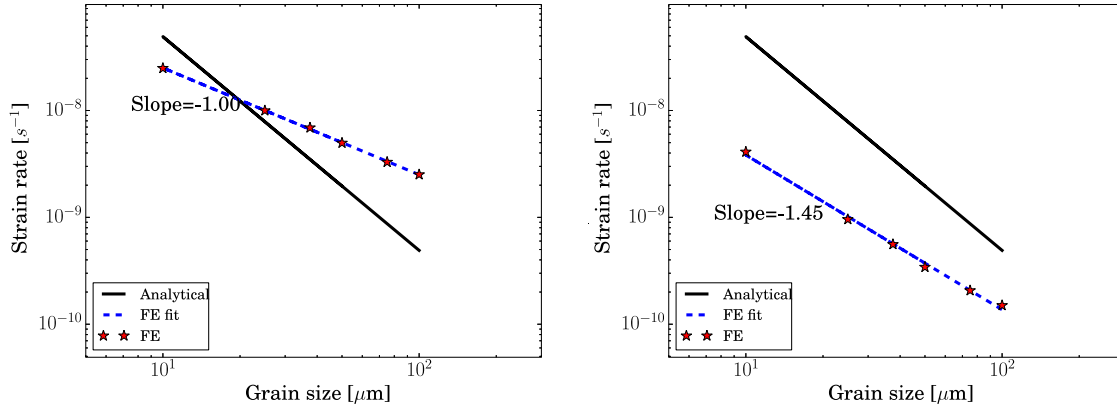


Figure 3.10: Strain rate dependence on stress. Data taken from [127].

of notable influence on the mechanical behaviour [54]. Note that, in order to obtain realistic results, K_{sv} had to be multiplied by a factor ten compared to the $4\mu\text{m}$ case. The dependence on the grain size is shown on fig. 3.11, for the case of a $2\mu\text{m}$ grain boundary width.



(a) Strain rate dependence on grain size

(b) Strain rate dependence on grain size, ignoring grain boundary deformation process

Figure 3.11: Comparison between the macroscopic Herring-Nabarro creep law and the finite element simulations results using a source term in the grain boundary of width $2\mu\text{m}$. According to eq. (3.46), the slopes predicted analytically have a value of -2 .

In the case study 3, a slip rate exponent, $n = 4$ in eq. (3.25), was used as parameter in the slip rate eq. (3.25), as it is a reasonable value for dislocation creep and close to that of 4.5 found experimentally in [127]. When there is no hardening, no slip threshold and no diffusion creep, then the macroscopic response of the simulated polycrystal exhibits a slope of 4. In the present case, in the presence of work hardening, the global response is more complex and different apparent exponent values are obtained, as it is well known when modelling creep in

metals [16, 72].

3.5 Conclusions

A framework to model diffusion creep in polycrystals has been proposed, where individual grains and grain boundaries are explicitly modelled. It has been pointed out that, in the presence of diffusion, the material point definition should be handled with care, as material lines drawn on the solid become blurred as diffusion occurs. Nevertheless, it is still possible to define and quantify a strain in such cases, as long as moderate diffusion and relatively small concentration of vacancies are considered. It has been demonstrated that:

- Simple considerations of atom and vacancy motion have led to the definition of an inelastic diffusional strain rate on a perfect lattice, which has been related to the gradient of the vacancy flux.
- In order to retrieve the well known Herring diffusion potential formula, one has to define an anisotropic eigenstrain within the grain boundary regions, related to the normal of the grain boundary surface. Hence, any mechanical loading applied to the polycrystal directly induces vacancy motion, which, in turn, leads to creep strain.

The proposed diffusion induced deformation mechanism has been enriched by a classical crystal plasticity constitutive framework to account for the effects of dislocation creep. The framework has been implemented in a finite element model, with a detailed description of grain boundaries geometry and properties. The simulations that have been carried out show that:

- Strong heterogeneities are obtained at the intragranular level, especially at triple junctions.
- Anisotropic elasticity and dislocation induced plasticity promote the diffusion of vacancies and lead to higher diffusional strain rates, by developing stress gradients in the polycrystal.
- Classical macroscopic strain rate dependence on stress and grain size, that is $\dot{\epsilon} = f(\sigma, d_g^{-2})$, are obtained, when using Dirichlet boundary conditions in the GB region. The use of a sink term also leads to a consistent macroscopic trend.
- The model predicts a smooth transition from diffusion dominated to dislocation dominated regime, depending on level of the applied stress, as observed experimentally for copper [127].

Direct coupling of vacancy diffusion and dislocation climb was recently introduced in [51]. The continuum model presented therein could be complemented by the effect of the vacancy flux gradient in a straightforward manner. The proposed modelling framework is capable of reproducing Coble creep by properly choosing the diffusion parameters in the bulk and in the grain boundary regions. Also grain boundary sliding and damage are necessary mechanisms to be added to the present model to obtain a realistic picture of creep mechanisms at the continuum polycrystalline level. The complete approach, containing the competing mechanisms of bulk and grain boundary diffusion, remains challenging and should be the objective of future work.

Modeling radiation damage: a stress-diffusion - Cahn-Hilliard framework

Radiation damage introduces vacancies in large excess in the material. Their diffusion and their effects on the mechanical behaviour of polycrystalline aggregates have been investigated in the previous chapters. When the vacancy concentration exceeds a critical value, voids form in the material, degrading its properties and leading to void swelling, for instance. Hence, a Cahn-Hilliard framework is proposed to study the void nucleation and growth in irradiated metals, whereby the previously proposed stress-diffusion couplings are included.

Résumé

Un modèle de type Cahn-Hilliard est employé afin de prédire la nucléation et la croissance de cavités dans des polycristaux irradiés, prenant en compte l'évolution des défauts ponctuels. Les équations de diffusion des lacunes et des auto-interstitiels sont enrichies pour prendre en compte leur production due aux cascade d'irradiation, ainsi que leur recombinaison mutuelle. Le modèle est couplé à la mécanique via l'introduction d'une déformation libre dépendant de la concentration de défauts ponctuels, menant à une équation de Cahn-Hilliard modifiée pour rendre compte du gonflement. Deux applications sont présentées: l'influence de la contrainte sur la croissance d'une cavité dans une matrice sur-saturée en lacunes d'une part, et l'évolution de l'endommagement dans un polycristal d'autre part. Les résultats montrent une légère accélération de la cinétique de la croissance due aux contraintes. De plus, l'utilisation de paramètres dépendants de la dose d'irradiation, tels que la diffusivité ou la vitesse de recombinaison des défauts, entraîne une distribution de défaut tout à fait différente du cas utilisant des paramètres constants.

Summary

A Cahn-Hilliard approach is used to model void nucleation and growth in irradiated polycrystalline metals, taking into account the evolution of vacancies and self-interstitials. The diffusion equations for vacancies and self-interstitials are complemented to take into account the production of point defects due to irradiation cascades, the mutual recombination of defects and their evacuation through grain boundaries. The model is coupled to stress via the introduction of a concentration-dependent eigenstrain, which leads to a modified Cahn-Hilliard equation that enables the effects of swelling to be accounted for. Two applications are presented: the first one deals with the influence of stress on the growth of a void in an irradiated matrix, and the second with damage evolution due to irradiation in a thin film. It is shown that mechanical coupling leads to accelerated void growth, and that dpa dependent parameters, such as diffusivity or recombination rate, yield a completely different distribution of defects in a polycrystal.

Contents

4.1	Introduction	55
4.2	The Cahn-Hilliard equation	56
4.3	Choice of homogeneous free energy	58
4.3.1	Polynomial energy	59
4.3.2	Logarithmic form	60
4.4	Choice of mobility	60
4.4.1	Summary	62
4.5	Elementary solutions to the Cahn Hilliard equations	62
4.5.1	Identification of interface width and energy	62
4.5.1.1	Interface energy	62
4.5.1.2	Interface width	64
4.5.2	Critical wavelength	66
4.6	Application of the micromorphic approach to the Cahn-Hilliard equation	67
4.7	Stress-diffusion coupled Cahn-Hilliard framework for nuclear reactors applications	68
4.7.1	Balance laws	69
4.7.2	Constitutive equations	69
4.7.2.1	Choice of state variables, free energy partition, and dissipation	70
4.7.2.2	Choice of free energy	71
4.8	Choice of parameters	73
4.9	Single void growth	76
4.10	Damage evolution in an irradiated Fe polycrystal	78
4.11	Concluding remarks and future work	78

4.1 Introduction

In order to build safe and long lasting nuclear power plants, materials submitted to extreme environments are being extensively studied both experimentally and numerically. Such materials must withstand high temperatures, corrosive environments, extreme stress and radiation damage. The latter involves point defects production, voids and bubbles formation, radiation hardening, embrittlement, swelling, etc.

A radiation damage event in a crystalline material can be defined by decomposing it into its successive steps [125]:

- A highly energetic particle, for example a neutron or an ion, interacts with a lattice atom.
- The incident particle transfers kinetic energy to this lattice atom, which is then displaced from its lattice position and thus becomes the primary knock-on atom (PKA).
- The PKA moves throughout the lattice, displacing other atoms on its way.
- This produces a displacement cascade: each atom displaces other atoms, which in turn displace other atoms . . . until their kinetic energy vanishes.

In the present approach, the cascade itself is not explicitly modeled, as the length and time scales ($10^{-11}s$) are below the continuum description. As detailed later, one will only consider a source term in the diffusion equations to model this production of point defects over time. These point defects are of two types, as illustrated on fig. 4.1:

- vacancies, that are empty lattice sites,
- self interstitial atoms (SIA).

After a cascade event, the lattice contains many point defects, which are the origin of all observed effects. A brief description of some of the radiation induced defects are given next. Interstitials

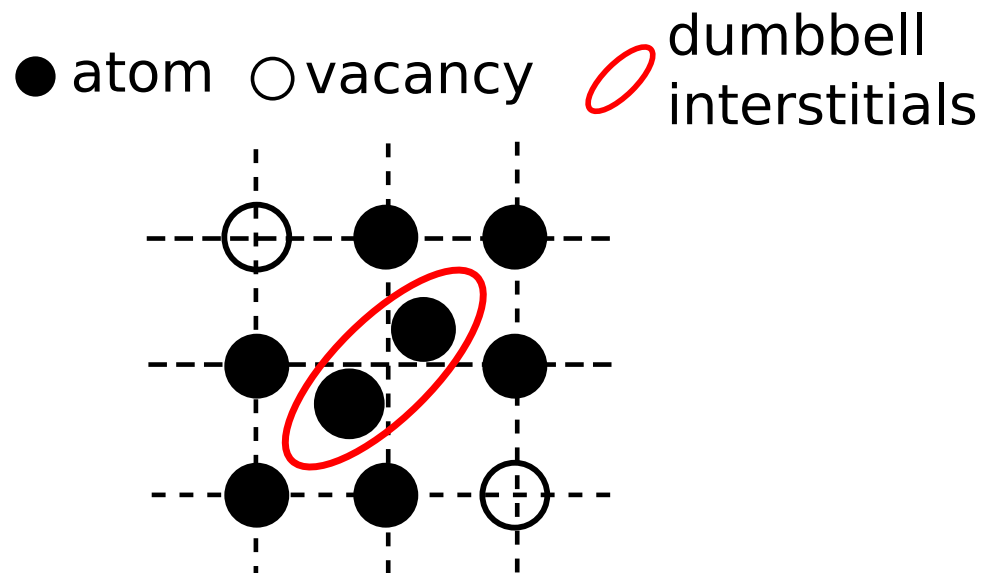


Figure 4.1: Schematic of the considered basic point defects: vacancies and self-interstitial atoms (SIA)

are usually atoms occupying a position in a crystal that is not a regular lattice site, for example,

octahedral and tetrahedral sites in cubic lattices. In irradiated metals, He is one of the most important radiation produced interstitial. SIA differ from classical interstitials (like C in Fe), on two points. First, they are in fact the same atoms that form the host lattice, hence *self*-interstitial. Second, the stable position for SIA in metals is the dumbbell, or split-interstitial, where two atoms share one regular lattice site, see fig. 4.1. This also means that the displacement induced by this large defect on the surrounding atoms, called relaxation volume, is larger than for classical, smaller interstitials. Their migration energy is very low (< 0.15 eV), and their formation energy high (> 2.0 eV).

Vacancies are simply missing atom on a lattice site. They have low formation energy (< 2.0 eV), low relaxation volume ($0.1 - 0.5 \Omega$, with Ω the atomic volume), and high migration energy (> 0.5 eV). Vacancies often bind together to form n-vacancy clusters. The properties of these clusters, mainly binding energy and migration energy, can differ drastically from n to n+1. Finally, a vacancy can bind with a helium atom to produce a very stable defect. In the present modeling, the vacancy concentration, c^v , does not distinguish between these sub-species. Instead, average properties are used, sometimes obtained from spatially resolved stochastic cluster dynamics simulations [40].

Vacancies, as well as interstitials, can form 2D clusters and lead to dislocation loops. These loops will shrink or grow, depending on the type of point defects they are absorbing, until they reach a critical stable size. While the multiplication of dislocations itself leads to hardening of the material, interactions between dislocations and other irradiation produced defects also contributes to the irradiation hardening, as voids and point defects impede dislocation glide.

Finally, vacancies and helium can form voids and bubbles, respectively. This can lead to tenth of percent of volumetric swelling in a reactor component and significantly alter the mechanical properties. It is then of interest to study the nucleation and growth of voids in the material, in order to find ways of preventing or limiting their proliferation, and couple it to stress in order to predict swelling, for instance. Voids can be thought of as a second phase in the material, and standard numerical tools can hence be used. Sharp interface models require the tracking of the interface between the solid and the void, as well as an interface velocity law. In contrast, one can use diffuse interface models, where the interface motion is driven by diffusion processes. Phase-field [110, 68] and Cahn-Hilliard [26] approaches, typically used for solidification problems, are becoming popular to study void growth and irradiation problems [87, 86, 7]. However, even though a Cahn-Hilliard approach coupled to elastic deformation has been proposed in [74] to study the lithiation of a representative spheroidal-shaped particle of a phase-separating electrode material, the effect of stress and plastic deformation on the void growth is still to be investigated

This chapter will focus on the point defects production, migration and evacuation, as well as on void nucleation and growth, in pure crystalline materials. First, the Cahn-Hilliard equation is recalled in Section 4.2, and analytical solutions are derived in Section 4.5. Second, the micromorphic implementation is detailed in Section 4.6. Then, the framework is extended in Section 4.7 to take into account irradiation processes, stress, and plastic deformation. Finally, two applications are presented. One deals with the growth of a void (Section 4.9), and the other with the evolution of damage in a Fe thin film and in a polycrystal aggregate, using spatially resolved stochastic cluster dynamics data as input (Section 4.10).

4.2 The Cahn-Hilliard equation

The Cahn-Hilliard equation [26, 24] describes the temporal and spatial evolution of a conserved order parameter in systems where the free energy depends on the order parameter and on its gradient. Typically, the order parameter is the concentration itself. There are mainly two ways

of deriving this equation. In the classical one, most constitutive laws are assumed a priori, and the diffusion potential is defined as the variational derivative of the free energy. An alternative approach is that proposed by Gurtin based on a unified thermodynamical framework [58] to circumvent the limitations of the classical method. Here, the balance laws are separated from the constitutive laws, and microforces are introduced as work conjugates to the order parameter and its gradient. The merit of the approach is that it defines unambiguously boundary conditions for finite bodies. Here, we use the method of virtual power as illustrated by [46, 4].

In this section, the Cahn-Hilliard equation will be derived for a single diffusive specie, c . The stress coupling will be described in Section 4.7. The state variables are chosen to be:

$$STATE = \{c, \underline{\nabla} c\}. \quad (4.1)$$

The internal power is given by,

$$\mathcal{P}^i(c^*) = \int_V \pi c^* - \underline{\xi} \cdot \underline{\nabla} c^* dV, \quad (4.2)$$

where, π , the microforce, and $\underline{\xi}$, the microstress, are associated to the virtual quantities c^* and $\underline{\nabla} c^*$, respectively. In turn, the external power is given by,

$$\mathcal{P}^e(c^*) = \int_{\partial V} \zeta c^* dS, \quad (4.3)$$

where ζ is the external force. By writing $\mathcal{P}^i + \mathcal{P}^e = 0$, the balance equations for the microforces are obtained as,

$$\pi + \underline{\nabla} \cdot \underline{\xi} = 0, \quad (4.4a)$$

$$\underline{\xi} \cdot \underline{n} = -\zeta. \quad (4.4b)$$

In turn, the balance law for the species concentration, c , is:

$$\dot{c} = -\underline{\nabla} \cdot \underline{J} \quad (4.5)$$

Recalling the first law of thermodynamics,

$$\int_V \dot{e} dV = -\mathcal{P}^i, \quad (4.6)$$

where, e , is the internal energy per unit volume. Furthermore, the second law states that:

$$\int_V \dot{s} T - \underline{\nabla} \cdot (\mu \underline{J}) dV \geq 0, \quad (4.7)$$

where, s is the entropy, T the temperature, μ the diffusion potential and \underline{J} the flux. The Helmholtz free energy density, ψ , is decomposed into a homogeneous part, $\psi_0(c)$, and an interfacial part, $\psi_{int}(\underline{\nabla} c)$, as:

$$\begin{aligned} \psi(c, \underline{\nabla} c) &= \psi_0(c) + \psi_{int}(\underline{\nabla} c) \\ \psi_{int}(\underline{\nabla} c) &= \frac{1}{2} \alpha \underline{\nabla} c \cdot \underline{\nabla} c, \end{aligned} \quad (4.8)$$

where, α , is a coefficient which will be shown to be related to the interface width and energy in Section 4.5. Using, $\psi = e - Ts$, and the species balance, eq. (4.5), the dissipation inequality follows,

$$\left(-\pi + \mu - \frac{\partial \psi}{\partial c} \right) \dot{c} + \left(\underline{\xi} - \frac{\partial \psi}{\partial \underline{\nabla} c} \right) \cdot \underline{\nabla} \dot{c} - \underline{J} \cdot \underline{\nabla} \mu \geq 0. \quad (4.9)$$

The evolution laws are then expressed as,

$$\mu - \pi = \frac{\partial \psi}{\partial c}, \quad (4.10a)$$

$$\underline{\xi} = \frac{\partial \psi}{\partial \underline{\nabla} c} = \alpha \underline{\nabla} c. \quad (4.10b)$$

In order for the dissipation, eq. (4.9), to remain positive, the flux is commonly expressed as,

$$\underline{J} = -L \underline{\nabla} \mu, \quad (4.11)$$

where, L , is the mobility. The mobility can be chosen constant or to depend on c , in which case it is called *degenerate mobility* [43, 103]. The choice of L is discussed in Section 4.4. Using the balance equation, eq. (4.4a), in the evolution laws, eq. (4.10), gives the following form of the diffusion potential,

$$\mu = \frac{\partial \psi}{\partial c} + \pi = \frac{\partial \psi}{\partial c} - \operatorname{div} \underline{\xi} = \frac{\partial \psi}{\partial c} - \alpha \underline{\nabla}^2 c. \quad (4.12)$$

Finally, from the above expression for μ , and that of the flux, eq. (4.11), in the balance law for c , eq. (4.5), yields the classical Cahn-Hilliard expression,

$$\dot{c} = -L \left(\underline{\nabla}^2 \frac{\partial \psi}{\partial c} - \alpha \underline{\nabla}^4 c \right), \quad (4.13)$$

where the mobility, L , has been assumed constant.

One can notice that this expression requires the computation of the 4th gradient of c . Numerically in finite elements, this would require the use of higher order shape functions. An alternative method is to use the micromorphic approach as in [103, 46], where two lower order equations are solved. The model re-formulation using a micromorphic approach will be presented in Section 4.6.

4.3 Choice of homogeneous free energy

Different choices of non-convex homogeneous free energy functions are possible, with a trade off between simplicity of the analytical solutions and numerical efficiency. A quadratic form allows for the derivation of an analytical expression of concentration distribution in the interface and of the interface energy. Nevertheless, the concentration can reach unrealistic values (larger than 1 or smaller than 0). On the other hand, a logarithmic form, derived from statistical physics considerations, ensures that the concentration stays in the $[0, 1]$ range, but only estimates of interface width and energy can be obtained, as the calibration of such energy based on the choice of minima, spinodal points, interface energy and interface width is not straightforward, as will be detailed in Section 4.8.

The homogeneous free energy is classically chosen non convex, with two wells defining two stable phases α and β , as shown in the generic fig. 4.2. The equilibrium concentration of these two phases, c_{eq}^α and c_{eq}^β , are defined by the common tangent rule and are called binodal points. Furthermore, the two convex regions are separated by a non convex region, delimited by the two spinodal points, c_s^α and c_s^β , which are given by the solutions of the following equation:

$$\frac{\partial^2 \psi_0}{\partial c^2} = 0. \quad (4.14)$$

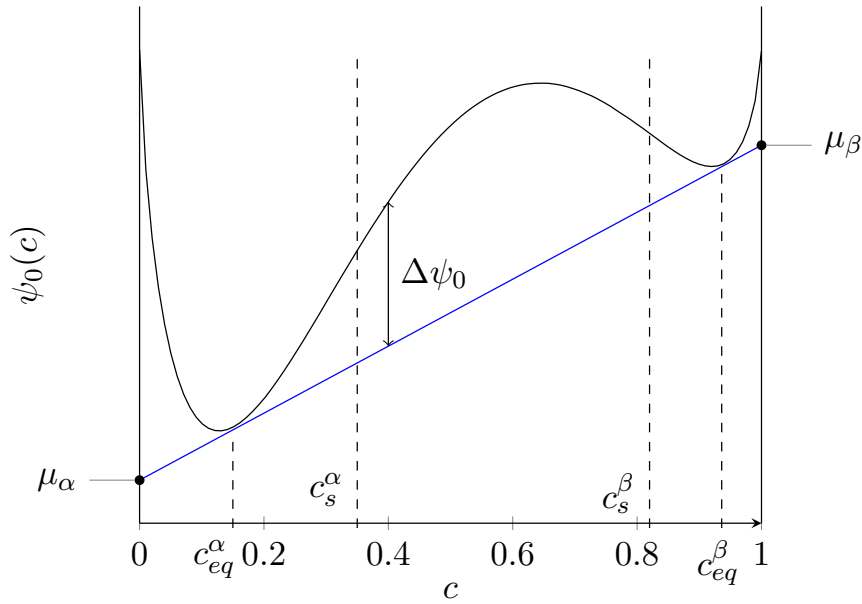


Figure 4.2: Example of a non-convex homogeneous chemical free energy, ψ_0 . The two minima are denoted c_{eq}^α and c_{eq}^β . The two convex wells are separated by a non convex region, delimited by the spinodal points c_s^α and c_s^β .

4.3.1 Polynomial energy

The simplest choice for the chemical free energy consists of a quadratic form [9]:

$$\psi_0(c) = \frac{16W}{(c_{eq}^\beta - c_{eq}^\alpha)^4} (c - c_{eq}^\alpha)^2 (c - c_{eq}^\beta)^2, \quad (4.15)$$

which, for minima in 0 and 1, reduces to:

$$\psi_0(c) = 16Wc^2(1 - c)^2. \quad (4.16)$$

The energy is then symmetric with respect to $c = 0.5$, and the coefficient W is the amplitude of the energy barrier, $W = \Delta\psi_0(c = 0.5)$. For the particular case of eq. (4.16), $\frac{\partial^2\psi_0}{\partial c^2}$ is expressed as follows:

$$\begin{aligned} \frac{\partial^2\psi_0}{\partial c^2} &= 32W(6c^2 - 6c + 1) \\ c_s^\alpha &= -\frac{\sqrt{3}}{6} + \frac{1}{2} \simeq 0.211 \\ c_s^\beta &= \frac{\sqrt{3}}{6} + \frac{1}{2} \simeq 0.789 \end{aligned} \quad (4.17)$$

where c_s^α and c_s^β are the two roots. Finally, an arbitrary polynomial can be used, in order to fine-tune the desired system properties:

$$\psi_0(c) = a_c c^4 + b_c c^3 + c_c c^2 + d_c c + e_c. \quad (4.18)$$

The five coefficients, a_c to e_c in eq. (4.18), can be chosen to verify, for instance, the desired following properties,

$$\begin{aligned}
 c_{eq}^\alpha &= \text{vacancy equilibrium in solid} \\
 c_{eq}^\alpha \text{ is a minimum: } &\frac{\partial \psi_0}{\partial c}(c_{eq}^\alpha) = 0 \\
 c_{eq}^\beta &= 1 \\
 c_{eq}^\beta \text{ is a minimum: } &\frac{\partial \psi_0}{\partial c}(c_{eq}^\beta) = 0 \\
 c_s^\alpha \text{ is the first spinodal point: } &\frac{\partial^2 \psi_0}{\partial c^2}(c_s^\alpha) = 0
 \end{aligned} \tag{4.19}$$

4.3.2 Logarithmic form

Another common form of the chemical free energy is given by [26, 57],

$$\psi_0 = \frac{RT}{\Omega_0} (c \ln(c) + (1 - c) \ln(1 - c)) + \omega c(1 - c) , \tag{4.20}$$

where R is the perfect gas constant, T the temperature, Ω_0 the molar volume, and ω a parameter analogous to W . For simplicity, it is normalised as found in [74],

$$\bar{\psi}_0 = c \ln(c) + (1 - c) \ln(1 - c) + \bar{\omega} c(1 - c) , \tag{4.21}$$

where $\bar{\omega} = \frac{\Omega_0}{RT} \omega$. The two spinodal points are given as,

$$[c_s^\alpha, c_s^\beta] = \left[\frac{1}{2\bar{\omega}} \left(\bar{\omega} - \sqrt{\bar{\omega}(\bar{\omega} - 2)} \right), \frac{1}{2\bar{\omega}} \left(\bar{\omega} + \sqrt{\bar{\omega}(\bar{\omega} - 2)} \right) \right] , \tag{4.22}$$

for $\bar{\omega} \geq 2$. Using $\bar{\omega} = 3$ as proposed by [74] in eq. (4.21), and illustrated in fig. 4.3, leads to $\frac{\partial^2 \psi_0}{\partial c^2}$ having the same two roots as for the quadratic form, eq. (4.16), namely

$$\begin{aligned}
 \frac{\partial^2 \psi_0}{\partial c^2} &= \frac{6c^2 - 6c + 1}{c(1 - c)} , \\
 c_s^\alpha &= -\frac{\sqrt{3}}{6} + \frac{1}{2} \simeq 0.211 \\
 c_s^\beta &= \frac{\sqrt{3}}{6} + \frac{1}{2} \simeq 0.789
 \end{aligned} \tag{4.23}$$

4.4 Choice of mobility

As stated in Section 4.2, the mobility, L , can be chosen constant or to depend on c (degenerated). If the constant mobility raises no problem, some restrictions apply on the degenerated one, as presented below. If the mobility, L , is assumed constant, eq. (4.13) gives

$$\mathbf{J} = -L \left(\frac{\partial^2 \psi}{\partial c^2} \nabla c - \alpha \nabla^3 c \right) , \tag{4.24a}$$

$$\dot{c} = L \left[\frac{\partial^3 \psi}{\partial c^3} (\nabla c)^2 + \frac{\partial^2 \psi}{\partial c^2} \nabla^2 c - \alpha \nabla^4 c \right] . \tag{4.24b}$$

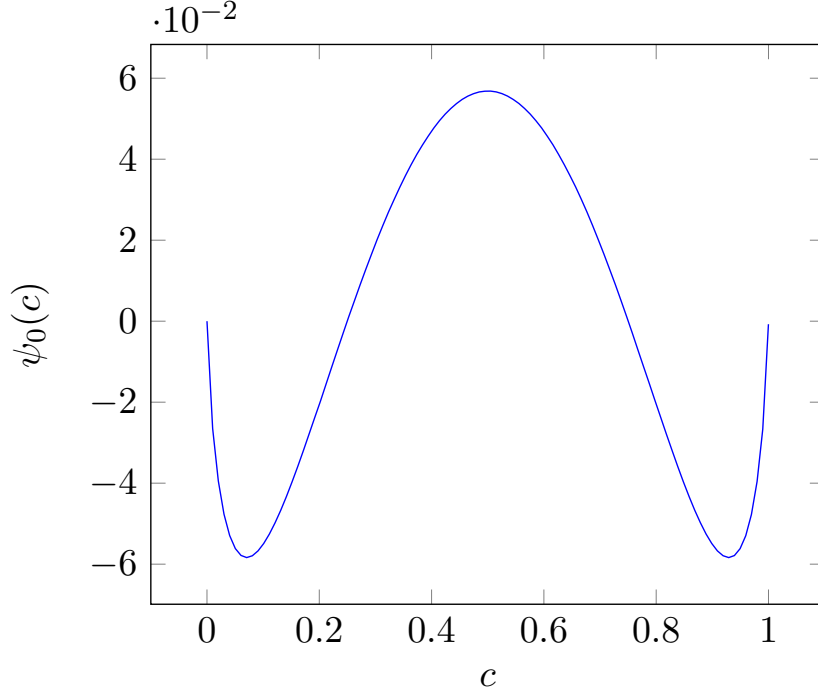


Figure 4.3: Profile of the normalized double well logarithmic energy, $\bar{\psi}_0(c)$, with $\bar{\omega} = 3$

If the mobility is instead assumed degenerated, $L(c)$, eq. (4.13) gives

$$\underline{J} = -L(c) \left(\frac{\partial^2 \psi}{\partial c^2} \underline{\nabla} c - \alpha \underline{\nabla}^3 c \right), \quad (4.25a)$$

$$\dot{c} = \frac{\partial L}{\partial c} \underline{\nabla} c + L(c) \left(\frac{\partial^2 \psi}{\partial c^2} \underline{\nabla}^2 c - \alpha \underline{\nabla}^4 + \frac{\partial^3 \psi}{\partial c^3} (\underline{\nabla} c)^2 \right), \quad (4.25b)$$

and the mobility can be chosen freely. For classical diffusion theories, it is common to express the mobility as,

$$L(c) = D \left(\frac{\partial^2 \psi}{\partial c^2} \right)^{-1}, \quad (4.26a)$$

$$= \frac{D}{32W(6c^2 - 6c + 1)}, \text{ for quadratic energy} \quad (4.26b)$$

$$= \frac{Dc(1-c)}{6c^2 - 6c + 1}, \text{ for logarithmic energy} \quad (4.26c)$$

such that the Fickian expression of the flux, $J = -D\underline{\nabla} c$, is retrieved. Here, D is the diffusion coefficient. However, in the present non classical theory, the flux becomes infinite twice due to the term $L\alpha\underline{\nabla}^3 c$, as seen in eq. (4.26c). In [74], the following expression is proposed,

$$L(c) = \frac{D\Omega_0}{RT} c(1-c), \quad (4.27)$$

which is in fact the mobility for classical theory with a log energy [120]. Furthermore, this ensures that the flux vanishes in each pure phase (c close to 0 or 1). For a logarithmic energy, the Fickian contribution vanishes twice in the interface but remains bounded since it is now expressed as,

$$\underline{J} = -D(6c^2 - 6c + 1)\underline{\nabla} c + D\bar{\alpha}c(1-c)\underline{\nabla}^3 c, \quad (4.28)$$

using normalised quantities.

4.4.1 Summary

In Table 4.1, some possible choices of energies and mobilities, as well as the corresponding flux, have been reported. It is readily seen that cases B and D are unacceptable. Indeed, the non classical term becomes infinite for two values of c , which are necessarily encountered in the interface. For cases A, C and E, the Fickian term vanishes twice, which is not surprising, since phase separation requires uphill diffusion [103]. The two roots of $\frac{\partial^2 \psi}{\partial c^2}$ are reminded to be the spinodal points bounding the spinodal regions where phase separation can occur.

4.5 Elementary solutions to the Cahn Hilliard equations

4.5.1 Identification of interface width and energy

4.5.1.1 Interface energy

According to [26], the interfacial free energy at equilibrium is “by definition the difference per unit area of interface between the actual free energy of the system and that which it would have if the properties of the phases were continuous throughout”. In other words, the energy of the system that remains once the energy of each pure phase is removed is the spatial integral:

$$\begin{aligned} \gamma &= \int_{-\infty}^{+\infty} \psi_0 + \frac{1}{2} \alpha (\nabla c)^2 - c \mu_\beta^{eq} - (1-c) \mu_\alpha^{eq} dx \\ &= \int_{-\infty}^{+\infty} \Delta \psi_0 + \frac{1}{2} \alpha (\nabla c)^2 dx, \end{aligned} \quad (4.29)$$

where μ_α^{eq} and μ_β^{eq} are the chemical potential of species α and β , as defined in fig. 4.2, and $\Delta \psi_0 \hat{=} \psi_0 - c \mu_\beta^{eq} - (1-c) \mu_\alpha^{eq}$. The following relation can be obtained [26]

$$\Delta \psi_0 - \frac{1}{2} \alpha (\nabla c)^2 = cst = 0, \quad (4.30)$$

where the constant is 0 due to boundary conditions (both terms tend to 0 when $x \rightarrow \pm\infty$). Hence, using a change of variables and substituting eq. (4.30) in 4.29 leaves,

$$\gamma = 2 \int_{-\infty}^{+\infty} \Delta \psi_0 dx = \sqrt{2\alpha} \int_{c_\alpha}^{c_\beta} \sqrt{\Delta \psi_0} dc \quad (4.31)$$

For the particular choice of the quadratic energy, eq. (4.16), $\mu_\alpha = \mu_\beta = 0$, so that:

$$\gamma = \sqrt{2\alpha} \int_0^1 \sqrt{\psi_0} dc \quad (4.32)$$

which leads to,

$$\gamma = \sqrt{2\alpha} \int_0^1 4\sqrt{W} c(1-c) dc = \frac{4\sqrt{\alpha W}}{3\sqrt{2}}. \quad (4.33)$$

Energy	Mobility	Flux	Case
$\psi(c) = 16Wc^2(1-c)^2$	$L = \text{cst}$	$\underline{J} = -L(32W(6c^2 - 6c + 1)\underline{\nabla}c - \alpha\underline{\nabla}^3c)$	A
	$L(c) = D\left(\frac{\partial^2\psi}{\partial c^2}\right)^{-1} = \frac{D}{32W(6c^2 - 6c + 1)}$	$\underline{J} = -D\underline{\nabla}c + \alpha\frac{D}{32W(6c^2 - 6c + 1)}\underline{\nabla}^3c$	B
$\bar{\psi} = c\ln(c) + (1-c)\ln(1-c) + 3c(1-c)$	$L = \text{cst}$	$\underline{J} = -L\left(\frac{6c^2 - 6c + 1}{c(1-c)}\underline{\nabla}c - \alpha\underline{\nabla}^3c\right)$	C
	$L(c) = D\left(\frac{\partial^2\psi}{\partial c^2}\right)^{-1} = \frac{Dc(1-c)}{6c^2 - 6c + 1}$	$\underline{J} = -D\underline{\nabla}c + \alpha\frac{Dc(1-c)}{6c^2 - 6c + 1}\underline{\nabla}^3c$	D
	$L(c) = \frac{D\Omega_0}{RT}c(1-c)$	$\underline{J} = -\frac{D\Omega_0}{RT}(-c^2 - 6c + 1)\underline{\nabla}c + \alpha\frac{D\Omega_0}{RT}c(1-c)\underline{\nabla}^3c$	E

Table 4.1: Expression of the flux and the Cahn-Hilliard equation, depending on the choice of energy and mobility

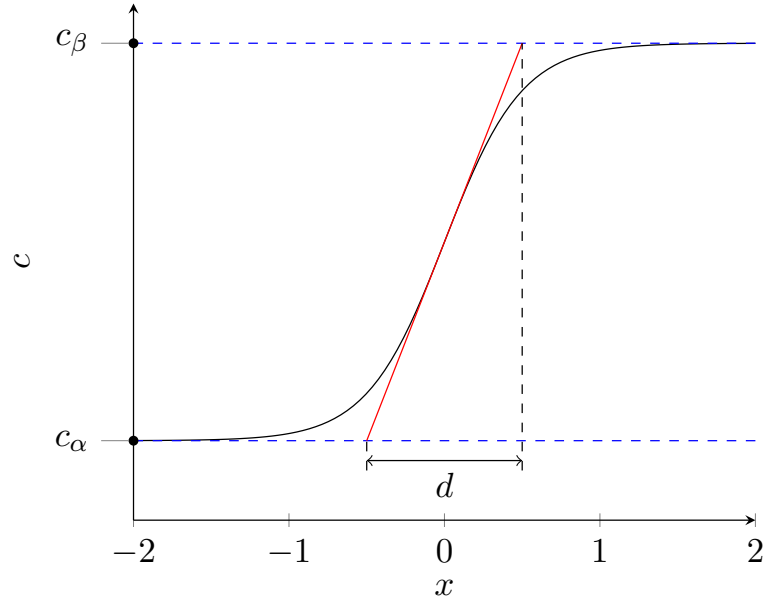


Figure 4.4: Interface profile for the concentration c . The interface thickness, d , is here defined as in [26, 74]

For the particular choice of the logarithmic energy, eq. (4.21), $\mu_\alpha = \mu_\beta = \psi_0(c_\alpha) = \psi_0(c_\beta)$, so that

$$\gamma = \sqrt{2\alpha} \int_{c_\alpha}^{c_\beta} \sqrt{\psi_0 - \psi_0(c_\alpha)} dc \quad (4.34a)$$

$$\simeq 0.29\sqrt{\alpha} \text{ for } \bar{\omega} = 3, \text{ using a numerical integration,} \quad (4.34b)$$

$$\simeq \sqrt{\alpha(\psi_0(0.5) - \psi_0(c_\alpha))} (c_\beta - c_\alpha), \text{ using a geometrical approximation based on fig. 4.4.} \quad (4.34c)$$

4.5.1.2 Interface width

It is also possible to determine an exact or approximated interface width for quadratic and logarithmic energies, respectively.

Quadratic energy: If the free energy is chosen to have minima in 0 and 1, as proposed in [9],

$$\psi_0(c) = 16Wc^2(c-1)^2, \quad (4.35)$$

then the concentration field in the steady state solution of eq. (4.13) is given by

$$c(x) = 0.5 \left(1 + \tanh \left(\frac{x}{\sqrt{\frac{\alpha}{8W}}} \right) \right), \quad (4.36)$$

The tanh solution is typical of phase field and Cahn-Hilliard problems, and pertains to the more general tanh methods [62, 119]. In fact, one can start from eq. (4.13) to obtain a simpler

equation for which eq. (4.36) is a solution. Here,

$$\begin{aligned}\frac{\partial\psi_0}{\partial c} - \alpha\nabla^2 c &= 0 \\ \frac{\partial\psi_0}{\partial c} \frac{\partial c}{\partial x} - \alpha\nabla^2 c \frac{\partial c}{\partial x} &= 0 \\ \psi_0 - \frac{\alpha}{2} \left(\frac{\partial c}{\partial x} \right)^2 &= 0 \text{ by integration,}\end{aligned}\tag{4.37}$$

which, using eq. (4.35), simplifies into:

$$\begin{aligned}\frac{\partial c}{\partial x} &= \sqrt{\frac{32W}{\alpha}} c(1-c) \\ dx &= \sqrt{\frac{\alpha}{32W}} \frac{1}{c(1-c)} dc.\end{aligned}\tag{4.38}$$

When the above equation is integrated over λ , then the interface width defined from $c = z$ to $c = 1 - z$, $z \in]0, 0.5[$, becomes

$$\begin{aligned}\int_{-\lambda/2}^{\lambda/2} dx &= \int_z^{1-z} \sqrt{\frac{\alpha}{32W}} \frac{1}{c(1-c)} dc \\ \lambda &= \sqrt{\frac{\alpha}{8W}} \log\left(\frac{1-z}{z}\right) \\ \lambda &= \sqrt{\frac{\alpha}{8W}} f_\lambda\end{aligned}\tag{4.39}$$

Finally, by inverting eqs. (4.33) and (4.39), one obtains:

$$\begin{aligned}W &= \frac{3\gamma f_\lambda}{8\lambda} \\ \alpha &= \frac{3\gamma\lambda}{f_\lambda}\end{aligned}\tag{4.40}$$

In summary, the following physical quantities are introduced to replace the free energy coefficients α and W in eqs. (4.8) and (4.35):

$$\delta = \sqrt{\frac{\alpha}{8W}},\tag{4.41a}$$

$$\lambda = f_\lambda \delta = f_\lambda \sqrt{\frac{\alpha}{8W}},\tag{4.41b}$$

$$f_\lambda = \log\left(\frac{0.95}{0.05}\right) \simeq 2.94 \text{ for } z=0.05,\tag{4.41c}$$

$$\gamma = \frac{4\sqrt{\alpha W}}{3\sqrt{2}}.\tag{4.41d}$$

Finally, the equilibrium profile is given by:

$$c(x) = 0.5 \left(1 - \tanh\left(\frac{f_\lambda x}{\lambda}\right) \right).\tag{4.42}$$

Logarithmic energy: As shown in [26, 74], an estimate of the interface thickness, d , (different from λ) can be obtained geometrically, see fig. 4.4, as,

$$d = (c_\beta - c_\alpha) \left(\frac{dc}{dx}(x=0) \right)^{-1} \quad (4.43a)$$

$$= (c_\beta - c_\alpha) \sqrt{\frac{\alpha}{2\Delta\psi_0^{max}}} \text{ using eq. (4.30) .} \quad (4.43b)$$

4.5.2 Critical wavelength

Instability conditions are required for the decomposition to occur when the mean concentration value is between the two spinodal points. Let the mobility, L , be constant, and the energy be quadratic, eq. (4.16), such that the Cahn-Hilliard equation, eq. (4.24), simplifies to:

$$\dot{c} = L \left(\frac{\partial^2 \psi_0}{\partial c^2} \nabla^2 c - \alpha \nabla^4 c \right) , \quad (4.44)$$

and define c_m such that $\Delta\psi_0$ is maximum, that is when $c_m = 0.5$. Suppose a 1D distribution of the form:

$$c(x, t = 0) = c_m + \varepsilon \sin(\beta x) , \text{ with } \beta = \frac{2\pi}{l} , \quad (4.45)$$

where, l , is the wavelength. Substitution of the noise, eq. (4.45), in the Cahn-Hilliard equation, eq. (4.44), yields:

$$\begin{aligned} \frac{\partial \varepsilon}{\partial t} &= -L\beta^2 \left(\frac{\partial^2 \psi}{\partial c^2} \Big|_{c_m} - \alpha\beta^2 \right) \varepsilon \\ &= L\beta^2 (16W - \alpha\beta^2) \varepsilon \\ &\hat{=} R(\beta)\varepsilon , \end{aligned} \quad (4.46)$$

where, $R(\beta)$, is the amplification factor [9]. The solution of eq. (4.46) is of the form,

$$\varepsilon(t) = \varepsilon(0) \exp(R(\beta)t) . \quad (4.47)$$

Then, the evolution of the system depends on the sign of $R(\beta)$: if R is negative, the system tends to an homogeneous state, otherwise, decomposition occurs. The critical wavelength is then given by:

$$R(\beta) > 0 \quad (4.48a)$$

$$16W - \alpha\beta^2 > 0 \quad (4.48b)$$

$$l > \frac{\pi}{2} \sqrt{\frac{\alpha}{W}} = l_{crit} , \quad (4.48c)$$

and decomposition occurs if $l > l_{crit}$. Similarly, for a logarithmic energy, the critical length is given by:

$$l_{crit} = 2\pi \sqrt{\frac{\alpha}{4 - 2\bar{\omega}}} , \quad (4.49)$$

which indicates that decomposition never occurs for $\bar{\omega} > 2$. While this has been verified for the quadratic energy, it is not what is observed in the simulations with logarithmic energies, for a reason yet unknown.

4.6 Application of the micromorphic approach to the Cahn-Hilliard equation

The procedure follows the work presented in [46]. The state variables are chosen to be:

$$\text{STATE} = \{c, c_\chi, \underline{\nabla} c_\chi\} , \quad (4.50)$$

where, c , is the concentration, c_χ the micromorphic variable, and $\underline{\nabla} c_\chi$ its gradient. The internal power is given by,

$$\mathcal{P}^i = \int_V \pi c_\chi^* - \underline{\xi} \cdot \underline{\nabla} c_\chi^* dV , \quad (4.51)$$

where, π and $\underline{\xi}$, are the microforces associated to the virtual quantities c_χ^* and $\underline{\nabla} c_\chi^*$, respectively. In turn, the external power is restricted to contact forces,

$$\mathcal{P}^e = \int_{\partial V} \zeta c_\chi^* dS , \quad (4.52)$$

where, ζ s the external forces. By writing $\mathcal{P}^i + \mathcal{P}^e = 0$, the balance equations for the microforces are obtained, as,

$$\begin{aligned} \pi + \underline{\nabla} \cdot \underline{\xi} &= 0 , \\ \underline{\xi} \cdot \underline{n} &= -\zeta . \end{aligned} \quad (4.53)$$

Recall the first law of thermodynamics,

$$\int_V \dot{e} dV = -\mathcal{P}^i , \quad (4.54)$$

where e is the internal energy per unit volume. The second law states that:

$$\int_V \dot{s} T - \underline{\nabla} \cdot (\mu \underline{\mathbf{J}}) dV \geq 0 , \quad (4.55)$$

where, s is the entropy, T , the absolute temperature, μ the diffusion potential and $\underline{\mathbf{J}}$ the flux. The balance law for the species concentration, c , is:

$$\dot{c} = -\underline{\nabla} \cdot \underline{\mathbf{J}} \quad (4.56)$$

Using $\psi = e - Ts$, the Helmholtz free energy density, and the species balance eq. (4.56), the dissipation inequality follows, as,

$$\left(-\pi - \frac{\partial \psi}{\partial c_\chi} \right) \dot{c}_\chi + \left(\underline{\xi} - \frac{\partial \psi}{\partial \underline{\nabla} c_\chi} \right) \cdot \underline{\nabla} \dot{c}_\chi + \left(\mu - \frac{\partial \psi}{\partial c} \right) \dot{c} - \underline{\mathbf{J}} \cdot \underline{\nabla} \mu \geq 0 . \quad (4.57)$$

Assuming that the thermodynamical forces are independent of the rate of change of state variables, the state laws become,

$$\begin{aligned} \mu &= \frac{\partial \psi}{\partial c} , \\ \pi &= -\frac{\partial \psi}{\partial c_\chi} , \\ \underline{\xi} &= \frac{\partial \psi}{\partial \underline{\nabla} c_\chi} . \end{aligned} \quad (4.58)$$

The free energy is decomposed into three additive contributions: the homogeneous free energy, $\psi_0(c)$, the penalisation energy, $\psi_{pen}(c, c_\chi)$, and the interface energy, $\psi_{int}(\underline{\nabla} c_\chi)$, as

$$\begin{aligned}\psi &= \psi_0(c) + \psi_{pen}(c, c_\chi) + \psi_{int}(\underline{\nabla} c_\chi) \\ \psi_{pen}(c, c_\chi) &= \frac{1}{2} H_\chi (c - c_\chi)^2 \\ \psi_{int}(\underline{\nabla} c_\chi) &= \frac{1}{2} \alpha \underline{\nabla} c_\chi \cdot \underline{\nabla} c_\chi\end{aligned}\tag{4.59}$$

The parameter H_χ should be chosen sufficiently large so that c_χ tends to c . The state laws are then expressed as,

$$\pi = H_\chi (c - c_\chi) ,\tag{4.60a}$$

$$\mu = \frac{\partial \psi_0}{\partial c} + \frac{\partial \psi_{pen}}{\partial c} = \frac{\partial \psi_0}{\partial c} + H_\chi (c - c_\chi) = \frac{\partial \psi_0}{\partial c} + \pi ,\tag{4.60b}$$

$$\underline{\xi} = \alpha \underline{\nabla} c_\chi .\tag{4.60c}$$

In the absence of external forces,

$$\pi = -\underline{\nabla} \cdot \underline{\xi} = -\underline{\nabla} \cdot (\alpha \underline{\nabla} c_\chi) = -\alpha \underline{\nabla}^2 c_\chi ,\tag{4.61}$$

which leads to a new expression of the diffusion potential,

$$\mu = \frac{\partial \psi_0}{\partial c} - \alpha \underline{\nabla}^2 c_\chi .\tag{4.62}$$

It can be noted that by combining eqs. (4.60a) and (4.61), one obtains an equation similar to equation (19) derived in [118]:

$$c = c_\chi - \frac{\alpha}{H_\chi} \underline{\nabla}^2 c_\chi .\tag{4.63}$$

The flux is chosen as,

$$\begin{aligned}\underline{\mathbf{J}} &= -L(c) \underline{\nabla} \mu \\ &= -L(c) \underline{\nabla} \left(\frac{\partial \psi_0}{\partial c} - \alpha \underline{\nabla}^2 c_\chi \right) .\end{aligned}\tag{4.64}$$

Since $\lim_{H_\chi \rightarrow \infty} c_\chi = c$, the classical expression of the flux is retrieved, and the mobility can be chosen as in Section 4.4, depending on the choice of free energy.

4.7 Stress-diffusion coupled Cahn-Hilliard framework for nuclear reactors applications

In this section, the framework introduced in Section 4.6 is complemented to describe the irradiation problems described in the introduction, coupled with the elasto-visco-plasticity model introduced in Chapter 3. Two average concentrations of defect are taken into account: c^i , the self-interstitial (SIA) concentration, and c^v , the vacancies concentration. The model will be used to study the evolution of voids in irradiated metals with and without external load.

4.7.1 Balance laws

The internal power is given by,

$$\mathcal{P}^i = \int_V \pi c_\chi^* - \underline{\xi} \cdot \underline{\nabla} c_\chi^* - \underline{\sigma} : \underline{\nabla} \underline{u}^* dV , \quad (4.65)$$

where, π and $\underline{\xi}$, are the microforces associated to the virtual quantities c_χ^* and $\underline{\nabla} c_\chi^*$, respectively, and, $\underline{\sigma}$, the stress tensor, associated to the virtual velocity \underline{u}^* . In turn, the external power is given by,

$$\mathcal{P}^e = \int_V \underline{f} \cdot \underline{u}^* dv + \int_{\partial V} \zeta c_\chi^* + \underline{t} \cdot \underline{u}^* dS , \quad (4.66)$$

where, ζ and \underline{f} are the external forces. Using $\mathcal{P}^i + \mathcal{P}^e = 0$, the balance laws are obtained, as

$$\begin{aligned} \pi + \underline{\nabla} \cdot \underline{\xi} + f^\chi &= 0 , \\ \zeta - \underline{\xi} \cdot \underline{n} &= 0 , \end{aligned} \quad (4.67)$$

and:

$$\begin{aligned} \underline{\nabla} \cdot \underline{\sigma} + \underline{f} &= 0 , \\ \underline{t} - \underline{\sigma} \cdot \underline{n} &= 0 . \end{aligned} \quad (4.68)$$

They are completed by the balance laws for vacancies,

$$\dot{c}^v = -\text{div} \underline{J}^v + s^v(c^i, c^v, \phi^{\text{GB}}) , \quad (4.69)$$

and self interstitials,

$$\dot{c}^i = -\text{div} \underline{J}^i + s^i(c^i, c^v, \phi^{\text{GB}}) . \quad (4.70)$$

In eqs. (4.69) and (4.70), s^v and s^i are source/sink terms, and \underline{J}^i and \underline{J}^v are the fluxes of SIA and vacancies, respectively. The variable ϕ^{GB} is recalled to be a stationary phase-field, introduced to interpolate physical properties between their bulk ($\phi^{\text{GB}} = 0$) and grain boundary ($\phi^{\text{GB}} = 1$) values in eq. (3.36). For the current purpose, the source terms are chosen as [125, 86]:

$$\begin{aligned} s^i &= K_0 - K_{iv}(\phi^{\text{GB}})c^i c^v - K_{si}(\phi^{\text{GB}})c^i , \\ s^v &= K_0 - K_{iv}(\phi^{\text{GB}})c^i c^v - K_{sv}(\phi^{\text{GB}})c^v , \end{aligned} \quad (4.71)$$

where K_0 is the production term, K_{iv} a recombination factor, and K_{si} and K_{sv} are sink terms.

4.7.2 Constitutive equations

Recall the first law of thermodynamics,

$$\int_V \dot{e} dV = -\mathcal{P}^i , \quad (4.72)$$

where e is the internal energy density per unit volume. The second law states that:

$$\int_V T \dot{s} + \mu^i s^i + \mu^v s^v dV - \int_{\partial V} (\mu^i \underline{J}^i + \mu^v \underline{J}^v) \cdot \underline{n} dS \geq 0 , \quad (4.73)$$

where, μ^i and μ^v are the diffusion potentials associated to SIA and vacancies. Using $\psi = e - Ts$, the Helmholtz free energy density, together with the second and first principles, eqs. (4.72)

and (4.73), and the balances equations, eqs. (4.69) and (4.70), yields the dissipation inequality, as

$$-\pi \dot{c}_\chi + \underline{\xi} \cdot \underline{\nabla} \dot{c}_\chi + \underline{\sigma} : \underline{\dot{\xi}} - \underline{\mathbf{J}}^i \cdot \underline{\nabla} \mu^i - \underline{\mathbf{J}}^v \cdot \underline{\nabla} \mu^v - \dot{\psi} \geq 0. \quad (4.74)$$

The total strain is partitioned into its different components in each phase,

$$\underline{\xi} = \underline{\xi}^{e,k} + \underline{\xi}^{*,k}(c^i, c^v) + \underline{\xi}^{\text{in-diff},k} + \underline{\xi}^{\text{in-disl},k}, \text{ with } k = \{\alpha, \beta\}, \quad (4.75)$$

where, $\underline{\xi}^{e,k}$, is the elastic strain, $\underline{\xi}^{*,k}(c^i, c^v)$, the eigenstrain due to relaxation around point defects (see eq. (2.4)), $\underline{\xi}^{\text{in-diff},k}$, the inelastic diffusional strain (see eq. (3.23)), and $\underline{\xi}^{\text{in-disl}}$, the inelastic strain arising from dislocation glide and climb. The eigenstrain (eqs. (3.38) and (3.38)) is chosen as,

$$\underline{\xi}^*(c^i, c^v) = \underline{\eta}^i(\phi^{\text{GB}}) (c^i - c_{ref}^i(\phi^{\text{GB}})) \quad (4.76a)$$

$$+ \underline{\eta}^v(\phi^{\text{GB}}) (c^v - c_{ref}^v(\phi^{\text{GB}}))$$

$$\underline{\eta}^k(\phi^{\text{GB}}) = (1 - \phi^{\text{GB}}) \eta^{\text{k,bulk}} \underline{\mathbf{I}} + \phi^{\text{GB}} \eta^{\text{k,GB}} \underline{\mathbf{n}} \otimes \underline{\mathbf{n}}, \text{ with } k = \{i, v\}. \quad (4.76b)$$

Consider the following phase indicator variable,

$$\phi = \frac{c^v - c_\alpha}{c_\beta - c_\alpha}, \quad (4.77)$$

which takes the value 1 for $c^v = c_\beta$ and 0 for $c^v = c_\alpha$. Define an interpolation function, h ,

$$h(\phi(c^v)) = \phi^2 (3 - 2\phi), \quad (4.78)$$

$$\bar{h} = 1 - h,$$

so that it has minima at 0 and 1, and verify $\frac{\partial^2 h}{\partial \phi^2} = 0$ at 0 and 1. Finally suppose that the following interpolation schemes, corresponding to Voigt homogenisation [4, 5], as

$$\underline{\sigma} = h \underline{\sigma}^\alpha + \bar{h} \underline{\sigma}^\beta \quad (4.79a)$$

$$\underline{\xi} = \underline{\xi}^\alpha = \underline{\xi}^\beta \quad (4.79b)$$

$$\underline{\xi}^* = h \underline{\xi}^{*,\alpha} + \bar{h} \underline{\xi}^{*,\beta} \quad (4.79c)$$

$$\underline{\xi}^{\text{in-diff}} = h \underline{\xi}^{\text{in-diff},\alpha} + \bar{h} \underline{\xi}^{\text{in-diff},\beta} \quad (4.79d)$$

$$\underline{\xi}^{\text{in-disl}} = h \underline{\xi}^{\text{in-disl},\alpha} + \bar{h} \underline{\xi}^{\text{in-disl},\beta} \quad (4.79e)$$

For a given choice of interpolation/homogenisation scheme, it is possible to calculate the chemical equilibrium shift due to stresses, and a possible interface excess energy. However, this is out of the scope of the present work, and the Voigt approach was chosen to allow for an easy mixing of mechanical behaviour. Further discussions can be found in, for instance, [41, 91, 36].

4.7.2.1 Choice of state variables, free energy partition, and dissipation

The free energy is chosen to depend on a set of state variables, as

$$\text{STATE} = \left(c_\chi, \underline{\nabla} c_\chi, c^i, c^v, \underline{\xi}^{e-\alpha}, \underline{\xi}^{e-\beta}, s_g^\alpha, s_g^\beta, \phi^{\text{GB}} \right), \quad (4.80)$$

where, $\underline{\xi}^{e-\alpha}$ and $\underline{\xi}^{e-\beta}$ are the elastic strain in phases α and β , and s_g^α and s_g^β are internal variables, corresponding to strain hardening in phases α and β . Using eqs. (4.75), (4.79) and (4.80)

in eq. (4.74), yields the corresponding dissipation inequality:

$$\begin{aligned}
 & \left(-\pi - \frac{\partial\psi}{\partial c_\chi} \right) \dot{c}_\chi + \left(\underline{\xi} - \frac{\partial\psi}{\partial \underline{\nabla} c_\chi} \right) \cdot \underline{\nabla} \dot{c}_\chi \\
 & + \left(h\bar{\sigma}^\alpha - \frac{\partial\psi}{\partial \underline{\xi}^{e-\alpha}} \right) : \dot{\underline{\xi}}^{e-\alpha} + \left(h\bar{\sigma}^\beta - \frac{\partial\psi}{\partial \underline{\xi}^{e-\beta}} \right) : \dot{\underline{\xi}}^{e-\beta} \\
 & + \left(-\frac{\partial\psi}{\partial c^v} + \mu^v + h\bar{\eta}^{v,\alpha} : \bar{\sigma}^\alpha + \bar{h}\bar{\eta}^{v,\beta} : \bar{\sigma}^\beta \right) \dot{c}^v \\
 & + \left(-\frac{\partial\psi}{\partial c^i} + \mu^i + h\bar{\eta}^{i,\alpha} : \bar{\sigma}^\alpha + \bar{h}\bar{\eta}^{i,\beta} : \bar{\sigma}^\beta \right) \dot{c}^i \\
 & + h\bar{\sigma}^\alpha : \left(\dot{\underline{\xi}}^{\text{in-diff},\alpha} + \dot{\underline{\xi}}^{\text{in-disl},\alpha} \right) + \bar{h}\bar{\sigma}^\beta : \left(\dot{\underline{\xi}}^{\text{in-diff},\beta} + \dot{\underline{\xi}}^{\text{in-disl},\beta} \right) \\
 & - \underline{j}^i \cdot \underline{\nabla} \mu^i - \underline{j}^v \cdot \underline{\nabla} \mu^v - \frac{\partial\psi}{\partial s_g^\alpha} \dot{s}_g^\alpha - \frac{\partial\psi}{\partial s_g^\beta} \dot{s}_g^\beta \geq 0
 \end{aligned} \tag{4.81}$$

Assuming that the thermodynamical forces are independent of the rate of change of state variables, the corresponding state laws are,

$$\begin{aligned}
 \pi &= -\frac{\partial\psi}{\partial c_\chi} \\
 \underline{\xi} &= \frac{\partial\psi}{\partial \underline{\nabla} c_\chi} \\
 h\bar{\sigma}^\alpha &= \frac{\partial\psi}{\partial \underline{\xi}^{e-\alpha}} \\
 \bar{h}\bar{\sigma}^\beta &= \frac{\partial\psi}{\partial \underline{\xi}^{e-\beta}} \\
 \mu^v &= \frac{\partial\psi}{\partial c^v} - h\bar{\eta}^{v,\alpha} : \bar{\sigma}^\alpha - \bar{h}\bar{\eta}^{v,\beta} : \bar{\sigma}^\beta \\
 \mu^i &= \frac{\partial\psi}{\partial c^i} - h\bar{\eta}^{i,\alpha} : \bar{\sigma}^\alpha - \bar{h}\bar{\eta}^{i,\beta} : \bar{\sigma}^\beta .
 \end{aligned} \tag{4.82}$$

The dissipation equation, eq. (4.81), then reduces to contributions from the viscoplastic power, diffusion induced dissipation, and energy storage due to hardening:

$$\begin{aligned}
 & h\bar{\sigma}^\alpha : \left(\dot{\underline{\xi}}^{\text{in-diff},\alpha} + \dot{\underline{\xi}}^{\text{in-disl},\alpha} \right) + \bar{h}\bar{\sigma}^\beta : \left(\dot{\underline{\xi}}^{\text{in-diff},\beta} + \dot{\underline{\xi}}^{\text{in-disl},\beta} \right) \\
 & - \underline{J}^i \cdot \underline{\nabla} \mu^i - \underline{J}^v \cdot \underline{\nabla} \mu^v - \frac{\partial\psi}{\partial s_g^\alpha} \dot{s}_g^\alpha - \frac{\partial\psi}{\partial s_g^\beta} \dot{s}_g^\beta \geq 0 .
 \end{aligned} \tag{4.83}$$

4.7.2.2 Choice of free energy

The Helmholtz free energy density is chosen to have the following contributions:

$$\begin{aligned}
 \psi &= \psi_0(c^i, c^v, c_\chi, \phi^{\text{GB}}) + \psi_{pen}(c^v, c_\chi) + \psi_{int}(\underline{\nabla} c_\chi) \\
 & + \psi_{mech} \left(c^v, \underline{\xi}^{e-\alpha}, \underline{\xi}^{e-\beta}, s_g^\alpha, s_g^\beta \right) ,
 \end{aligned} \tag{4.84}$$

where, ψ_0 , is the chemical energy, ψ_{pen} , the penalisation energy, ψ_{int} , the interface energy, and ψ_{mech} , the mechanical energy. In particular, the penalisation and interface energy are chosen as

follows,

$$\psi_{pen}(c^v, c_\chi) = \frac{1}{2} H_\chi (c^v - c_\chi)^2, \quad (4.85a)$$

$$\psi_{int}(\nabla c_\chi) = \frac{1}{2} \alpha \nabla c_\chi \cdot \nabla c_\chi. \quad (4.85b)$$

Here, the micromorphic variable, c_χ , is coupled to the vacancy concentration, c^v , as we are interested in modelling void evolution under irradiation. In turn, the mechanical energy is interpolated using the function, $h(\phi)$,

$$\begin{aligned} \psi_{mech} \left(c^v, \underline{\xi}^{e-\alpha}, \underline{\xi}^{e-\beta}, s_g^\alpha, s_g^\beta \right) &= h(\phi(c^v)) f_{mech}^\alpha \left(\underline{\xi}^{e-\alpha}, s_g^\alpha \right) \\ &+ \bar{h}(\phi(c^v)) f_{mech}^\beta \left(\underline{\xi}^{e-\beta}, s_g^\beta \right), \end{aligned} \quad (4.86)$$

where, f_{mech}^α and f_{mech}^β , are the mechanical energies in phase α and β , respectively defined as:

$$f_{mech}^k \left(\underline{\xi}^{e-k}, s_g^k \right) = \frac{1}{2} \underline{\xi}^{e-k} : \underline{\Lambda}^k : \underline{\xi}^{e-k} + f_{mech,p}^k(s_g^k), \text{ with } k = \{\alpha, \beta\}. \quad (4.87)$$

This treatment of the mechanical energy differs from the Kachaturyan-type scheme [74], where the elasticity modulus itself depends on c^v . As in the previous section, the homogeneous energy can be chosen to be quadratic, logarithmic, or even polynomial. For simplicity, only the development using a logarithmic energy will be presented, as it can be adapted to any choice of homogeneous energy in a straightforward manner. The homogeneous chemical free energy is expressed as:

$$\psi_0(c^i, c^v, \phi^{GB}) = \frac{E_f^i(\phi^{GB})}{\Omega_0} c^i + \frac{RT}{\Omega_0} \left[c^i \ln c^i + c^v \ln c^v + (1 - c^i - c^v) \ln(1 - c^i - c^v) \right] + \omega c^v (1 - c^v) \quad (4.88)$$

With the breakdown given in eqs. (4.84) and (4.88), the state laws are expressed as,

$$\pi = -\frac{\partial \psi}{\partial c_\chi} = -\frac{\partial \psi_{pen}}{\partial c_\chi} = H_\chi (c^v - c_\chi) \quad (4.89a)$$

$$\underline{\xi} = \frac{\partial \psi}{\partial \nabla c_\chi} = \frac{\partial \psi_{int}}{\partial \nabla c_\chi} = \alpha \nabla c_\chi \quad (4.89b)$$

$$h \underline{\sigma}^\alpha = \frac{\partial \psi}{\partial \underline{\xi}^{e-\alpha}} = h \frac{\partial f_{mech}^\alpha}{\partial \underline{\xi}^{e-\alpha}} = h \underline{\Lambda} : \underline{\xi}^{e-\alpha} \quad (4.89c)$$

$$\bar{h} \underline{\sigma}^\beta = \frac{\partial \psi}{\partial \underline{\xi}^{e-\beta}} = \bar{h} \frac{\partial f_{mech}^\beta}{\partial \underline{\xi}^{e-\beta}} = \bar{h} \underline{\Lambda} : \underline{\xi}^{e-\beta} \quad (4.89d)$$

$$\underline{\mu}^v = \frac{\partial \psi}{\partial c^v} - h \underline{\eta}^{v,\alpha} : \underline{\sigma}^\alpha - \bar{h} \underline{\eta}^{v,\beta} : \underline{\sigma}^\beta \quad (4.89e)$$

$$= \frac{\partial \psi_0}{\partial c^v} + \frac{\partial \psi_{pen}}{\partial c^v} + \frac{\partial \psi_{mech}}{\partial c^v} - h \underline{\eta}^{v,\alpha} : \underline{\sigma}^\alpha - \bar{h} \underline{\eta}^{v,\beta} : \underline{\sigma}^\beta \quad (4.89f)$$

$$= \frac{\partial \psi_0}{\partial c^v} - \frac{\partial \psi_{pen}}{\partial c_\chi} + \frac{\partial \psi_{mech}}{\partial c^v} - h \underline{\eta}^{v,\alpha} : \underline{\sigma}^\alpha - \bar{h} \underline{\eta}^{v,\beta} : \underline{\sigma}^\beta \quad (4.89g)$$

$$= \frac{\partial \psi_0}{\partial c^v} + \pi + \frac{\partial h}{\partial c^v} \left(f_{mech}^\alpha - f_{mech}^\beta \right) - h \underline{\eta}^{v,\alpha} : \underline{\sigma}^\alpha - \bar{h} \underline{\eta}^{v,\beta} : \underline{\sigma}^\beta \quad (4.89h)$$

$$\underline{\mu}^i = \frac{\partial \psi}{\partial c^i} - h \underline{\eta}^{i,\alpha} : \underline{\sigma}^\alpha - \bar{h} \underline{\eta}^{i,\beta} : \underline{\sigma}^\beta \quad (4.89i)$$

$$= \frac{\partial \psi_0}{\partial c^i} - h \underline{\eta}^{i,\alpha} : \underline{\sigma}^\alpha - \bar{h} \underline{\eta}^{i,\beta} : \underline{\sigma}^\beta \quad (4.89j)$$

The mechanical coupling is visible in eqs. (4.89h) and (4.89i). In both cases, the eigenstrain introduces an extra term proportional to the stress. Moreover, for vacancies, the diffusion potential, eq. (4.89h), contains a term proportional to the difference of elastic energy of each phase. As we are dealing with voids, which have no elastic energy, the latter term is expected to have a visible influence on the kinetics. In the absence of external forces, we recall that:

$$\pi = -\underline{\nabla} \cdot \underline{\xi} = -\underline{\nabla} \cdot (\alpha \underline{\nabla} c_\chi) = -\alpha \underline{\nabla}^2 c_\chi \quad (4.90)$$

The vacancy flux is expressed as:

$$\begin{aligned} \underline{J}^v &= -L^v \underline{\nabla} \mu^v \\ &= -L^v \underline{\nabla} \left(\frac{\partial \psi_0}{\partial c^v} + \pi + \frac{\partial h}{\partial c^v} (f_{mech}^\alpha - f_{mech}^\beta) \right. \\ &\quad \left. - h \underline{\eta}^{v,\alpha} : \underline{\sigma}^\alpha - \bar{h} \underline{\eta}^{v,\beta} : \underline{\sigma}^\beta \right) \\ &= -L^v \underline{\nabla} \left(\frac{\partial \psi_0}{\partial c^v} - \alpha \underline{\nabla}^2 c_\chi + \frac{\partial h}{\partial c^v} (f_{mech}^\alpha - f_{mech}^\beta) \right. \\ &\quad \left. - h \underline{\eta}^{v,\alpha} : \underline{\sigma}^\alpha - \bar{h} \underline{\eta}^{v,\beta} : \underline{\sigma}^\beta \right) \end{aligned} \quad (4.91)$$

where the mobility L^v is isotropic. A modified Cahn-Hilliard equation for the case where L is constant, can now be readily obtained,

$$\begin{aligned} \dot{c}^v &= L^v \underline{\nabla}^2 \left(\frac{\partial \psi_0}{\partial c^v} - \alpha \underline{\nabla}^2 c_\chi \right. \\ &\quad \left. + \frac{\partial h}{\partial c^v} (f_{mech}^\alpha - f_{mech}^\beta) - h \underline{\eta}^{v,\alpha} : \underline{\sigma}^\alpha - \bar{h} \underline{\eta}^{v,\beta} : \underline{\sigma}^\beta \right) + s^v, \end{aligned} \quad (4.92)$$

where the mechanical coupling described by the diffusion potential is clearly visible. The SIA flux is expressed as:

$$\underline{J}^i = -L^i \underline{\nabla} \mu^i, \quad (4.93)$$

where the mobility is chosen as,

$$L^i = \frac{D^v \Omega_0}{RT} c^i (1 - c^i). \quad (4.94)$$

4.8 Choice of parameters

Whatever the choice of homogeneous free energy density ψ_0 , it has been shown, in Section 4.5, that every set of parameters can be related to two physical quantities: the surface energy, γ , and the interface width, λ . The surface energy for metals is of the order of 1 J.m^{-2} [129], even though some concessions on this value are often made in simulations [86]. Indeed, the parameters are tightly coupled and affect other properties, especially for the logarithmic energy, such as binodal and spinodal points. The interface, in reality, is a few atoms thick. To be described correctly, an interface must spawn through at least 6 finite elements. For a simulation box of a few hundred nanometers and an interface width of 1 nm, the computational cost is very high. Binodal points depends on the problems at hand: here, the model is used to simulate voids in a pure metal. Hence, one of these points should be $c_{eq}^\beta = 1$, and the other the equilibrium vacancy concentration. As it is very small, it will be chosen to be 0 for quadratic energy, and as close as possible to the real value for the logarithmic energy. Finally, the spinodal points

cannot be chosen for the quadratic energy, as they do not depend on the parameters λ and γ (or on α and W), eq. (4.17). This is not the case for the logarithmic energy, and an approximate theoretical value [125] will be derived next.

The Gibbs free energy of a system containing a distribution of vacancy clusters, G , is:

$$G = G_0 + \sum_n \rho^0(n) G_n - kT \sum_n \ln(w_n) \quad (4.95)$$

where, G_0 is the free energy of the perfect solid, $\rho^0(n)$ is the distribution of vacancy cluster of size n , G_n is the Gibbs free energy needed to form a void of size n , k is the Boltzmann constant, and w_n the number of ways of removing $\rho^0(n)$ voids in the solid. The energy G_n , can be expressed as,

$$\begin{aligned} G_n &= E_n + \text{trace}(\boldsymbol{\sigma})\Omega_0 n - T s_n \\ &\simeq E_n \text{ for simplicity,} \end{aligned} \quad (4.96)$$

where s_n is the entropy associated with the removal of a cluster of size n , and E_n is the formation energy of a cluster of size n , which can be approximated by its surface energy, Γ_v . A void of radius r_v is composed by n_r vacancies of volume Ω_0 :

$$n_r = \frac{4\pi r_v^3}{3\Omega_0}, \quad (4.97)$$

and its surface energy is:

$$\Gamma_v = 4\pi r_v^2 \gamma. \quad (4.98)$$

Inserting eq. (4.97) in eq. (4.98) yields,

$$E_n \simeq \Gamma_v = (36\pi\Omega_0^2)^{1/3} n_r^{2/3} \gamma. \quad (4.99)$$

If the crystal has a lattice site density of $n^\#$, then w_n , the number of ways of removing $\rho^0(n)$ voids in the solid, is

$$\begin{aligned} w_n &= n^{\rho^0(n)} \frac{n^\# \left(\frac{n^\#}{n} - \rho^0(n) \right) \cdots \left(\frac{n^\#}{n} - n\rho^0(n) + \rho^0(n) \right)}{\rho^0(n)!} \\ &= n^{\rho^0(n)} \frac{\left(\frac{n^\#}{n} \right)!}{\left(\frac{n^\#}{n} - \rho^0(n) \right)! (\rho^0(n))!}. \end{aligned} \quad (4.100)$$

The diffusion potential of a void of size n is:

$$\mu_n = \frac{\partial G}{\partial \rho^0(n)}. \quad (4.101)$$

Using eqs. (4.95), (4.100) and (4.101) and Stirlings approximation ($\ln(a!) \simeq a \ln(a) - a$), the diffusion potential can be expressed as,

$$\mu_n = E_n + kT \ln \left(\frac{\rho^0(n)}{n^\#} \right), \quad (4.102)$$

where it has been assumed that $n^\# \gg n\rho^0(n)$. For a mono vacancy, eq. (4.102) yields

$$\mu_v = E_v + kT \ln \left(\frac{c^v}{n^\#} \right). \quad (4.103)$$

The molar equilibrium concentration is given by,

$$m c_{eq}^v = n^\# \exp\left(\frac{E_f^v}{kT}\right), \quad (4.104)$$

and substitution in eq. (4.103) leaves:

$$\mu_v = kT \ln\left(\frac{c^v}{m c_{eq}^v}\right) = kT \ln(S_v), \quad (4.105)$$

where S_v is defined as the supersaturation of vacancies. The equilibrium condition corresponds to the equality of chemical potentials:

$$n\mu_v = \mu_n. \quad (4.106)$$

Finally, one can express $\rho^0(n)$ and ΔG_n^0 , using the above equations:

$$\rho^0(n) = n^\# \exp\left(-\frac{\Delta G_n^0}{kT}\right) \quad (4.107a)$$

$$\Delta G_n^0 = -nkT \ln(S_v) + (36\pi\Omega_0^2)^{1/3} \gamma n^{2/3}. \quad (4.107b)$$

On fig. 4.5, there is a critical number of vacancies, n_c , above which an embryo will grow into a

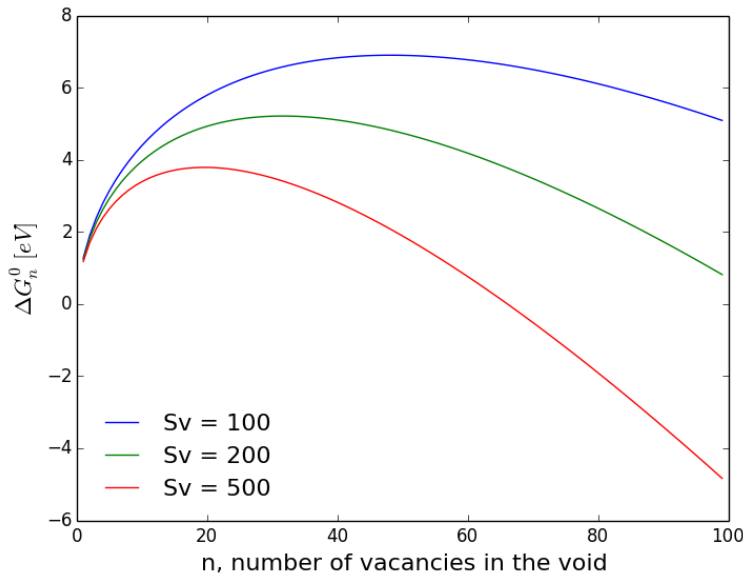


Figure 4.5: Evolution of the free energy of formation of a void. There is a critical number of vacancies, n_c , above which an embryo will grow into a void.

void, for a given level of supersaturation, S_v , according to the solution of the following equation:

$$\frac{\partial \Delta G_n^0}{\partial n} = 0 = -kT \ln(S_v) + (36\pi\Omega_0^2)^{1/3} \frac{2}{3} \gamma n^{-1/3}. \quad (4.108)$$

Assuming an interface width of $\lambda = 1$ nm, the minimum void size in the Cahn-Hilliard framework has a radius of λ . Hence, the number of vacancies in the smallest observable void, for example in copper (with $\Omega_0 = 1, 18.10^{-29} m^3$), is

$$n_{min} = \frac{4\pi\lambda^3}{3\Omega_0} \simeq 530. \quad (4.109)$$

The spinodal point can be found by finding $S_{v,crit}$ for a critical number of vacancies, $n_c = n_{min} = 530$, as:

$$S_v = \exp\left(\frac{(36\pi\Omega_0^2)^{1/3} \frac{2}{3}\gamma n_{min}^{-1/3}}{kT}\right). \quad (4.110)$$

For instance, at $T = 450^\circ\text{C}$, one finds $S_{v,crit} = 7.92$, which corresponds to a mean vacancy concentration of:

$$c_{crit}^v = S_{v,crit} c_{eq}^v = S_{v,crit} \exp\left(-\frac{E_f^v}{kT}\right) \simeq 8,6.10^{-7}, \quad (4.111)$$

for a formation energy of a vacancy of $\sim 1\text{eV}$ [125].

Hence, one can sum up the target system properties as follows:

- Surface energy, $\gamma = 1\text{J.m}^{-2}$
- Interface width, $\lambda = 1\text{ nm}$
- Vacancy equilibrium concentration in the solid (phase α): $c_{eq}^\alpha = \exp\left(-\frac{E_f^v}{kT}\right)$, which can be approximated by 0.
- Vacancy concentration in the void (phase β): $c_{eq}^\beta = 1$
- Spinodal point, for copper at $T = 450^\circ\text{C}$, $c_s^\alpha \simeq 8c_{eq}^\alpha \simeq 1.10^{-6}$.

Table 4.2 summarizes the evolution of various characteristic values for the logarithmic energy. The surface energy, γ , is computed using the approximation given by eq. (4.34). If reasonable values can be attained for the binodal points, the interface energy and the interface width, one has to make a compromise concerning the spinodal points. Indeed, even though the first spinodal point, $c_s^\alpha \simeq 10^{-2}$, is one order of magnitude lower than that for the quadratic energy ($c_s^\alpha \simeq 10^{-1}$), it is still four orders of magnitude higher than the targeted value of $\simeq 1.10^{-6}$.

4.9 Single void growth

As a first step towards modeling irradiation damage, the growth of a single void is first considered. Phase field models have been used previously in the literature for that purpose. In [66], the authors used a Cahn Hilliard approach to study the migration of a single void in a temperature gradient. Mixed phase field Cahn-Hilliard model was used in [105] to investigate void growth in a vacancy supersaturated matrix first, and in an irradiated matrix, afterward. Their model was later enriched to take self-interstitials (SIA) and grain boundaries into account [86, 7], and study void nucleation in a polycrystal. However, grain boundary treatment is delicate, and mechanical aspects were not taken into consideration. The following work investigates the mechanical effects, described in Chapters 2 and 3, on the growth kinetics of a single void. The voids are modeled as the phase where $c^v = 1$. In order to be realistic, their Young's modulus should be zero. However, such a large mechanical contrast between the two phases is numerically difficult, and, instead, the void phase is chosen to be a very compliant elastic phase, with a Young's modulus a hundred to a thousand times smaller than the actual solid phase.

An illustration of the void is given fig. 4.6. A quadratic energy is used, and only vacancies are taken into consideration. The parameters used in the simulation are given in Table 4.3. The coefficient η^v introduces the mechanical coupling which can be excessive in small strain simulations: in [125], for copper, η^v is given to be $-0,2$ for a single vacancy. Here, it is limited

$\bar{\omega}$	$\alpha[J.m^{-1}]$	Binodal point c_{eq}^α	Spinodal point c_s^α	$\gamma[J.m^{-2}]$	$\lambda[nm]$
3 [74]	$1, 51.10^{-7}$ [74]	7.07e-2	0.21	3.0	28
4	$1, 51.10^{-7}$	2.13e-2	0.15	5.3	18
5	$1, 51.10^{-7}$	7.19e-3	0.11	7.1	14
6	$1, 51.10^{-7}$	2.55e-3	0.092	8.5	12
8	$1, 51.10^{-7}$	3.37e-4	0.067	10.9	9.7
10	$1, 51.10^{-7}$	4.54e-5	0.053	12.8	8.2
12	$1, 51.10^{-7}$	4.54e-5	0.043	14.5	7.3
14	$1, 51.10^{-7}$	4.54e-5	0.037	16.0	6.7
16	$1, 51.10^{-7}$	4.54e-5	0.032	17.3	6.1
16	$1, 51.10^{-8}$	1.13e-7	0.032	5.5	1.9
16	$3, 77.10^{-9}$	1.13e-7	0.032	2.7	0.97
16	$1, 51.10^{-9}$	1.13e-7	0.032	1.7	0.6
20	$7.54.10^{-8}$	2.06e-9	0.026	14.0	3.8
20	$7.54.10^{-9}$	2.06e-9	0.026	4.9	1.2

Table 4.2: Properties of the system, depending on the choice of the coefficients $\bar{\omega}$ and α for a logarithmic energy, for $T = 450^\circ$ C.

λ [nm]	$\gamma[J.m^{-2}]$	$D^v[m^2.s^{-1}]$	$\eta^{v,\alpha}$	$\eta_{ref}^{v,\beta}$	E^α [GPa]	E^β [GPa]
2	1	1.10^{-14}	-0.05	-0.05	110	0.11

Table 4.3: Parameters used in the simulation of a single void growth.

to $-0,05$ or $-0,01$. An initial void of radius 6 nm, with $c^v = 1$, is placed in a supersaturated matrix, where $c^v = 0.05$, and symmetry conditions are applied on $x=0$ and $y=0$. A no-flux condition is imposed on the outer arc, and the simulations are run in plane strain. The model is first used in a purely diffusional case (i.e. $\eta = 0$), then coupled to elasticity, and finally the gradient of the flux (Chapter 3) is added as an extra deformation mechanism.

Due to the supersaturation of vacancies in the solid, the cavity grows until an equilibrium is reached. In fig. 4.7a, the growth is slightly faster when the diffusion is coupled to elasticity, and that the inelastic diffusive strain does not modify this kinetics. The stresses are concentrated slightly ahead of the interfacial region, fig. 4.7b, in an isotropic manner, as no external loads are applied in this case. The same simulations has been performed, using a source term K_0 in eq. (4.71) with a value of $2, 8.10^{-4} dpa.s^{-1}$.

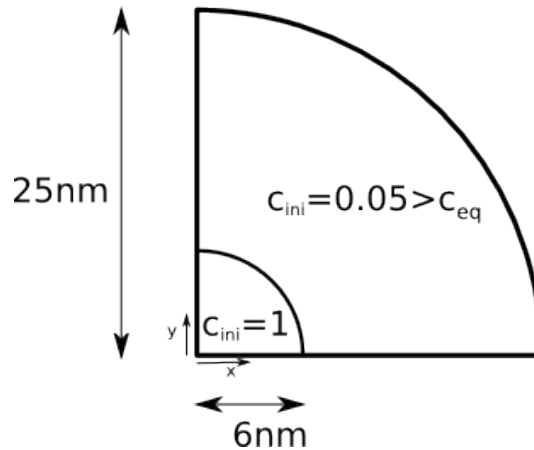


Figure 4.6: Single void growth simulation set-up. An initial void of radius 6 nm is placed in a vacancy supersaturated matrix, and symmetry conditions are applied at $x=0$ and $y=0$. A no-flux condition is imposed on the outer arc.

4.10 Damage evolution in an irradiated Fe polycrystal

This last section is concerned with defect evolution in a polycrystalline aggregate, using spatially resolved stochastic cluster dynamics (SRSCD) [40] as data input for the Cahn-Hilliard model. The objective is to see how the evolution of the diffusivity and recombination parameter with the dose influences the evolution of the system.

Cascades are implanted into thin iron foils at a constant rate and the resulting defects are allowed to migrate through the material and exit at the free surfaces. The layer thickness is set to 300 nm, the temperature is 450°C, and the dpa rate $2,8 \cdot 10^{-4} dpa s^{-1}$ [60]. The profiles of vacancies and SIA are then fitted on a 1D case using eqs. (4.69) to (4.71) with $K_s = 0$, with boundary condition $c^v = c^i = 0$ at the free surfaces.

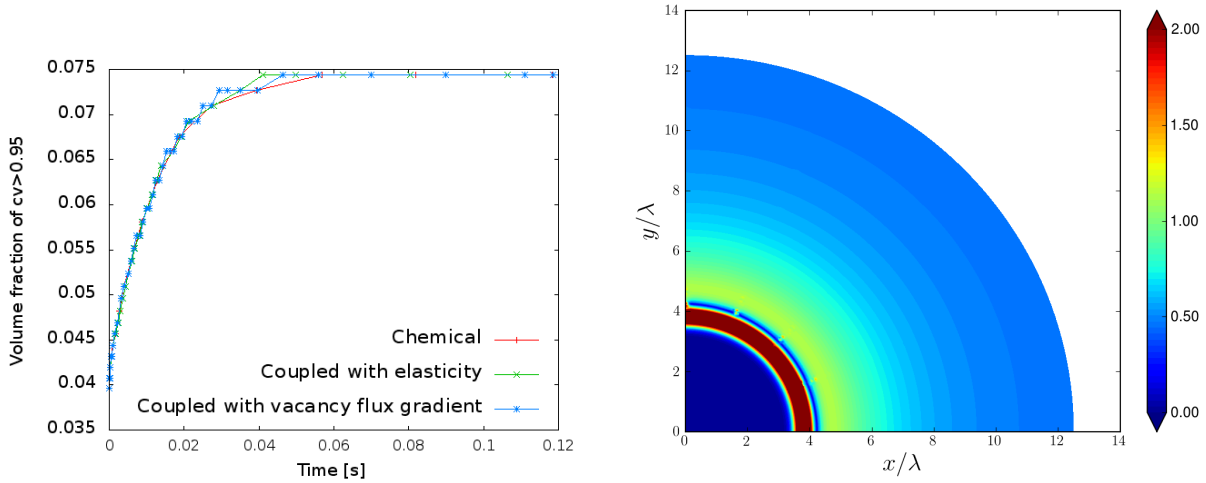
Finally, the same parameters have been employed for a polycrystal composed of hexagonal grains, assuming that grain boundaries act as sinks for defects. However, instead of using a Dirichlet boundary condition, the terms K_{si} and K_{sv} in eq. (4.71) are chosen such that the defect concentration remains close to equilibrium. The distribution of defects after 1 dpa are shown in figs. 4.8 and 4.9, where the influence of the proposed set of parameters, Table 4.4, is clear.

4.11 Concluding remarks and future work

A framework to model irradiation effects in polycrystals, which relies upon a Cahn-Hilliard approach coupled to mechanics, has been proposed. It has been pointed out that the choice of mobility must depend on the choice of homogeneous energy, as some cases may lead to an infinite value of the vacancy flux at the interface. The introduction of a concentration-dependent eigenstrain yields a modified Cahn-Hilliard equation, eq. (4.92), whereby the kinetics is influenced by stress and by the elastic energy difference between the two phases.

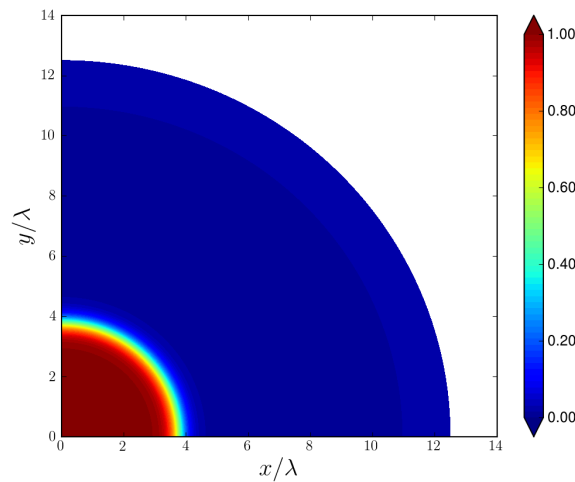
The model has been applied to two cases: the growth of a single void in a supersaturated and irradiated matrix, and the irradiation of a thin film using cluster dynamics informed parameters.

As for the single void, simulations of increasing complexity have been performed to investigate the growth kinetics and the stress distribution around the void. The novel framework for creep proposed in Chapter 3, whereby the gradient of the vacancy flux induces inelastic



(a) Growth kinetics of a single void in a supersaturated matrix, as the time evolution of the volume fraction of $c^v > 0.95$, which explains the stair-shape profile of the results shown.

(b) Mises equivalent stress [GPa] in the steady state for the elastic case.



(c) Concentration c^v , for the elastic case.

Figure 4.7: The growth of an initial void of radius 6 nm in a supersaturated matrix has been simulated. The growth kinetics (a) is slightly larger in the case of stress-diffusion coupling. The (b) Mises equivalent stress, and (c) vacancy concentration are shown at the steady state.

DPA	$D_v[nm^2s^{-1}]$
10^{-4}	18327.0
10^{-3}	551.5
10^{-2}	21.8
10^{-1}	1.7
1	0.2

DPA	$K_{iv}[s^{-1}]$
10^{-4}	25.0
10^{-3}	5.3
10^{-2}	1.7
10^{-1}	1.1
1	1.0

DPA	$D_i[nm^2s^{-1}]$
10^{-4}	151779.8
10^{-3}	38870.8
10^{-2}	9842.4
10^{-1}	1941.0
1	511.0

Table 4.4: DPA dependent parameters D_i , D_v and K_{iv} used to simulate the evolution of point defects in an irradiated polycrystalline aggregate.

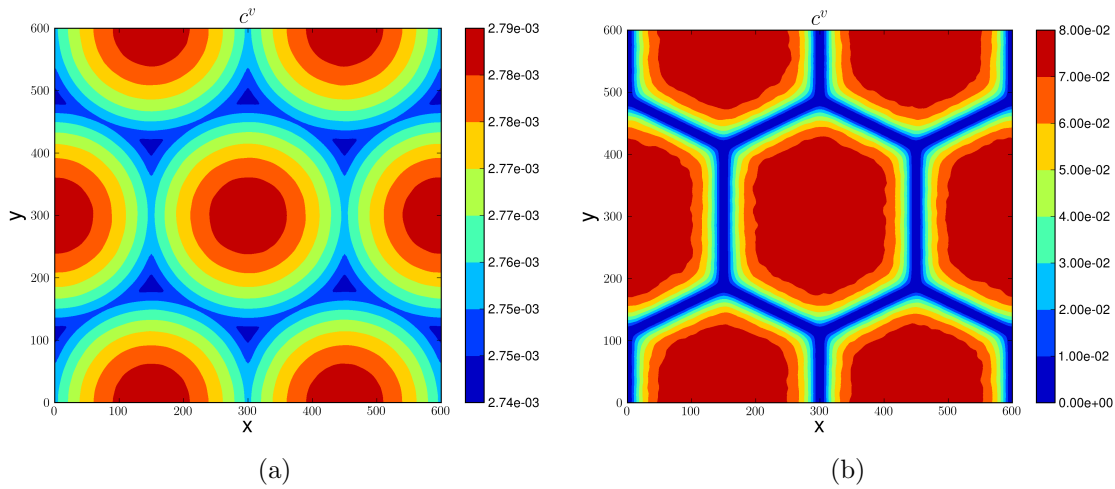


Figure 4.8: Predicted vacancy distribution of an irradiated Fe polycrystal after 1 dpa, using (a) constant parameters (D_i , D_v and K_{iv}) and (b) effective parameters

deformation, has been coupled to the Cahn-Hilliard equations, and applied to the void growth. Creep conditions were expected to modify the shape of the void. However, the complexity of the couplings prevented the computations to come to a term due to a lack of convergence. In order to extract further results from the model, more refined numerical schemes will be needed. Mechanical coupling and Young's modulus contrasts between the matrix and the void could also be reduced, while still being able to draw trends, that is, stress seems to increase the kinetics, according to eq. (4.92). When the initial voids is placed in a supersaturated matrix, it has been found out that the stress induced by the eigenstrain slightly increases the growth kinetics, and that the maximum von Mises stress is localised ahead of the interface.

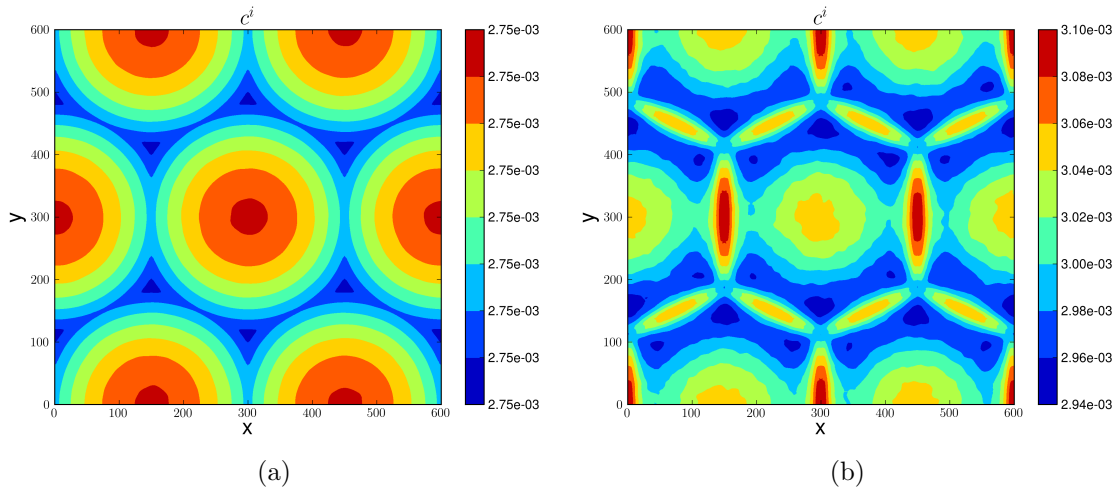


Figure 4.9: Predicted SIA distribution of an irradiated Fe polycrystal after 1 dpa, using (a) constant parameters (D_i, D_v and K_{iv}) and (b) effective parameters

Simulations based on cluster dynamics have been performed, where parameters have been used which implicitly take into account helium and vacancy cluster distributions. The irradiation of a thin film, where the free surfaces are assumed to have a zero defect concentration, has been performed using SRSCD simulations within the Radinterfaces project. The present diffusion model was applied to a polycrystal, with the grain diameter were taken identical as the thickness of the film, but with the grain boundaries acting as imperfect sinks. The void nucleation process, depending on the dose and on the grain size, remains to be investigated using the fully coupled Cahn-Hilliard model. It has been shown that the defect distribution is greatly modified whether or not cluster dynamics informed parameters are used.

Mechanical and irradiation behaviour of nano-crystalline multilayers

The migration of point defects, their clustering has been investigated in the previous chapter at the scale of a polycrystalline aggregate. The growth of a single void has been successfully simulated using a coupled stress-diffusion Cahn-Hilliard framework. It is now of interest to apply this model to nano-crystalline multilayers, which show promising resistance to irradiation damage. The framework is extended to take into account the special properties of the layer interfaces, such as their mechanical behaviour and interactions with point defects. The model is used to investigate the deformation behaviour of Cu-Nb multilayers, the effect of elastic anisotropy on the system yield stress, and the formation of a void denuded zone close to the interface.

Résumé

Un cadre de plasticité cristalline, inspiré d'observations expérimentales et de simulations atomiques, est mis en place afin d'étudier le comportement mécanique de multicouches nano-cristallines. Des simulations de tractions sont réalisées en 3D, sur des systèmes Cu-Nb présentant différentes orientations cristallines. Les résultats montrent que les interfaces obtenues par déposition et par laminage ne donnent pas la limite élastique la plus élevée, et que le rôle de l'anisotropie élastique est négligeable. Cependant, l'orientation cristalline des couches seule ne suffit pas à rendre compte du comportement mécanique du système, puisque l'interface elle-même contribue grandement au comportement via ses interactions avec les dislocations. Une zone affectée par l'interface est alors définie, dans laquelle le comportement des dislocations est modifié afin de tenir compte du phénomène physique précité. Enfin, un modèle de Cahn-Hilliard est utilisé afin de simuler la nucléation et la croissance de cavité dans un multicouche sous irradiation. Les résultats obtenus, prédisant une zone dépourvue de cavités de part et d'autre de l'interface, sont qualitativement en adéquation avec les observations expérimentales.

Summary

Motivated by experimental observations and atomistic simulations, a continuum crystal plasticity framework has been developed to study the mechanical behaviour of nano-multilayers. Firstly, tensile test simulations have been performed on 3D, periodic bilayers, with different interface orientation relationships. The results showed that the interfaces obtained by physical vapor deposition and accumulated roll bonding does not yield the optimum yield stress. Secondly, comparisons between stress strain curves, obtained in tension and shear, have shown that elastic anisotropy yields the same behaviour as elastic isotropy. However, the interface properties do not depend on the orientation of the adjacent crystals alone. Since at this scale, the macroscopic behaviour is largely driven by the interface properties, an interface affected zone has been used, in which dislocation were allowed to be absorbed. Furthermore, to model the interface shearable character, it was treated as a slip plane. Finally, a Cahn-Hilliard framework, was used to study nucleation and growth of voids in a multilayer, by including defects balance laws accounting for the interface properties. Simulations were shown to be in qualitative agreement with experimental observations, by predicting a void-denuded zone close to the interface.

Contents

5.1	Introduction	85
5.2	Modeling approach	87
5.3	Application: mechanical behaviour of Cu-Nb systems	89
5.3.1	Interface orientation relationship influence on the macroscopic mechanical behaviour	89
5.3.2	Effect of elastic anisotropy	94
5.3.3	Hard and shearable interfaces	96
5.4	Void nucleation and evolution under irradiation	98
5.5	Conclusions and recommendations for future work	99

5.1 Introduction

One class of newly designed material is currently receiving growing attention from the international community: nanoscale multilayers, composed of alternate layers of two immiscible metals. They exhibit, in particular, ultra high strength, high hardness, radiation damage resistance and thermal stability. In nanoscale materials, the density of interfaces (interphase boundaries, grain boundaries) is very high and the macroscopic behaviour is driven by interface processes. For instance, the interfaces represent obstacles for moving dislocations and sinks for irradiation defects.

Multilayers can be manufactured by severe plastic deformation, such as ball milling and accumulated roll bonding (ARB), physical vapor deposition (PVD), or electro-deposition. ARB consists in successive steps of rolling, cutting and stacking, starting from two sheets of metals, and resulting in a nanoscale multilayer, see fig. 5.1 [20, 21].

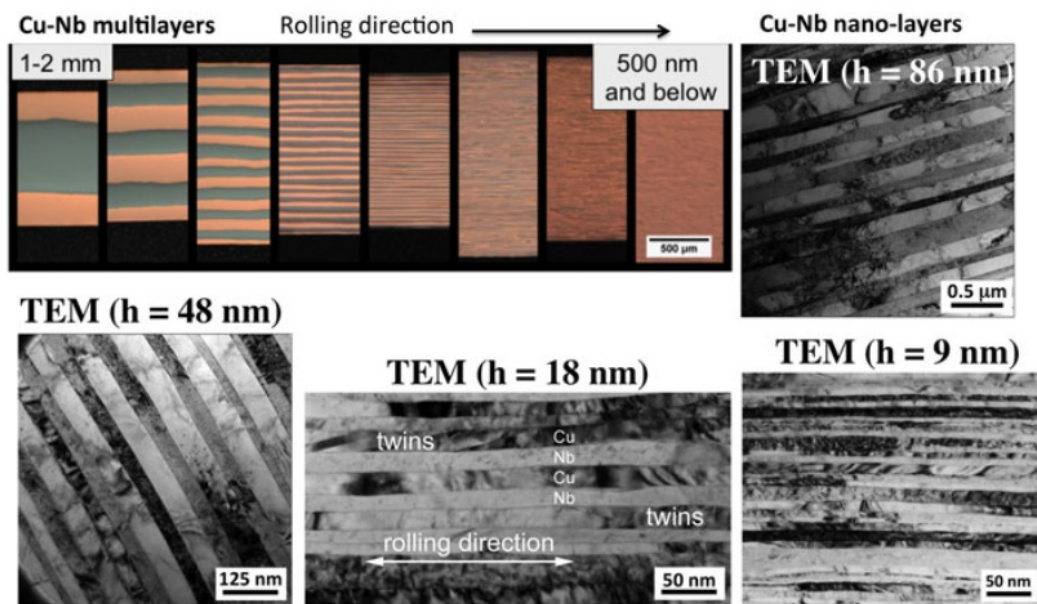


Figure 5.1: Cu-Nb ARB samples fabricated with different individual layer thicknesses ranging from 1 mm to 500 nm (in the upper left photo) and less than 100 nm, as shown in the TEM micrographs [20]. Down to 9 nm, the layered structure is very well defined.

One can summarize the principal characteristics of such systems as perceived from a continuum modeling perspective:

- There is a transition in the microscopic deformation behaviour, from a Hall Petch mode at the μ and sub- μ scale, to a confined layer slip in the 10-100 nm range. Indeed, there is no longer the possibility of piling-up dislocations when the layer thickness is too small, and it is generally difficult for dislocations to cross the layer interface. Inside the layer, the behaviour is then dominated by dislocation interactions [89, 1]. A movie of confined layer slip in Cu-Nb is shown in fig. 5.2.
- Physical Vapor Deposition (PVD) processes tend to form thermodynamically driven, incoherent interfaces with low energy, oriented along $\{111\}\langle 111\rangle\text{Cu} // \{110\}\langle 110\rangle\text{Nb}$ planes¹.

¹ $\{xxx\}$ represents the common plane of the two crystals at the interface, and $\langle yyy \rangle$ a common direction, contained into the interface plane. Together, they represent the interface relationship

Figure 5.2: Movie obtained by in-situ TEM of confined layer slip observed by [75] during nano indentation of a Cu-Nb sample.

On the other hand, accumulated roll bonding (ARB) processes will create $\{112\}\langle 110\rangle$ Cu // $\{112\}\langle 111\rangle$ Nb interfaces [59, 78]. The corresponding interfaces, observed by HRTEM, are shown in fig. 5.3.

- PVD interfaces can act as dislocation sources and sinks, and can be sheared by dislocations, in contrast to ARB interfaces that may also absorb dislocations but have a higher shear strength [122, 109, 22].
- Voids denuded zones (VDZ) in irradiated Cu/Nb nanolayers have been measured to characterise the sink efficiency of the interfaces and grain boundaries (GB), and can be classified from the most to the least efficient, as,
 - non $\Sigma 3$ Cu grain boundaries
 - $\Sigma 3$ Cu grain boundary and ARB Cu/Nb interfaces
 - PVD Cu/Nb interfaces
- Cu GB themselves contain numerous voids, thus weakening their inherent strength, whereas the Cu/Nb interface remains void-free [59].

In the literature, most of the effort has been focused on experimental techniques and atomistic scale modeling. Numerous experimental observations are reported ergo [75, 30, 18, 77], on the characterisation of the interface structure with HRTEM, micropillar compression tests, and bulk uniaxial tests. Many atomistic studies can be found in the literature, dealing with mechanical properties of interfaces ergo [65, 122, 121], resistance to irradiation [70, 76], or both [39, 124, 132, 79]. A few of the above mentioned studies propose larger scale models, based on DDD or crystal plasticity approaches to reproduce the observed results. In particular, Sobie et al

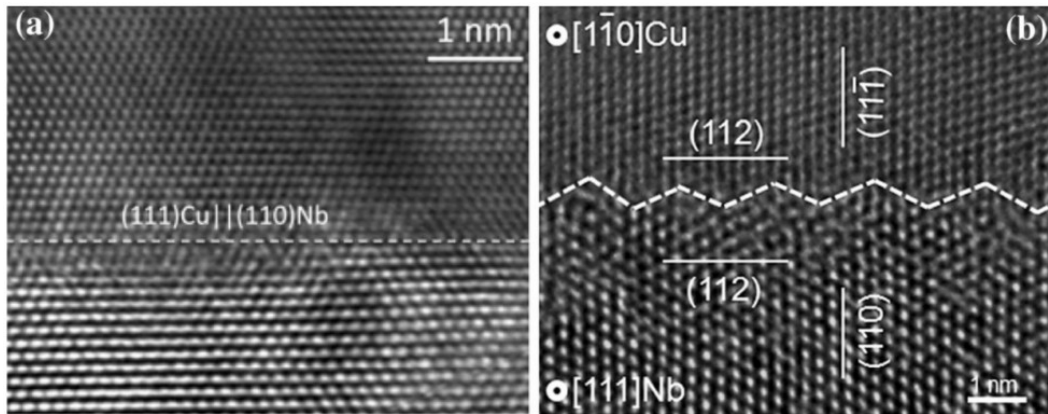


Figure 5.3: Cu-Nb interfaces observed in [78] using HRTEM on a (a) PVD sample, and (b) ARB sample.

[108] in a DDD model, proposed two bounds for the material strength based on the interface behaviour: hard (dislocations are preserved in the interface) or shearable (dislocation cores are absorbed by the interface). MD simulations are then used to verify that the actual behaviour lies between these two bounds. Recently, Mayeur et al [81] argued that classical crystal plasticity approaches failed to describe the physics of the fcc/bcc interfaces. They proposed a model where an interface affected zone is defined and given specific properties. In particular, “slip system activity is presumed to be biased towards systems that permit slip transfer across the interface” in the interface affected zone. This idea of modeling the interface as a separate material was used previously in this work although in a different manner, as will be detailed in Section 5.2, to reproduce the results of [108].

The objectives of this chapter are twofold: (i) to model at the continuum crystal plasticity level the mechanical behaviour of a nano-layer based on experimental observations and atomistic simulations, and (ii) to ascertain that the proposed Cahn-Hilliard framework is able to simulate the void nucleation and growth inside a nanolayer, and reproduce the void denuded zone observed around the interface. The present chapter is structured as follows. The model for the interface, dealing with its mechanical behaviour and interaction with point defects, will be described in Section 5.2 using the concept of interface affected zone. Next, the mechanical elastoplastic behaviour of Cu-Nb systems and the effect of elastic anisotropy will be simulated in Section 5.3. Finally, for a multilayer undergoing irradiation, the model will be shown to be able to reproduce the experimentally observed void denuded zone close to an interface in Section 5.4. Unless specified otherwise, the model will be applied to Cu-Nb systems, as they are for now the most widely studied systems.

5.2 Modeling approach

As stated in the introduction, the layer interfaces have specific properties which condition the macroscopic behaviour. Hence, the layer interfaces will be modelled using a phase-field-type method. A diffuse parameter field, ϕ^{int} , is defined such that it takes the value 1 at the interface, and 0 within a layer, see fig. 5.4. The profile between 0 and 1 is chosen in the same manner as eq. (3.36) in the form of a cosh function, with thickness δ^{int} . The behaviour of the interface is then interpolated base on the behaviour of the adjacent layers. Each layer is composed of a set of material points, which have either Cu or Nb properties and a unique crystalline orientation. The real interface is a few atoms thick, depending on the interface orientation. However, since

the studied layer thickness is of the order of 100 nm, such a thin interface would require far too many elements. Hence, for the sake of computational tractability, the modeled interface will be a few nanometers thick. The coordinate system xy given in fig. 5.4 will be used throughout this chapter.

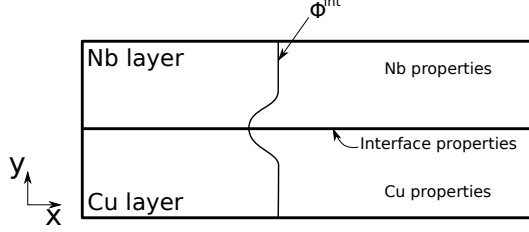


Figure 5.4: Finite element modeling of a Cu-Nb system. Each layer is represented by a set of material points. A diffuse field, ϕ^{int} , is used to interpolate the single crystal and the interface properties.

The crystal plasticity framework, described in Chapter 3, will be recalled briefly next, and modified to take the interface into account. Furthermore, the resulting mechanical constitutive laws are embedded in the general Cahn-Hilliard framework presented in Chapter 4. Let the total strain be partitioned into its different contributions in each phase α (solid) and β (void),

$$\underline{\varepsilon}^k = \frac{1}{2}\underline{\varepsilon}^{e,k} + \underline{\varepsilon}^{*,k}(c^i, c^v) + \underline{\varepsilon}^{in-disl,k}, \text{ with } k = \{\alpha, \beta\}, \quad (5.1)$$

where, $\underline{\varepsilon}^{e,k}$, is the elastic strain, $\underline{\varepsilon}^{*,k}(c^i, c^v)$, the eigenstrain due to relaxation around point defects (see eq. (4.76)), and $\underline{\varepsilon}^{in-disl,k}$, the inelastic strain arising from dislocation glide and climb. Recalling the definition of $\underline{\varepsilon}^{in-disl,k}$ for a phase k :

$$\dot{\underline{\varepsilon}}^{in-disl,k} = \frac{1}{2} \sum_s \dot{\gamma}^s (\underline{m}^s \otimes \underline{n}^s + \underline{n}^s \otimes \underline{m}^s), \quad (5.2)$$

where, s , is the slip system. The flow rule is chosen as a power law, as

$$\dot{\gamma}^s = \left\langle \frac{|\tau^s| - S^s}{K_s} \right\rangle^n \text{sign}(\tau^s), \quad (5.3)$$

where, τ^s is the resolved shear stress, S^s the slip resistance, and K_s and n flow rule parameters. In turn, the slip resistance is given by,

$$S^s = S_0 + \lambda G b^s \sqrt{\sum_{m=1}^N h^{sm} \rho^m}, \quad (5.4)$$

where, b^s , is the norm of the Burgers vector, λ a scaling parameter, $h^{sm} = w_1 + (1 - w_2)\delta^{sm}$ the interaction matrix, and ρ^m the dislocation density on the slip system m . Here, S_0 represents in a simple way the fact that the macroscopic yield point is very high in nanolayers. The evolutionary equation for the dislocation density, as given in [31], is modified to take into account the dislocation core spreading [108] at the interface, by adding a dislocation absorption coefficient, B_{sd} , so that

$$\dot{\rho}^s = \frac{C}{b^s} \left[K \sqrt{\sum_m \rho^m} - 2d\rho^s \right] |\dot{\gamma}^s| - B_{sd}(\phi^{int}) \rho^s. \quad (5.5)$$

Case	x	y
A	$Cu\langle 100 \rangle // Nb\langle 100 \rangle$	$Cu\langle 001 \rangle // Nb\langle 110 \rangle$
B	$Cu\langle 100 \rangle // Nb\langle 112 \rangle$	$Cu\langle 001 \rangle // Nb\langle 110 \rangle$
C	$Cu\langle 110 \rangle // Nb\langle 112 \rangle$	$Cu\langle 111 \rangle // Nb\langle 110 \rangle$
D (ARB orientation)	$Cu\langle 112 \rangle // Nb\langle 112 \rangle$	$Cu\langle 111 \rangle // Nb\langle 110 \rangle$

Table 5.1: Crystallographic orientations of the x and y axes in fig. 5.4, given for copper and niobium for the four different types of simulations.

A similar equation was used in [2], to account for the annihilation of dislocations by a moving grain boundary. The term B_{sd} is the interpolation of a bulk and an interface value as:

$$B_{sd} = \phi^{int} B_{sd}^{int} + (1 - \phi^{int}) B_{sd}^{bulk} . \quad (5.6)$$

Finally, the interface is treated itself as a crystallographic slip plane to model its shearable character [123]. The normal of the slip plane coincides with the interface normal, and the slip directions are in the interface plane. In fig. 5.4, the normal to the added slip plane is the direction y, and the slip directions oriented along 0° , 60° and 120° with respect to the axis x.

5.3 Application: mechanical behaviour of Cu-Nb systems

5.3.1 Interface orientation relationship influence on the macroscopic mechanical behaviour

In this section, a simple crystal plasticity model is used to investigate the influence of the orientation relationship of the interface on the deformed shape and on the macroscopic stress strain curves. The model used in this section is neither based on dislocation density, nor on the field ϕ^{int} . Four Cu-Nb orientation relationships, given Table 5.1, are studied: each crystal is progressively rotated so that the complexity of the interface increases. Cases A to C are purely theoretical, and Case D corresponds to the interface obtained using accumulated roll bonding (ARB) processing. Periodic boundary conditions are used and each layer of copper and niobium is 200 nm thick, in order to compare simulations with the experiments performed in [20]. We hence define the mean strain, $E_{ij} = \langle \varepsilon_{ij} \rangle$, and the mean stress, $\Sigma_{ij} = \langle \sigma_{ij} \rangle$. A mean deformation of $E_{xx} = 0.05$ is imposed, the remaining components of the mean stress Σ being set to zero. The material parameters are given in Table 5.3, and the list of slip systems in Table 5.2. For copper, the coefficient K_s was taken from [31]. The remaining coefficients have been identified to match the experimental results of [20], with the order of magnitude given in [61]. The corresponding experimental bulk tensile stress-strain curves [20], for a Cu-Nb multilayer manufactured by ARB, are given in fig. 5.5. It can be seen from this figure that hardening is negligible so it can be henceforth neglected. The behaviour used in the simulations is elastic perfectly plastic, with isotropic elasticity (the effect of elastic anisotropy will be investigated in Section 5.3.2).

As shown in fig. 5.7, the predicted mechanical responses of the bi-layer for each tested case are almost identical, except for C. Despite the fact that, for Cu and Nb, the respective single crystal response for Cases B and C are identical, fig. 5.6, the multilayer response is different. This may be explained with the help of figs. 5.8a and 5.8b, where the slip on each system in the Cu and Nb layers are plotted. Due to stronger incompatibility in the interface for Case C, more

System number	Plane and direction	System number	Plane and direction
1	(111)[$\bar{1}01$]	7	($\bar{1}11$)[$0\bar{1}1$]
2	(111)[$0\bar{1}1$]	8	($\bar{1}11$)[110]
3	(111)[$\bar{1}10$]	9	($\bar{1}11$)[101]
4	($\bar{1}\bar{1}1$)[$\bar{1}01$]	10	($\bar{1}\bar{1}1$)[$\bar{1}10$]
5	($\bar{1}\bar{1}1$)[011]	11	($\bar{1}\bar{1}1$)[101]
6	($\bar{1}\bar{1}1$)[110]	12	($\bar{1}\bar{1}1$)[011]

Table 5.2: List of the slip system used for the fcc and bcc materials [47]. Even though they are fundamentally different, they are both taken to be identical in the case of small strains. Indeed, the slip plane and slip direction of a fcc crystal are the slip direction and slip plane, respectively, of a bcc crystal. Hence eq. (5.2) remains the same for bcc and fcc systems.

	E [GPa]	ν	n	K_s [MPa.s ^{-1/n}]	$S_c = constant$ [MPa]
Cu	110	0.34	4	20 [31]	200
Nb	105	0.4	4	20	300

Table 5.3: Material parameters used to study the interface orientation relationship influence on the macroscopic stress strain curves

A	B	C	D
σ_{xx}	$\sigma_{xx}, \sigma_{zz}, \sigma_{zx}$	$\sigma_{xx}, \sigma_{zz}, \sigma_{zx}$	$\sigma_{xx}, \sigma_{zz}, \sigma_{zx}$

Table 5.4: Non-zero stress tensor components for each case.

slip systems are activated after 2% strain. Finally, the deformed shapes (magnified 5 times), along with the list of activated slip systems, are shown in fig. 5.9. For complex interfaces such as Cases C and D, the deformed shape is strongly 3-dimensional, even though only two systems are activated for Case D, see in fig. 5.8c. Finally, elastic anisotropy effects with modulus given in Tables 5.5 and 5.6, are introduced in the model for test Case D (accumulated roll bonding sample). The stress stress curve is the same as for isotropy, but two additional slip systems are activated, as seen in fig. 5.8d. It is interesting to note that, even though the mean stress components Σ_{ij} vanish for $ij \neq xx$ in the system, the individual components in the layer do not. The non zero stress tensor components per layer are shown in Table 5.4

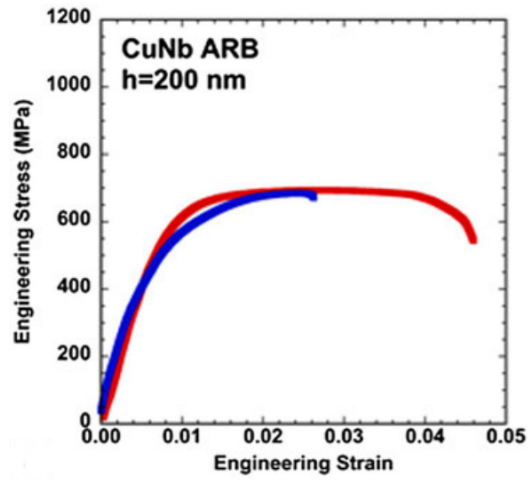


Figure 5.5: Bulk tensile stress-strain curves for a Cu-Nb ARB multilayer, tested along the transverse (blue) and longitudinal (red) direction [20]. Here, transverse and longitudinal directions refer to the rolling directions of the ARB processing.

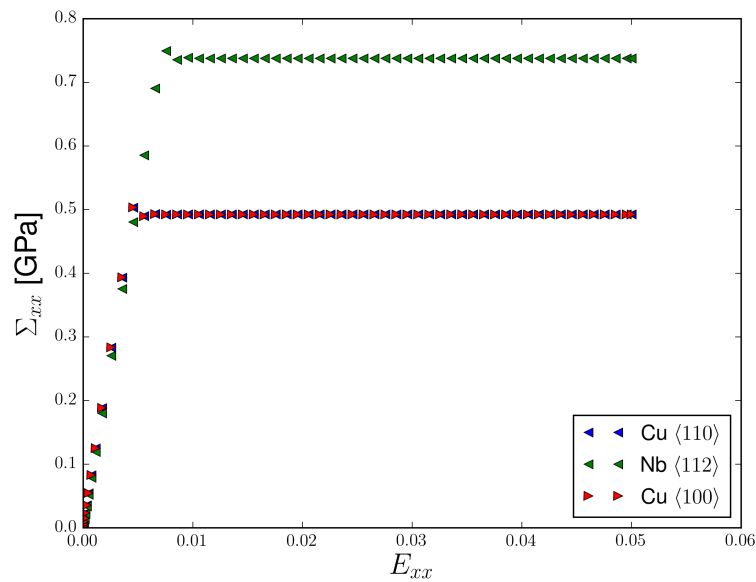


Figure 5.6: Simulated tensile stress-strain curves for elastically isotropic single crystals. The curves for single crystal Cu are identical for Case B $\langle 100 \rangle$ and C $\langle 110 \rangle$ orientations.

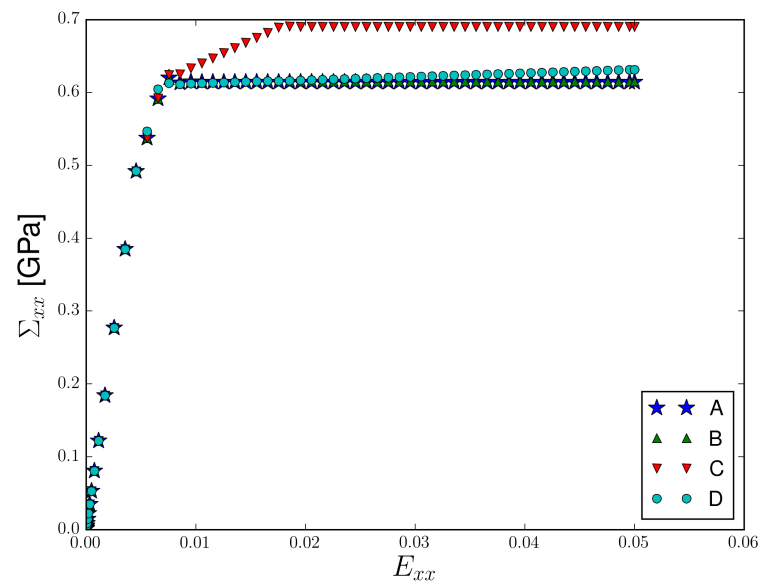
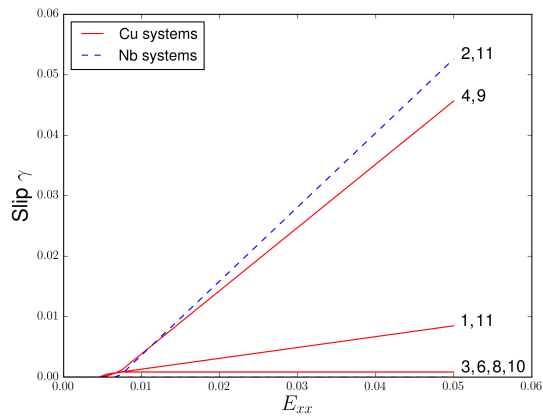
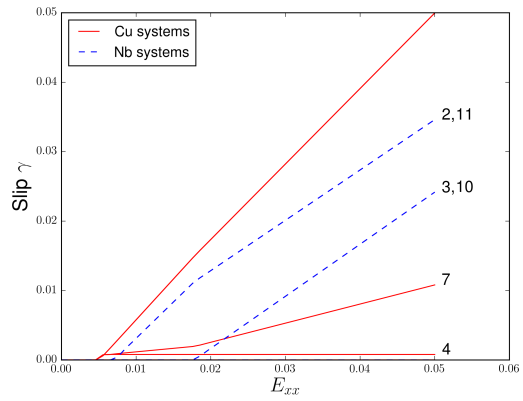


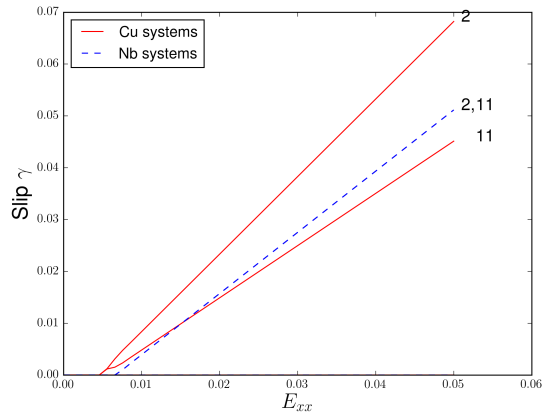
Figure 5.7: Simulated tensile stress-strain curves for a Cu-Nb multilayer with isotropic elasticity. For the curve C, the plateau starting around 2% of strain is due to late activation of two slip system in niobium, as seen in fig. 5.8b.



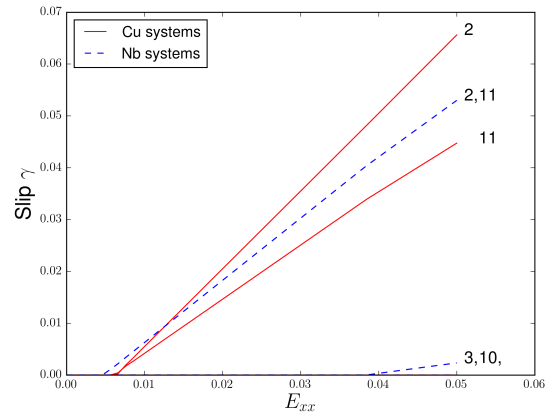
(a) Slip on every system in a Cu-Nb multilayer, for Case B



(b) Slip on every system in a Cu-Nb multilayer, for Case C



(c) Slip on every system in a Cu-Nb multilayer, for Case D



(d) Slip on every system in a Cu-Nb multilayer, for Case D (ARB), using elastic anisotropy.

Figure 5.8: Activity of the slip system, for Cases (a) B, (b) C, and (c) D. Finally, Case D has been simulated again using d elastic anisotropy for Cu and Nb, which leads to the activation of two additional slip systems.

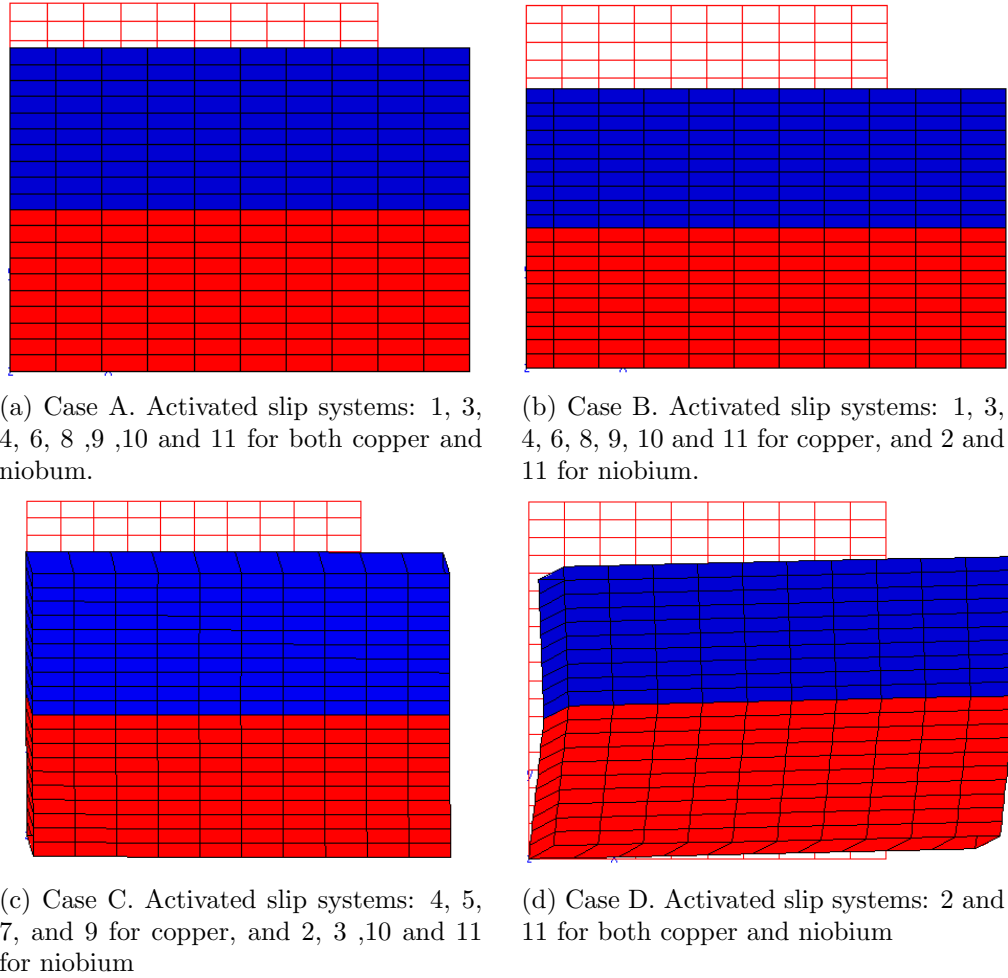


Figure 5.9: Deformed shape (magnified 5 times), for each test case, along with the list of activated slip systems. The copper is the lower layer, and niobium the upper one.

5.3.2 Effect of elastic anisotropy

Copper and niobium exhibit cubic elasticity with strongly different anisotropy factors, 3.21 and 0.46, respectively. To investigate the influence of this property on the mechanical behaviour of the system, various mechanical loading conditions have been considered on a Cu-Nb periodic bi-layer, in 3D, whereas the interface between the layers is considered sharp. The layer thickness is 200 nm, with orientation relationship corresponding to those used in [1], that is: the copper layer is oriented such that the horizontal x axis (fig. 5.4) is parallel to the $[1\bar{1}2]$ direction, and the vertical y axis to the $[1\bar{1}\bar{1}]$ direction. The niobium layer is oriented such that the x axis corresponds to the $[1\bar{1}2]$ direction, and the y axis to the $[110]$ direction. The z axis is then parallel $[110]$ for copper and $[\bar{1}1\bar{1}]$ for niobium.

The elastic moduli are taken from [61]. The remaining parameters have been fitted to reproduce the DDD results provided in [108] with the order of magnitude given in [61], thus taking into account the enhanced nanolayer strength. The simulation parameters are shown in Tables 5.5 and 5.6.

The material is tested along directions x (also noted T, to facilitate comparison with [108]) and z (noted L). The stress-strain curve for a volume element of copper and niobium is shown in

C_{11} [GPa]	C_{12} [GPa]	C_{44} [GPa]	n	K_s [MPa.s ⁻¹]	S_0 [MPa]	G [GPa]	G_0 [GPa]
179.5	126.4	82.5	4	20	50	45	49
C	b [nm]	K	d [nm]	w1	w2	λ	
15	0.257	$1,41.10^{-2}$	1	1.5	1.2	0.3	

Table 5.5: Material parameters for copper used to ascertain the effect of anisotropic elasticity on the mechanical behaviour of a Cu-Nb multilayer

C_{11} [GPa]	C_{12} [GPa]	C_{44} [GPa]	n	K_s [MPa.s ⁻¹]	S_0 [MPa]	G [GPa]	G_0 [GPa]
242.0	121.2	28.0	4	20	50	37.5	41.2
C	b [nm]	K	d [nm]	w1	w2	λ	
5	0.257	$1,41.10^{-2}$	1	1.5	1.2	0.3	

Table 5.6: Material parameters for niobium used to ascertain the effect of anisotropic elasticity on the mechanical behaviour of a Cu-Nb multilayer

fig. 5.10. In the FE simulations, the plastic anisotropy of niobium observed in [108] is retrieved. However, the response of copper is similar in both directions, whereas plastic anisotropy is observed in [108].

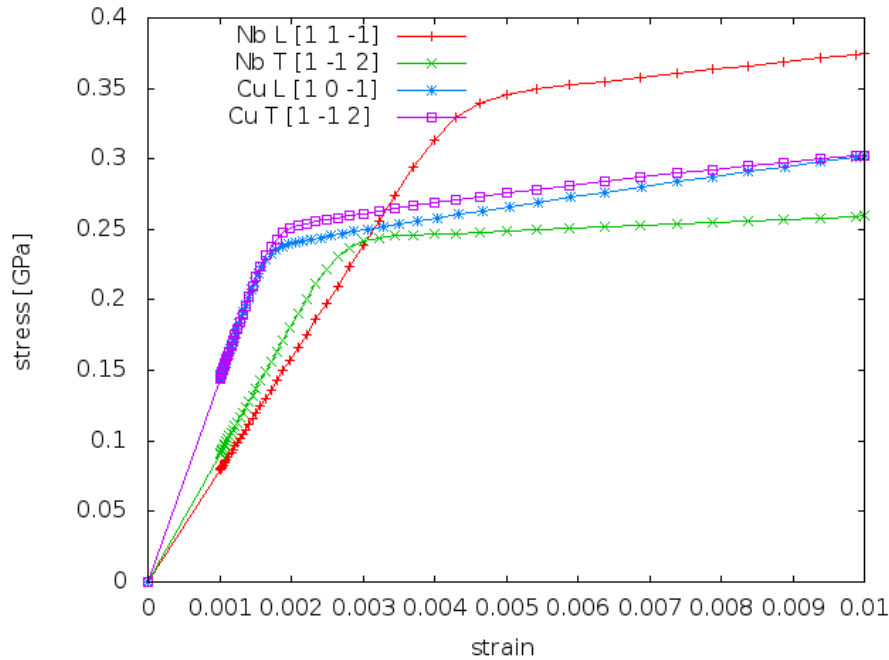


Figure 5.10: Stress strain curves for single crystalline copper and single crystalline niobium, simulated in tension along two orthogonal directions contained in the interface plane.

The stress strain curves corresponding to an applied mean strain of $E_{xx} = 0.05$ (T) and $E_{yy} = 0.05$ (L) for a Cu-Nb multilayer are shown in fig. 5.11. Furthermore, the simulations

are performed for both isotropic and anisotropic elasticity, while using the plasticity model presented in Section 5.2. The absorption coefficient for dislocations, B_{sd} , is here taken equal to zero. In [108], DDD simulations were performed to investigate the effect of elastic mismatch and plastic anisotropy in Cu-Nb multilayer. Elastic isotropy was used, and the layer interfaces acted as impenetrable barriers for dislocations. Tensile tests were simulated in the transverse (T) and longitudinal (L) directions (relative to the rolling direction), and the results revealed an isotropic behaviour. Furthermore, Cu-Cu and Nb-Nb systems were tested to remove the effect of elastic mismatch, while keeping the influence of the interface on the dislocation glide, evidencing plastic anisotropy. In the present work, the macroscopic response is effectively isotropic and, surprisingly, elastic anisotropy yields the same behaviour as elastic isotropy.

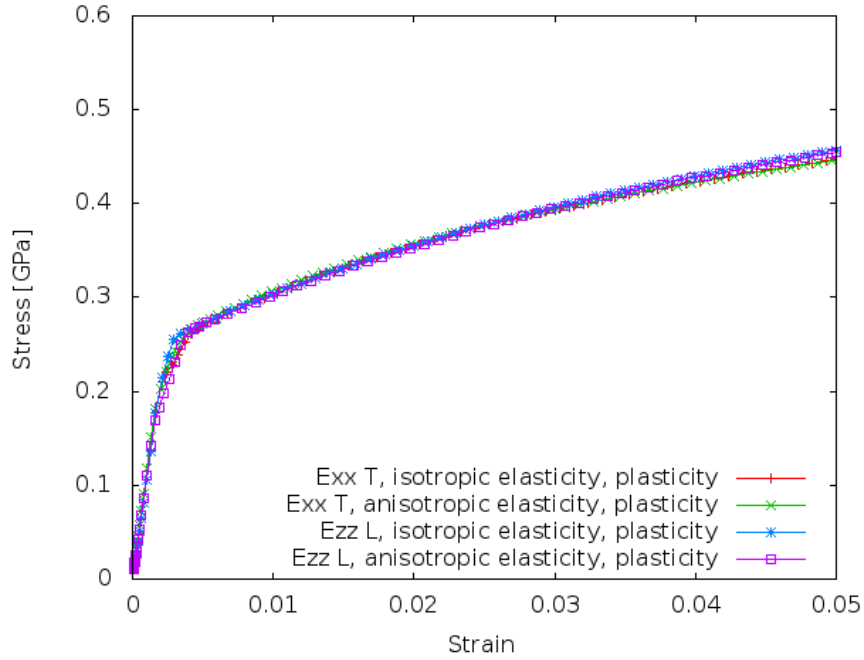


Figure 5.11: Stress strain curve for a Cu-Nb bilayer, simulated in tension along two orthogonal directions contained in the interface plane.

Finally, simulations with imposed mean shear strain E_{xy} are performed, see figs. 5.12 and 5.13. In the figures, the accumulated plastic strain is defined as $\int_t \sqrt{\frac{2}{3}} \dot{\epsilon}^{\text{in-disl}} : \dot{\epsilon}^{\text{in-disl}} dt$. Here again, there is little difference between the isotropic and anisotropic elasticity cases.

5.3.3 Hard and shearable interfaces

In what follows, the interface is modelled such that it is able to absorb dislocations, by adding an absorption or static recovery-type term in the evolution law for the dislocation density, as described by eq. (5.5). Furthermore, the interface is treated as a 13rd slip plane to model its shearable character evidenced in [122, 123]. The normal to this slip plane coincides with the interface normal, and the slip directions are taken to form angles of 0, 60 and 120° with the x axis (fig. 5.4). The material properties are interpolated using the static phase-field ϕ^{int} , described in Section 5.2. The copper and niobium properties are given in Tables 5.5 and 5.6, and the dislocation absorption coefficient at the interface, B_{sd}^{int} , has been given the value of $0.01s^{-1}$. The value of this parameter is unknown, and further MD simulation should allow for

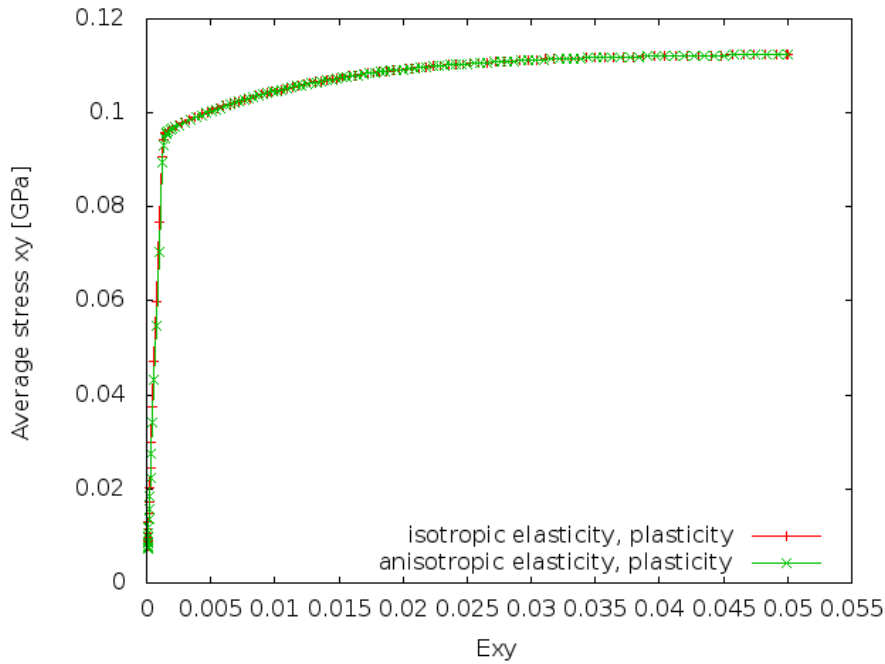


Figure 5.12: Stress strain curve for a Cu-Nb bilayer, simulated in simple shear with an imposed mean strain of $E_{xy}=0.05$.

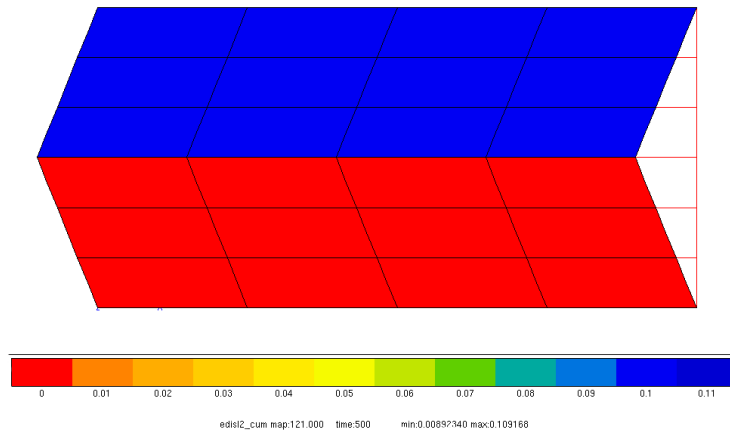


Figure 5.13: Accumulated plastic strain, for an imposed mean shear strain of $E_{xy}=0.05$, in the deformed shape.

identification. The width of the diffuse interface is set to 40 nm, for computation tractability as stated in the introduction, and a parametric study remains to be conducted. For the case of tension along x , the only contribution is that of the dislocation absorption coefficient in the interface plane, since the Schmid factor of the additional system is 0 for this loading. In the case of shear, both the additional slip systems and the dislocation absorption coefficient B_{sd}^{int} contribute to the macroscopic mechanical response. The resulting stress-strain curves are shown in fig. 5.14. In each case, the hard interface yields a higher yield stress. The deformed shape is also affected by the presence of the additional slip plane. As seen in fig. 5.15, the overall shape remains that of a “v”. However, it is readily seen that the region close to the interface carries

more deformation than the bulk.

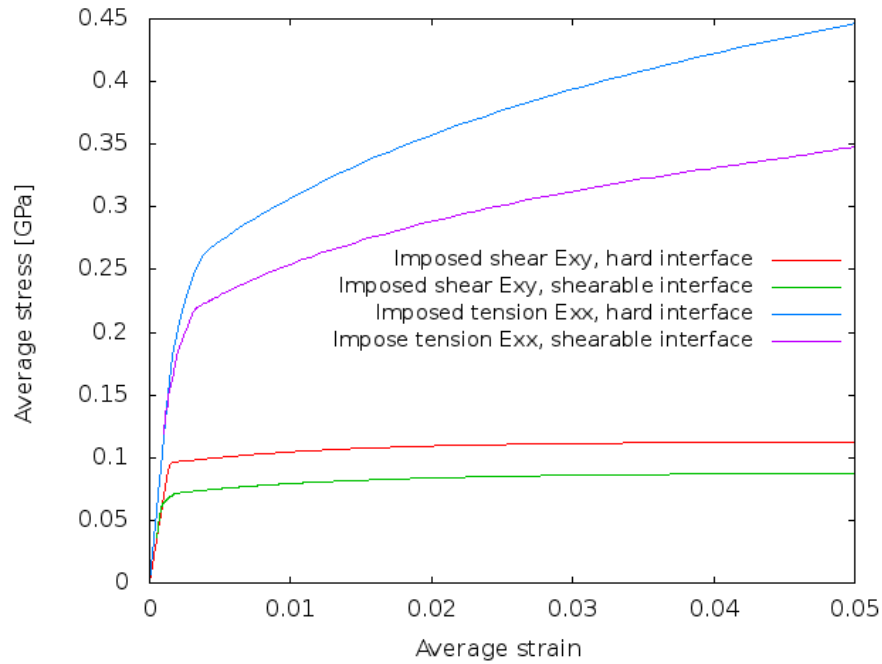


Figure 5.14: Macroscopic stress-strain curve showing a comparison between the hard and shearable interface models. The shearable model gives a softer behaviour.

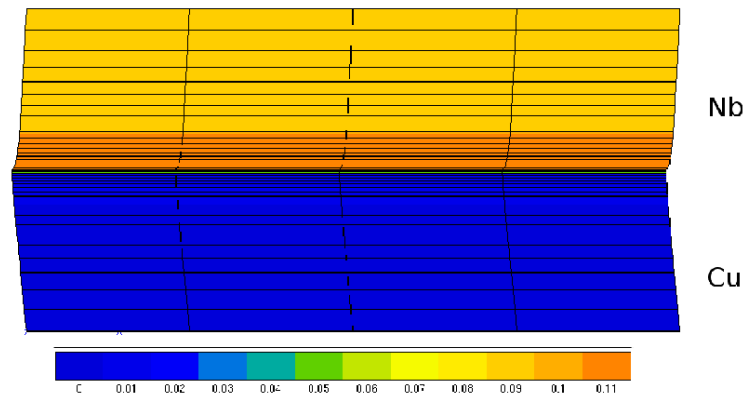


Figure 5.15: Accumulated plastic strain for an imposed mean shear strain of $E_{xy}=0.05$, for the case of a shearable interface. The plastic activity is more intense in the niobium layer, close to the interface.

5.4 Void nucleation and evolution under irradiation

The objective of this section is to demonstrate the ability of the proposed Cahn-Hilliard framework, Chapter 4, to reproduce the experimentally observed void denuded zone in a multilayer undergoing irradiation. The influence of the mechanical coupling is not shown as the results of the computations are not available yet. To further simplify the computations and obtain a

$\Omega_0[m^3.mol^{-1}]$	$\alpha[J.m^{-1}]$	$\bar{\omega}$	$k^{i,\alpha} = k^{i,\beta} [J.m^{-3}]$	$c_{\alpha}^{i,eq} = c_{\beta}^{i,eq}$
10^{-5}	$1, 5.10^{-8}$	16	$2, 13.10^9$	0
Diffusivities D [$m^2.s^{-1}$]	$K_{iv}^{int}[s^{-1}]$	$K_{iv}^{bulk}[s^{-1}]$		
10^{-14}	10^{-2}	10^{-4}		

Table 5.7: Material parameters used to simulate the void-denuded zone around an interface in a multilayer system.

better numerical convergence, the free energy is simplified from eq. (4.88), by decoupling the contribution of self interstitial atoms (SIA) and vacancies to the free energy density:

$$\begin{aligned} \psi_0(c^i, c^v) = & \frac{RT}{\Omega_0} [c^v \ln c^v + (1 - c^v) \ln(1 - c^v)] \\ & + \frac{1}{2} k^{i,\alpha} (c^i - c_{\alpha}^{i,eq})^2 + \frac{1}{2} k^{i,\beta} (c^i - c_{\beta}^{i,eq})^2 + \omega c^v (1 - c^v), \end{aligned} \quad (5.7)$$

where, $k^{i,\alpha}$ and $k^{i,\beta}$ are the chemical curvatures for SIA in the phases α and β , and $c_{\alpha}^{i,eq}$ and $c_{\beta}^{i,eq}$ the equilibrium concentration of SIA in the phases α and β , respectively.

Periodic boundary conditions are applied since here no distinction is made between the material properties of the two layers, given in Table 5.7. The layer thickness is 100 nm, the interface thickness for the diffuse field ϕ^{int} is taken to be 10 nm, the temperature 450°C, the dpa rate $2, 8.10^{-4} dpa.s^{-1}$ [60], and irradiation is performed during $10^7 s$. The defect recombination parameters are chosen in order to observe a void denuded zone. These parameters, together with the interface affected zone thickness should be chosen to reproduce the experimental results. The layer interface is such that SIA-vacancies recombination occurs at a higher rate than in the bulk, with K_{iv}^{bulk} [70, 76], with $K_{iv}^{int} > K_{iv}^{bulk}$ (see eqs. (4.69) to (4.71)).

The predicted evolution of the vacancy field is shown in figs. 5.16 and 5.17. As time increases, more and more defects are created due to irradiation. Some of them are recombined in the bulk and in the interface affected zone. When the mean concentration inside a layer exceeds the spinodal point, nucleation occurs randomly at its interior. The region close to the interface remains relatively free of defects and voids, as recombination of defects is enhanced in this region, and its rate is high enough so that the spinodal point is never reached.

5.5 Conclusions and recommendations for future work

In this work, crystal plasticity, together with a Cahn-Hilliard model, has been used to study the behaviour of nanolayers under irradiation. First, the effect of crystal orientation, and hence the interface orientation relationship, has been investigated. Stress strain curves of Cu-Nb multilayers, processed by accumulated roll bonding (ARB) techniques, have been simulated. Furthermore, it has been shown that the deformation mode of such ARB multilayer are very complex, with a strong 3D character. The simplified model predicts possible higher yield stress for other orientations, for instance, $\{100\} \langle 001 \rangle$ Cu // $\{112\} \langle 110 \rangle$ Nb, which are nevertheless not encountered in actually processed bi-layer of these type. The effect of elastic anisotropy has also been investigated, for the case of an ARB Cu-Nb multilayer. The mechanical behaviour and yield stress are then same as the isotropic elasticity case, both in shear and tension in the longitudinal and transverse directions. However, the orientation relationship alone does not determine the mechanical behaviour. Indeed, the interface has different shape for PVD and ARB, for instance,

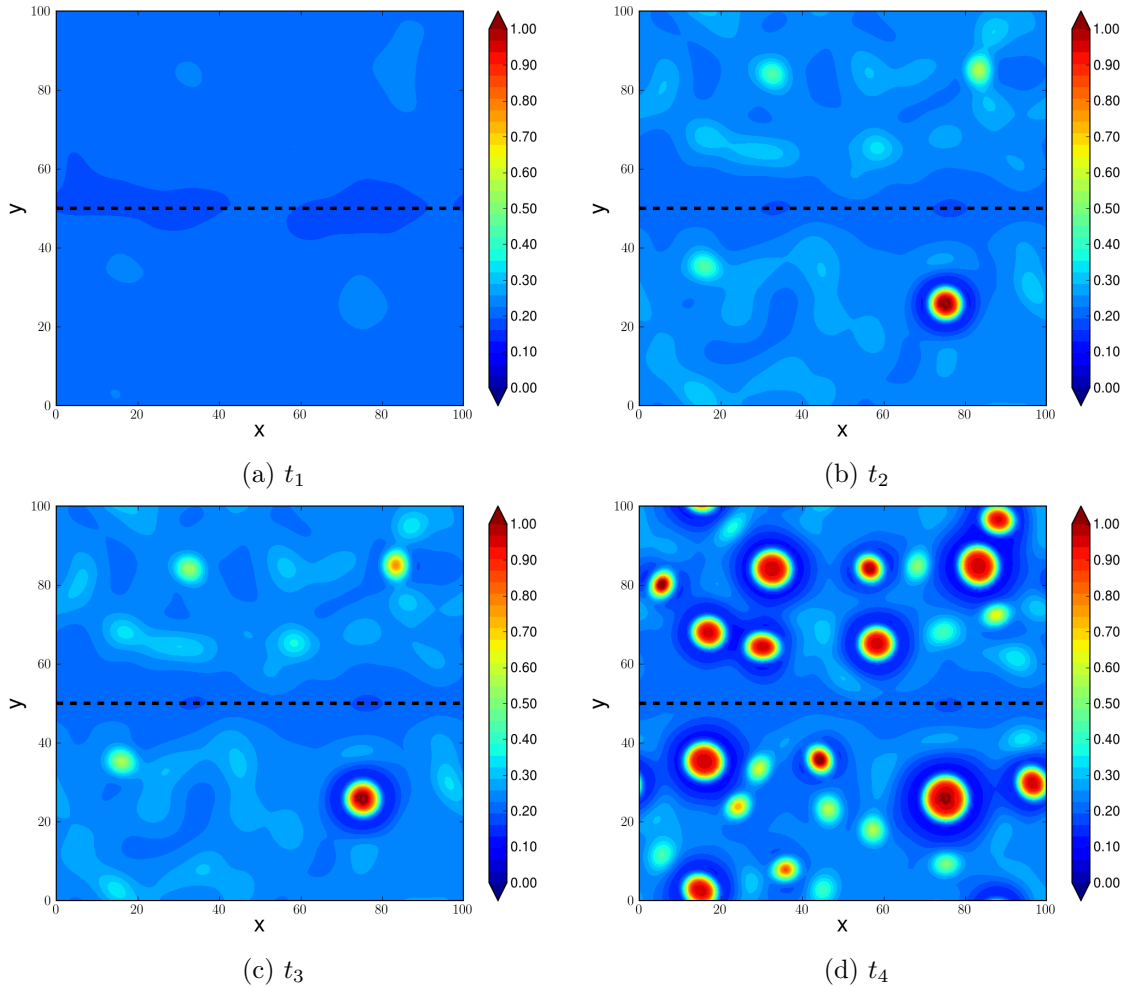


Figure 5.16: Evolution of the vacancy concentration in a bilayer with layer thickness 100 nm. One can observe a small denuded zone close to the interface, represented by a dotted black line.

as seen using HRTEM in fig. 5.3. It is likely that this determines the shearable character of the interface [77, 122] and its ability to absorb or allow the transmission of dislocations [78]. For this reason, the crystal plasticity model has been enhanced, by adding an interface affected zone, where dislocations can be absorbed. Furthermore, in this region the interface can be treated as an extra slip plane to model its shearable character. The model predicts a softer response if the shearable model is used instead of the hard one [108]. However, the precise influence of the dislocation recovery term is still to be studied.

Second, the evolution of point defects inside a multilayer has been studied using a Cahn-Hilliard framework to model nucleation and growth of voids under irradiation. It is known that interfaces can act as preferential zones for point defects recombination and can also act as a sink. As for as Cu-Nb interfaces is concerned, it was shown in [70, 76] that interface interactions with defects were very complex and vary in space at the nano scale. In particular, it was shown that the interstitial emission and recombination events are likely to be the origin of the interface stability under irradiation. At the present nano-scale, this process has been modelled as a recombination term $K_{iv}c^i c^v$ in the balance equations for SIA and vacancies, preferentially active in the interface affected zone. This model has allowed to successfully simulate the void denuded zone observed close to the interfaces. It is different to the one proposed in [86, 7], on mainly

Figure 5.17: Video of the evolution of the vacancy concentration in a bilayer with layer thickness 100 nm. One can observe a small denuded zone close to the interface, represented by a dotted black line.

three points. First, the present model introduces possible complex mechanical couplings with diffusion, which for instance, in the presence of defects sinks, allows to model grain boundary deformation. Second, no phase field is considered here, and only the gradient of the vacancy concentration is included in the free energy: this reduces the number of degrees of freedom while still being able to model void nucleation and growth. Finally, it has been applied to multilayer interfaces, instead of grain boundaries, which have a different behaviour. Even if voids-denuded zones are observed around both grain boundaries and multilayer interfaces, voids can be seen inside the grain boundaries themselves [60] (and not reproduced in [86, 7]), but not in layer interfaces. The presence of voids in the grain boundary remains a modeling problem. A possible solution may be to introduce a grain boundary energy in the model. In the present work, a parametric study, investigating the influence of the sink and recombination terms as well as the interface width remains to be performed. The layers were assumed to have identical material properties. In reality, diffusion is slower in niobium and voids are mainly observed in the copper layers [59].

Finally, the framework presented in this chapter and in Chapter 4 includes stress-diffusion couplings: first due to the relaxation around voids and vacancy, and second, due to inelastic deformations arising from the gradient of the vacancy flux. The influence on kinetics, mechanical behaviour and void distribution of such a coupling has not been investigated here due to time constraints, but will surely constitute a promising direction for future research.

Conclusions and prospects for future work

Résumé

Le but de ce travail fut de poser un cadre thermodynamique, à l'échelle continue, permettant l'étude du comportement mécanique de nano multicouches sous irradiation, couplé à la diffusion. Les résultats obtenus se classent dans trois catégories: couplage mécanique-diffusion, nucléation et croissance de cavités, et comportement mécanique de systèmes Cu-Nb.

Dans la littérature, s'il est couramment accepté que les contraintes influencent la diffusion, la réciproque est souvent négligée. L'introduction d'une déformation libre dépendant de la concentration permet d'obtenir un premier couplage, en modifiant le potentiel chimique avec des termes proportionnels à la contrainte. Un choix judicieux de cette déformation permet de différencier la contribution du grain de celle du joint de grains, et d'obtenir le potentiel de Herring. Ainsi, toute contrainte appliquée au polycristal provoque une hétérogénéité de potentiel, et donc déclenche un flux de lacunes. On montre que ce flux de lacunes est lié à la vitesse de déformation de fluage. Des simulations éléments finis ont été réalisées et mettent en évidence les points suivants:

- Des hétérogénéités fortes sont prédites au niveau intra granulaire, en particulier près des points triples.*
- L'anisotropie élastique, en favorisant l'apparition de gradients de contrainte, mène à une vitesse de déformation de fluage plus élevé.*
- Les dépendances classiques de la vitesse de fluage à la taille de grain et à la contrainte sont obtenues, à savoir $\dot{\epsilon} = f(\sigma, d_g^{-2})$.*
- Une transition fluage diffusion - fluage dislocation est prédite par le modèle, en accord avec les observations expérimentales.*

Afin de modéliser l'évolution de cavité, un modèle de Cahn-Hilliard a été utilisé et couplé à la mécanique. Les équations de diffusion ont en outre été modifiées afin de rendre compte

des interactions lacunes-interstitiels et défauts ponctuels - interfaces. Lors de simulations de croissance d'une cavité, il a été mis en évidence que les contraintes générées lors de la croissance n'avaient en pratique pas d'influence sur la cinétique de croissance. Ce modèle a été appliqué à un nano multi-couches irradié. Conformément aux observations expérimentales, une zone dénuée de cavités est observée près des interfaces entre les couches.

Enfin, un modèle mécanique a été développé et appliqué à un système Cu-Nb. Le concept de zone affectée par l'interface a permis de traiter de manière rudimentaire l'interaction des dislocations avec les interfaces. Différentes orientations relatives entre les couches de cuivre et niobium ont été simulées afin d'obtenir des courbes de traction, en calibrant le modèle sur un système $\{112\}\langle 110\rangle$ Cu // $\{112\}\langle 111\rangle$ Nb dont les résultats expérimentaux sont disponibles. Une déformée fortement 3D est en outre prédite. Le modèle peut être complété afin de rendre compte du transfert du glissement à l'interface en fonction de l'orientation relative des couches, ce qui devrait avoir une influence importante lors de simulations de laminage.

The goal of this work has been to derive a thermodynamics continuum framework to study the irradiation behaviour of nanocrystalline multilayers, whereby the mechanical behaviour is explicitly coupled to vacancy diffusion. As vacancies and self interstitials (SIA) are the primary defects produced by irradiation, their diffusion in a heterogeneous stress field has first been studied (Chapter 2). The proposed framework was then extended, in order to obtain the detailed strain field inside the grains, arising from vacancy motion and leading to creep (Chapter 3). Next, a Cahn-Hilliard approach was incorporated, allowing to simulate void nucleation and growth due to irradiation (Chapter 4). Finally, the framework was applied to the study of Cu-Nb multilayers, demonstrating, among others, the ability of the model to reproduce experimental stress-strain curves and void-denuded zones (Chapter 5).

The main results fall into three categories: coupled stress-diffusion, void nucleation and growth, and mechanical behaviour of Cu-Nb multilayers.

6.1 Coupling stress, strain, and diffusion of point defects

It is commonly accepted in the literature that stress influences the diffusion of point defects. However, the influence of point defects on stress and strain is often neglected. Usually, to obtain the equilibrium stress and composition fields, a coupled solution of the equations governing mechanical and chemical equilibrium is required. As Cahn and Larché demonstrated thirty years ago for an elastic behaviour, it is however possible to solve a modified mechanical problem alone, using open system elastic constants derived at constant diffusion potential. The technique also relies on the definition of a concentration dependent eigenstrain, which introduces a stress-dependent term in the diffusion potential. The mechanical solution is then used to calculate analytically the concentration field. In the present work, it has been shown that the procedure can be extended to plasticity in a straightforward manner. When the vacancy concentration remains below 0.1, one can then significantly reduce computational time by solving only the mechanical problem of interest to obtain the equilibrium coupled solution. The transient solutions were obtained through the fully coupled finite element implementation.

When using experimental techniques like the grid method to obtain strain fields, one tracks the displacement of group of atoms. In the present continuum mechanics approach, the material point has been chosen to be this group of atoms. Since the most probable way for an atom to move on a lattice site is to exchange places with a vacancy, it became clear that deformation could be related to vacancy diffusion. First of all, a thermodynamically-consistent diffusion-stress

coupling framework has been developed for elasto-viscoplastic solids. It is known since Herring [63] that the diffusion potential in grain boundaries is modified by the normal component of the traction vector acting on the grain boundary surface. This difference of potential between grain boundaries leads to vacancy diffusion, which, in turn, leads to creep. Grain boundaries have then been explicitly introduced in present model, using a static phase field. With a new definition of the eigenstrain related to the normal of the grain boundary surface, the Herring diffusion potential was retrieved within the proposed framework. Hence, any mechanical loading applied to the polycrystal directly induced vacancy motion. Considerations on this vacancy motion led to a diffusional strain rate related to the gradient of the vacancy flux. Simulations have been carried out, and it has been shown that:

- Strong heterogeneities are predicted at the intragranular level, especially at triple junctions.
- Anisotropic elasticity and dislocation-induced plasticity promote the diffusion of vacancies and lead to higher diffusional strain rates, by developing stress gradients within the polycrystal.
- Classical macroscopic dependence of strain-rate on stress and grain size, that is $\dot{\epsilon} = f(\sigma, d_g^{-2})$, is obtained.
- The model predicts a smooth transition from diffusion dominated to dislocation dominated regime, depending on level of the applied stress, as observed experimentally in copper [127].

As stated above, incompatibilities arise, which should be accommodated by GB sliding, especially at triple junctions. The corresponding formulations could be introduced in the proposed model. Such approaches also account for GB opening and cracking, including cavitation at triple junctions. The present work concentrated on the diffusion induced creep strain contributions. The combination of diffusion and GB sliding and opening processes presents a challenging task of future work.

6.2 Void nucleation and growth in irradiated crystalline materials

During irradiation, when vacancies are not evacuated at a sufficient rate, their average concentration increases, and eventually exceeds a critical value, leading to void nucleation and growth. In this work, a Cahn-Hilliard approach has been relied upon to model these phenomena. A non-convex free energy has been chosen to define two phases in the material: solid and void. It has been stressed that the choice of mobility must depend on the choice of homogeneous energy potential, as some cases may lead to infinite value of the flux in the metal/void interface. The use of a concentration-dependent eigenstrain yields a modified Cahn-Hilliard equation, whereby the kinetics is influenced by stress and by the difference of elastic stored energy between the two phases. It has been shown that the coupled formulation slightly increases the growth kinetics of a single void.

The model has then been applied to the irradiation of a multilayer, where layer interfaces act as preferential zones for point defects recombination. The balance equations for point defects have hence been modified to take this process into account, localised in a zone of finite width. A simulation of irradiation of a multilayer has then been performed. Nucleation of voids is effectively observed in the bulk when the vacancy concentration becomes greater than the spinodal value, but the interface zone remains void free. This qualitatively matches the experimentally

observed void-denuded zones. In order to obtain a quantitative agreement, the main parameters of the model - the defects recombination rate and the layer interface affected zone width - need to be adjusted. Furthermore, the influence of the mechanical coupling on the kinetics and voids distribution remains to be investigated, and the associated void swelling quantified.

6.3 Mechanical behaviour of Cu-Nb multilayers

In addition to self-healing properties, the multilayers also exhibit outstanding mechanical properties. As a first step, the influence of the crystallographic character of the interface on the mechanical behaviour has been investigated, using a standard crystal plasticity model. Four Cu-Nb orientation relationships have been studied, progressively rotating the crystals toward $\{112\}\langle 110\rangle$ Cu // $\{112\}\langle 111\rangle$ Nb, which is the interface orientation of Cu-Nb multilayers processed by accumulated roll bonding (ARB) techniques. The experimental bulk tensile stress-strain curves in [20] have been reproduced numerically on a 3D periodic bilayer, and show that the multilayer adopts a “v” shape. The model also predicts possible higher yield stresses for $\{100\}\langle 001\rangle$ Cu // $\{112\}\langle 110\rangle$ Nb, an interface which is nevertheless not encountered in reality. However, the orientation relationship alone is not sufficient to describe the mechanical behaviour of multilayers systems. The computational power nowadays enable modelling numerically at the continuum nano-scale the physical processes occurring in the multilayers. The metallic bilayer interface exhibit, in particular, strong interactions with dislocations. Hence the idea of proposing a crystal plasticity modeling framework that modifies the slip activity close to the interface, as proposed simultaneously in [81]. Here, the interface was treated as a crystallographic slip plane to model its shearable character [123], and acted as a dislocation recovery zone [122]. The results are qualitative, and the parameters used in the simulations should be tried and calibrated from the results of atomistic simulations and experiments. The obtained deformed shape showed no major change, and the macroscopic stress strain curves in tension and shear exhibited a lower yield stress. Finally, the interaction of dislocations with interfaces could be refined from the simple recovery term to a more elaborate model. For instance, slip transfer could be taken into account [96],[81] and references therein, and better dislocation emission treatment [95, 19]. Such detailed description should be applicable to a wider panel of interfaces, depending on processing techniques and layer thickness, to predict the macroscopic mechanical behaviour.

6.4 Long-term perspectives

The numerical techniques presented here rely on standard finite elements methods. A micro-morphic approach has been followed to avoid the use of higher order finite elements, otherwise necessary for a Cahn-Hilliard model [55]. However, in the proposed model, it is required to compute the gradient of the strain tensor and of the vacancy flux. Currently, those quantities, which are computed at the Gauss points, are extrapolated to the nodes in order to obtain their gradient using the derivative of the shape functions, and their gradient interpolated again back to the Gauss points. If this seems numerically acceptable for simple problems such as the ones of Chapter 2, it is certainly not for the fully coupled stress-diffusion-Cahn-Hilliard framework. Furthermore, it is possible to develop an approach allowing the use of symmetric solver [84, 85], which is not the case here. Presently, the numerical implementation requires the use of a non symmetric solvers, more costly in memory and CPU time. Such implementation would certainly ease the computations, which are extremely non-linear, especially when coupled to mechanics and irradiation. Finally, the local behaviour integration benefits from important CPU multi-threading, for simulations with a large number of finite elements. It would then be interesting

to investigate a possible massive parallelisation for the behaviour integration using GP-GPU techniques [42, 71, 83].

Fundamentals aspects of coupled stress-diffusion and irradiation modeling still require some further thoughts. First, the concept of sinks for point defects at interfaces is questionable at this scale, despite it being used in the literature. It introduces mass loss in the system if the volume change is not taken into account and, more importantly, does not describe the physical process in a realistic manner. For that reason, this idea has not been used in the presented simulations: interfaces has been modeled only as a SIA-vacancy recombination zone. Second, the fundamental thermodynamics aspects of the proposed diffusion creep model, relying on the gradient of the vacancy flux, remains to be explored, in particular regarding dissipation. Finally, it is know that, under irradiation, voids are observed inside grain boundaries, even in presence of a void-denuded zone. To account for this process in the model, one could introduce a grain boundary energy, so that void nucleation becomes energetically favorable by replacing the grain boundary energy with a void surface energy of lower magnitude, as was done for He in Cu-Nb systems [67].

As for the multilayers, other systems than Cu-Nb have shown promising properties [50, 90]. In the Radinterfaces project, many systems has been experimentally produced and mechanically characterised. For example, deposited Cu-W coatings have shown fully crystalline interfaces down to a 5 nm layer-thickness, and Zr-Nb systems exhibited highly crystalline, columnar growth, and a well ordered interface. The framework proposed in the present PhD thesis can be applied to such systems, as the physical principles remains the same as for Cu-Nb multilayer systems.

Derivation of open system elastic constants

Contrary to the approach presented in [28], the derivation is here based on the enthalpy, $h(c, \underline{\sigma}, p, \underline{\alpha})$, for simplicity. The diffusion potential and the strain tensor components can be expressed as

$$\mu = \left. \frac{\partial h}{\partial c} \right|_{\sigma_{ij}}, \quad \text{and} \quad -\epsilon_{ij} = \left. \frac{\partial h}{\partial \sigma_{ij}} \right|_c. \quad (\text{A.1})$$

From equation (A.1), the so-called Maxwell relation can be obtained:

$$\left. \frac{\partial \mu}{\partial \sigma_{kl}} \right|_c = \frac{\partial^2 h}{\partial \sigma_{kl} \partial c} = \frac{\partial^2 h}{\partial c \partial \sigma_{kl}} = - \left. \frac{\partial \epsilon_{kl}}{\partial c} \right|_{\sigma_{kl}} \quad (\text{A.2})$$

Recalling that the strain can be partitioned as,

$$\underline{\epsilon} = \underline{\epsilon}^e + \underline{\underline{H}}(c - c_{ref}) + \underline{\epsilon}_{ref}^* + \underline{\epsilon}^p \quad (\text{A.3})$$

and expressing the elastic strain tensor in terms of the stress tensor and the compliance tensor, $\underline{\underline{S}} = \underline{\underline{C}}^{-1}$, yields,

$$\underline{\epsilon} = \underline{\underline{S}} : \underline{\sigma} + \underline{\underline{H}}(c - c_{ref}) + \underline{\epsilon}_{ref}^* + \underline{\epsilon}^p \quad (\text{A.4})$$

Differentiating the strain components at fixed internal variables,

$$d\epsilon_{ij} = \left. \frac{\partial \epsilon_{ij}}{\partial \sigma_{kl}} \right|_c d\sigma_{kl} + \left. \frac{\partial \epsilon_{ij}}{\partial c} \right|_{\sigma_{ij}} dc, \quad (\text{A.5})$$

and the diffusion potential, μ ,

$$d\mu = \left. \frac{\partial \mu}{\partial \sigma_{kl}} \right|_c d\sigma_{kl} + \left. \frac{\partial \mu}{\partial c} \right|_{\sigma_{ij}} dc, \quad (\text{A.6})$$

solving for dc in eq. (A.6),

$$dc = \left(d\mu - \frac{\partial\mu}{\partial\sigma_{kl}} \Big|_c d\sigma_{kl} \right) \left(\frac{\partial\mu}{\partial c} \Big|_{\sigma_{ij}} \right)^{-1}, \quad (\text{A.7})$$

and substituting the Maxwell relation into equation (A.7) leaves,

$$dc = \left(d\mu + \frac{\partial\epsilon_{kl}}{\partial c} \Big|_{\sigma_{kl}} d\sigma_{kl} \right) \left(\frac{\partial\mu}{\partial c} \Big|_{\sigma_{ij}} \right)^{-1}. \quad (\text{A.8})$$

Finally, substituting equation (A.8) into equation (A.5) and re-arranging yields,

$$d\epsilon_{ij} = \left(\frac{\partial\epsilon_{ij}}{\partial\sigma_{kl}} \Big|_c + \frac{\partial\epsilon_{ij}}{\partial c} \Big|_{\sigma_{ij}} \frac{\partial\epsilon_{kl}}{\partial c} \Big|_{\sigma_{kl}} \left(\frac{\partial\mu}{\partial c} \Big|_{\sigma_{ij}} \right)^{-1} \right) d\sigma_{kl} + \frac{\partial\epsilon_{ij}}{\partial c} \Big|_{\sigma_{ij}} d\mu. \quad (\text{A.9})$$

Cahn and Larché [27] defined the term in brackets in equation (A.9) as the *open system compliance* at a constant potential μ , or \mathcal{S}_{ijkl}^0 . Thus,

$$\mathcal{S}_{ijkl}^0 = \frac{\partial\epsilon_{ij}}{\partial\sigma_{kl}} \Big|_{\mu} = \frac{\partial\epsilon_{ij}}{\partial\sigma_{kl}} \Big|_c + \left(\frac{\partial\epsilon_{ij}}{\partial c} \Big|_{\sigma_{ij}} \frac{\partial\epsilon_{kl}}{\partial c} \Big|_{\sigma_{kl}} \right) \left(\frac{\partial\mu}{\partial c} \Big|_{\sigma_{ij}} \right)^{-1}. \quad (\text{A.10})$$

The expression for the open system compliance defined above can be obtained by recalling the following relations,

$$\frac{\partial\epsilon_{ij}}{\partial\sigma_{kl}} \Big|_c = \underset{\sim}{\mathfrak{S}}_{ijkl}, \quad \text{and} \quad \frac{\partial\epsilon_{ij}}{\partial c} \Big|_{\sigma_{kl}} = H_{ij}. \quad (\text{A.11})$$

Then, equation (2.40) is retrieved.

Finite element derivatives

This appendix contains the stiffness matrices components necessary for a finite element implementation of the Cahn Hilliard framework. The diffusion potential and the free energy derivatives with respect to the state variables are given in the next appendix, for a given choice of free energy density.

B.1 Terms K_{uX}

$$\frac{\partial \underline{\sigma}}{\partial \underline{\xi}} = h \frac{\partial^2 f_{mech}^\alpha}{\partial \underline{\xi}^{e-\alpha^2}} + \bar{h} \frac{\partial^2 f_{mech}^\beta}{\partial \underline{\xi}^{e-\beta^2}} \quad (\text{B.1})$$

$$\frac{\partial \underline{\sigma}}{\partial c^i} = 0 \quad (\text{B.2})$$

$$\frac{\partial \underline{\sigma}}{\partial c^v} = \frac{\partial h}{\partial \phi} \frac{\partial \phi}{\partial c^v} (\underline{\sigma}^\alpha - \underline{\sigma}^\beta) \quad (\text{B.3})$$

$$\frac{\partial \underline{\sigma}}{\partial c_\chi} = 0 \quad (\text{B.4})$$

B.2 Terms $K_{c^i X}$

$$\begin{aligned} \frac{\partial \underline{\mathbf{J}}^i}{\partial \underline{\xi}} = & -L^i \left(\frac{\partial^2 \mu^i}{\partial c^i \partial \underline{\xi}} \underline{\nabla} c^i + \frac{\partial^2 \mu^i}{\partial c^v \partial \underline{\xi}} \underline{\nabla} c^v + \frac{\partial^2 \mu^i}{\partial c_\chi \partial \underline{\xi}} \underline{\nabla} c_\chi \right. \\ & \left. + \frac{\partial^2 \mu^i}{\partial \phi^{GB} \partial \underline{\xi}} \underline{\nabla} \phi^{GB} + \frac{\partial^2 \mu^i}{\partial \underline{\xi} \partial \underline{\xi}} : \underline{\nabla} \underline{\xi} + \frac{\partial \mu^i}{\partial \underline{\xi}} \underline{\nabla} \right) \end{aligned} \quad (\text{B.5})$$

$$\begin{aligned} \frac{\partial \underline{\mathbf{J}}^i}{\partial c^i} = & -\frac{\partial L^i}{\partial c^i} \underline{\nabla} \mu^i - L^i \left(\frac{\partial^2 \mu^i}{\partial c^{i2}} \underline{\nabla} c^i + \frac{\partial \mu^i}{\partial c^i} \underline{\nabla} + \frac{\partial^2 \mu^i}{\partial c^i \partial c^v} \underline{\nabla} c^v + \frac{\partial^2 \mu^i}{\partial c^i \partial c_\chi} \underline{\nabla} c_\chi \right. \\ & \left. + \frac{\partial^2 \mu^i}{\partial c^i \partial \phi^{GB}} \underline{\nabla} \phi^{GB} + \frac{\partial^2 \mu^i}{\partial c^i \partial \underline{\xi}} : \underline{\nabla} \underline{\xi} \right) \end{aligned} \quad (\text{B.6})$$

$$\begin{aligned} \frac{\partial \underline{\mathbf{J}}^i}{\partial c^v} = & -\frac{\partial L^i}{\partial c^v} \underline{\nabla} \mu^i - L^i \left(\frac{\partial^2 \mu^i}{\partial c^i \partial c^v} \underline{\nabla} c^i + \frac{\partial^2 \mu^i}{\partial c^{v2}} \underline{\nabla} c^v + \frac{\partial \mu^i}{\partial c^v} \underline{\nabla} + \frac{\partial^2 \mu^i}{\partial c^v \partial c_\chi} \underline{\nabla} c_\chi \right. \\ & \left. + \frac{\partial^2 \mu^i}{\partial c^v \partial \phi^{\text{GB}}} \underline{\nabla} \phi^{\text{GB}} + \frac{\partial^2 \mu^i}{\partial c^v \partial \underline{\boldsymbol{\xi}}} : \underline{\nabla} \underline{\boldsymbol{\xi}} \right) \end{aligned} \quad (\text{B.7})$$

$$\begin{aligned} \frac{\partial \underline{\mathbf{J}}^i}{\partial c_\chi} = & -\frac{\partial L^i}{\partial c_\chi} \underline{\nabla} \mu^i - L^i \left(\frac{\partial^2 \mu^i}{\partial c^i \partial c_\chi} \underline{\nabla} c^i + \frac{\partial^2 \mu^i}{\partial c^v \partial c_\chi} \underline{\nabla} c^v + \frac{\partial^2 \mu^i}{\partial c_\chi^2} \underline{\nabla} c_\chi + \frac{\partial \mu^i}{\partial c_\chi} \underline{\nabla} + \frac{\partial \mu^i}{\partial c_\chi} \underline{\nabla} \right. \\ & \left. + \frac{\partial^2 \mu^i}{\partial c_\chi \partial \phi^{\text{GB}}} \underline{\nabla} \phi^{\text{GB}} + \frac{\partial^2 \mu^i}{\partial c_\chi \partial \underline{\boldsymbol{\xi}}} : \underline{\nabla} \underline{\boldsymbol{\xi}} \right) \end{aligned} \quad (\text{B.8})$$

B.3 Terms $K_{c^v X}$

$$\begin{aligned} \frac{\partial \underline{\mathbf{J}}^v}{\partial \underline{\boldsymbol{\xi}}} = & -L^v \left(\frac{\partial^2 \mu^v}{\partial c^i \partial \underline{\boldsymbol{\xi}}} \underline{\nabla} c^i + \frac{\partial^2 \mu^v}{\partial c^v \partial \underline{\boldsymbol{\xi}}} \underline{\nabla} c^v + \frac{\partial^2 \mu^v}{\partial c_\chi \partial \underline{\boldsymbol{\xi}}} \underline{\nabla} c_\chi \right. \\ & \left. + \frac{\partial^2 \mu^v}{\partial \phi^{\text{GB}} \partial \underline{\boldsymbol{\xi}}} \underline{\nabla} \phi^{\text{GB}} + \frac{\partial^2 \mu^v}{\partial \underline{\boldsymbol{\xi}} \partial \underline{\boldsymbol{\xi}}} : \underline{\nabla} \underline{\boldsymbol{\xi}} + \frac{\partial \mu^v}{\partial \underline{\boldsymbol{\xi}}} \underline{\nabla} \right) \end{aligned} \quad (\text{B.9})$$

$$\begin{aligned} \frac{\partial \underline{\mathbf{J}}^v}{\partial c^i} = & -\frac{\partial L^v}{\partial c^i} \underline{\nabla} \mu^v - L^v \left(\frac{\partial^2 \mu^v}{\partial c^{i2}} \underline{\nabla} c^i + \frac{\partial^2 \mu^v}{\partial c^i \partial c^v} \underline{\nabla} c^v + \frac{\partial^2 \mu^v}{\partial c^i \partial c_\chi} \underline{\nabla} c_\chi \right. \\ & \left. + \frac{\partial^2 \mu^v}{\partial c^i \partial \phi^{\text{GB}}} \underline{\nabla} \phi^{\text{GB}} + \frac{\partial^2 \mu^v}{\partial c^i \partial \underline{\boldsymbol{\xi}}} : \underline{\nabla} \underline{\boldsymbol{\xi}} + \frac{\partial \mu^v}{\partial c^i} \underline{\nabla} \right) \end{aligned} \quad (\text{B.10})$$

$$\begin{aligned} \frac{\partial \underline{\mathbf{J}}^v}{\partial c^v} = & -\frac{\partial L^v}{\partial c^v} \underline{\nabla} \mu^v - L^v \left(\frac{\partial^2 \mu^v}{\partial c^i \partial c^v} \underline{\nabla} c^i + \frac{\partial^2 \mu^v}{\partial c^{v2}} \underline{\nabla} c^v + \frac{\partial \mu^v}{\partial c^v} \underline{\nabla} + \frac{\partial^2 \mu^v}{\partial c^v \partial c_\chi} \underline{\nabla} c_\chi \right. \\ & \left. + \frac{\partial^2 \mu^v}{\partial c^v \partial \phi^{\text{GB}}} \underline{\nabla} \phi^{\text{GB}} + \frac{\partial^2 \mu^v}{\partial c^v \partial \underline{\boldsymbol{\xi}}} : \underline{\nabla} \underline{\boldsymbol{\xi}} \right) \end{aligned} \quad (\text{B.11})$$

$$\begin{aligned} \frac{\partial \underline{\mathbf{J}}^v}{\partial c_\chi} = & -\frac{\partial L^v}{\partial c_\chi} \underline{\nabla} \mu^v - L^v \left(\frac{\partial^2 \mu^v}{\partial c^i \partial c_\chi} \underline{\nabla} c^i + \frac{\partial^2 \mu^v}{\partial c^v \partial c_\chi} \underline{\nabla} c^v + \frac{\partial^2 \mu^v}{\partial c_\chi^2} \underline{\nabla} c_\chi + \frac{\partial \mu^v}{\partial c_\chi} \underline{\nabla} \right. \\ & \left. + \frac{\partial^2 \mu^v}{\partial c_\chi \partial \phi^{\text{GB}}} \underline{\nabla} \phi^{\text{GB}} + \frac{\partial^2 \mu^v}{\partial c_\chi \partial \underline{\boldsymbol{\xi}}} : \underline{\nabla} \underline{\boldsymbol{\xi}} \right) \end{aligned} \quad (\text{B.12})$$

B.4 Terms $K_{c_\chi X}$

$$\frac{\partial \pi}{\partial \underline{\boldsymbol{\xi}}} = -\frac{\partial^2 \psi_{\text{mech}}}{\partial c_\chi \partial \underline{\boldsymbol{\xi}}} \quad (\text{B.13})$$

$$\frac{\partial \underline{\boldsymbol{\xi}}}{\partial \underline{\boldsymbol{\xi}}} = -\frac{\partial^2 \psi}{\partial \underline{\boldsymbol{\xi}} \partial c_\chi} = 0 \quad (\text{B.14})$$

$$\frac{\partial \pi}{\partial c^i} = -\frac{\partial^2 \psi}{\partial c^i \partial c_\chi} \quad (\text{B.15})$$

$$\frac{\partial \underline{\boldsymbol{\xi}}}{\partial c^i} = 0 \quad (\text{B.16})$$

$$\frac{\partial \pi}{\partial c^v} = -\frac{\partial^2 \psi}{\partial c^v \partial c_\chi} \quad (\text{B.17})$$

$$\frac{\partial \underline{\xi}}{\partial c^v} = 0 \quad (\text{B.18})$$

$$\frac{\partial \pi}{\partial c_\chi} = -\frac{\partial^2 \psi}{\partial c_\chi^2} \quad (\text{B.19})$$

$$\frac{\partial \underline{\xi}}{\partial c_\chi} = \frac{\partial^2 \psi}{\partial \underline{\nabla} c_\chi^2} \frac{\partial \underline{\nabla} c_\chi}{\partial c_\chi} = \alpha \underline{\nabla} \quad (\text{B.20})$$

Cahn Hilliard framework

C.1 Normalisation

In order to ease the numerical calculations, the normalisation of all the equations is performed, through the input parameters. For a logarithmic chemical free energy, a reference energy, E_{norm} , diffusivity, D_{norm} , length, L_{norm} , and time, T_{norm} , are defined as

$$\begin{aligned} E_{norm} &= \frac{RT}{\Omega_0} \\ D_{norm} &= D^{v,\beta} \\ L_{norm} &= \lambda \\ T_{norm} &= \frac{L_{norm}^2}{D_{norm}} \end{aligned} \quad (C.1)$$

Then, the free energy is expressed as:

$$\bar{\psi} = c^v \ln c^v + (1 - c^v) \ln(1 - c^v) + \bar{\omega} c^v (1 - c^v) + \frac{1}{2} \bar{\alpha} |\nabla c^v|^2 + \bar{H}_\chi (c^v - c_\chi) + \bar{\psi}_{0,i} + \bar{\psi}_{mech}, \quad (C.2)$$

with,

$$\begin{aligned} \bar{\omega} &= \frac{\omega}{E_{norm}} \\ \bar{\alpha} &= \frac{\alpha}{E_{norm} L_{norm}^2} \\ \tilde{\alpha} &= \frac{\alpha}{E_{norm}} \\ \bar{H}_\chi &= \frac{H_\chi}{E_{norm}} \\ \bar{E}^k &= \frac{E^k}{E_{norm}}, \text{ with } k = \{\alpha, \beta\} \\ \bar{k}^i &= \frac{k^i}{E_{norm}} \end{aligned} \quad (C.3)$$

C.2 Derivatives needed for numerical implementation

This appendix contains the derivatives present in the stiffness matrices, used for a finite element implementation of the fully coupled Cahn-Hilliard framework Chapter 4. They are first given for the diffusion potential in term of free energy derivatives. Then the free energy derivatives themselves are given.

C.2.1 Diffusion potential

The derivatives of the diffusion potentials with respect to the state variables are given below.

$$\underline{\nabla} \mu^i = \frac{\partial \mu^i}{\partial \underline{\xi}} \underline{\nabla} \underline{\xi} + \frac{\partial \mu^i}{\partial c^i} \underline{\nabla} c^i + \frac{\partial \mu^i}{\partial c^v} \underline{\nabla} c^v + \frac{\partial \mu^i}{\partial c_\chi} \underline{\nabla} c_\chi + \frac{\partial \mu^i}{\partial \phi^{\text{GB}}} \underline{\nabla} \phi^{\text{GB}} \quad (\text{C.4})$$

$$\underline{\nabla} \mu^v = \frac{\partial \mu^v}{\partial \underline{\xi}} \underline{\nabla} \underline{\xi} + \frac{\partial \mu^v}{\partial c^i} \underline{\nabla} c^i + \frac{\partial \mu^v}{\partial c^v} \underline{\nabla} c^v + \frac{\partial \mu^v}{\partial c_\chi} \underline{\nabla} c_\chi + \frac{\partial \mu^v}{\partial \phi^{\text{GB}}} \underline{\nabla} \phi^{\text{GB}} \quad (\text{C.5})$$

C.2.1.1 First order

Interstitials

$$\frac{\partial \mu^i}{\partial \underline{\xi}} = h \left(-\tilde{\eta}^{i,\alpha} : \frac{\partial^2 f_{\text{mech}}^\alpha}{\partial \underline{\xi}^{e-\alpha} \partial \underline{\xi}^{e-\alpha}} \right) + \bar{h} \left(-\tilde{\eta}^{i,\beta} : \frac{\partial^2 f_{\text{mech}}^\beta}{\partial \underline{\xi}^{e-\beta} \partial \underline{\xi}^{e-\beta}} \right) \quad (\text{C.6})$$

$$\frac{\partial \mu^i}{\partial c^i} = \frac{\partial^2 \psi}{\partial c^{i2}} = \frac{\partial^2 \psi_0}{\partial c^{i2}} \quad (\text{C.7})$$

$$\begin{aligned} \frac{\partial \mu^i}{\partial c^v} &= \frac{\partial^2 \psi}{\partial c^i \partial c^v} + \frac{\partial h}{\partial c^v} \left(-\tilde{\eta}^{i,\alpha} : \frac{\partial f_{\text{mech}}^\alpha}{\partial \underline{\xi}^{e-\alpha}} + \tilde{\eta}^{i,\beta} : \frac{\partial f_{\text{mech}}^\beta}{\partial \underline{\xi}^{e-\beta}} \right) \\ &= \frac{\partial^2 \psi_0}{\partial c^i \partial c^v} + \frac{\partial h}{\partial c^v} \left(-\tilde{\eta}^{i,\alpha} : \frac{\partial f_{\text{mech}}^\alpha}{\partial \underline{\xi}^{e-\alpha}} + \tilde{\eta}^{i,\beta} : \frac{\partial f_{\text{mech}}^\beta}{\partial \underline{\xi}^{e-\beta}} \right) \end{aligned} \quad (\text{C.8})$$

$$\frac{\partial \mu^i}{\partial c_\chi} = \frac{\partial^2 \psi}{\partial c^i \partial c_\chi} = 0 \quad (\text{C.9})$$

$$\begin{aligned} \frac{\partial \mu^i}{\partial \phi^{\text{GB}}} &= \frac{\partial^2 \psi}{\partial c^i \partial \phi^{\text{GB}}} - h \frac{\partial \tilde{\eta}^{i,\alpha}}{\partial \phi^{\text{GB}}} : \frac{\partial f_{\text{mech}}^\alpha}{\partial \underline{\xi}^{e-\alpha}} - \bar{h} \frac{\partial \tilde{\eta}^{i,\beta}}{\partial \phi^{\text{GB}}} : \frac{\partial f_{\text{mech}}^\beta}{\partial \underline{\xi}^{e-\beta}} \\ &= -h \frac{\partial \tilde{\eta}^{i,\alpha}}{\partial \phi^{\text{GB}}} : \frac{\partial f_{\text{mech}}^\alpha}{\partial \underline{\xi}^{e-\alpha}} - \bar{h} \frac{\partial \tilde{\eta}^{i,\beta}}{\partial \phi^{\text{GB}}} : \frac{\partial f_{\text{mech}}^\beta}{\partial \underline{\xi}^{e-\beta}} \end{aligned} \quad (\text{C.10})$$

Vacancies

$$\frac{\partial \mu^v}{\partial \underline{\xi}} = \frac{\partial^2 \psi}{\partial c^v \partial \underline{\xi}} - h \tilde{\eta}^{v,\alpha} : \frac{\partial^2 f_{\text{mech}}^\alpha}{\partial \underline{\xi}^{e-\alpha} \partial \underline{\xi}^{e-\alpha}} - \bar{h} \tilde{\eta}^{v,\beta} : \frac{\partial^2 f_{\text{mech}}^\beta}{\partial \underline{\xi}^{e-\beta} \partial \underline{\xi}^{e-\beta}} \quad (\text{C.11})$$

$$\frac{\partial \mu^v}{\partial c_\chi} = \frac{\partial^2 \psi}{\partial c^v \partial c_\chi} = \frac{\partial^2 \psi_{\text{pen}}}{\partial c^v \partial c_\chi} \quad (\text{C.12})$$

$$\frac{\partial \mu^v}{\partial c^i} = \frac{\partial^2 \psi}{\partial c^i \partial c^v} = \frac{\partial^2 \psi_0}{\partial c^i \partial c^v} \quad (\text{C.13})$$

$$\frac{\partial \mu^v}{\partial c^v} = \frac{\partial^2 \psi}{\partial c^{v2}} - \frac{\partial h}{\partial c^v} \left(\tilde{\eta}^{v,\alpha} : \frac{\partial f_{mech}^\alpha}{\partial \xi^{e-\alpha}} - \tilde{\eta}^{v,\beta} : \frac{\partial f_{mech}^\beta}{\partial \xi^{e-\beta}} \right) \quad (C.14)$$

$$\frac{\partial \mu^v}{\partial \phi^{GB}} = -h \frac{\partial \tilde{\eta}^{v,\alpha}}{\partial \phi^{GB}} : \frac{\partial f_{mech}^\alpha}{\partial \xi^{e-\alpha}} - \bar{h} \frac{\partial \tilde{\eta}^{v,\beta}}{\partial \phi^{GB}} : \frac{\partial f_{mech}^\beta}{\partial \xi^{e-\beta}} \quad (C.15)$$

C.2.1.2 Second order

Interstitials

$$\frac{\partial^2 \mu^i}{\partial c^i \partial \xi} = 0 \quad (C.16)$$

$$\frac{\partial^2 \mu^i}{\partial c^v \partial \xi} = \frac{\partial h}{\partial c^v} \left(-\tilde{\eta}^{i,\alpha} : \frac{\partial^2 f_{mech}^\alpha}{\partial \xi^{e-\alpha} \partial \xi^{e-\alpha}} + \tilde{\eta}^{i,\beta} : \frac{\partial^2 f_{mech}^\beta}{\partial \xi^{e-\beta} \partial \xi^{e-\beta}} \right) \quad (C.17)$$

$$\frac{\partial^2 \mu^i}{\partial c_\chi \partial \xi} = 0 \quad (C.18)$$

$$\frac{\partial^2 \mu^i}{\partial \xi \partial \phi^{GB}} = h \left(-\frac{\partial \tilde{\eta}^{i,\alpha}}{\partial \phi^{GB}} : \frac{\partial^2 f^\alpha}{\partial \xi^{e-\alpha} \partial \xi^{e-\alpha}} \right) + \bar{h} \left(-\frac{\partial \tilde{\eta}^{i,\beta}}{\partial \phi^{GB}} : \frac{\partial^2 f^\beta}{\partial \xi^{e-\beta} \partial \xi^{e-\beta}} \right) \quad (C.19)$$

$$\frac{\partial^2 \mu^i}{\partial \xi \partial \xi} = 0 \quad (C.20)$$

$$\frac{\partial^2 \mu^i}{\partial c^{i2}} = \frac{\partial^3 \psi}{\partial c^{i3}} = \frac{\partial^3 \psi_0}{\partial c^{i3}} \quad (C.21)$$

$$\frac{\partial^2 \mu^i}{\partial c^i \partial c^v} = \frac{\partial^3 \psi}{\partial c^{i2} \partial c^v} \quad (C.22)$$

$$\frac{\partial^2 \mu^i}{\partial c^i \partial c_\chi} = \frac{\partial^3 \psi}{\partial c^{i2} \partial c_\chi} = 0 \quad (C.23)$$

$$\begin{aligned} \frac{\partial^2 \mu^i}{\partial c^i \partial \phi^{GB}} &= \frac{\partial^3 \psi_0}{\partial c^{i2} \partial \phi^{GB}} \\ &= 0 \end{aligned} \quad (C.24)$$

$$\frac{\partial^2 \mu^i}{\partial c^{v2}} = \frac{\partial^3 \psi_0}{\partial c^{v2} \partial c^i} + \frac{\partial^2 h}{\partial c^{v2}} \left(-\tilde{\eta}^{i,\alpha} : \frac{\partial f^\alpha}{\partial \xi^{e-\alpha}} + \tilde{\eta}^{i,\beta} : \frac{\partial f^\beta}{\partial \xi^{e-\beta}} \right) \quad (C.25)$$

$$\begin{aligned} \frac{\partial^2 \mu^i}{\partial c^v \partial c_\chi} &= \frac{\partial^3 \psi_0}{\partial c^i \partial c^v \partial c_\chi} \\ &= 0 \end{aligned} \quad (C.26)$$

$$\begin{aligned} \frac{\partial^2 \mu^i}{\partial c^v \partial \phi^{GB}} &= \frac{\partial^3 \psi_0}{\partial c^i \partial c^v \partial \phi^{GB}} + \frac{\partial h}{\partial c^v} \left(-\frac{\partial \tilde{\eta}^{i,\alpha}}{\partial \phi^{GB}} : \frac{\partial f_{mech}^\alpha}{\partial \xi^{e-\alpha}} + \frac{\partial \tilde{\eta}^{i,\beta}}{\partial \phi^{GB}} : \frac{\partial f_{mech}^\beta}{\partial \xi^{e-\beta}} \right) \\ &= \frac{\partial h}{\partial c^v} \left(-\frac{\partial \tilde{\eta}^{i,\alpha}}{\partial \phi^{GB}} : \frac{\partial f_{mech}^\alpha}{\partial \xi^{e-\alpha}} + \frac{\partial \tilde{\eta}^{i,\beta}}{\partial \phi^{GB}} : \frac{\partial f_{mech}^\beta}{\partial \xi^{e-\beta}} \right) \end{aligned} \quad (C.27)$$

$$\frac{\partial^2 \mu^i}{\partial c_\chi^2} = \frac{\partial^3 \psi_0}{\partial c_\chi^2 \partial c^i} = 0 \quad (\text{C.28})$$

$$\frac{\partial^2 \mu^i}{\partial c_\chi \partial \phi^{\text{GB}}} = 0 \quad (\text{C.29})$$

Vacancies

$$\frac{\partial^2 \mu^v}{\partial c^i \partial \xi} = 0 \quad (\text{C.30})$$

$$\begin{aligned} \frac{\partial^2 \mu^v}{\partial c^v \partial \xi} &= \frac{\partial^3 \psi}{\partial c^{v2} \partial \xi} - \frac{\partial h}{\partial c^v} \left(\tilde{\eta}^{v,\alpha} : \frac{\partial^2 f_{mech}^\alpha}{\partial \xi^{e-\alpha} \partial \xi^{e-\alpha}} - \tilde{\eta}^{v,\beta} : \frac{\partial^2 f_{mech}^\alpha}{\partial \xi^{e-\beta} \partial \xi^{e-\beta}} \right) \\ &= \frac{\partial^2 h}{\partial c^{v2}} \frac{\partial f_{mech}^\alpha}{\partial \xi^{e-\alpha}} + \frac{\partial^2 \bar{h}}{\partial c^{v2}} \frac{\partial f_{mech}^\beta}{\partial \xi^{e-\beta}} - \frac{\partial h}{\partial c^v} \left(\tilde{\eta}^{v,\alpha} : \frac{\partial^2 f_{mech}^\alpha}{\partial \xi^{e-\alpha} \partial \xi^{e-\alpha}} - \tilde{\eta}^{v,\beta} : \frac{\partial^2 f_{mech}^\alpha}{\partial \xi^{e-\beta} \partial \xi^{e-\beta}} \right) \end{aligned} \quad (\text{C.31})$$

$$\frac{\partial^2 \mu^v}{\partial c_\chi \partial \xi} = 0 \quad (\text{C.32})$$

$$\frac{\partial^2 \mu^v}{\partial \xi \partial \phi^{\text{GB}}} = -h \frac{\partial \tilde{\eta}^{v,\alpha}}{\partial \phi^{\text{GB}}} : \frac{\partial^2 f_{mech}^\alpha}{\partial \xi^{e-\alpha} \partial \xi^{e-\alpha}} - \bar{h} \frac{\partial \tilde{\eta}^{v,\beta}}{\partial \phi^{\text{GB}}} : \frac{\partial^2 f_{mech}^\alpha}{\partial \xi^{e-\beta} \partial \xi^{e-\beta}} \quad (\text{C.33})$$

$$\frac{\partial^2 \mu^v}{\partial \xi \partial \xi} = \frac{\partial^3 \psi}{\partial \xi^2 \partial c^v} = \frac{\partial h}{\partial c^v} \frac{\partial^2 f_{mech}^\alpha}{\partial \xi^{e-\alpha^2}} + \frac{\partial \bar{h}}{\partial c^v} \frac{\partial^2 f_{mech}^\beta}{\partial \xi^{e-\beta^2}} \quad (\text{C.34})$$

$$\frac{\partial^2 \mu^v}{\partial c^i^2} = \frac{\partial^3 \psi_0}{\partial c^i^2 \partial c^v} \quad (\text{C.35})$$

$$\frac{\partial^2 \mu^v}{\partial c^i \partial c^v} = \frac{\partial^3 \psi_0}{\partial c^{v2} \partial c^i} \quad (\text{C.36})$$

$$\frac{\partial^2 \mu^v}{\partial c^i \partial c_\chi} = 0 \quad (\text{C.37})$$

$$\frac{\partial^2 \mu^v}{\partial c^i \partial \phi^{\text{GB}}} = 0 \quad (\text{C.38})$$

$$\frac{\partial^2 \mu^v}{\partial c^v \partial \xi} = 0 \quad (\text{C.39})$$

$$\begin{aligned} \frac{\partial^2 \mu^v}{\partial c^{v2}} &= \frac{\partial^3 \psi}{\partial c^{v3}} - \frac{\partial^2 h}{\partial c^{v2}} \left(\tilde{\eta}^{v,\alpha} : \frac{\partial f_{mech}^\alpha}{\partial \xi^{e-\alpha}} - \tilde{\eta}^{v,\beta} : \frac{\partial f_{mech}^\beta}{\partial \xi^{e-\beta}} \right) \\ &= \frac{\partial^3 \psi_0}{\partial c^{v3}} + \frac{\partial^3 h}{\partial c^{v3}} \left(f_{mech}^\alpha - f_{mech}^\beta \right) - \frac{\partial^2 h}{\partial c^{v2}} \left(\tilde{\eta}^{v,\alpha} : \frac{\partial f_{mech}^\alpha}{\partial \xi^{e-\alpha}} - \tilde{\eta}^{v,\beta} : \frac{\partial f_{mech}^\beta}{\partial \xi^{e-\beta}} \right) \end{aligned} \quad (\text{C.40})$$

$$\begin{aligned} \frac{\partial^2 \mu^v}{\partial c^v \partial c_\chi} &= \frac{\partial^3 \psi_{pen}}{\partial c^{v2} \partial c_\chi} \\ &= 0 \end{aligned} \quad (\text{C.41})$$

$$\frac{\partial^2 \mu^v}{\partial c^v \partial \phi^{\text{GB}}} = 0 \quad (\text{C.42})$$

$$\frac{\partial^2 \mu^v}{\partial c_\chi^2} = 0 \quad (\text{C.43})$$

$$\frac{\partial^2 \mu^v}{\partial c_\chi \partial \phi^{\text{GB}}} = 0 \quad (\text{C.44})$$

C.2.2 Free energy

The derivatives of the free energy with respect to the state variable are given below, for each contribution: chemical (for the logarithmic one), interfacial, and mechanical.

C.2.2.1 First order

Interfacial

$$\frac{\partial \psi_{pen}}{\partial c_\chi} = -H_\chi (c^v - c_\chi) \quad (\text{C.45})$$

$$\frac{\partial \psi_{pen}}{\partial c^v} = H_\chi (c^v - c_\chi) \quad (\text{C.46})$$

$$\frac{\partial \psi_{int}}{\partial \underline{\nabla} c_\chi} = \alpha \underline{\nabla} c_\chi \quad (\text{C.47})$$

Chemical Logarithmic

$$\frac{\partial \psi_0}{\partial c^v} = \frac{RT}{\Omega_0} \ln \left(\frac{c^v}{1 - c^i - c^v} \right) + \omega (1 - 2c^v) \quad (\text{C.48})$$

$$\frac{\partial \psi_0}{\partial c^i} = \frac{E_f^i}{\Omega_0} + \frac{RT}{\Omega_0} \ln \left(\frac{c^i}{1 - c^i - c^v} \right) \quad (\text{C.49})$$

Quad

$$\frac{\partial \psi_0}{\partial c^v} = \frac{\partial h}{\partial c^v} (f_{0,i}^\alpha - f_{0,i}^\beta) + 16W (4c^{v3} - 6c^{v2} + 2c^v) \quad (\text{C.50})$$

$$\begin{aligned} \frac{\partial \psi_0}{\partial c^i} &= h \frac{\partial f_{0,i}^\alpha}{\partial c^i} + \bar{h} \frac{\partial f_{0,i}^\beta}{\partial c^i} \\ &= h k^{i,\alpha} (c^i - c_{eq,\alpha}^i) + \bar{h} k^{i,\beta} (c^i - c_{eq,\beta}^i) \end{aligned} \quad (\text{C.51})$$

Mechanical

$$\frac{\partial f_{mech}^k}{\partial \underline{\xi}^{e-k}} = \underline{\Lambda}^k : \underline{\xi}^{e-k}, \text{ with } k = \{\alpha, \beta\} \quad (\text{C.52})$$

$$\frac{\partial \psi_{mech}}{\partial c_\chi} = \frac{\partial h}{\partial c^v} (f_{mech}^\alpha - f_{mech}^\beta) \quad (\text{C.53})$$

C.2.2.2 Second order

Interfacial

$$\frac{\partial^2 \psi_{pen}}{\partial c^v \partial c_\chi} = -H_\chi \quad (\text{C.54})$$

$$\frac{\partial^2 \psi_{pen}}{\partial c_\chi^2} = H_\chi \quad (\text{C.55})$$

$$\frac{\partial^2 \psi_{pen}}{\partial c^v^2} = H_\chi \quad (\text{C.56})$$

Chemical Logarithmic

$$\frac{\partial^2 \psi_0}{\partial c^i^2} = \frac{RT}{\Omega_0} \frac{1 - c^v}{c^i(1 - c^i - c^v)} \quad (\text{C.57})$$

$$\frac{\partial^2 \psi_0}{\partial c^v^2} = \frac{RT}{\Omega_0} \frac{1 - c^i}{c^v(1 - c^i - c^v)} - 2\omega \quad (\text{C.58})$$

$$\frac{\partial^2 \psi_0}{\partial c^i \partial c^v} = \frac{RT}{\Omega_0} \frac{1}{1 - c^i - c^v} \quad (\text{C.59})$$

Quadratic

$$\frac{\partial^2 \psi_0}{\partial c^i^2} = h k^{i,\alpha} + \bar{h} k^{i,\beta} \quad (\text{C.60})$$

$$\frac{\partial^2 \psi_0}{\partial c^v^2} = \frac{\partial^2 h}{\partial c^v^2} (f_{0,i}^\alpha - f_{0,i}^\beta) + 16W (12c^{v2} - 12c^v + 2) \quad (\text{C.61})$$

$$\frac{\partial^2 \psi_0}{\partial c^i \partial c^v} = \frac{\partial h}{\partial c^v} \left(\frac{\partial f_{0,i}^\alpha}{\partial c^i} - \frac{\partial f_{0,i}^\beta}{\partial c^i} \right) \quad (\text{C.62})$$

Mechanical

$$\frac{\partial^2 f_{mech}^k}{\partial \underline{\xi}^{e-k} \partial \underline{\xi}^{e-k}} = \Lambda^k, \text{ with } k = \{\alpha, \beta\} \quad (\text{C.63})$$

$$\frac{\partial^2 \psi_{mech}}{\partial c^v \partial \underline{\xi}} = \frac{\partial h}{\partial c^v} \left(\frac{\partial f_{mech}^\alpha}{\partial \underline{\xi}^{e-\alpha}} - \frac{\partial f_{mech}^\beta}{\partial \underline{\xi}^{e-\beta}} \right) \quad (\text{C.64})$$

$$\frac{\partial^2 \psi_{mech}}{\partial c^v^2} = \frac{\partial^2 h}{\partial c^v^2} (f_{mech}^\alpha - f_{mech}^\beta) \quad (\text{C.65})$$

C.2.2.3 Third order

Logarithmic

$$\frac{\partial^3 \psi_0}{\partial c^{i^3}} = \frac{RT}{\Omega_0} \left(-\frac{1}{c^{i^2}} - \frac{1}{(1 - c^i - c^v)^2} \right) \quad (\text{C.66})$$

$$\frac{\partial^3 \psi_0}{\partial c^{i^2} \partial c^v} = \frac{RT}{\Omega_0} \left(-\frac{1}{(1 - c^i - c^v)^2} \right) \quad (\text{C.67})$$

$$\frac{\partial^3 \psi_0}{\partial c^{v^2} \partial c^i} = \frac{RT}{\Omega_0} \left(-\frac{1}{(1 - c^i - c^v)^2} \right) \quad (\text{C.68})$$

$$\frac{\partial^3 \psi_0}{\partial c^{v^3}} = \frac{RT}{\Omega_0} \left(-\frac{1}{c^{v^2}} - \frac{1}{(1 - c^i - c^v)^2} \right) \quad (\text{C.69})$$

Quadratic

$$\frac{\partial^3 \psi_0}{\partial c^{i^3}} = 0 \quad (\text{C.70})$$

$$\frac{\partial^3 \psi_0}{\partial c^{i^2} \partial c^v} = 0 \quad (\text{C.71})$$

$$\frac{\partial^3 \psi_0}{\partial c^{v^2} \partial c^i} = \frac{\partial^2 h}{\partial c^{v^2}} \left(\frac{\partial f_{0,i}^\alpha}{\partial c^i} - \frac{\partial f_{0,i}^\beta}{\partial c^i} \right) \quad (\text{C.72})$$

$$\frac{\partial^3 \psi_0}{\partial c^{v^3}} = \frac{\partial^3 h}{\partial c^{v^3}} (f_{0,i}^\alpha - f_{0,i}^\beta) + 16W (24c^v - 12) \quad (\text{C.73})$$

C.2.3 Misc

Miscellaneous derivatives needed in the numerical implementation, such as the one related to the interpolation functions, are given in this section.

$$\begin{aligned} \frac{\partial \tilde{\eta}^{i,\alpha}}{\partial \phi_{\text{GB}}} &= -\eta_{\text{bulk}}^{i,\alpha} \underline{\mathbf{I}} + \eta_{\text{GB}}^{i,\alpha} \underline{\mathbf{n}} \otimes \underline{\mathbf{n}} \\ \frac{\partial \tilde{\eta}^{i,\beta}}{\partial \phi_{\text{GB}}} &= -\eta_{\text{bulk}}^{i,\beta} \underline{\mathbf{I}} + \eta_{\text{GB}}^{i,\beta} \underline{\mathbf{n}} \otimes \underline{\mathbf{n}} \\ \frac{\partial \tilde{\eta}^{v,\alpha}}{\partial \phi_{\text{GB}}} &= -\eta_{\text{bulk}}^{v,\alpha} \underline{\mathbf{I}} + \eta_{\text{GB}}^{v,\alpha} \underline{\mathbf{n}} \otimes \underline{\mathbf{n}} \\ \frac{\partial \tilde{\eta}^{v,\beta}}{\partial \phi_{\text{GB}}} &= -\eta_{\text{bulk}}^{v,\beta} \underline{\mathbf{I}} + \eta_{\text{GB}}^{v,\beta} \underline{\mathbf{n}} \otimes \underline{\mathbf{n}} \end{aligned} \quad (\text{C.74})$$

Phase indicator:

$$\frac{\partial \phi}{\partial c^v} = \frac{1}{c_\beta - c_\alpha} \quad (\text{C.75})$$

$$\begin{aligned} \frac{\partial h}{\partial c^v} &= \frac{\partial h}{\partial \phi} \frac{\partial \phi}{\partial c^v} \\ \frac{\partial h}{\partial \phi} &= 6(-\phi^2 + \phi) \end{aligned} \quad (\text{C.76})$$

$$\begin{aligned}\frac{\partial^2 h}{\partial c^v{}^2} &= \frac{\partial^2 h}{\partial \phi^2} \left(\frac{\partial \phi}{\partial c^v} \right)^2 + \frac{\partial h}{\partial \phi} \frac{\partial^2 \phi}{\partial c^v{}^2} \\ \frac{\partial^2 h}{\partial \phi^2} &= 6(-2\phi + 1)\end{aligned}\tag{C.77}$$

$$\begin{aligned}\frac{\partial^3 h}{\partial c^v{}^3} &= \frac{\partial^3 h}{\partial \phi^3} \left(\frac{\partial \phi}{\partial c^v} \right)^3 \\ \frac{\partial^3 h}{\partial \phi^3} &= -12\end{aligned}\tag{C.78}$$

Sources terms:

$$\frac{\partial s^i}{\partial c^i} = (-K_{iv}c^v - K_{si})\bar{h}\tag{C.79}$$

$$\frac{\partial s^i}{\partial c^v} = (-K_{iv}c^i)\bar{h} + \frac{\partial \bar{h}}{\partial \phi} \frac{\partial \phi}{\partial c^v} (K_0 - K_{iv}c^i c^v - K_{si}c^i)\tag{C.80}$$

$$\frac{\partial s^i}{\partial c_\chi} = 0\tag{C.81}$$

$$\frac{\partial s^i}{\partial \phi^{\text{GB}}} = \frac{\partial K_{iv}}{\partial \phi^{\text{GB}}} c^i c^v - \frac{\partial K_{si}}{\partial \phi^{\text{GB}}}\tag{C.82}$$

$$\frac{\partial s^v}{\partial c^i} = \bar{h}(-K_{iv}c^v)\tag{C.83}$$

$$\frac{\partial s^v}{\partial c^v} = \frac{\partial \bar{h}}{\partial c^v} (K_0 - K_{iv}c^i c^v - K_{sv}c^v) + \bar{h}(-K_{iv}c^i - K_{sv})\tag{C.84}$$

$$\frac{\partial s^v}{\partial c_\chi} = 0\tag{C.85}$$

$$\frac{\partial s^v}{\partial \phi^{\text{GB}}} = \frac{\partial K_{iv}}{\partial \phi^{\text{GB}}} c^i c^v - \frac{\partial K_{si}}{\partial \phi^{\text{GB}}}\tag{C.86}$$

Appendix **D**

Code samples



Bibliography

- [1] N. Abdolrahim, H. M. Zbib, and D. F. Bahr. “Multiscale modeling and simulation of deformation in nanoscale metallic multilayer systems”. *International journal of plasticity* 52 (2014), pp. 33–50. DOI: 10.1016/j.ijplas.2013.04.002 (cit. on pp. 85, 94).
- [2] G. Abrivard, E. P. Busso, S. Forest, and B. Appolaire. “Phase field modelling of grain boundary motion driven by curvature and stored energy gradients, part i: theory and numerical implementation”. *Philosophical magazine* 92.28-30 (2012), pp. 3618–3642 (cit. on pp. 21, 34, 41, 44, 89).
- [3] G. Abrivard, E. Busso, S. Forest, and B. Appolaire. “Phase field modelling of grain boundary motion driven by curvature and stored energy gradients. part ii: application to recrystallisation”. *Philosophical magazine* 92.28-30 (2012), pp. 3643–3664. DOI: 10.1080/14786435.2012.717726. eprint: <http://dx.doi.org/10.1080/14786435.2012.717726> (cit. on p. 41).
- [4] K. Ammar, B. Appolaire, G. Cailletaud, F. Feyel, and S. Forest. “Finite element formulation of a phase field model based on the concept of generalized stresses”. *Computational materials science* 45.3 (2009), pp. 800–805. DOI: 10.1016/j.commatsci.2008.09.015 (cit. on pp. 57, 70).
- [5] K. Ammar, B. Appolaire, G. Cailletaud, and S. Forest. “Phase field modeling of elastoplastic deformation induced by diffusion controlled growth of a misfitting spherical precipitate”. *Philosophical magazine letters* 91.3 (2011), pp. 164–172 (cit. on p. 70).
- [6] L. Anand. “A thermo-mechanically-coupled theory accounting for hydrogen diffusion and large elastic-viscoplastic deformations of metals”. *International journal of solids and structures* 48.6 (2011), pp. 962–971 (cit. on p. 13).
- [7] A. El-Azab, K. Ahmed, S. Rokkam, and T. Hochrainer. “Diffuse interface modeling of void growth in irradiated materials. mathematical, thermodynamic and atomistic perspectives”. *Current opinion in solid state and materials science* (2014), pp. 90–98. DOI: 10.1016/j.cossms.2014.01.002 (cit. on pp. 8, 56, 76, 100, 101).

- [8] X.-M. Bai, A. F. Voter, R. G. Hoagland, M. Nastasi, and B. P. Uberuaga. “Efficient annealing of radiation damage near grain boundaries via interstitial emission”. *Science* 327.5973 (2010), pp. 1631–1634. DOI: 10.1126/science.1183723. eprint: <http://www.sciencemag.org/content/327/5973/1631.full.pdf> (cit. on p. 7).
- [9] R. W. Balluffi, S. Allen, and W. Carter. *Kinetics of materials*. John Wiley & Sons, 2005 (cit. on pp. 13, 36, 37, 40, 59, 64, 66).
- [10] R. Balluffi and R. Mehl. “Grain boundary diffusion mechanisms in metals”. *Metallurgical transactions a* 13.12 (1982), pp. 2069–2095. DOI: 10.1007/BF02648378 (cit. on p. 42).
- [11] R. Balluffi and L. Seigle. “Growth of voids in metals during diffusion and creep”. *Acta metallurgica* 5.8 (1957), pp. 449–454. DOI: 10.1016/0001-6160(57)90063-9 (cit. on p. 8).
- [12] F. Barbe, S. Forest, and G. Cailletaud. “Intergranular and intragranular behavior of polycrystalline aggregates. part 2: results”. *International journal of plasticity* 17.4 (2001), pp. 537–563. DOI: 10.1016/S0749-6419(00)00062-0 (cit. on pp. 33, 49).
- [13] A. Barbu and J.-P. Massoud. “Comportement des matériaux dans le cœur des REP”. *Techniques de l’ingénieur matériaux pour le nucléaire* (2014) (cit. on p. 2).
- [14] L. Bassman, K. Garikipati, and M. Deal. “Computational modeling with a new lattice-based continuum formulation for the coupled thermodynamic and mechanical equilibrium of polycrystalline solids”. *1999 international conference on modeling and simulation of microsystems*. PUBLISHING OFFICE, 308 ONE KENDALL SQ BLDG 600, CAMBRIDGE, MA 02139 USA: COMPUTATIONAL PUBLICATIONS, 1999, pp. 459–462 (cit. on p. 8).
- [15] V. Berdichevsky, P. Hazzledine, and B. Shoykhet. “Micromechanics of diffusional creep”. *International journal of engineering science* 35.10-11 (1997), pp. 1003–1032. DOI: 10.1016/S0020-7225(97)00005-0 (cit. on pp. 8, 33, 38).
- [16] J. Besson, G. Cailletaud, J.-L. Chaboche, and S. Forest. *Non-linear mechanics of materials*. Springer, 2010 (cit. on pp. 7, 19, 21, 44, 52).
- [17] I. Beyerlein, A. Caro, M. Demkowicz, N. Mara, A. Misra, and B. Uberuaga. “Radiation damage tolerant nanomaterials”. *Materials today* 16.11 (2013), pp. 443–449. DOI: 10.1016/j.mattod.2013.10.019 (cit. on p. 4).
- [18] I. Beyerlein, J. Mayeur, R. McCabe, S. Zheng, J. Carpenter, and N. Mara. “Influence of slip and twinning on the crystallographic stability of bimetal interfaces in nanocomposites under deformation”. *Acta materialia* 72 (2014), pp. 137–147. DOI: 10.1016/j.actamat.2014.03.041 (cit. on pp. 8, 86).
- [19] I. J. Beyerlein, N. A. Mara, D. Bhattacharyya, D. J. Alexander, and C. T. Necker. “Texture evolution via combined slip and deformation twinning in rolled silver–copper cast eutectic nanocomposite”. *International journal of plasticity* 27.1 (2011), pp. 121–146. DOI: <http://dx.doi.org/10.1016/j.ijplas.2010.05.007> (cit. on p. 106).
- [20] I. J. Beyerlein, N. A. Mara, J. S. Carpenter, T. Nizolek, W. M. Mook, T. A. Wynn, R. J. McCabe, J. R. Mayeur, K. Kang, S. Zheng, J. Wang, and T. M. Pollock. “Interface-driven microstructure development and ultra high strength of bulk nanostructured Cu-Nb multilayers fabricated by severe plastic deformation”. *Journal of materials research* 28 (13 July 2013), pp. 1799–1812. DOI: 10.1557/jmr.2013.21 (cit. on pp. 85, 89, 91, 106).

- [21] I. J. Beyerlein, J. R. Mayeur, S. Zheng, N. A. Mara, J. Wang, and A. Misra. “Emergence of stable interfaces under extreme plastic deformation”. *Proceedings of the national academy of sciences* (2014). DOI: [10.1073/pnas.1319436111](https://doi.org/10.1073/pnas.1319436111). eprint: <http://www.pnas.org/content/early/2014/03/06/1319436111.full.pdf+html> (cit. on pp. 5, 85).
- [22] I. J. Beyerlein, J. Wang, and R. Zhang. “Mapping dislocation nucleation behavior from bimetal interfaces”. *Acta materialia* 61.19 (2013), pp. 7488–7499. DOI: <http://dx.doi.org/10.1016/j.actamat.2013.08.061> (cit. on p. 86).
- [23] C. Bouchet, B. Tanguy, J. Besson, and S. Bugat. “Prediction of the effects of neutron irradiation on the charpy ductile to brittle transition curve of an a508 pressure vessel steel”. *Computational materials science* 32.3-4 (Mar. 2005), pp. 294–300. DOI: [10.1016/j.commatsci.2004.09.039](https://doi.org/10.1016/j.commatsci.2004.09.039) (cit. on p. 3).
- [24] J. W. Cahn, C. M. Elliott, and A. Novick-Cohen. “The Cahn-Hilliard equation with a concentration dependent mobility: motion by minus the laplacian of the mean curvature”. *European journal of applied mathematics* 7 (03 June 1996), pp. 287–301. DOI: [10.1017/S0956792500002369](https://doi.org/10.1017/S0956792500002369) (cit. on p. 56).
- [25] J. Cahn. “Thermodynamic aspects of cottrell atmospheres”. *Philosophical magazine* (2013), pp. 1–6 (cit. on pp. 7, 13).
- [26] J. Cahn and J. Hilliard. “Free energy of a nonuniform system. i. interfacial free energy”. *The journal of chemical physics* 28 (Feb. 1958), pp. 258–267. DOI: [10.1063/1.1744102](https://doi.org/10.1063/1.1744102) (cit. on pp. 56, 60, 62, 64, 66).
- [27] J. Cahn and F. Larché. “A linear theory of thermochemical equilibrium of solids under stress”. *Acta metallurgica* 21 (1973), pp. 1051–1063 (cit. on pp. 7, 13, 34, 110).
- [28] J. Cahn and F. Larché. “The interactions of composition and stress in crystalline solids”. *Acta metallurgica* 33 (1985), pp. 331–357 (cit. on pp. 13, 18, 19, 33, 34, 39, 109).
- [29] L. Capolungo, D. Spearot, M. Cherkaoui, D. McDowell, J. Qu, and K. Jacob. “Dislocation nucleation from bicrystal interfaces and grain boundary ledges: relationship to nanocrystalline deformation”. *Journal of the mechanics and physics of solids* 55.11 (2007), pp. 2300–2327. DOI: [10.1016/j.jmps.2007.04.001](https://doi.org/10.1016/j.jmps.2007.04.001) (cit. on p. 42).
- [30] J. Carpenter, S. Vogel, J. LeDonne, D. Hammon, I. Beyerlein, and N. Mara. “Bulk texture evolution of Cu-Nb nanolamellar composites during accumulative roll bonding”. *Acta materialia* 60.4 (2012), pp. 1576–1586. DOI: [10.1016/j.actamat.2011.11.045](https://doi.org/10.1016/j.actamat.2011.11.045) (cit. on p. 86).
- [31] K.-S. Cheong and E. P. Busso. “Discrete dislocation density modelling of single phase FCC polycrystal aggregates”. *Acta materialia* 52.19 (2004), pp. 5665–5675. DOI: [10.1016/j.actamat.2004.08.044](https://doi.org/10.1016/j.actamat.2004.08.044) (cit. on pp. 34, 39, 48, 88–90).
- [32] A. D. L. Claire and A. Rabinovitch. “A mathematical analysis of diffusion in dislocations. iii. diffusion in a dislocation array with diffusion zone overlap”. *Journal of physics c: solid state physics* 16.11 (1983), p. 2087 (cit. on p. 39).
- [33] E. Clouet. “The vacancy-edge dislocation interaction in fcc metals: a comparison between atomic simulations and elasticity theory”. *Acta materialia* 54.13 (2006), pp. 3543–3552 (cit. on p. 23).
- [34] U. N. R. Commission. *Pressurized water reactors*. 2014. URL: <http://www.nrc.gov/reactors/pwrs.html> (cit. on p. 3).
- [35] A. Cottrell. *An introduction to metallurgy*. 2nd edition. Edward Arnold, 1975 (cit. on pp. 16, 40).

- [36] V. De Rancourt, K. Ammar, B. Appolaire, E. P. Busso, T. Couvant, and S. Forest. “Homogenization of viscoplasticity constitutive laws using a phase field approach: thermodynamic formulation and application to crystal plasticity”. *Journal of mechanics and physics of solid* (2015) (cit. on p. 70).
- [37] M. J. Demkowicz, R. G. Hoagland, B. P. Uberuaga, and A. Misra. “Influence of interface sink strength on the reduction of radiation-induced defect concentrations and fluxes in materials with large interface area per unit volume”. *Phys. rev. b* 84 (10 2011), p. 104102. DOI: 10.1103/PhysRevB.84.104102 (cit. on p. 42).
- [38] M. Demkowicz, A. Misra, and A. Caro. “The role of interface structure in controlling high helium concentrations”. *Current opinion in solid state and materials science* 16.3 (2012), pp. 101–108. DOI: 10.1016/j.cossms.2011.10.003 (cit. on p. 4).
- [39] M. Demkowicz and L. Thilly. “Structure, shear resistance and interaction with point defects of interfaces in cu–nb nanocomposites synthesized by severe plastic deformation”. *Acta materialia* 59.20 (2011), pp. 7744–7756. DOI: 10.1016/j.actamat.2011.09.004 (cit. on p. 86).
- [40] A. Y. Dunn, L. Capolungo, E. Martinez, and M. Cherkaoui. “Spatially resolved stochastic cluster dynamics for radiation damage evolution in nanostructured metals”. *Journal of nuclear materials* 443.1–3 (2013), pp. 128–139. DOI: 10.1016/j.jnucmat.2013.07.009 (cit. on pp. 56, 78).
- [41] A. Durga, P. Wollants, and N. Moelans. “Evaluation of interfacial excess contributions in different phase-field models for elastically inhomogeneous systems”. *Modelling and simulation in materials science and engineering* 21.5 (2013), p. 055018 (cit. on p. 70).
- [42] A. Dziekonski, P. Sypek, A. Lamecki, and M. Mrozowski. “Finite element matrix generation on a GPU”. *Progress in electromagnetics research-pier* 128 (2012), pp. 249–265. DOI: 10.2528/PIER12040301 (cit. on p. 107).
- [43] C. Elliott and H. Garcke. “On the Cahn-Hilliard equation with degenerate mobility”. *Siam journal on mathematical analysis* 27.2 (1996), pp. 404–423 (cit. on p. 58).
- [44] F. D. Fischer and J. Svoboda. “Substitutional diffusion in multicomponent solids with non-ideal sources and sinks for vacancies”. *Acta materialia* 58.7 (2010), pp. 2698–2707. DOI: 10.1016/j.actamat.2010.01.003 (cit. on p. 33).
- [45] F. Fischer and J. Svoboda. “Chemically and mechanically driven creep due to generation and annihilation of vacancies with non-ideal sources and sinks”. *International journal of plasticity* 27.9 (2011), pp. 1384–1390 (cit. on p. 33).
- [46] S. Forest. “The micromorphic approach to plasticity and diffusion”. *Continuum models and discrete systems* 11. Ed. by P. des Mines. 2007, pp. 105–111 (cit. on pp. 8, 57, 58, 67).
- [47] D. François, A. Pineau, and A. Zaoui. *Mechanical behaviour of materials*. Dordrecht: Springer, 2012 (cit. on pp. 34, 42, 43, 45, 90).
- [48] H. Frost and F. Ashby. *Deformation-mechanism maps: the plasticity and creep of metals and ceramics*. Pergamon Press, 1982 (cit. on p. 25).
- [49] K. Garikipati, L. Bassman, and M. Deal. “A lattice-based micromechanical continuum formulation for stress-driven mass transport in polycrystalline solids”. *Journal of the mechanics and physics of solids* 49.6 (2001), pp. 1209–1237. DOI: 10.1016/S0022-5096(00)00081-8 (cit. on pp. 8, 33, 34, 42, 43, 49).

- [50] S. Garroni, S. Enzo, and F. Delogu. “Mesostructural refinement in the early stages of mechanical alloying”. *Scripta materialia* 83 (2014), pp. 49–52. DOI: <http://dx.doi.org/10.1016/j.scriptamat.2014.04.007> (cit. on p. 107).
- [51] M. G. Geers, M. Cottura, B. Appolaire, E. P. Busso, S. Forest, and A. Villani. “Coupled glide-climb diffusion-enhanced crystal plasticity”. *Journal of the mechanics and physics of solids* 70 (2014), pp. 136–153. DOI: 10.1016/j.jmps.2014.05.007 (cit. on pp. 33, 35, 36, 39, 52).
- [52] L. Gelebart. *Micromechanical modelling of volume diffusion creep in a polycrystalline solid: a stress-diffusion coupled problem*. Private communications. 2008 (cit. on p. 33).
- [53] R. Ghosh. “Creep life predictions of engineering components: problems & prospects”. *Procedia engineering* 55 (2013), pp. 599–606. DOI: 10.1016/j.proeng.2013.03.301 (cit. on p. 39).
- [54] R. Gifkins. “Grain-boundary sliding and its accommodation during creep and superplasticity”. *Metallurgical transactions a* 7.8 (1976), pp. 1225–1232. DOI: 10.1007/BF02656607 (cit. on pp. 42, 51).
- [55] H. Gómez, V. M. Calo, Y. Bazilevs, and T. J. Hughes. “Isogeometric analysis of the Cahn-Hilliard phase-field model”. *Computer methods in applied mechanics and engineering* 197.49–50 (2008), pp. 4333–4352. DOI: 10.1016/j.cma.2008.05.003 (cit. on p. 106).
- [56] V. Grychanyuk, I. Tsukrov, and T. Gross. “Numerical modeling of grain boundary effects in the diffusional creep of copper interconnect lines”. *International journal of fracture* 127.2 (2004), pp. L149–L154. DOI: 10.1023/B:FRAC.0000035089.16019.12 (cit. on pp. 8, 33).
- [57] E. Guggenheim. *Mixtures: the theory of the equilibrium properties of some simple classes of mixtures solutions and alloys*. Clarendon Press, 1952 (cit. on p. 60).
- [58] M. E. Gurtin. “Generalized Ginzburg-Landau and Cahn-Hilliard equations based on a microforce balance”. *Physica d* 92.3-4 (1996), pp. 178–192. DOI: 10.1016/0167-2789(95)00173-5 (cit. on p. 57).
- [59] W. Han, M. J. Demkowicz, N. A. Mara, E. Fu, S. Sinha, A. D. Rollett, Y. Wang, J. S. Carpenter, I. J. Beyerlein, and A. Misra. “Design of radiation tolerant materials via interface engineering”. *Advanced materials* 25.48 (2013), pp. 6975–6979. DOI: 10.1002/adma.201303400 (cit. on pp. 4, 8, 86, 101).
- [60] W. Han, M. Demkowicz, E. Fu, Y. Wang, and A. Misra. “Effect of grain boundary character on sink efficiency”. *Acta materialia* 60.18 (2012), pp. 6341–6351. DOI: 10.1016/j.actamat.2012.08.009 (cit. on pp. 7, 78, 99, 101).
- [61] B. Hansen, J. Carpenter, S. Sintay, C. Bronkhorst, R. McCabe, J. Mayeur, H. Mourad, I. Beyerlein, N. Mara, S. Chen, and G. G. III. “Modeling the texture evolution of cu/nb layered composites during rolling”. *International journal of plasticity* 49 (2013), pp. 71–84. DOI: 10.1016/j.ijplas.2013.03.001 (cit. on pp. 89, 94).
- [62] W. Hereman and W. Malfliet. “The tanh method: a tool to solve nonlinear partial differential equations with symbolic software”. *9th world multi-conference on systemics, cybernetics and informatics*. 2005, pp. 165–168 (cit. on p. 64).
- [63] C. Herring. “Diffusional viscosity of a polycrystalline solid”. *Journal of applied physics* 21 (1950), pp. 437–445 (cit. on pp. 7, 33, 34, 42, 105).
- [64] J. P. Hirth and J. Lothe. *Theory of dislocation*. 2nd edition. John Wiley & Sons, 1982 (cit. on pp. 7, 13, 24, 26).

- [65] R. Hoagland, R. Kurtz, and C. H. Jr. “Slip resistance of interfaces and the strength of metallic multilayer composites”. *Scripta materialia* 50.6 (2004), pp. 775–779. DOI: 10.1016/j.scriptamat.2003.11.059 (cit. on p. 86).
- [66] S. Y. Hu and J. Henager C. H. “Phase-field simulation of void migration in a temperature gradient”. *Acta materialia* 58.9 (2010), pp. 3230–3237. DOI: 10.1016/j.actamat.2010.01.043 (cit. on p. 76).
- [67] A. Kashinath, A. Misra, and M. J. Demkowicz. “Stable storage of helium in nanoscale platelets at semicoherent interfaces”. *Phys. rev. lett.* 110 (8 Feb. 2013), p. 086101. DOI: 10.1103/PhysRevLett.110.086101 (cit. on p. 107).
- [68] S. G. Kim, W. T. Kim, and T. Suzuki. “Phase-field model for binary alloys”. *Physical review e* 60.6 (1999), pp. 7186–7197. DOI: 10.1103/PhysRevE.60.7186 (cit. on p. 56).
- [69] R. Kobayashi, J. A. Warren, and W. C. Carter. “A continuum model of grain boundaries”. *Phys. d* 140.1-2 (2000), pp. 141–150. DOI: 10.1016/S0167-2789(00)00023-3 (cit. on p. 40).
- [70] K. Kolluri and M. J. Demkowicz. “Formation, migration, and clustering of delocalized vacancies and interstitials at a solid-state semicoherent interface”. *Physical review b* 85.20 (2012). DOI: 10.1103/PhysRevB.85.205416 (cit. on pp. 4, 8, 86, 99, 100).
- [71] D. Komatitsch, G. Erlebacher, D. Goeddeke, and D. Michea. “High-order finite-element seismic wave propagation modeling with MPI on a large GPU cluster”. *Journal of computational physics* 229.20 (Oct. 2010), pp. 7692–7714. DOI: 10.1016/j.jcp.2010.06.024 (cit. on p. 107).
- [72] J. Lemaitre and J. Chaboche. *Mechanics of solid materials*. Cambridge University Press, 1994 (cit. on pp. 15–17, 52).
- [73] *L’énergie nucléaire du futur : quelles recherches pour quels objectifs ?* Le Moniteur Editions, 2005 (cit. on pp. 2, 3).
- [74] C. V. D. Leo, E. Rejovitzky, and L. Anand. “A Cahn-Hilliard-type phase-field theory for species diffusion coupled with large elastic deformations: application to phase-separating li-ion electrode materials”. *Journal of the mechanics and physics of solids* (2014), pages. DOI: 10.1016/j.jmps.2014.05.001 (cit. on pp. 56, 60, 61, 64, 66, 72, 77).
- [75] N. Li, J. Wang, A. Misra, and J. Y. Huang. “Direct observations of confined layer slip in cu/nb multilayers”. *Microscopy and microanalysis* 18 (05 Oct. 2012), pp. 1155–1162. DOI: 10.1017/S143192761200133X (cit. on p. 86).
- [76] X. Liu, B. P. Uberuaga, M. J. Demkowicz, T. C. Germann, A. Misra, and M. Nastasi. “Mechanism for recombination of radiation-induced point defects at interphase boundaries”. *Physical review b* 85.1 (2012). DOI: 10.1103/PhysRevB.85.012103 (cit. on pp. 8, 86, 99, 100).
- [77] S. Mao, S. Özerinç, W. P. King, R. S. Averback, and S. J. Dillon. “Effect of irradiation damage on the shear strength of Cu-Nb interfaces”. *Scripta materialia* 90–91 (2014), pp. 29–32. DOI: 10.1016/j.scriptamat.2014.07.009 (cit. on pp. 86, 100).
- [78] N. A. Mara and I. J. Beyerlein. “Review: effect of bimetal interface structure on the mechanical behavior of Cu-Nb fcc-bcc nanolayered composites”. *Journal of materials science* 49.19 (Oct. 2014), pp. 6497–6516. DOI: 10.1007/s10853-014-8342-9 (cit. on pp. 5, 8, 86, 87, 100).

- [79] E. Martinez, A. Caro, and I. J. Beyerlein. “Atomistic modeling of defect-induced plasticity in Cu-Nb nanocomposites”. *Physical review b* 90.5 (Aug. 2014). DOI: 10.1103/PhysRevB.90.054103 (cit. on pp. 8, 86).
- [80] G. A. Maugin. “On the thermomechanics of continuous media with diffusion and/or weak nonlocality”. *Archive of applied mechanics* 75.10-12 (2006), pp. 723–738 (cit. on p. 13).
- [81] J. Mayeur, I. Beyerlein, C. Bronkhorst, and H. Mourad. “Incorporating interface affected zones into crystal plasticity”. *International journal of plasticity* (2014), pages. DOI: 10.1016/j.ijplas.2014.08.013 (cit. on pp. 87, 106).
- [82] D. McDowell and F. Dunne. “Microstructure-sensitive computational modeling of fatigue crack formation”. *International journal of fatigue* 32.9 (2010), pp. 1521–1542. DOI: 10.1016/j.ijfatigue.2010.01.003 (cit. on p. 33).
- [83] Y. Mellbin, H. Hallberg, and M. Ristinmaa. “Accelerating crystal plasticity simulations using GPU multiprocessors”. *International journal for numerical methods in engineering* 100.2 (Oct. 2014), pp. 111–135. DOI: 10.1002/nme.4724 (cit. on p. 107).
- [84] C. Miehe, F. E. Hildebrand, and L. Böger. “Mixed variational potentials and inherent symmetries of the cahn–hilliard theory of diffusive phase separation”. *Proceedings of the royal society a: mathematical, physical and engineering science* 470.2164 (2014). DOI: 10.1098/rspa.2013.0641. eprint: <http://rspa.royalsocietypublishing.org/content/470/2164/20130641.full.pdf+html> (cit. on p. 106).
- [85] C. Miehe, S. Mauthe, and H. Ulmer. “Formulation and numerical exploitation of mixed variational principles for coupled problems of Cahn-Hilliard-type and standard diffusion in elastic solids”. *International journal for numerical methods in engineering* 99.10 (Sept. 2014), pp. 737–762. DOI: 10.1002/nme.4700 (cit. on p. 106).
- [86] P. C. Millett, A. El-Azab, S. Rokkam, M. Tonks, and D. Wolf. “Phase-field simulation of irradiated metals part I: void kinetics”. *Computational materials science* 50 (2011), pp. 949–959 (cit. on pp. 8, 30, 42, 49, 56, 69, 73, 76, 100, 101).
- [87] P. C. Millett, S. Rokkam, A. El-Azab, M. Tonks, and D. Wolf. “Void nucleation and growth in irradiated polycrystalline metals: a phase-field model”. *Modelling and simulation in materials science and engineering* 17.6 (2009). DOI: 10.1088/0965-0393/17/6/064003 (cit. on pp. 8, 56).
- [88] Y. Mishin, J. A. Warren, R. F. Sekerka, and W. J. Boettinger. “Irreversible thermodynamics of creep in crystalline solids”. *Phys. rev. b* 88 (18 2013), p. 184303. DOI: 10.1103/PhysRevB.88.184303 (cit. on pp. 33, 42, 49).
- [89] A. Misra, J. Hirth, and R. Hoagland. “Length-scale-dependent deformation mechanisms in incoherent metallic multilayered composites”. *Acta materialia* 53.18 (2005), pp. 4817–4824. DOI: 10.1016/j.actamat.2005.06.025 (cit. on p. 85).
- [90] M. Monclús, M. Karlik, M. Callisti, E. Frutos, J. LLorca, T. Polcar, and J. Molina-Aldareguía. “Microstructure and mechanical properties of physical vapor deposited cu/w nanoscale multilayers: influence of layer thickness and temperature”. *Thin solid films* 571, Part 2 (2014), pp. 275–282. DOI: <http://dx.doi.org/10.1016/j.tsf.2014.05.044> (cit. on p. 107).
- [91] J. Mosler, O. Shchyglo, and H. M. Hojjat. “A novel homogenization method for phase field approaches based on partial rank-one relaxation”. *Journal of the mechanics and physics of solids* 68 (2014), pp. 251–266. DOI: 10.1016/j.jmps.2014.04.002 (cit. on p. 70).

- [92] H. M. Mourad and K. Garikipati. “Advances in the numerical treatment of grain-boundary migration: coupling with mass transport and mechanics”. *Computer methods in applied mechanics and engineering* 196.1-3 (2006), pp. 595–607. DOI: [10.1016/j.cma.2006.06.005](https://doi.org/10.1016/j.cma.2006.06.005) (cit. on p. 33).
- [93] A. Musienko, G. Cailletaud, and O. Diard. “Damage, opening and sliding of grain boundaries”. *Iutam symposium on multiscale modeling and characterization of elastic-inelastic behavior of engineering materials*. Ed. by S. Ahzi, M. Cherkaoui, M. Khaleel, H. Zbib, M. Zikry, and B. Lamatina. Vol. 114. Springer Netherlands, 2004, pp. 149–156. DOI: [10.1007/978-94-017-0483-0_19](https://doi.org/10.1007/978-94-017-0483-0_19) (cit. on p. 43).
- [94] A. Musienko and G. Cailletaud. “Simulation of inter- and transgranular crack propagation in polycrystalline aggregates due to stress corrosion cracking”. *Acta materialia* 57.13 (2009), pp. 3840–3855. DOI: <http://dx.doi.org/10.1016/j.actamat.2009.04.035> (cit. on p. 43).
- [95] S. R. Niezgodna, A. K. Kanjarla, I. J. Beyerlein, and C. N. Tomé. “Stochastic modeling of twin nucleation in polycrystals: an application in hexagonal close-packed metals”. *International journal of plasticity* 56 (2014), pp. 119–138. DOI: <http://dx.doi.org/10.1016/j.ijplas.2013.11.005> (cit. on p. 106).
- [96] L. Patriarca, W. Abuzaid, H. Sehitoglu, and H. J. Maier. “Slip transmission in bcc fcc polycrystal”. *Materials science and engineering: a* 588 (2013), pp. 308–317. DOI: <http://dx.doi.org/10.1016/j.msea.2013.08.050> (cit. on p. 106).
- [97] M. Paukshto. “Diffusion-induced stresses in solids”. *International journal of fracture* 97.1-4 (1999), pp. 227–236 (cit. on p. 13).
- [98] V. Pavlina and Y. Podstrigach. “Residual stresses due to diffusion in an elastic homogeneous plate”. *Soviet materials science : a transl. of fiziko-khimicheskaya mekhanika materialov / academy of sciences of the ukrainian ssr* 4.4 (1971), pp. 279–283. DOI: [10.1007/BF00722614](https://doi.org/10.1007/BF00722614) (cit. on pp. 7, 13).
- [99] F. Pérez-Pérez and R. Smith. “Structural changes at grain boundaries in bcc iron induced by atomic collisions”. *Nuclear instruments and methods in physics research section b: beam interactions with materials and atoms* 164-165 (2000), pp. 487–494. DOI: [10.1016/S0168-583X\(99\)01141-6](https://doi.org/10.1016/S0168-583X(99)01141-6) (cit. on p. 7).
- [100] J. Philibert. *Diffusion et transport de matière dans les solides*. Éd. de Physique, 1985 (cit. on p. 35).
- [101] Y. Podstrigach and V. Pavlina. “Differential equations of thermodynamic processes in n-component solid solutions”. *Soviet materials science : a transl. of fiziko-khimicheskaya mekhanika materialov / academy of sciences of the ukrainian ssr* 1.4 (1966), pp. 259–264. DOI: [10.1007/BF00714880](https://doi.org/10.1007/BF00714880) (cit. on pp. 7, 13).
- [102] Y. Podstrigach and P. Shevchuk. “Diffusion phenomena and stress relaxation in the vicinity of a spherical void”. *Soviet materials science : a transl. of fiziko-khimicheskaya mekhanika materialov / academy of sciences of the ukrainian ssr* 4.2 (1969), pp. 140–145. DOI: [10.1007/BF00715566](https://doi.org/10.1007/BF00715566) (cit. on pp. 7, 13).
- [103] A. Rajagopal, P. Fischer, E. Kuhl, and P. Steinmann. “Natural element analysis of the Cahn-Hilliard phase-field model”. *Computational mechanics* 46.3 (Aug. 2010), pp. 471–493. DOI: [10.1007/s00466-010-0490-4](https://doi.org/10.1007/s00466-010-0490-4) (cit. on pp. 58, 62).

- [104] H. Rauh and D. Simon. “Diffusion process of point-defects in the stress-field of edge dislocations”. *Physica status solidi a - applied research* 46.2 (1978), pp. 499–510 (cit. on p. 13).
- [105] S. Rokkam, A. El-Azab, P. Millett, and D. Wolf. “Phase field modeling of void nucleation and growth in irradiated metals”. *Modelling and simulation in materials science and engineering* 17.6 (2009), p. 064002. DOI: 10.1088/0965-0393/17/6/064002 (cit. on pp. 8, 76).
- [106] M. Samaras, P. M. Derlet, H. Van Swygenhoven[†], and M. Victoria. “Radiation damage near grain boundaries”. *Philosophical magazine* 83.31-34 (2003), pp. 3599–3607. DOI: 10.1080/14786430310001600222. eprint: <http://www.tandfonline.com/doi/pdf/10.1080/14786430310001600222> (cit. on p. 7).
- [107] P. Shewmon. *Diffusion in solids*. Wiley, 1989 (cit. on p. 25).
- [108] C. Sobie, M. G. McPhie, L. Capolungo, and M. Cherkaoui. “The effect of interfaces on the mechanical behaviour of multilayered metallic laminates”. *Modelling and simulation in materials science and engineering* 22.4 (2014), p. 045007 (cit. on pp. 8, 87, 88, 94–96, 100).
- [109] D. E. Spearot, M. A. Tschopp, K. I. Jacob, and D. L. McDowell. “Tensile strength of \bar{j} 100 \bar{i} and \bar{j} 110 \bar{i} tilt bicrystal copper interfaces”. *Acta materialia* 55.2 (2007), pp. 705–714. DOI: 10.1016/j.actamat.2006.08.060 (cit. on p. 86).
- [110] I. Steinbach. “Phase-field models in materials science”. *Modelling and simulation in materials science and engineering* 17.7 (Oct. 2009), p. 073001. DOI: doi:10.1088/0965-0393/17/7/073001 (cit. on p. 56).
- [111] Z. Suo. “A continuum theory that couples creep and self-diffusion”. *Journal of applied mechanics-transactions of the asme* 71.5 (2004), pp. 646–651. DOI: 10.1115/1.1781176 (cit. on pp. 8, 33).
- [112] J. Svoboda, F. D. Fischer, and P. Fratzl. “Diffusion and creep in multi-component alloys with non-ideal sources and sinks for vacancies”. *Acta materialia* 54.11 (2006), pp. 3043–3053. DOI: 10.1016/j.actamat.2006.02.041 (cit. on pp. 33, 35).
- [113] J. Svoboda, F. Fischer, P. Fratzl, and A. Kroupa. “Diffusion in multi-component systems with no or dense sources and sinks for vacancies”. *Acta materialia* 50.6 (2002), pp. 1369–1381. DOI: 10.1016/S1359-6454(01)00443-8 (cit. on p. 33).
- [114] C. Sweeney, W. Vorster, S. Leen, E. Sakurada, P. McHugh, and F. Dunne. “The role of elastic anisotropy, length scale and crystallographic slip in fatigue crack nucleation”. *Journal of the mechanics and physics of solids* 61.5 (2013), pp. 1224–1240. DOI: 10.1016/j.jmps.2013.01.001 (cit. on p. 33).
- [115] B. Tanguy, A. Parrot, F. Clemendot, and G. Chas. “Assessment of pressure vessel steel irradiation embrittlement up to 40 years using local approach to fracture modelling. application to the french surveillance program”. *Proceedings of the asme pressure vessels and piping conference, vol 3: design and analysis*. Ed. by P. Mertiny. ASME, Pressure Vessels & Pip Div. American Society Mechanical Engineers, 2012, pp. 701–708 (cit. on p. 3).
- [116] J. Thomas and C. Chopin. “Modeling of coupled deformation-diffusion in non-porous solids”. *International journal of engineering science* 37.1 (1999), pp. 1–24 (cit. on pp. 13, 21, 44).

- [117] I. Tsukrov, V. M. Grychanyuk, and T. S. Gross. “Finite element modeling of diffusional creep with explicit consideration of enhanced vacancy diffusivity in a finite region adjacent to the grain interface”. *Mechanics of advanced materials and structures* 15.6-7 (2008), pp. 533–539 (cit. on pp. 8, 33, 34, 42).
- [118] R. L. J. M. Ubachs, P. J. G. Schreurs, and M. G. D. Geers. “A nonlocal diffuse interface model for microstructure evolution of tin-lead solder”. *Journal of the mechanics and physics of solids* 52.8 (2004), pp. 1763–1792. DOI: 10.1016/j.jmps.2004.02.002 (cit. on p. 68).
- [119] Y. Ugurlu and D. Kaya. “Solutions of the Cahn-Hilliard equation”. *Computers and mathematics with applications* 56.12 (2008), pp. 3038–3045. DOI: 10.1016/j.camwa.2008.07.007 (cit. on p. 64).
- [120] A. Villani, E. P. Busso, K. Ammar, S. Forest, and M. G. Geers. “A fully coupled diffusional-mechanical formulation: numerical implementation, analytical validation, and effects of plasticity on equilibrium”. *Archive of applied mechanics* 84.9-11 (2014), pp. 1647–1664. DOI: 10.1007/s00419-014-0860-z (cit. on pp. 11, 40, 44, 61).
- [121] J. Wang, R. Hoagland, J. Hirth, and A. Misra. “Atomistic modeling of the interaction of glide dislocations with “weak” interfaces”. *Acta materialia* 56.19 (2008), pp. 5685–5693. DOI: 10.1016/j.actamat.2008.07.041 (cit. on p. 86).
- [122] J. Wang, R. Hoagland, J. Hirth, and A. Misra. “Atomistic simulations of the shear strength and sliding mechanisms of copper-niobium interfaces”. *Acta materialia* 56.13 (2008), pp. 3109–3119. DOI: 10.1016/j.actamat.2008.03.003 (cit. on pp. 86, 96, 100, 106).
- [123] J. Wang, R. Hoagland, and A. Misra. “Mechanics of nanoscale metallic multilayers: from atomic-scale to micro-scale”. *Scripta materialia* 60.12 (2009), pp. 1067–1072. DOI: 10.1016/j.scriptamat.2008.11.035 (cit. on pp. 8, 89, 96, 106).
- [124] J. Wang, K. Kang, R. Zhang, S. Zheng, I. Beyerlein, and N. Mara. “Structure and property of interfaces in ARB cu/nb laminated composites”. *Jom* 64.10 (2012), pp. 1208–1217. DOI: 10.1007/s11837-012-0429-7 (cit. on pp. 5, 86).
- [125] G. S. Was. *Fundamentals of radiation materials sciences*. Springer, 2007 (cit. on pp. 23, 55, 69, 74, 76).
- [126] Y. Wei and L. Anand. “Grain-boundary sliding and separation in polycrystalline metals: application to nanocrystalline fcc metals”. *Journal of the mechanics and physics of solids* 52.11 (2004), pp. 2587–2616. DOI: <http://dx.doi.org/10.1016/j.jmps.2004.04.006> (cit. on p. 43).
- [127] B. Wilshire and A. Battenbough. “Creep and creep fracture of polycrystalline copper”. *Materials science and engineering: a* 443.1-2 (2007), pp. 156–166 (cit. on pp. 35, 43, 44, 47, 49, 51, 52, 105).
- [128] B. Wilshire and C. Palmer. “Grain size effects during creep of copper”. *Scripta materialia* 46.7 (2002), pp. 483–488. DOI: 10.1016/S1359-6462(01)01247-7 (cit. on p. 43).
- [129] K. Wojciechowski. “Surface energy of metals: theory and experiment”. *Surface science* 437.3 (1999), pp. 285–288. DOI: 10.1016/S0039-6028(99)00741-4 (cit. on p. 73).
- [130] F.-Z. Xuan, S.-S. Shao, Z. Wang, and S.-T. Tu. “Coupling effects of chemical stresses and external mechanical stresses on diffusion”. *Journal of physics d - applied physics* 42.1 (2009), p. 015401 (cit. on p. 13).

- [131] F. Yang. “Interaction between diffusion and chemical stresses”. *Materials science and engineering a- structural materials properties microstructure and processing* 409 (2005), pp. 153–159 (cit. on p. 13).
- [132] L. Zhang and M. J. Demkowicz. “Morphological stability of Cu-Nb nanocomposites under high-energy collision cascades”. *Applied physics letters* 103.6, 061604 (2013), pages. DOI: 10.1063/1.4817785 (cit. on p. 86).



Index

- Accumulated roll bonding, 86
- Balance laws
 - SIA, 69
 - vacancies, 69
- Cahn-Hilliard
 - equation, 58, 73
 - free energy Partition, 71
 - solution
 - critical wavelength, 66
 - interface profile, 65
- Coupling
 - composition dependent eigenstrain, 14
 - equilibrium composition field, 18
 - equilibrium stress field, 18
- Creep
 - diffusion-induced inelastic strain rate, 39
- Eigenstrain
 - choice for Herring diffusion potential, 41

 - composition dependent, 14
- Energy
 - free, partition, 15
 - free, partition, Cahn-Hilliard, 71
 - interface, Cahn-Hilliard, 62
- Equilibrium
 - stress coupled composition field, 18
- Grain
 - phase field description, 41
- Interface
 - multilayers, orientation, 86
 - energy, Cahn-Hilliard, 62
 - profile, Cahn-Hilliard, 65
 - width, Cahn-Hilliard, 65
- Irradiation
 - cascade, 55
 - point defects, 55
- Multilayers
 - processing, 85
- Physical vapor deposition, 86

Modélisation Multiphysique de l'Endommagement par Irradiation de Laminés Nanocristallins

Résumé: Les nano-composites multicouches métalliques cristallins sont capables d'évacuer les défauts ponctuels produits par irradiation, grâce à leur densité d'interface élevée. Ils permettent de retarder le gonflement et de minimiser le fluage, qui mènent à la ruine du matériau. L'objectif de cette thèse est de développer un cadre thermodynamique à l'échelle continue meso et nano-scopique, rendant compte des principaux phénomènes physiques à l'oeuvre dans ces laminés irradiés. Principalement trois points sont abordés: le couplage diffusion-mécanique et le fluage, la nucléation et croissance de cavités sous irradiation, et le comportement mécanique des multicouches.

La micro-structure du matériau est ici entièrement modélisée, afin de précisément rendre compte de son influence sur le comportement du matériau. Le fluage par diffusion est traité via une approche originale où le tenseur des vitesses de déformation est directement relié au gradient du flux de lacunes. Un modèle de type Cahn-Hilliard est utilisé afin de prédire la nucléation et la croissance des cavités. Dans les systèmes multicouches, une zone affecté par l'interface est définie, dans laquelle les dislocations peuvent être annihilées.

Le modèle est implémenté numériquement via la méthode des éléments finis. Des simulations de fluage couplé à la diffusion de lacunes sont pour la première fois réalisé sur des agrégats polycristallins, prédisant des champs de déformation intra-granulaire fortement hétérogènes. De plus, la vitesse de fluage macroscopique obtenue met en évidence les dépendances classiques à la taille de grain ainsi qu'à la contrainte appliquée. Lors des simulations d'irradiation de multicouches, des zones libres de cavités sont prédites de part et d'autre des interfaces, en accord avec les observations expérimentales. Enfin, des essais de traction sont simulés sur des systèmes Cu-Nb en 3D, mettant en évidence un mode de déformation complexe, et un effet moindre de l'anisotropie élastique.

Mots clefs: couplage mécanique diffusion, fluage, cavité, Cahn-Hilliard, laminés nanocristallins, irradiation.

A Multi-Physics Modelling Framework to Describe the Behaviour of Nano-Scale Multilayer Systems Undergoing Irradiation Damage

Abstract: In irradiated materials, the clustering of point defects such as vacancies and self interstitial atoms gives rise to creep, void swelling. Nanoscale metallic multilayer systems have been shown to have the ability to evacuate such point defects, hence delaying the occurrence of critical damage. The objective of this work is to develop a thermodynamically consistent continuum framework at the meso and nano-scales, which accounts for the major physical processes encountered in such metallic multilayer systems and is able to predict their microstructural evolution and behaviour under irradiation. Mainly three physical phenomena are addressed in the present work: stress-diffusion coupling and diffusion induced creep, the void nucleation and growth in multilayer systems under irradiation, and the interaction of dislocations with the multilayer interfaces.

In this framework, the microstructure is explicitly modeled, in order to account accurately for their effects on the system behaviour. The diffusion creep strain rate is related to the gradient of the vacancy flux. A Cahn-Hilliard approach is used to model void nucleation and growth, and the diffusion equations for vacancies and self interstitial atoms are complemented to take into account the production of point defects due to irradiation cascades, the mutual recombination of defects and their evacuation through grain boundaries. In metallic multilayers, an interface affected zone is defined, where dislocations cores are able to spread.

The model is then implemented numerically using the finite elements method. Simulations of biaxial creep of polycrystalline aggregates coupled with vacancy diffusion are performed for the first time, and predict strongly heterogeneous viscoplastic strain fields. The classical macroscopic strain rate dependence on the stress and grain size is also retrieved. Void denuded zones close to the multilayer interfaces are obtained in irradiation simulations of a multilayer, in agreement with experimental observations. Finally, tensile tests of Cu-Nb multilayers are simulated in 3D, where it is shown that the effect of elastic anisotropy is negligible, and evidencing a complex deformation mode.

Keywords: stress-diffusion coupling, creep, voids, Cahn-Hilliard, multilayers, irradiation.